DOE/SF/11564-20
(DE86000301)

FOSSIL ENERGY

SUPRI HEAVY OIL RESEARCH PROGRAM

Ninth Annual Report
October 1, 1984—September 30, 1985

SUPRI TR-52

By
William E. Brigham
Louis M. Castanier
Theodore T. Sumida

October 1986

Stanford University Petroleum Research Institute
Stanford, California

Bartlesville Project Office
U. S. DEPARTMENT OF ENERGY
Bartlesville, Oklahoma

DISCLAIMER

Printed in the United States of America. Available from:
National Technical Information Service
U.S. Department of Commerce
5285 Port Royal Road
Springfield, VA 22161

NTIS price codes
Paper copy: **A10**
Microfiche copy: **A01**

DOE/SF/11564-20
Distribution Category UC-92a

SUPRI HEAVY OIL RESEARCH PROGRAM
NINTH ANNUAL REPORT
October 1, 1984—September 30, 1985

SUPRI TR-52

By
William E. Brigham, Principal Investigator
Louis M. Castanier, Technical Manager
Theodore T. Sumida, Administrative Manager, ed.

October 1986

Work Performed Under Contract No. AC03-81SF11564

H. J. Lechtenberg, Technical Project Officer
San Francisco Operations Office
Fossil Energy Division
1333 Broadway
Oakland, California

Prepared for
U.S. Department of Energy
Assistant Secretary for Fossil Energy

Prepared by
Stanford University Petroleum Research Institute
Stanford University
Stanford, California 94305

ACKNOWLEDGEMENTS

This research is carried out under the Department of Energy contract DE-AC03-81-SF11564. Special thanks are due to Harold Lechtenberg, DOE project officer for his support of the program to the members of SUPRI Industrial Advisory Committee for their suggestions and comment, and to all the student research assistants who contributed to this report.

DISCLAIMER

TABLE OF CONTENTS

SCOPE OF RESEARCH

The Stanford University Petroleum Research Institute (SUPRI) was established in 1976 with the primary purpose of pursuing enhanced oil recovery research. Principal financial support comes from the U.S. Department of Energy, augmented by grants from the oil industry. Industrial support was formalized in 1980 with the formation of the SUPRI Industrial Advisory Committee, whose representatives meet yearly with institute members to review and discuss the status of research projects. SUPRI is part of the Petroleum Engineering Department and coordinates its activities with the Department.

William E. Brigham is the Principal Investigator. Faculty associates include K. Aziz, F.M. Orr, Jr., R.N. Horne, S.S. Marsden, Jr., A.J. Horn, and H.J. Ramey, Jr. A technical and administrative staff of six support the 15-20 student research associates.

The SUPRI expenditures for fiscal year 1984-1985 were $790,000 from the DOE and $95,000 from the petroleum industry. Fifteen companies are members of the SUPRI Industrial Advisory Committee and participate in annual meetings.

The institute has five overall research objectives, which are delineated with a brief summary of SUPRI's recent research efforts below.

PROJECT 1: FLOW PROPERTIES STUDY

To assess the effects of temperature and pressure on relative permeability to oil and water, capillary pressure and electrical resistivity in petroleum reservoirs; and to correlate the data obtained in the laboratory with those at reservoir conditions.

Early results indicate that the absolute permeability to water decreases with a rise in temperature. These results were in agreement with some research work, but differed from other work. Our recent effort has shown that the absolute permeability to water is not dependent on temperature. This work is being extended to more heterogeneous systems.

Measurements were made of relative permeabilities to oil and water at moderate temperature for unconsolidated sands; results indicate that oil-water relative permeabilities are temperature-independent between 20°C and 90°C. Recent data extends this temperature range to 148°C with the same results. This work also explains the reasons for the apparent temperature dependence found in earlier experiments. This work will be continued with the introduction of clays, crude oils rather than refined oils, and greater heterogeneity in the system. Limestone cores will be tried.

During the past year, an apparatus was designed and built that will allow accurate and systematic measurements of capillary pressure curves on unconsolidated sands at reservoir conditions. This will be compared with results from a high temperature centrifuge.

PROJECT 2: IN-SITU COMBUSTION

To evaluate the different parameters affecting combustion field projects, including the study of the reaction kinetics of combustion in the presence of reservoir matrix and crude oil.

A model for the reaction kinetics of *in-situ* combustion was developed. Based on total oxygen consumption, it permits evaluation of the effects of several variables such as rock matrix, clay content, metallic compounds, temperatures, pressures and flow rates on the reaction rates.

Present work focuses in three main directions:

1. On the various processes that lead to fuel deposition (with emphasis on the cracking and coking zone),
2. Laboratory simulation of high-oxygen-concentration *in-situ* combustion, and
3. Methods of automating the experimental apparatus and data gathering for both types of experiment.

High oxygen combustion is being studied, including the effect of CO_2 in heavy oil at high pressure and temperature.

PROJECT 3: STEAM INJECTION WITH ADDITIVES

To develop a process allowing mobility control in steam drives in order to reduce gravity override and channeling of steam, primarily by use of surfactants/foams.

Research has aimed at answering several basic questions:

1. What are the criteria for foam generation and propagation in porous media and how stable are such systems?
2. What is the degree of surfactant partitioning and adsorption in porous media under reservoir conditions?
3. What is the phase interaction between aqueous surfactant solution and oil?
4. What is the mobility of a surfactant-gas system in porous media and what are the mechanisms governing the flow of such systems?

Screening of surfactants for thermal stability, adsorption and partitioning at elevated temperatures was conducted to find those suitable for steam injection and to find the reaction kinetics of surfactant degradation and the equilibrium partitioning coefficients. Various models (including two-dimensional homogeneous, two-dimensional layered and high-pressure, high-temperature, one-dimensional tube) were built to explore and quantify various flooding and foaming phenomena under differing conditions. A series of micromodels (both homogeneous and heterogeneous) were constructed and the pore-level behavior of foam propagation was observed. Since the surfactant/gas systems have been found to act quite differently when oil is present, the work is presently being extended to include interfacial tension measurement.

At the behest and with the financial support of DOE, a field experiment of *in-situ* foaming was begun in Bakersfield, California to verify and extend SUPRI's laboratory findings. Initiated in 1980 and completed 1984, the project has produced very encouraging results. Effects of other additives on steam injection are being studied.

PROJECT 4: RESERVOIR DEFINITION

To improve the techniques of well-to-well formation evaluation such as tracer tests, pressure transient tests, and well logging, and to facilitate the interpretation of such tests.

A method of interpretation has been developed for fall-off tests at the injection well which gives the volume burned in *in-situ* combustion or the volume swept in steam injection. This technique for analyzing fall-off tests has been successfully tested against field data in a number of cases, and new, more accurate models are now being developed to improve reliability.

A comprehensive analysis of the carbon-oxygen log was completed, including a comparison of the techniques developed by various service companies. Various logging techniques have been coded for hand calculators to facilitate interpretation.

A study was completed on the determination of the properties of layered reservoirs through analysis of well-to-well tracer flow at unity mobility ratio. This work will be extended to other mobility ratios and patterns. It will require an extensive and highly accurate computer simulation model in order to solve this problem. A study of the effect of crossflow in layered models is in progress.

A study of single-well tracer flow is in progress. In such tests, a slug of tracer material is injected in one well, allowed to react, and then is produced by the same well after a certain time. The goal is to improve and simplify the technique of analysis of such test.

Another well-testing technique being studied is interference testing in the presence of wellbore storage and skin with the goal of developing appropriate interpretation curves for when these problems are present.

PROJECT 5: FIELD SUPPORT SERVICES

To provide technical support in design and monitoring of enhanced oil recovery field experiments.

Primary effort has been the preliminary lab work and analysis leading to and supporting the steam injection/ *in-situ* foaming field experiment in Bakersfield, California. Other work includes testing of surfactants and cores from several companies, data analysis, and interpretation of well tests and well logs.

Also, a number of U.S. and foreign visitors have come to the laboratories to discuss their laboratory and field projects. This is an important aspect of our research for it *must* be disseminated to become useful.

PROJECT 1: FLOW PROPERTIES STUDY

This section deals with the study of flow properties at the conditions usually found in reservoirs undergoing thermal recovery processes.

1.1 RELATIVE PERMEABILITY STUDY
(Jianshe Wang)

1.1.1. BASIC CONCEPT

Reservoir analysis requires data on effective permeability. This flow characteristic of porous media cannot be directly computed because of the complex nature of the microscopic flow path. It is common to use an empirical approach to determine the effective relative permeability from relative permeability data.

Multi-phase flow is usually treated by deriving the effective permeability of each phase from the individual phase volumetric flow rate, pressure gradients, and viscosity

$$q_i = \frac{K_i A}{\mu_i} \frac{dP}{dl} \tag{1}$$

where:

q_i	= flowrate phase i
A	= cross section of the core
dP/dL	= pressure gradient
μ_i	= viscosity of phase i
K_i	= effective permeability of phase i

The effective permeability, K_i, is generally a function of saturation, wettability, pore geometry and saturation history in terms of drainage imbibition. But, for most cases, the effective permeability, K_i , is considered to be a single-valued function of fluid saturation only. If we normalize the effective permeability to some base permeability, the relative permeability curve vs saturation can be presented, and relative permeability can be stated as the ratio of effective permeability to a base permeability.

The base permeability can be absolute permeability like water permeability, dry air permeability, or effective permeability of the hydrocarbon phase at irreducible water saturation. Therefore, when we talk about relative permeability, it is important to know what base permeability it refers to because the three generally used bases can be quite different in their values for the same porous media.

There are two ways to measure relative permeability in the laboratory: the steady state and dynamic displacement methods. Steady-state relative permeability is directly measured by measuring the flowrates, viscosities, and pressure gradients when individual phases are flowing simultaneously through the porous media at a fixed portion. Calculations are done by directly using Eq. (1). The shortcoming of the steady-state method is that it is time consuming. It requires many hours for the flowrate and pressure drop to be stabilized, and needs a series of runs to cover the whole range of saturation. The dynamic displacement method is less time consuming. A complete relative permeability curve can be generated in a single run. In dynamic runs, one fluid displaces another. The effluent production of both phases and the

pressure drop are measured and the relative permeability can be calculated by using the following equations derived by Welge (1952) and Johnson *et al.* (1959):

$$\bar{S}_w - S_w = F_o W_i \tag{2}$$

$$\frac{K_{rw}}{K_{ro}} \frac{\mu_o}{\mu_w} = \frac{(1 - f_o)}{f_o} \tag{3}$$

$$\frac{f_o}{K_{ro}} = \frac{d\left[\frac{1}{W_2 I_r}\right]}{d\left[\frac{1}{W_i}\right]} \tag{4}$$

$$I_r = \frac{\left[\frac{q}{\Delta P}\right]_t}{\left[\frac{q}{\Delta P}\right]_s} \tag{5}$$

where

$\bar{S}_w$	= average water saturation in the core
S_{w2}	= water saturation at the core outlet
F_o	= fractional volume of oil
K_{rw}, K_{ro}	= relative permeability of water and oil
μ_w, μ_o	= viscosity of water and oil
W_i	= cumulative pore volume of injection
I_r	= relative injectivity
q	= total volumetric flowrate
ΔP	= pressure drop across the core

There are several ways of calculating relative permeability: numerical differential, graphical technique, and curve fitting. Curve fitting is used in this study. The equations used for the curve fitting were originally suggested by Chris MacAskill of Petrophysical Services, Inc. and later modified by Mark A. Miller (1983).

$$N_p = a_o + a_1[\ln(W_i)] + a_2[\ln(W_i)]^2 \tag{6}$$

$$\ln(W_i I_r) = b_o + b_1[\ln(W_i)] + b_2[\ln(W_i)]^2 \tag{7}$$

1.1.2. BRIEF SUMMARY OF PAST WORK

More than a hundred papers about relative permeability are available in the literature. In the last 20 years interest in temperature effects began to increase and much work has been done in this area. However, instead of providing answers relevant to temperature effects,

more questions resulted. The majority of past researchers who studied temperature effects claimed temperature dependence on S_w, S_{or}, relative permeability curves. Varying degrees of temperature effects were found.

The observed changes in relative permeability could be due to capillary number or the wettability changes with temperature as postulated by Poston *et al.* (1970).

However, as Amaefule and Handy (1982) indicated, for interfacial tension above 0.1 dynes/cm, relative permeability is independent of interfacial tension. In the study of endpoint saturation vs capillary number, N_c, temperature independence was found if N_c is below a 10^{-4}. We also know that most displacement experiments occur in a range of capillary numbers which are well below the point where the results are affected.

Different findings and points of view were found in SUPRI. Sufi (1982) studied the temperature effect on relative permeability of a clean sandpack and white oil. The interpretation of his work was that there was no temperature effect on relative permeability curves, S_{wi} and S_{or}.

A main finding of Sufi's work is that the irreducible water saturation was governed by the so-called viscous force, $q\mu_o$ (cc cp/min). The reduction of either flowrate or viscosity can cause an increase on S_{wi} (Fig. 1). Sufi also indicated that this finding may be used to explain past observations of increases of S_{wi} with temperature.

Residual oil saturation was found independent of the temperature level. However, there was actually a reduction in "practical residual saturation." The argument was that the shape change in the fractional flow curve which, due to the change of viscosity ratio with temperature, could result in a different S_{or} even when relative permeabilities remained constant at a certain flooding stage. That means that if water flooding is terminated at a fixed water cut, as most researchers did, great differences in saturation will result for the same water cut; and sufficient water injection would make the fractional flow curves reach to the final saturation. To achieve this final saturation is an experimental challenge because more than 150 PV of injection may be required. Unfortunately, we have not found a better way to solve this problem.

Mark Miller (1983) showed no temperature effects on relative permeability. Two important findings of his work were as follows:

1. A halt of the oil injection, when the oil was injected to build up the S_{wi}, caused the redistribution of fluid and/or pressure gradient field. In turn, that caused a higher oil relative permeability at irreducible water saturation. And this increase of oil relative permeability caused by the redistribution was also increased with the increase of temperature as shown in Fig. 2.
2. Because of the findings in No. 1, relative permeability should be calculated based on single-phase absolute permeability instead of oil effective permeability at irreducible water saturation.

The findings of Sufi and Miller regarding temperature effect on relative permeability was recently supported by M. Polikar *et al.* (1985) in their study on temperature effects on bitumen-water relative permeability.

In the face of contradictions and conflicts of the observed behavior and interpretations presented by researchers, we can probably say that we are still in a position to find more evidence or to reveal more unknowns about this important topic.

1.1.3. A NEW APPARATUS FOR RELATIVE PERMEABILITY EXPERIMENTS

Relative permeability data are sensitive not only to some known factors like saturation history but also to the experimental procedure and the accuracy of the primary measurement. The following problem areas were reported by previous researchers: the difficulties related to the material balance measurement and determination of the influence of dead volumes.

The first step of this study is to improve the apparatus by building an automatic data-gathering system to increase the frequency and accuracy of data points and to modify the fluid network for operational reliability and convenience.

1.1.4. MEASUREMENT SYSTEM

Figure 3 shows the automatic oil-water measuring system. The original idea was suggested by a representative of Conoco at the 1983 SUPRI Industrial Advisory Committee meeting. The total production of oil and water comes into the system through a production line (7). The mixture of oil and water then separates inside the oil confining cup (4). At the same time, some volume of water is produced through the overflow tube (2), and is then measured by an electronic balance (9). The changes of oil volume in the cup (4) is measured by its buoyancy force change through a thin wire (diameter 0.33 mm) connected to another electronic balance (10).

When water is flowing through point A, a slight pressure is needed to overcome the interfacial tension because an oil-wet tube is used. This pressure is provided by a water potential in the neck diameter tube (1) with a height from level A to level B. At the flowrate of 70 cc/hr, this pressure was found to be 14 mm water height that in turn changes the weight of the wire by 0.00116 *g*. This change is an error source.

The neck diameter tube serves two purposes. First, it provides an opening for the oil buoyancy measurement wire. Second, it creates more frequent slug flows from the total production tube. Because the tube diameter is small, a small amount of water provides the hydrostatic head needed to overcome the capillary force.

Digital and voltage signals from the two balances, pressure transducers, and thermocouples are sent to a computer. Time intervals are accounted for by a built-in clock in the computer.

This unit improves the flowrate measurement by 5% over the stopwatch-sight glass method used by previous researchers. The relative error for the oil volume measurement is less than 0.7% for 30 cc oil injected. Table 1 shows the calibration data. The entire apparatus is shown in Fig. 5.

A computer program was written for this apparatus in Basic A and has been proved by inputting published data. Figure 3 is the flow chart for that program.

1.1.5. TEST OF THE APPARATUS

Runs were made to test the entire apparatus. A sandpack of Ottawa sand (170-200 mesh), Blandol oil (30 cp viscosity at room temperature), and distilled water were used for the runs.

The results from the runs indicated the following:

1. The measurement system functions very well. Over 300 datapoints give a smooth production curve (Fig. 6).
2. An automatic water breakthrough judgment approach matches the visually judged breakthrough point. Its validity can be proved by the pressure drop curve (Fig. 7).
3. Curve fitting calculations match the raw data very well. Figure 8 shows the matching of the data of oil recovery vs water injection calculated by Eq. (6). Fig. 9 shows the data of injectivity times cumulative water injection vs water injection calculated by Eq. (7).
4. Figure 10 shows the relative permeability curve calculated by curve fitting method.

1.1.6. STABILITY

One of the main requirements of dynamic water flooding for obtaining relative permeability data is that the run should be carried out at stable flowing conditions to avoid the influence of viscous fingering and end effects.

Rapoport and Leas (1953), working with oil-wet cores, first proposed the concept of a scaling parameter, $L\mu_w v$ (cm^2 cp/min). Above a critical number, $L\mu_w v_x = 2$ approximately, the stabilized flooding condition is reached. Kyte and Rapoport (1958) conducted experiments on water-wet cores and observed similar behavior. The breakover scaling parameter $L\mu_w v_x = 1$ was found. A water-flooding stabilized condition can also be reached, as Kyte and Rapoport suggested, by applying a driving pressure gradient to which the capillary pressure is relatively small.

A recent and popular study on viscous fingering was present by Peters and Flock (1979). Based on theoretical considerations, they introduced a dimensionless number defined as

$$I_{sc} = \left(\frac{\mu_o}{\mu_w} - 1\right) \frac{v\mu_w d^2}{C^* \sigma k} \tag{8}$$

where

I_{sc} = viscous instability number
d = core diameter
C^* = empirical wettability number
σ = interfacial tension
k = absolute permeability
v = flowrate
μ_o, μ_w = viscosity of oil and water.

Stabilized flooding was found to be governed by this dimensionless number I_{sc}, and an unstable displacement will occur if the I_{sc} is beyond its breakpoint value as shown in Fig. 11. Although C*, the wettability number used in Eq. (8) should be empirically determined for any individual system, Peters and Flock suggested a value of 302.5 for a water-wet system. The coinciding number I_{sc} then is supposed to be 13.56.

Sufi's approach is selected because the experimental equipment was available and feasible for this work.

By graphing breakthrough recovery vs flowrate, Sufi found a relationship similar to that found by Peters and Flock (1979). As shown in Fig. 12, as the pump rate increases, breakthrough oil recovery remains constant. This indicates stable displacement. Above 100 cc/hr pump rate, the breakthrough recovery decreases sharply until it reaches a pseudostable region. Breakthrough at the pseudostable region is lower that that at the stable flooding region.

Runs at different rates were made and the results confirmed Sufi's finding. A pump rate of 100 cc/hr or less was found to satisfy the stability requirement. Higher breakthrough recoveries were found in that region. As shown in Table 2, the reason is that a less viscous oil was used and the mobility ratios were more favorable.

1.1.7. ACCOMPLISHMENTS TO DATE

1. Based upon the buoyancy principle, an automated data gathering and monitoring apparatus was built.
2. Successful flowrate, volumetric measurement calibration, and operational tests were conducted.
3. Stability study was made and 100 cc/hr or less pump rate was found to satisfy the stability requirement for the relative permeability experiment. This confirmed Sufi's finding.

Future studies will involve different cores and crude oils.

1.1.8. REFERENCES

1. Amaefule, J. O. and Handy, L.L.: "The Effect of Interfacial Tensions on Relative Oil/Water Permeabilities of Consolidated Porous Media," *Soc. Pet. Eng. J.* (June 1982), 371.

2. Johnson, E.F., Bossler, D. P., and Nauman, V.O.: "Calculation of Relative Permeability from Displacement Experiments," *Trans. AIME* (1959) 216,370.

3. Kyte, J.R. and Rapoport, L.A.: "Linear Waterflood Behaviour and End Effects in Water-Wet Porous Medium," *Trans. AIME* (1958) 213, 423.

4. Miller, M.A.: "Effect of Temperature on Oil-Water Relative Permeabilities of Unconsolidated and Consolidated Sands," Stanford Geothermal Prog., TR-64 (June 1983).

5. Polikar, M.: "Temperature Effects on Bitumen-Water Relative Permeabilities," Paper 85-36-14, presented at the 36th Annual Technical Meeting of Petroleum Society of CIM, Edmonton (June 2-5, 1985).

6. Peters, F. J. and Flock, D.L.: "The Onset of Instability During Two-Phase Immiscible Displacement in Porous Media," paper SPE 8371 presented at the 54th Annual Fall Technical Conference, SPE of AIME, Las Vegas (Sept. 23-26, 1979).

7. Poston, S.W., Ysrael, S., Hossain, A.K.M.S., Montgomery, E. F. III, and Ramey, H. J. Jr. : "The Effect of temperature on Irreducible Water Saturation and Relative Permeability of Unconsolidated Sands," *Soc. Pet. Eng. J.* (June 1970) 171.

8. Rapoport, L.A. and Leas, W.T.: "Properties of Linear Waterfloods," *Trans. AIME* (1953) 198, 139.

9. Sufi, A., Ramey, H.J. Jr., Brigham, W.E.: "Temperature Effects on Oil-Water Relative Permeabilities for Unconsolidated Sands," SUPRI TR-35, (DOE /ET/12056-35, November 1982).

10. Water Drive," *Trans. AIME* (1952), 195, 91.

TABLE 1
MEASUREMENT SYSTEM CALIBRATION DATA

Calibration Datum (May 1985)			
Injected Volume (cc)	Syringe Resolution	Measured Volume	Relative Error To Injection (%)
5.00	0.5	5.023	0.46
10.00	0.05	10.112	1.12
10.00	-	10.104	1.04
20.00	0.5	20.107	0.5
25.00	0.5	25.157	0.6
30.00	0.5	30.222	0.7

TABLE 2
BREAKTHROUGH RECOVERY VS. FLOW RATE

Breakthrough Recovery (PV%)	Flow Rate (cc/hr)
46.203	40
47.889	70
45.222	80
45.523	100

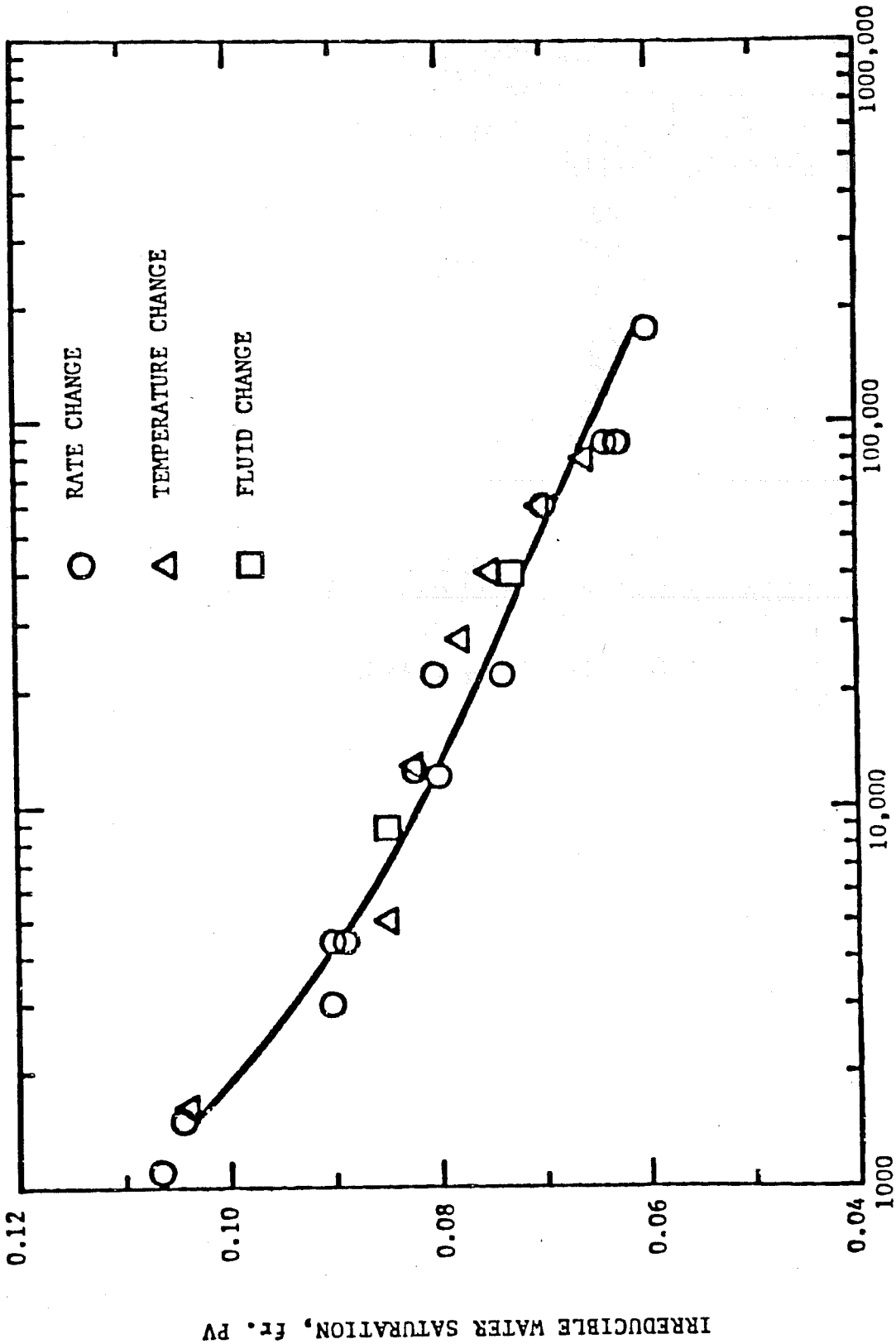

Fig. 1. Irreducible water saturation vs. viscous force (by Sufi).

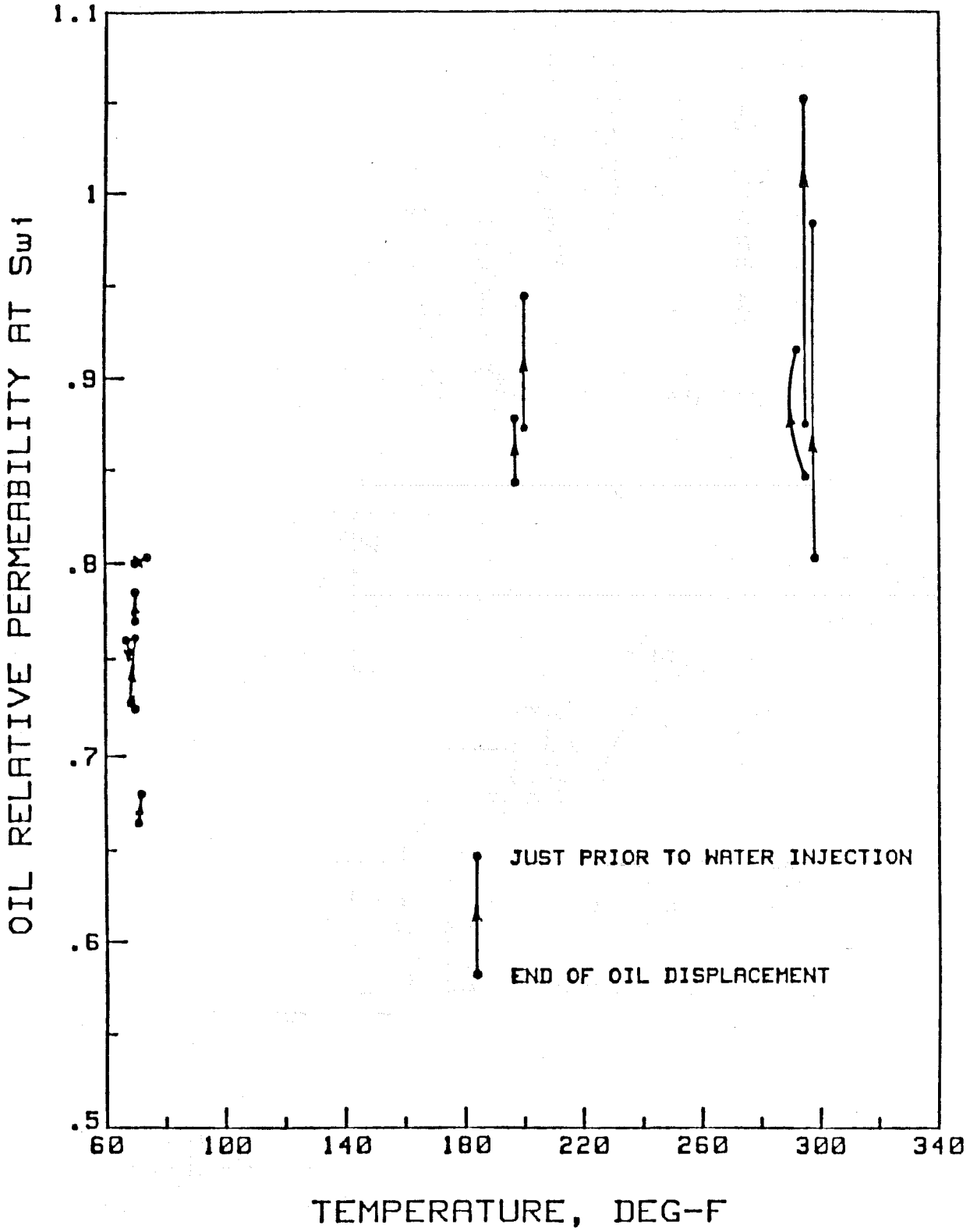

Fig. 2. Oil relative permeabilities at irreducible water saturation--showing changes from end of oil displacement to initiation of water displacement (by Miller).

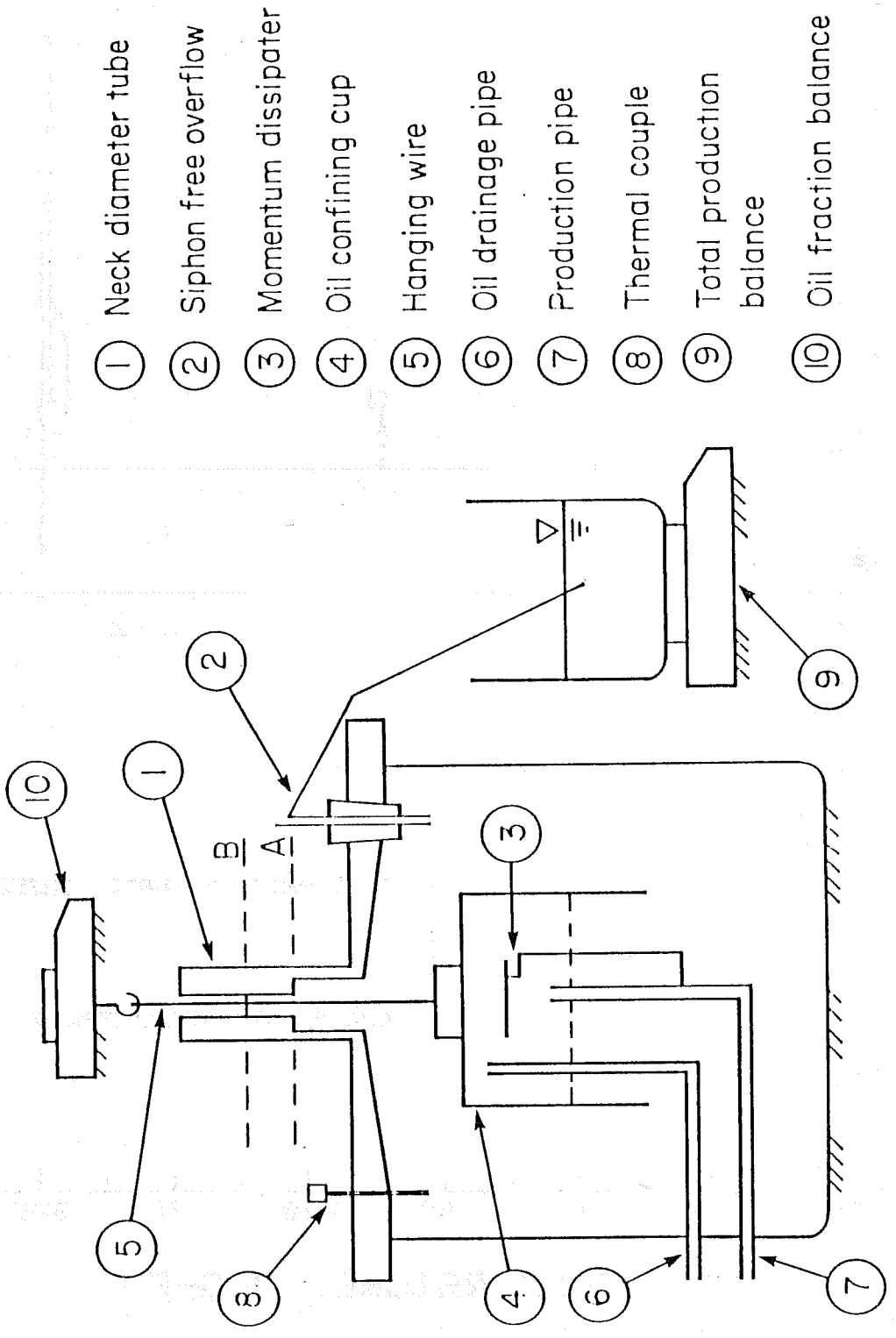

Fig. 3. Measurement unit.

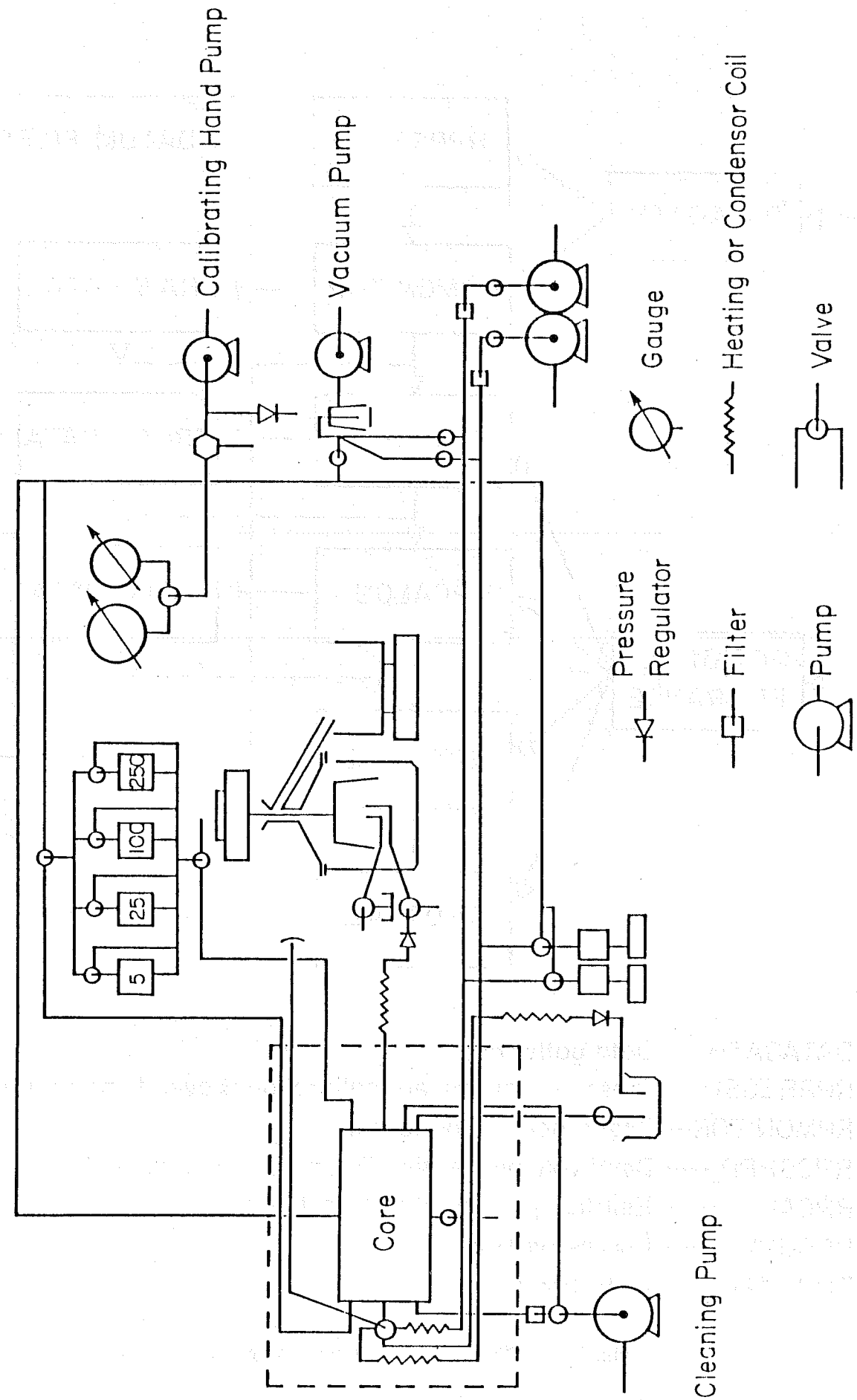

Fig. 4. Schematic diagram of relative permeability apparatus.

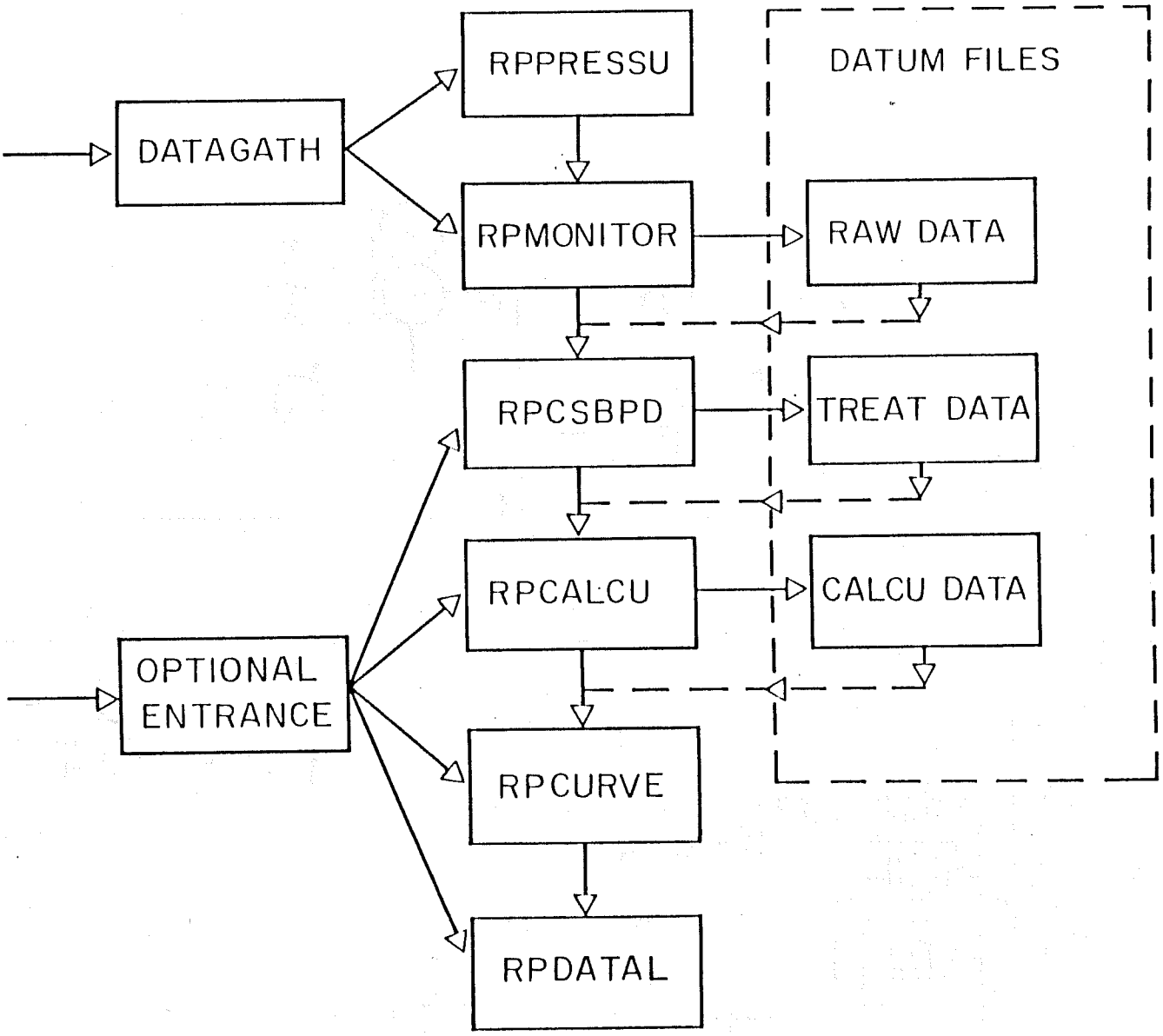

DATAGATH --Data gathering
RPPRESSU --Pressure transducers calibration & oven temperature check.
RPMONITOR--Test process monitoring.
RPCSBPD---Dead volume treating & random bad point deleting.
RPCALCU---Relative permeability calculation.
RPCURVE---Curves plotting.
RPDATAL---Data list out.

Fig. 5. Flow chart of computer program.

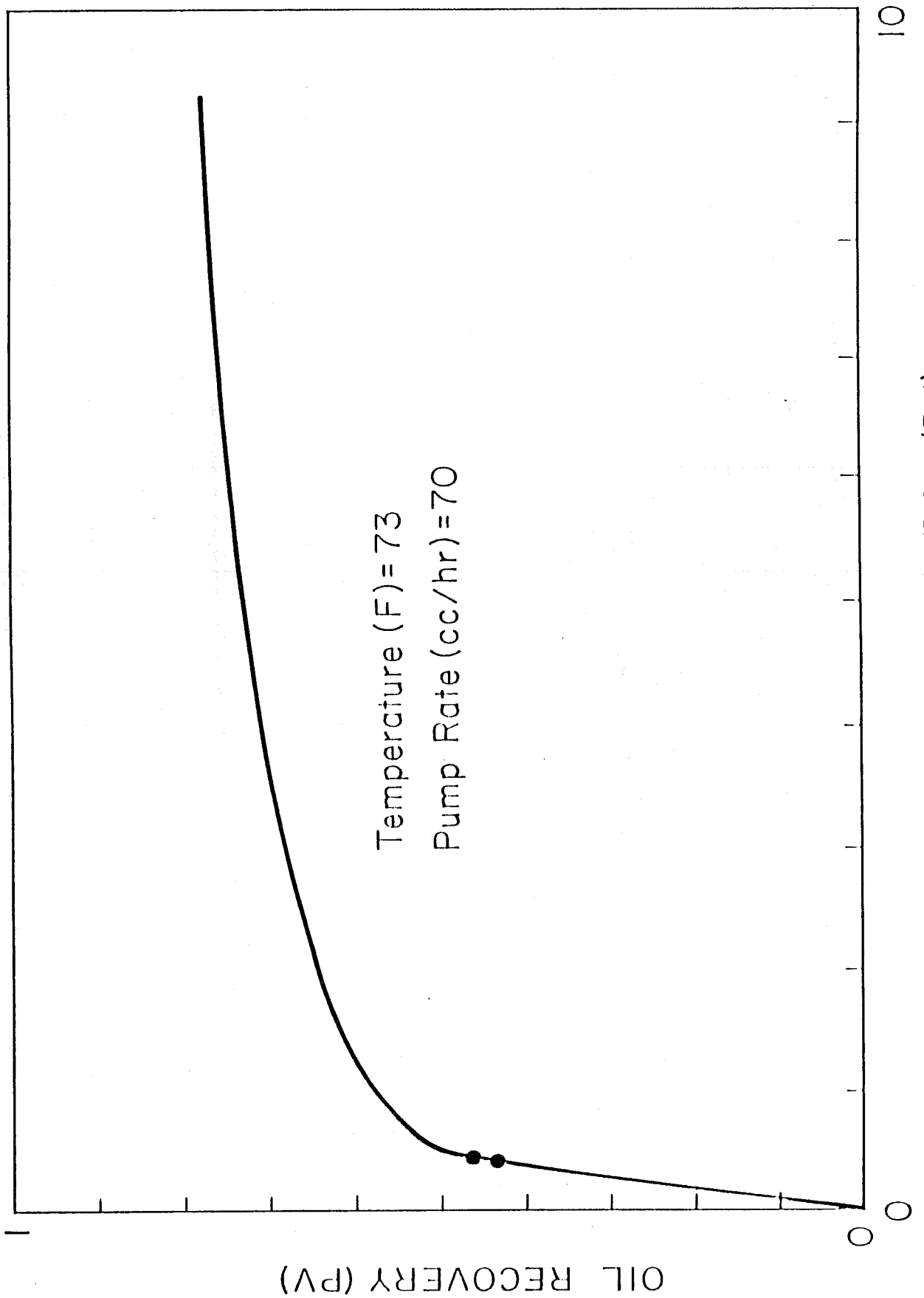

Fig. 6. Raw production data vs. water injection.

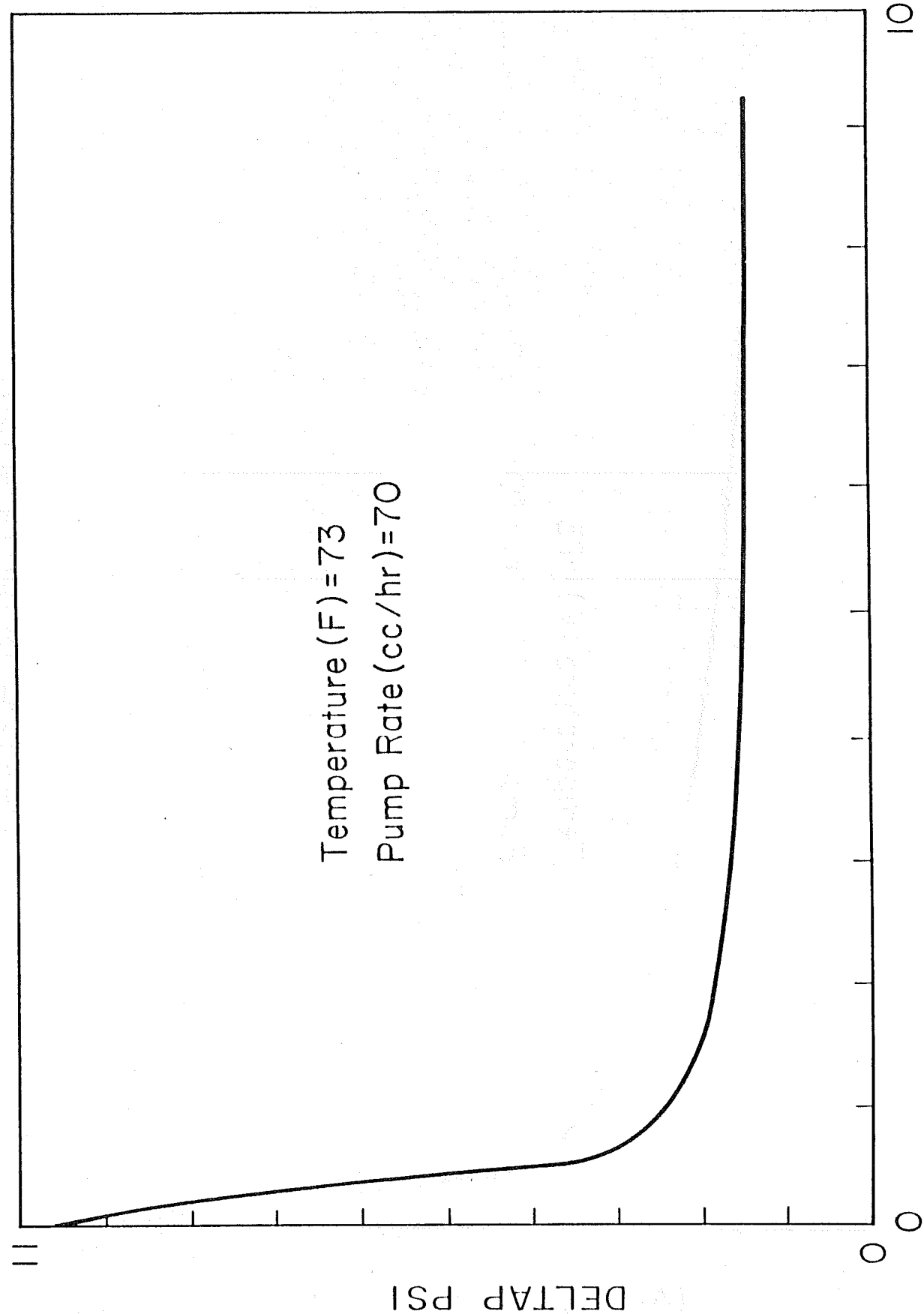

Fig. 7. Pressure drop vs. injection.

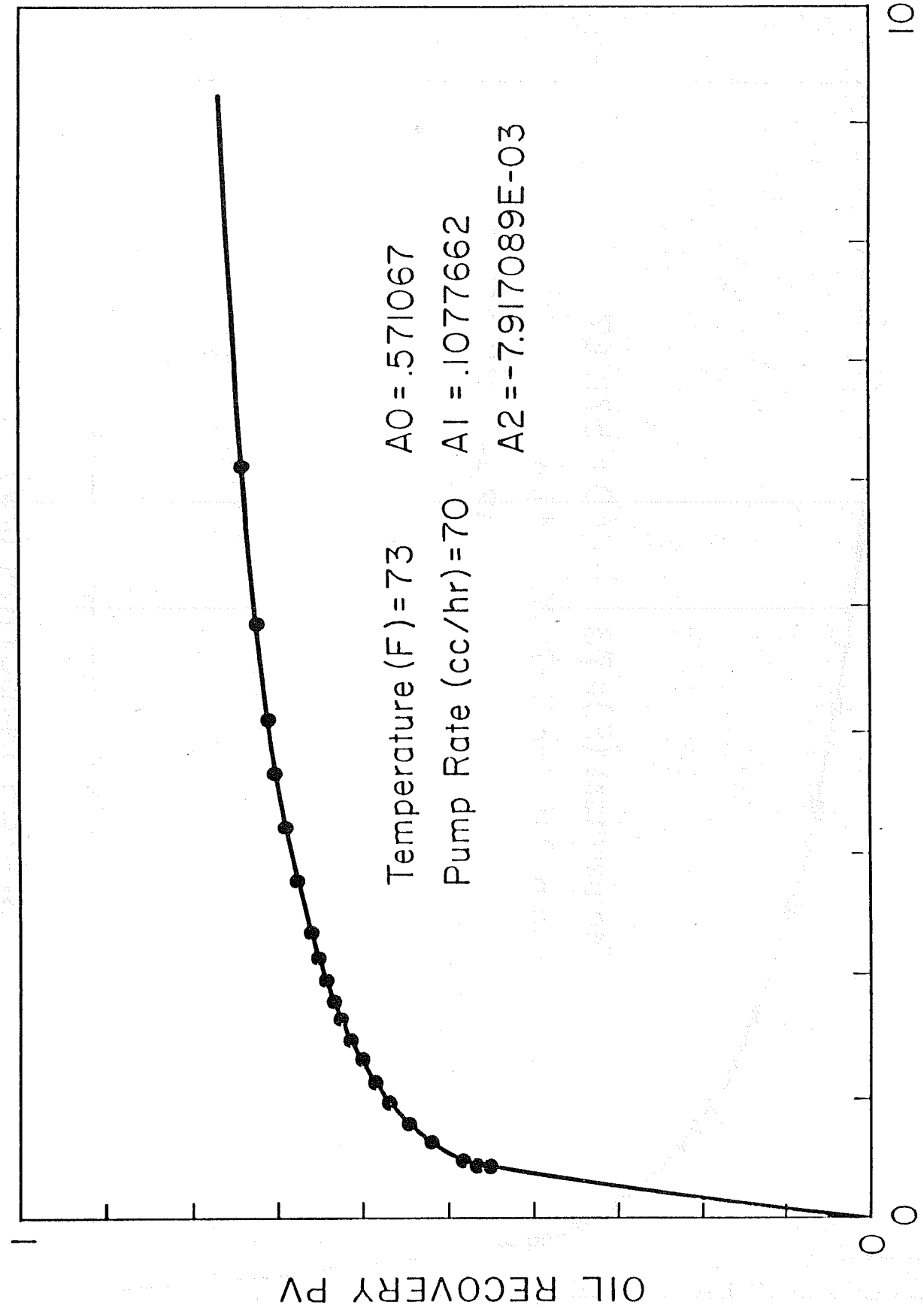

Fig. 8. Oil recovery fraction of PV vs injection.

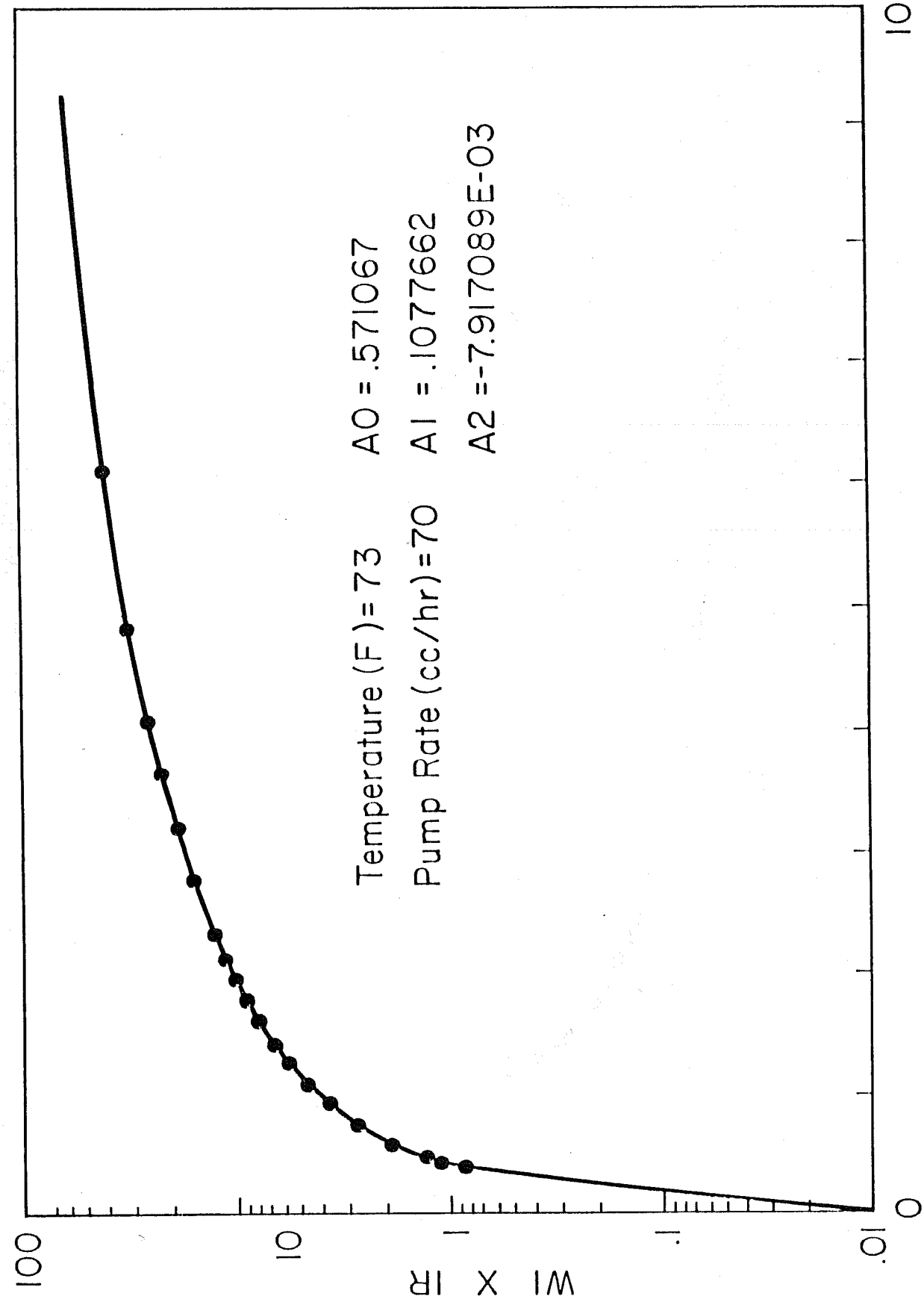

Fig. 9. Injectivity times injection vs. injection curve.

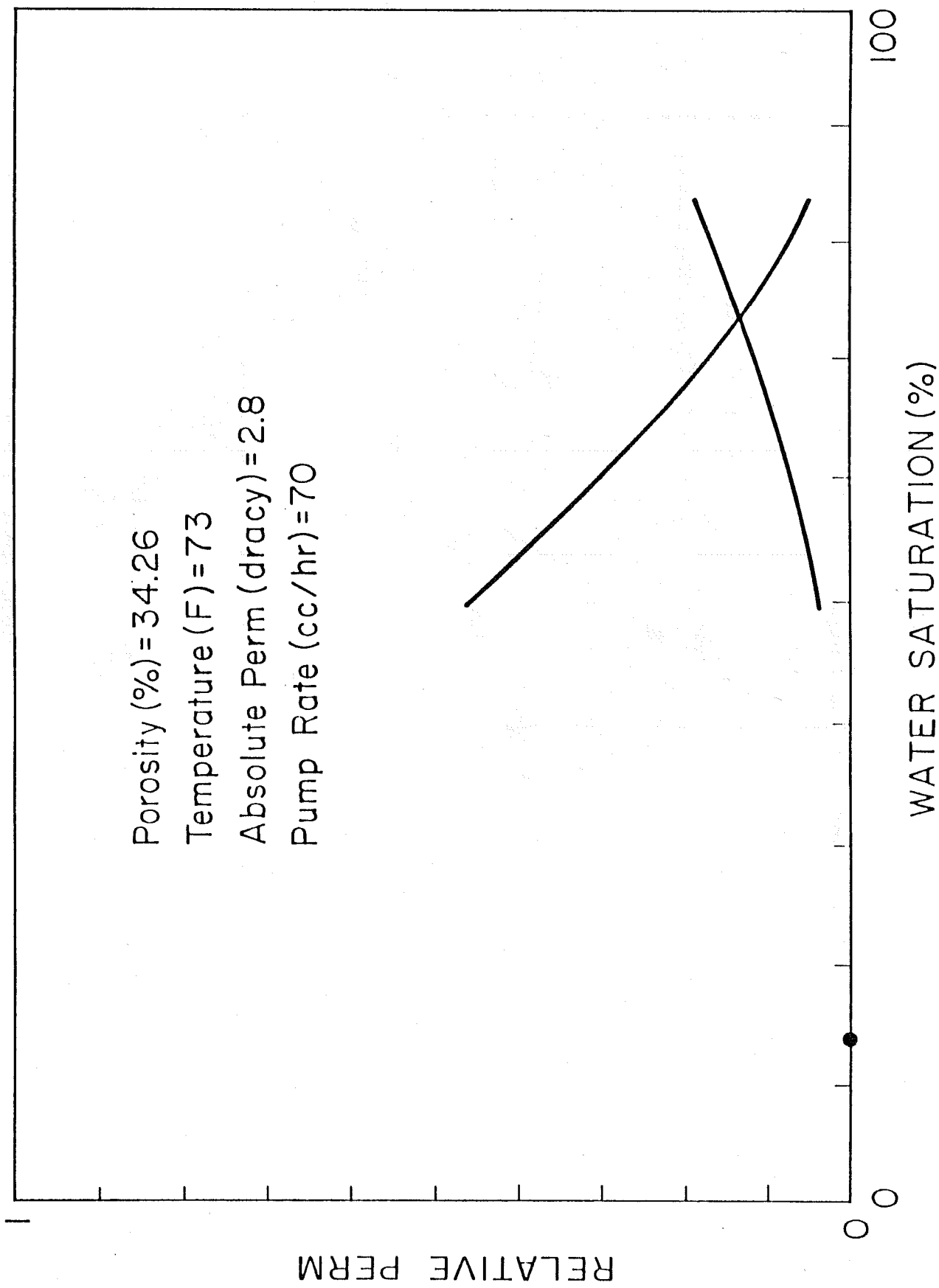

Fig. 10. Relative permeability.

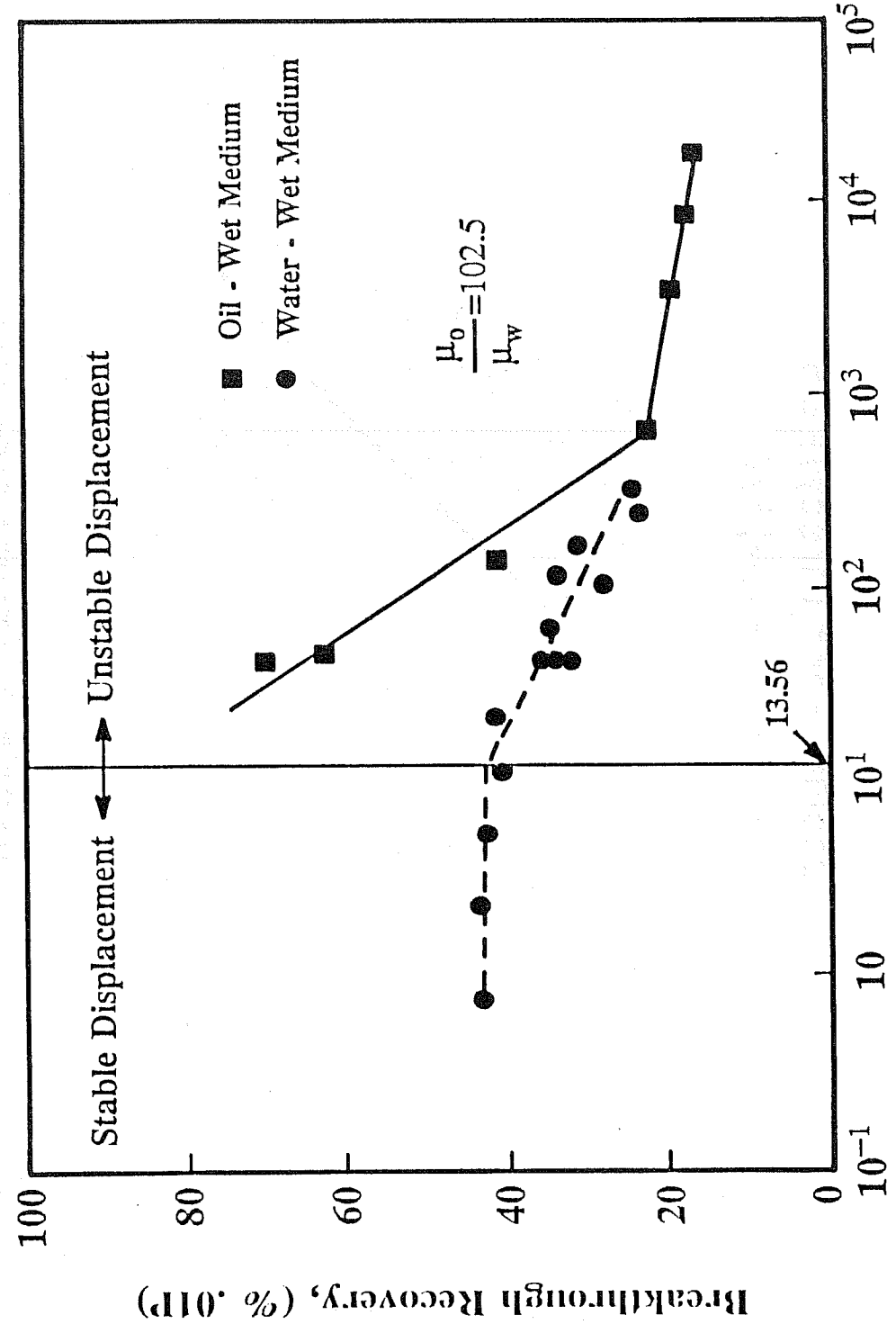

Fig. 11. Instability number vs. breakthrough recovery (by Peters, *et al.*).

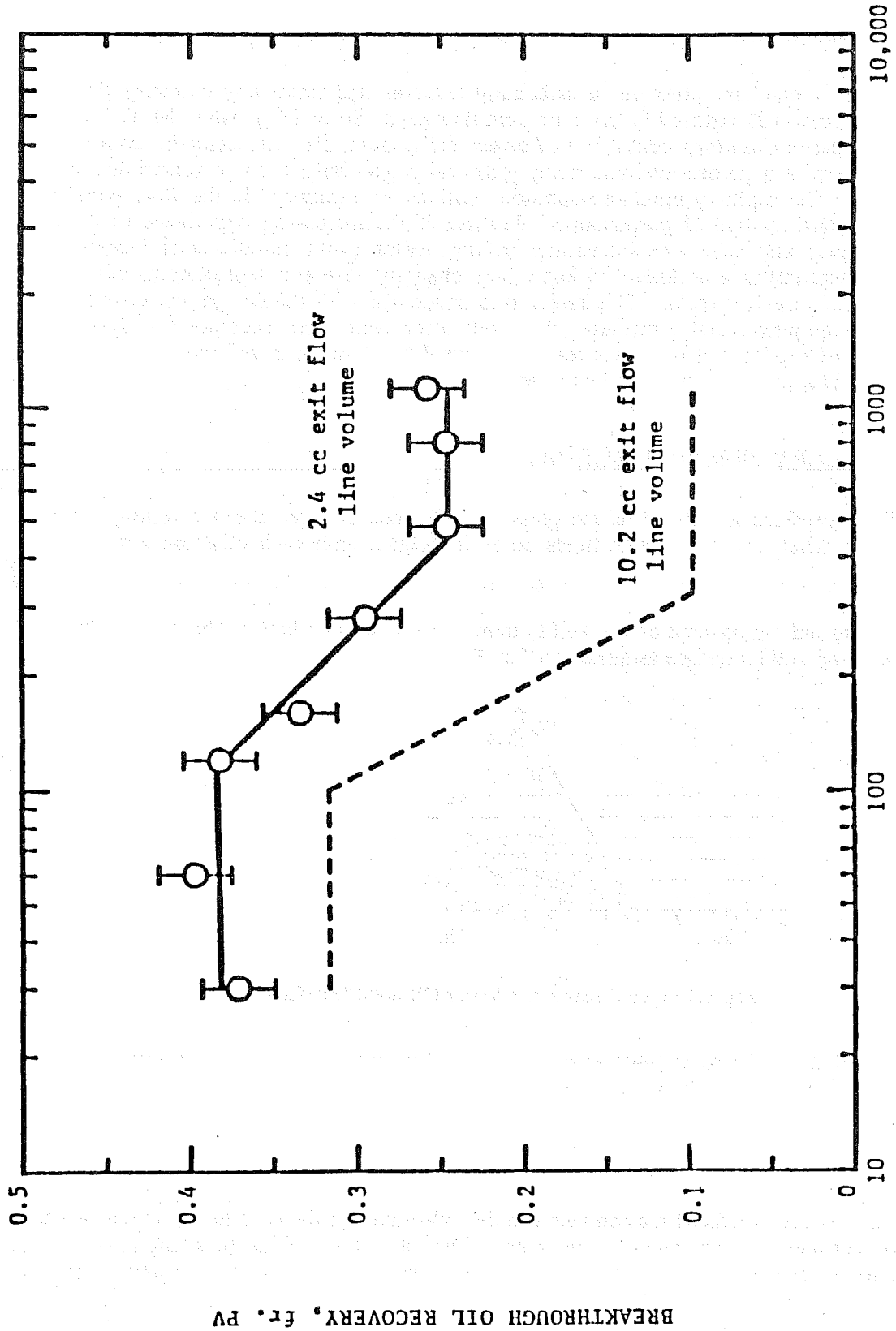

Fig. 12. Flow rate vs. breakthrough (by Sufi).

1.2 CAPILLARY PRESSURE IN FUNCTION OF TEMPERATURE
(Tim Coulter)

1.2.1. INTRODUCTION

The role of capillary pressure in estimating reserves and predicting recovery from oil reservoirs has been well covered in the petroleum literature. Since 1941, when M. C. Leverett published his paper *Capillary Behavior in Porous Solids* describing the essential concepts of capillary pressure in a porous medium, many technical papers have been presented documenting its effects. The capillary pressure-saturation relationship introduced in the 1941 paper has become a standard method of presentation. Because of the increasing importance of thermal recovery methods and with ever-increasing drilling depths (with simultaneous increases in reservoir temperature) it is necessary to know how changing reservoir temperatures will affect the capillarity of reservoir rocks. This research is concerned with the design and construction of laboratory equipment and procedures that will allow simplified, accurate and systematic measurements of capillary pressure curves on unconsolidated sands at reservoir conditions of confining pressure, pore pressure and temperature.

1.2.2. CAPILLARY PRESSURE THEORY

Capillary pressure is defined as the pressure difference between the nonwetting and the wetting phases when two immiscible fluids come in contact with each other on a solid substrate.

To understand the concept of wettability more clearly, we can look at the forces acting at a planar water-oil-solid interface as shown in Fig. 2.1.

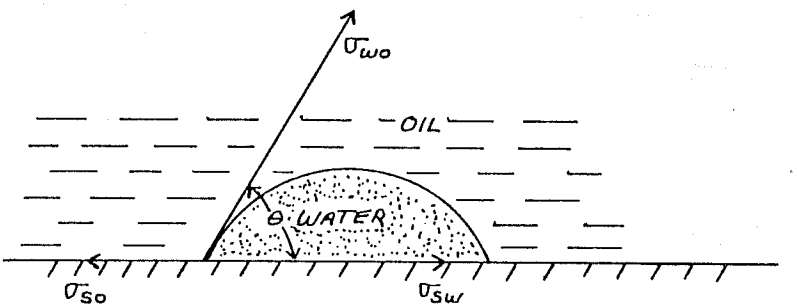

Fig. 2.1 Force Balance at a Water-Oil-Solid Interface

The balance of these forces is what enables us to define wettability as an adhesion tension, which is written in terms of the surface forces,

$$A_T = \sigma_{so} - \sigma_{sw} \tag{2.1}$$

The term, σ_{so}, is the interfacial tension between the substrate and the oil and σ_{sw} is the interfacial tension between the substrate and the water. Interfacial tension can be thought of as the amount of force per unit length required to create a new surface between the two immiscible

fluids. Since the forces must be in balance if there is no motion, the adhesion tension at the water/oil interface can also be written to include the contact angle θ:

$$A_T = \sigma_{wo} \cos \theta \tag{2.2}$$

By convention the contact angle, θ, is measured through the denser phase. A positive A_T means that the denser phase preferentially wets the rock and a negative A_T indicates that the less dense fluid is the wetting phase.

Now let us consider the rise of a fluid in a capillary tube as shown in Fig. 2.2. Through a force balance, we can derive Eq. (2.3) for the capillary pressure, P_c, in that tube:

$$P_c = p_o - p_w = \frac{2\pi r A_T}{\pi r^2} = \frac{2A_{TP}}{r_t} \quad , \tag{2.3}$$

where P_c is the pressure difference between the oil and the water at the oil/water interface. We can combine Eqs. (2.2) and (2.3) to define the capillary pressure in terms of the surface forces and the tube geometry:

$$P_c = \frac{2\sigma_{wo} \cos \theta}{r_t} \tag{2.4}$$

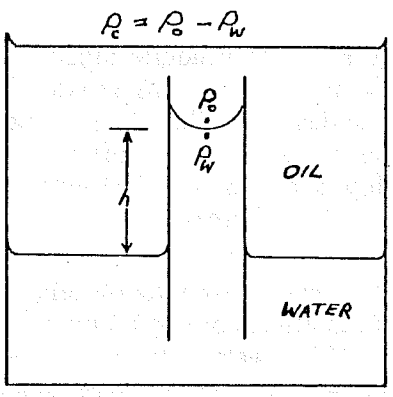

Fig. 2.2 Fluid Rise in a Capillary Tube

Plateau defined an equation for P_c in packings of uniform spheres where the wetting angle was zero and cos θ was unity:

$$P_c = \sigma_{wo} \left[\frac{1}{r_1} + \frac{1}{r_2} \right] \tag{2.5}$$

By assuming a pendular distribution of the wetting phase, he performed a force balance on the surface forces and wrote his equation in terms of the interfacial tension between the two fluids and the two pendular radii defined by Fig. 2.3.

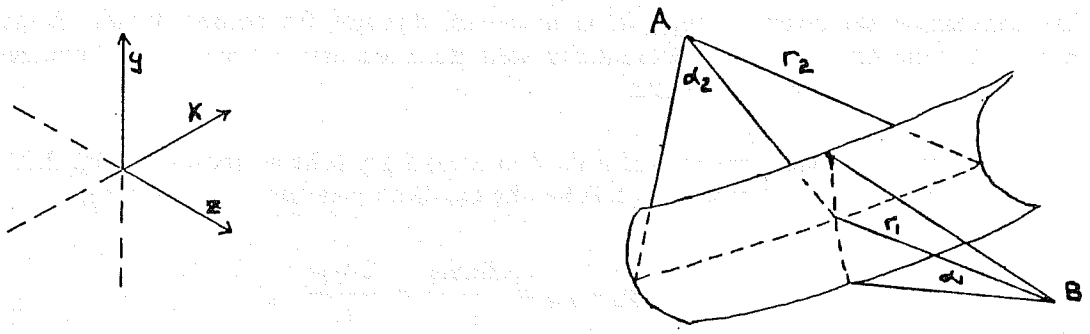

Fig. 2.3 Geometry of the Pendular Ring

Because r_1 and r_2 are nearly impossible to measure, we normally define a mean radius r_m and compare Eqs. (2.4) and (2.5):

$$\frac{1}{r_m} = \frac{1}{r_1} + \frac{1}{r_2} = \frac{2\cos\theta}{r_t} \tag{2.6}$$

In this way, the pore geometry from the pendular model can be related to the wettability and an equivalent average capillary tube radius. This relationship is not exact, because a porous medium is not made up of a series of capillary tubes, and the capillary pressure in a porous media has not been found to be directly proportional to the flat surface contact angle. Nevertheless, such a relationship is commonly expressed, for it points out that capillary pressure is a function of wettability, surface forces, and pore geometry.

An example of the capillary pressure-saturation relationship is shown graphically in Fig. 2.4. It will be used to explain the effects of capillarity on the movement of water and oil in a porous medium. Assume that a 100% water-saturated, water-wet core will be displaced by oil. This is known as drainage. Point A in Fig. 2.4 represents the start of this process. As the pressure in the oil phase increases, the oil-water interface bends inwards, desaturating the core slightly without moving the oil-water contact along the pore surface. This corresponds to Point B. At some point, the pressure drop is great enough to overcome the capillary forces in the largest pores and causes the oil to move into the core. This is depicted as Point C and is known as the threshold pressure. As the Δp increases, an apparent irreducible water saturation is reached where a further increase in pressure will result in only a very small change in S_{wi}. This is Point D of Fig. 2.4.

If the capillary pressure is reduced and the wetting phase is allowed to move back into the core, a curve shown as *imbibition,* in Fig. 2.4, results. The process proceeds until a residual oil saturation (S_{or}) is reached at a capillary pressure of zero as shown by Point E. The true residual oil saturation lies below $P_c = 0$, but this apparatus cannot measure negative capillary pressures.

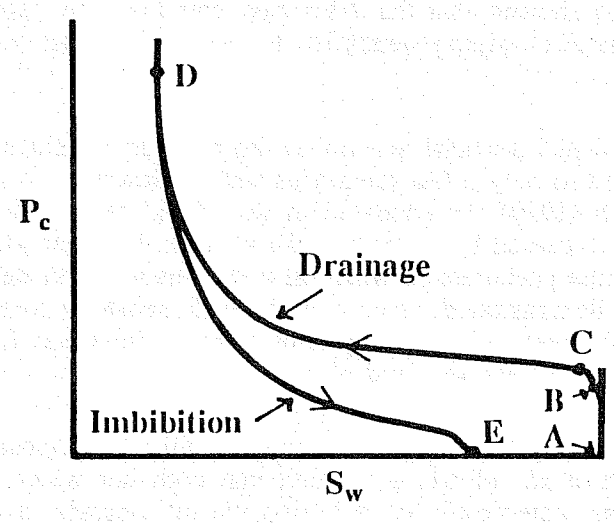

Fig. 2.4 Capillary Pressure Curve

1.2.3. LITERATURE SURVEY

The distribution and movement of fluids in oil reservoirs are influenced to a great extent by capillary forces which, in turn, depend upon the size and shape of the rock pores, the surface characteristics of the rock, and the interfacial tension between the fluid phases (Hocott, 1938).

M. C. Leverett (1941) defined a dimensionless term referred to as his *J*-function in an attempt to generalize the capillary pressure-saturation relationship in a porous system.

$$J(S_w) = \frac{P_c}{\sigma}\left[\frac{k}{\phi}\right]^{1/2} \tag{3.1}$$

k = permeability, cm^2

σ = interfacial tension, dynes/cm

ϕ = fractional porosity

Later, Rose and Bruce (1949) introduced the contact angle term to the relationship to account for wettability of porous media.

$$J(S_w) = \frac{P_c}{\sigma \cos 0}\left[\frac{k}{\phi}\right]^{1/2} \tag{3.2}$$

Bethel and Calhoun (1953) showed that the *J*-function could not be applied universally but suggested that published studies defining wettability by use of a contact angle were heading in the right direction.

Effects of wettability and interfacial tension on the recovery mechanism in dynamic systems have been well studied so only a few references will be described to give a general background. Wagner and Leach (1959) demonstrated in waterflood tests on unconsolidated cores that oil recovery could be increased by changing oil-wet rocks to water-wet conditions. Mungan (1966) observed the same phenomenon when oil-wet cores were flooded with 0.5*N NaOH*. Wagner and Leach (1966) demonstrated, using consolidated sandstone cores, that the displacement efficiency in both water-wet and oil-wet systems could be improved by a sufficient reduction in the interfacial tension between the fluid phases.

Temperature effects on displacement mechanisms are quite well documented but not very well understood. Willman *et al.* (1961) concluded that both hot water and steam injection increase oil recovery during waterfloods by reducting the oil viscosity and by increasing the thermal expansion of the oil. Using Berea sandstone, Habowski (1966) observed decreases in S_{or} by hot water flooding and noticed that S_{wi} increased with increases in temperature during hot oil flooding. He suggested that these results were due to a decrease in adhesion tension.

Poston *et al.* (1970) using unconsolidated sand, obtained results similar to Habowski and also attributed them to a lowering of adhesion tension. Lo and Mungan (1973) concluded that these findings could not be accounted for by changes in capillarity alone and that changes in the oil-water viscosity ratios were partly responsible. They noted a study by Everett and Haynes (1972) where the thickness of a residual film layer observed on a cylindrical capillary varied directly with the viscosity ratio of the displaced and the displacing fluids.

Sufi (1982) pointed out that the change in S_{or} observed with changes in temperature during waterfloods was not dependent on temperature but was indicative of the nature of the fractional flow curves. In other words, the previous experiments were not run to full completion, but rather, merely to practical laboratory limits. He also argued that increases in S_{wi} with increasing temperature during oil floods were due to capillary discontinuities and lowering viscosity ratios. The resulting saturation buildups at the end of the cores are known as end effects.

The literature on capillary pressure measurements is so extensive that only the most relevant papers dealing with temperature effects will be discussed. A section on theory was included to cover the basic concepts of capillary pressure.

Sinnokrot (1969) recorded capillary pressure curves for Berea and Bandera sandstones and for limestones of unknown source. Using the restored-state method, he found that S_{wi} increased in the Berea and Bandera cores with increasing temperatures. Slight changes in the limestone curves were observed but were considered to be negligible. In the absence of viscous forces, he concluded that wettability must be the most important factor. Sanyal (1971), using Berea and Boise sandstones, achieved the same results as Sinnokrot but concluded that thermal expansion of the sand grains was causing pore constrictions to trap more water at higher temperatures. Okandan (1973), studying the effects of temperature on capillary curves and contact angles, concluded that interfacial properties alone could not account for the increases in S_{wi} and decreases in S_{or} with increasing temperature. She suggested that the change in pore geometry due to thermal expansion was important.

The necessity for experimental research to be done under conditions closely simulating the real reservoir is stated in most of the previously mentioned papers. For example, both Mungan (1966) and Wagner and Leach (1966) found that working at surface conditions significantly changed the wettabilities of their cores. Kyle and Newman (1961) discovered that rock samples that were of intermediate wettability at surface conditions were found to be more water-wet under reservoir conditions. Dobrynin (1962) demonstrated that the main physical properties of rocks, i.e., porosity, permeability, density, resistivity and velocity of elastic waves, changed significantly with overburden pressure.

The conflicting results of the literature survey suggest that there are many questions that need to be answered concerning the role of capillarity in dynamic displacement as well as the individual and cumulative effects on wettability and pore geometry of changing temperature and pressure conditions. There are numerous papers in the literature that discuss the need to perform experiments as close to reservoir conditions as possible in order to provide answers.

The most common method for measuring capillary pressure is the restored-state method. Capillary pressure is measured as the difference between the two phases as decribed in Section 2. If the measurement is performed at atmospheric conditions, it is only necessary to maintain pressure control over one phase. But if a pore pressure closer to reservoir conditions is desired, accurate pressure control must be maintained over both phases with a known and controlled difference in pressure between the phases. In the past, the phase pressures were applied separately and independently, giving an additional source of error. At low capillary pressures, any instability or irregularity would lead to a proportionately greater fluctuation in capillary pressure with correspondingly larger changes in saturations and a poorer quality of the curve.

It is the goal of this research project to find some answers. In this literature search, no study was found that attempted to study capillary pressure curves in unconsolidated sands at simulated reservoir temperatures and pressures. New equipment had to be designed.

1.2.4. STATEMENT OF THE PROBLEM

This study is part of the rock properties research that is centered on investigating the effects of temperature on flow and static of properties of formations.

This work is primarily concerned with:

> Designing, building, and testing a capillary pressure instrument for use with unconsolidated sands in which reservoir conditions (i.e., temperature, pore pressure, and confining pressure) can be simulated. The restored-state method is being used.

1.2.5. EQUIPMENT AND PROCEDURE

The schematic diagram of the system is shown in Fig. 5.1. It is a single-charged system with nitrogen providing the pore pressure to keep the fluids that are in the core from vaporizing at higher temperatures. The equipment was designed to operate at a maximum temperature of 350°F and 350 psig pore pressure.

Fluid is moved into the core by a driving force created by raising the nitrogen-mercury side of a manometer pump. As oil moves into the core, water is displaced through a highly water-wet porous diaphragm that is impermeable to oil until an oil-water bubble pressure of at

least 40.0 psig is reached. The effluent is collected in the nitrogen-water arm of the manometer.

Once the system has reached equilibrium, the fluid heights in all three of the manometer vessels are measured with a traveling microscope that has 0.01 mm accuracy. These measurements are used to calculate saturations and pressure drops across the core. For a core of 40.0% porosity and thickness of 2.5 cm, a 1.0% change in saturation will result in approximately 5.4 mm change in height in the manometer. A 0.02 psig pressure drop corresponds approximately to a 1 mm change in height in the nitrogen-mercury side of the manometer. Hence, very small changes in saturation and pressure can be calculated accurately.

Confining pressure is provided by a hydraulic hand pump that is rated to 10,000 psia. A pressure relief valve has also been installed in the hydraulic system and was set for 3,000 psig. All the tubing is 1/8 in O.D. stainless steel, pressure rated to 10,000 psia.

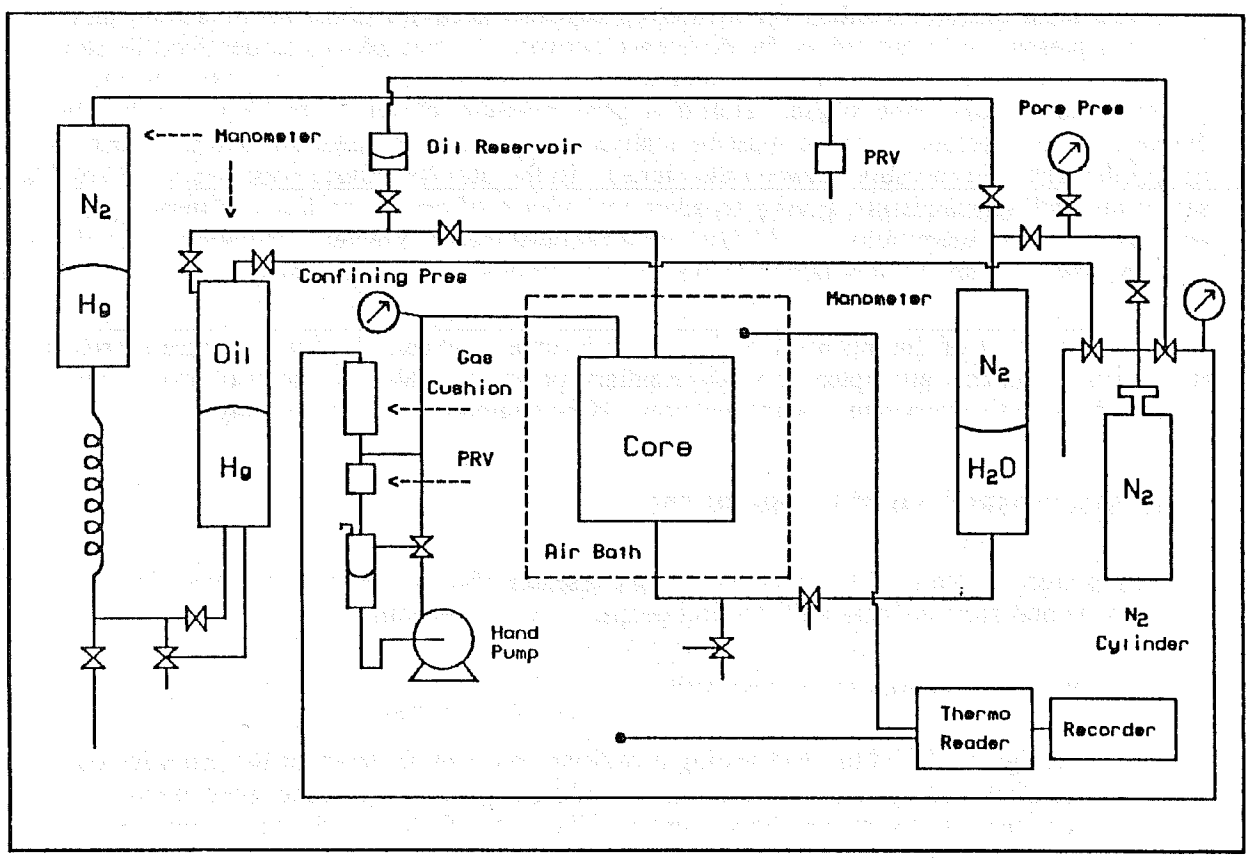

Figure 5.1 System Schematic

1.2.5.1. Pore Fluid System

The pore fluid system is shown in Fig. 5.2 The principal components are the manometers, which create a pressure drop across the core and measure the average water saturation in the sandpack, and the nitrogen cylinder, which provides the pore pressure. The manometers are identically constructed with two aluminum end pieces and two fluid reservoirs; a 1 inch O.D. 316 stainless steel cylinder with 5/64 inch wall thickness and a length of 26.5 inches and a high pressure sight glass with O.D. = 0.5 inch, I.D. = 0.25 inch, and a length of 19.2 inches. Calibration of the nitrogen-water manometer gives a value of 3.87 ±0.01 ml/cm.

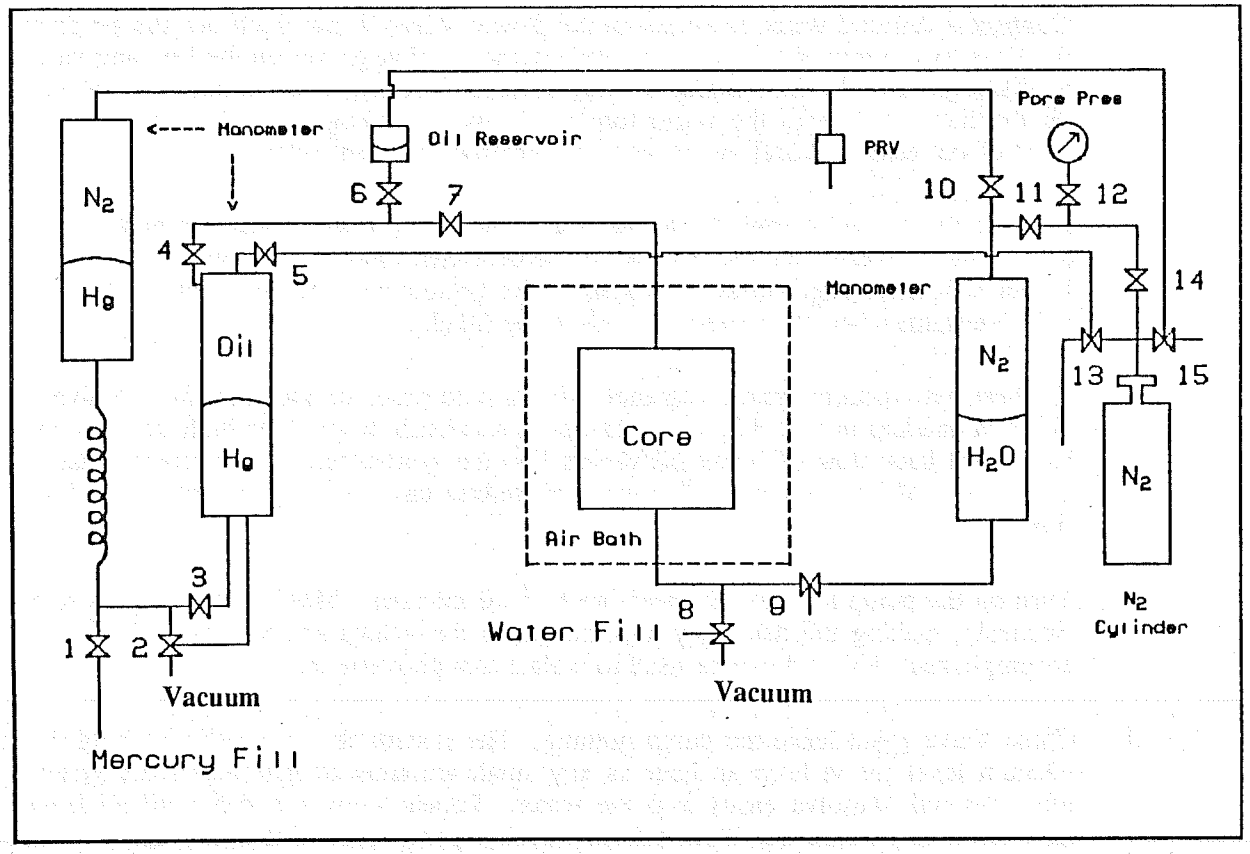

Figure 5.2 Pore Fluid System

Initial Loading of the System

Fluids must be introduced into the system with the system under vacuum to ensure that there will be no trapped gas in the lines. Too much emphasis cannot be placed on this point; and, because of the large number of fittings on the apparatus, care and patience must be exercised in order to achieve a good tight system with no leaks. The procedure is divided into two separate operations which will be discussed using Fig. 5.2 as a reference guide;

1. Filling the N_2–H_20 manometer and saturating the core
2. Filling the manometer pump, the N_2–Hg and Oil–Hg manometers

Because of the location of Valve 11 (see Section 5.1.5), the water side should be filled first. This will simplify the procedure.

Water Manometer. The water manometer is filled with the packed coreholder (see Section 5.2) connected to the water lines and a vacuum gauge on the oil inlet side. By filling to the gauge, the water level can be calculated at which the oil will contact the sand face. This point is needed for later saturation measurements as well as for threshold pressure determination. All valves will be assumed closed and the coreholder and vacuum pump disconnected unless otherwise stated. The following instructions should be used in order.

1. Connect a distilled water reservoir to the 3-way Valve 9 and flush out the air from the lines by opening the flow to the system and tapping gently on the line and valve to dislodge any obstinate bubbles. Open Valve 9 so there is communication with all the lines, and drain the water through Valve 8. Nitrogen can be used to push most of the water out and the vacuum will remove the remainder.

2. Connect the packed coreholder to the water line and connect a vacuum gauge, with a close-off valve, to the oil inlet on the coreholder. Since a vacuum in the coreholder will take longer to achieve than in the manometer, the condition in the core will determine when the system is ready to be filled.

3. Connect the vacuum pump, together with a cold trap, to the three-way Valve 8 outlet as marked in Fig. 5.2. The cold trap is necessary to produce high vacuum and to prevent back flow of pump oil vapors into the system resulting in contamination of the core and porous plate. Improper procedure can result in an explosive situation.

4. Turn on the pump to lower the pressure to 5-10 microns. Monitor the vacuum continuously, making the necessary adjustments to the valves and fittings, until this is accomplished. Valve 9 can be used to isolate any problem areas.

5. Close Valve 8 but leave the pump running. The system should be able to hold this vacuum level for at least an hour as any small amounts of gas left in the system after this will dissolve easily into the water. Repeat steps 4 and 5 until all leaks have been taken care of. Turn off the vacuum pump only if it is necessary. The pump is designed to operate continuously, not sporadically.

6. Open Valve 9 and allow water to fill to the top of the manometer. Check for any signs of leaks as the water rises in the glass sight column and do not let the water level disappear into the top end of the manometer. Don't underfill either, as it is much easier to drain water than it is to add water to the system.

7. Fill the gas lines and the manometer with nitrogen through Valves 11 and 14 and maintain a nominal pressure of 5-10 psig.

8. Close the vacuum gauge valve and open Valve 9 slowly, so water from the manometer saturates the core. This is a slow process that is dependent on rock type and thickness. It is better to allow too much time than too little for reaching 100% saturation.

9. When the fluid level in the manometer is steady, close Valve 9 and bleed off the gas pressure. Disconnect the vacuum system.

10. Uncap the piston shaft and allow the level in the water manometer to come to hydrostatic equilibrium with the opened connection. Disconnect the water reservoir and be sure all valves are closed.

Manometer Pump. The manometer pump may contain 300-350 ml of mercury so it is important that the proper equipment for handling mercury is available and that a sound procedure is followed. Mercury is toxic and any spills must be reported to the health services immediately. There should be a functional mercury trap (test before starting to fill) and marked containers for used mercury. Do not put contaminated mercury back into the same container with clean mercury. The filling vessels should take into consideration mercury's density and flow properties.

A cap should be on the outlet end of the oil line in the oven and all valves should be closed unless otherwise stated. Check the fluid level in the oil reservoir and fill it if deemed necessary.

1. Lower the mercury manometer to its lowest position and connect the mercury filling reservoir to Valve Outlet 1. Make sure that they are protected from foot traffic as these locations are at floor level and partially exposed.

2. Connect a vacuum pump along with a cold trap to the three-way Valve Outlet 2. Attach a vacuum gauge to Valve Outlet 13.

3. Open Valves 1, 2, 3, 5, and 13. The mercury reservoir has a control valve on it and this will be used to pass mercury into the system.

4. Turn the vacuum pump on to lower the pressure to 5-10 microns. Monitor the vacuum continuously making the necessary adjustments to the valves and fittings until this is accomplished. Valves 2, 3, and 5 can be used to help isolate any problem areas.

5. Close Valve 2 for vacuum testing. This can be frustrating and time consuming so patience and care must be exercised in order that a tight system may be achieved. The system must be able to hold the vacuum for two hours time as any trapped gas in the lines will affect the pressure determination. Take care of any small leaks and proceed.

6. Leave Valve 1 open and close Valves 3, 5, and 13.

7. Fill the mercury manometer until the fluid level is at the top of the sight glass. Close Valve 1 and the mercury fill valve. Remember that a perfect vacuum can only hold 76 cm of mercury so if more mercury is needed in the manometer, repeat Step 7 after completing Step 8.

8. Open Valve 3 slowly and allow the fluid levels to equilibrate at a level of about 10 cm. Raise the mercury manometer to adjust the mercury level in the *Oil–Hg* manometer. Close Valve 3.

9. Open Valve 6 and then Valve 4 to fill with oil. Close Valve 4 when the oil level in the reservoir stops moving. This step will take some time to complete due to the viscosity of the oil and small diameters of the tubing.

10. Open Valve 10 to fill the remaining void with nitrogen and then bleed off the pressure to atmospheric conditions.

11. Uncap the oil outlet connection to the coreholder and open Valves 7, 4, and 3 to allow oil to flow out until hydrostatic equilibrium is established in the manometer pump.

12. Disconnect the vacuum pump and the vacuum gauge.

Reloading the System

When it becomes necessary to replenish the fluids in the system without dismantling the apparatus or lowering the pore pressure, the following simple procedures should be used (refer to Fig. 5.2 as a reference guide). If the next experiment is to be performed at a lower pore pressure level than the previous one, the procedures in Sections 5.1.1 and 5.1.3 must be used to clean the system and load it.

Water Manometer. The water manometer should have as pure water as possible for each displacement run. The instructions provided in Section 5.1.1 under the heading "Water Manometer" should be followed when refilling the system with distilled water.

Manometer Pump. The manometer pump must be reloaded without lowering the pore pressure as this would cause dissolution of gas from the oil and form gas bubbles in the *Oil–Hg* manometer and lines. The apparatus is equipped with a pressurized oil reservoir to facilitate replacing oil lost during a displacement run. Since the system is still charged, Valves 10, 11, and 12 are kept open so pore pressure can be monitored. All other valves will be closed unless otherwise stated.

1. Attach an additional pressure gauge to the line extending from the three-way Valve 13 so the system and reservoir pressures can be monitored separately. Open Valves 13 and 15.

2. Pressurize the oil reservoir using the nitrogen cylinder until the reservoir pressure is at or above the pore pressure level desired.

3. Open Valves 3, 5. and 6 and allow oil to pass into the system, using the nitrogen bottle to maintain enough pressure differential to push the desired amount of new oil into the manometer pump. Turn off the nitrogen cylinder.

4. Close Valves 3, 5. and 6 and bleed off the nitrogen in the oil reservoir using the three-way Valve 15.

5. Close Valves 13 and 15 and remove the extra gauge.

Draining and Cleaning the System

Because there is little mixing of any of the fluids, the system requires little cleaning. However, it has been observed that a thin film will develop at the *Hg–Oil* contact and that an oxide layer may form at the N_2–*Hg* interface if the mercury is contaminated with oil. These should not affect the measurements when the fluid interfaces are still sharp enough to read and the films are minute in thickness; but over several runs it may become necessary to replace the fluids and clean the manometer pump. Replacing the type of oil used would also necessitate draining and cleaning the manometer pump. If oil enters into the water side of the system

because of a crack or leak in the porous plate, the water manometer and all its lines must be thoroughly cleaned. As the need dictates, the cleaning is essentially a two-part operation

1. The water manometer and fluid lines

2. The manometer pump and fluid lines.

Water Manometer. The water manometer must be kept clean of all other fluids. If oil intrusion should appear, the following procedures should be followed. It will be assumed that all valves are closed and that the coreholder is disconnected.

1. Make sure that the fluids are at atmospheric pressure by opening Valves 11, 12, 14, and 15.

2. Using Valve 9, drain the water and dispose of it properly.

3. Disassemble the manometer and clean it thoroughly, do not scratch the glass tube. Scratches could become stress concentration points when the system is under pressure. The lines can be cleaned by pumping solvents through them. Be sure to dispose of the contaminated solvents properly.

4. Reassemble the manometer, inspecting the parts for any possible wear and damage. Replace if necessary.

Manometer Pump. If it should be deemed necessary to clean the manometer pump or change from one oil to another, the following procedures should be followed. Have the proper equipment ready. This not only speeds up the procedure but also results in better handling of the fluids. There should be a mercury trap and properly marked containers for both contaminated fluids. Mercury is toxic and the utmost care must be taken to prevent any spillage. It will be assumed that the coreholder is disconnected and all valves are closed unless otherwise stated.

1. Make sure the fluids are at atmospheric pressure by bleeding off nitrogen using Valves 3, 10, 11, 12, 14, and 15. Use the pore pressure gauge and the sound of gas flow to determine when this is completed.

2. Close Valve 3 and lower the N_2–Hg manometer to its lowest position. This minimizes the hydrostatic pressure at Valve 1 through which the mercury is to be drained.

3. Using Valve 1 and especially provided containers, slowly and carefully drain the mercury from the left side manometer. The mercury trap must be at hand as there are always a few last drops that seem to get held back in the line. These usually can be freed by using the suction nozzle around the inside and outside of the valve opening. Be sure to close Valve 1 when this is completed.

4. Open Valves 4, 5, and 7 and drain the mercury from the *Oil–Hg* manometer through Valve 2. When oil starts to appear, close Valve 2.

5. Drain the remaining oil into a marked container for proper disposal as a hazardous fluid. Close Valve 2.

6. There will be some mercury left in the line that is closed by Valve 3. Check that Valve 1 is closed and open Valve 3 to allow the mercury to flow down to Valve 1. Drain using Procedure 5. above. Place the contaminated mercury in a safe storage place. Mercury can be cleaned and recycled.

7. The manometer pump can now be easily dismantled and cleaned but care must be taken with the glass tubes as any scratches will become stress concentration sites when the system is pressurized. Also, there will be mercury droplets throughout the lines so it is essential to have the mercury trap at hand during the disassembling. The lines can be cleaned by pumping solvents through them and into the proper disposal containers.

8. Reassemble the manometer pump. Inspect the parts for wear and damage. Replace if necessary.

1.2.5.2. Coreholder

Figure 5.3 is a schematic of the coreholder. This was designed to handle confining pressures up to 10,000 psia and temperatures up to 350°F. Confining pressures are limited by the low tensile strength of the ceramic porous diaphragm and the temperature range is limited by instability of the Viton gasket material at higher temperatures. Confining pressure is applied axially to the sandpack with a hydraulically operated piston press. Radial stress results from the horizontal expansion of the grains in the coreholder. Oil enters the coreholder at the inlet at the top and is distributed uniformly across the sandface by a 280 mesh wire screen. As oil moves into the sandpack, water is displaced through the semipermeable ceramic diaphragm which is held in place by a perforated steel plate with approximately 250 holes drilled in it. All the holes are connected by spider-web grooving so that water can be collected from the diaphragm and moved freely to the outlet and then into the manometer. All parts of the coreholder are constructed of 316 stainless steel except for the Viton gaskets and the porous semipermeable diaphragm. Figures 5.4 and 5.5 describe the coreholder in more detail by showing the dimensions of all the pieces and giving the sizes and locations of the O-rings. The O-rings will be discussed later in this section.

Component Preparation

Uniformity of procedure is tantamount to reproducibility and comparative analysis of the results. In the case of the porous diaphragm, a suitable procedure was arrived at only by painstaking trial and error. Any deviation from this procedure will probably result in breakage and termination of the experiment. In fact, many diaphrams were broken in the process of learning a valid procedure. Additional information on the porous diaphragm and porous medium can be found in Appendix A.

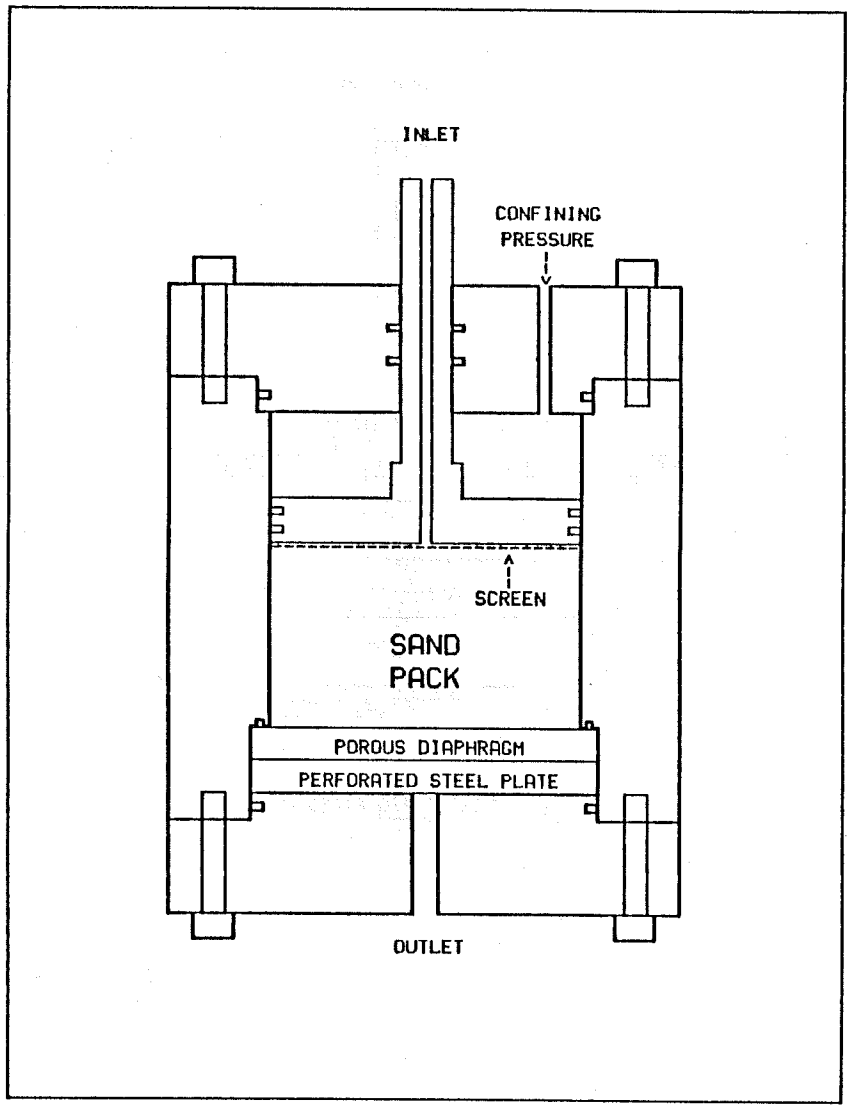

Figure 5.3 Coreholder

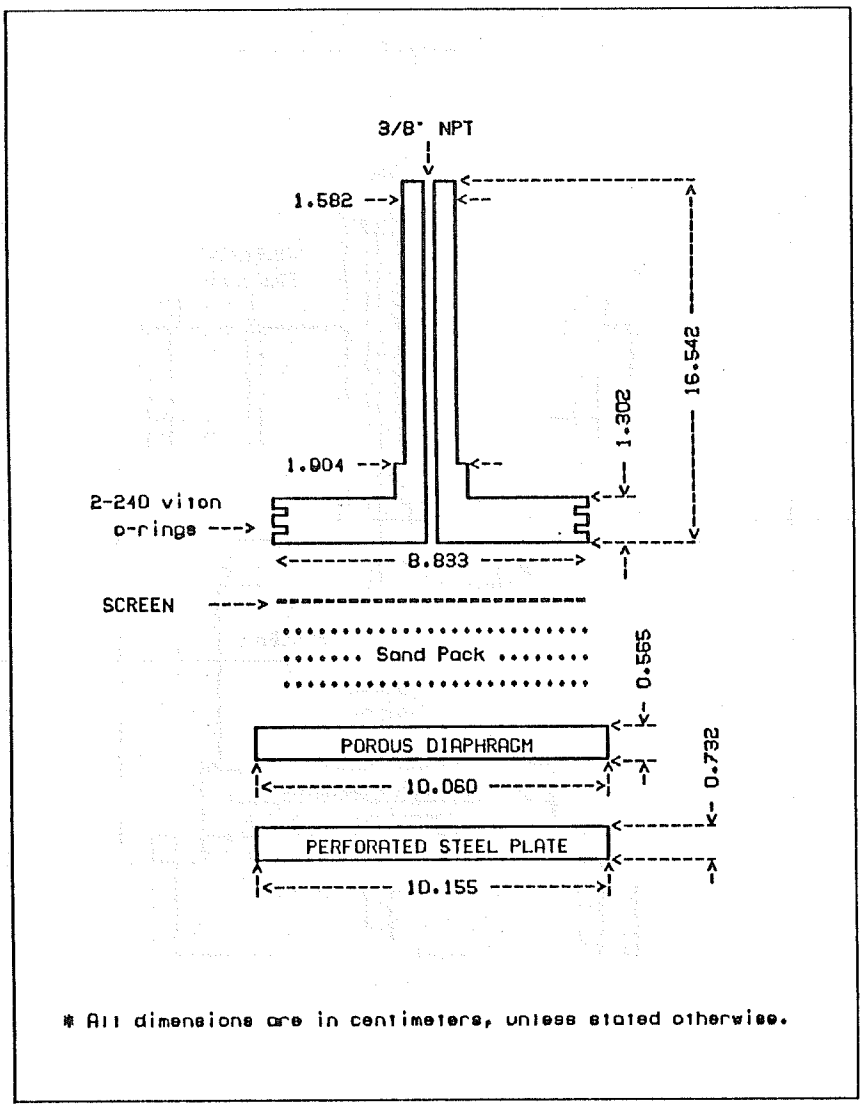

Figure 5.4 Coreholder Piston, Diaphragm and Perforated Plate.

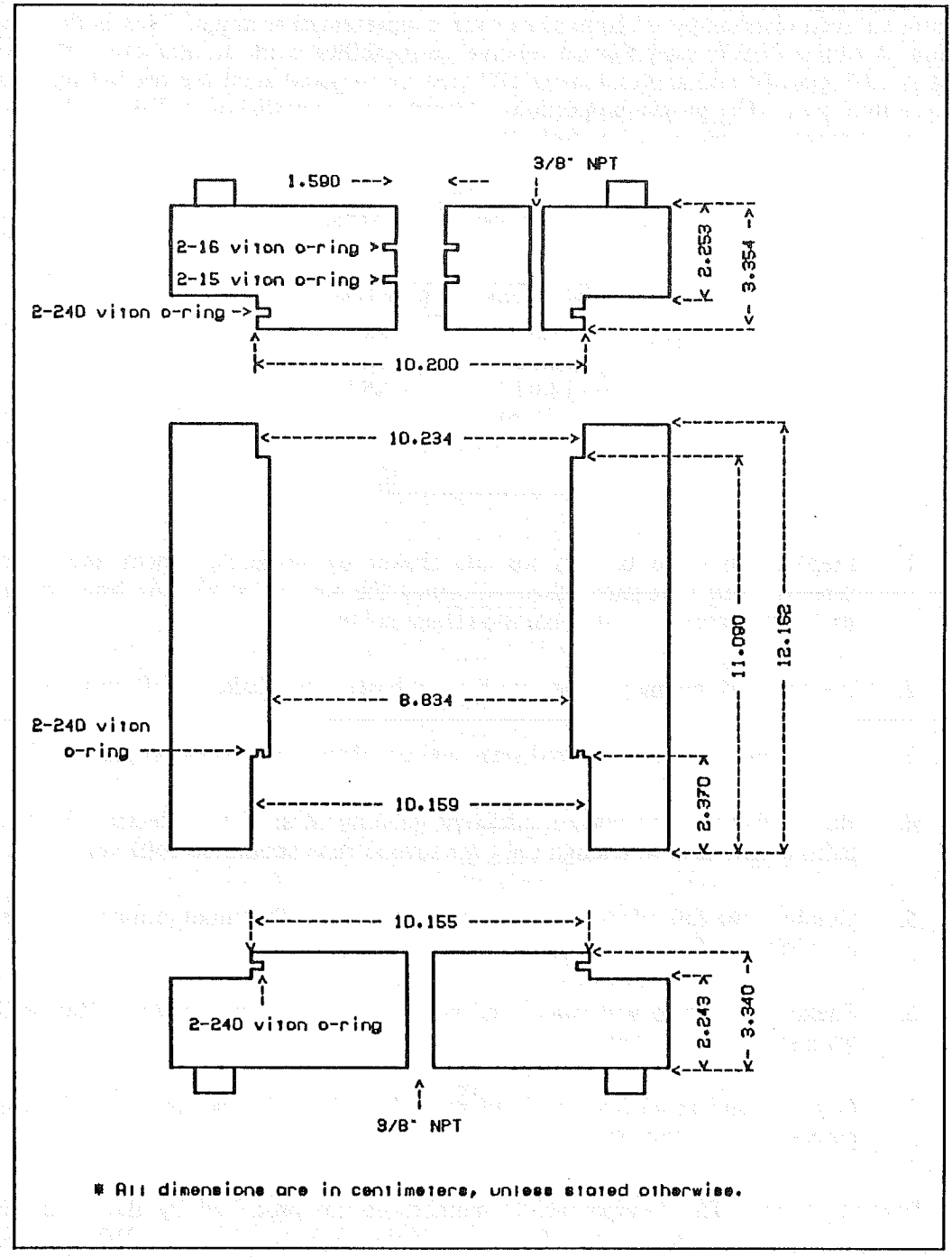

Figure 5.5 Coreholder Body

Sand Preparation. Ottawa sand was used as the core material and the blend was created to give an even distribution of grain sizes over a representative range. This is the same distribution as Miller (1983) used for his relative permeability work at Stanford. The density of sand is 2.65 gm/cm^3 and approximately 100 gms of prepared sand are needed for every 1 cm of core thickness. The proper proportions of grain sizes are shown in Table 5.1 and preparation and cleaning procedures are as follows:

TABLE 5.1
SAND SPECIFICATIONS

Mesh Size	% Mixture
100-120	25.0
120-140	35.0
140-170	25.0
170-200	15.0
	100.0

1. Prepare the sieve baskets for the shaker by inspecting them and cleaning the screens. For maximum sieve efficiency the screens should be brush-cleaned after each shake period. Assemble the screen column.

2. Put about 20 grams of sand into the top basket and shake for 10 minutes.

3. Collect the individual desired sizes and put them into marked containers.

4. Repeat this process until a sufficient quantity of sand is collected. Since this is a tedious task at best, enough sand for several runs should be collected.

5. Combine the four sizes to obtain the proper mix. The mixture must now be cleaned and dried, as follows.

6. Shake the mixture with water and pour off the dirty supernatant. Repeat this until the supernatant is clean.

7. Dry the sand in an oven and put in a clean dry container marked with the correct percentage of grain sizes.

Porous Plates. The semipermeable membranes are produced by the Coors Porcelain Company and have the dimensions 5.000 ± 0.060 in. O.D. × 0.025 ± 0.010 in. thick. The plates suitable for the experiments have a glazed outer diameter and have air-water threshold pressures greater than 60 psig. The ones without glaze do not have the proper wetting characteristics desirable for this experiment and should not be used. The porous plate is the most delicate part of the coreholder. It is a thin ceramic disc that is very weak when subjected to shearing forces and is susceptible to changes in wettability when touched.

Because of these properties, utmost care must be taken in preparing and choosing a disc to use. Surgical gloves should be worn and the discs should only be handled by the outside diameter to prevent contamination of the surfaces. This should be made clear to the machinist as well. Several discs should be prepared each time due to the turn around time in the shop and due to the rate of failure during machining and core packing.

1. Saturate the discs by evacuating and soaking them in distilled water. A cold trap should be used in conjunction with the vacuum pump to keep oil vapor from contaminating the discs. Store the saturated discs in distilled water.

2. The discs must be machined to 10.03 ± 0.025 cms O.D. (3.95 ± 0.01 in.) and both the top and bottom surfaces must be lapped to a fine finish. The lapping is necessary to ensure a minimum of shear forces on the plate and to provide a proper surface for the O-ring contact. This machining must be done with abrasives, using water as the cutting fluid. This process is necessary to minimize the impact of machining on the plates. Ginzen Laboratory at Stanford University can do this work, but plan ahead, as the lead time can be as long as one month.

3. The machined discs must now be x-rayed to identify the faulty ones. Although the discs have been visually inspected, it has been found that microcracks can exist that become stress points when the discs are subjected to compression. Stanford University Hospital provides a limited service for this analysis technique and the type of machine and exposure in milliamp-seconds are given in Table 5.2. Four discs can be x-rayed at a time and a broken plate that has been put back together should be used as a reference sample for comparison. Store the plates in distilled water after each exposure to prevent drying.

TABLE 5.2
X-RAY SPECIFICATIONS

Machine	Siemens A - Small Focus
Voltage	35 KV
Exposure	64 mAS

O-Ring Seals. The O-ring sizes and locations are given in Figures 5.4 and 5.5. Inspect the O-rings for wear and damage. The O-rings on the piston head and the plunger arm opening in the top end plate are especially susceptible to wear. Grease can be used on all the top flange gaskets to facilitate assembly of the coreholder but only water should be used on the others. With the exception of the porous plate compression sealing O-ring, all the seals work on a differential principle and thus there is no need to screw the bolts down too tightly. However, it is necessary to tighten the bottom flange enough to ensure a good seal of the porous plate O-ring. Since for most runs the maximum differential pressure is only 10-15 psi, care must be taken not to tighten the bolts too much and risk breaking the ceramic plate.

Assembling the Pieces

First, the bottom plate assembly must be put together and checked for leaks. It is advisable to use a center press, available in the machine shop, to provide uniform force on the end plate when the bottom flange is being secured. Use the following instructions and refer to Fig. 5.3.

1. Slide the porous plate, together with the perforated steel plate, into the coreholder until it rests on the O-ring. Be sure that the spider-web grooving is facing downward and help the plates along with both hands, one from the inside of the coreholder and one on the outside. This helps eliminate wedging due to the small tolerances. A surgical glove should be worn on the hand which is in contact with the porous membrane.

2. Put the bottom flange in place and, using a center press, gently push it down onto the plates. Put some high temperature grease on the bolts and screw them down until they are snug up against the flange. After all the bolts have been turned down, tighten each bolt about 1/8 of a turn more. The O-ring will only be required to hold a maximum differential pressure of approximately 8 psi so further tightening is not necessary on the bolts. This is a delicate operation and should be done systematically. Listen for any cracking sounds and inspect the porous plate when this is complete.

3. Pour the weighed sand into the coreholder and use the Plexiglas tamper to smooth the sand and give it uniform thickness. The tamper should be used along with the top flange and should be weighed along with the sand to maintain material balance as some sand will stick to the tool. This procedure can be done wet or dry depending on the experimentalists needs but it is thought that wet packing gives a tighter sandpack and thus is recommended. Remember to weigh the tool and the sand container when the packing is finished in order that a porosity determination can be made. The resulting porosity should be around 40-44%.

4. Clean the coreholder walls of any sand and place the wire screen on top of the sandpack.

5. Assemble the top flange and plunger assembly, using high temperature grease as a lubricant in the top flange O-rings. Don't put grease on the piston head O-rings; use only water.

6. Fit the piston head into the coreholder, being careful not to tear the O-rings, but don't push it down onto the sandpack. Bolt down the top flange firmly and systematically and slowly start pushing the plunger down onto the sandpack. Because the plunger neck is the only way gas may escape from the decreasing volume, a vortex is created at its mouth which will tend to relocate the surface sand. A slightly wet core will resist this phenomenon and if the plunger is moved slowly enough this should not be of any consequence. Cap the plunger when it rests on the sandface.

7. Pressure test the core. Attach a vacuum pump and cold trap to the water effluent side of the coreholder and put a vacuum gauge on the confining pressure reservoir. Evacuate the system and saturate it with distilled water.

8. By performing a bubbling test on the porous plate, the effectiveness of the O-ring seal can be determined. With the effluent side of the coreholder at atmospheric pressure, bubble nitrogen through the core, noting if any gas is produced from the effluent side. A gas pressure of 30 psig should be sufficient to proceed. If gas appears at lower pressures, tighten the bottom flange bolts gently and systematically until the gas stops or it is determined that the porous plate must be cracked. If the plate is cracked then start over again with a new one.

1.2.5.3. Temperature and Confining Pressure

In order to more closely model actual reservoir conditions it is necessary to use experimental temperatures and confining pressures near those found in the reservoirs. This apparatus is designed to accomplish this, however, problems with insuring the integrity of the porous membrane under high pressure restrict the upper limit of the confining pressure. The extent to which this limits the pressure needs to be studied. Use Fig. 5.6 as a guide for this section.

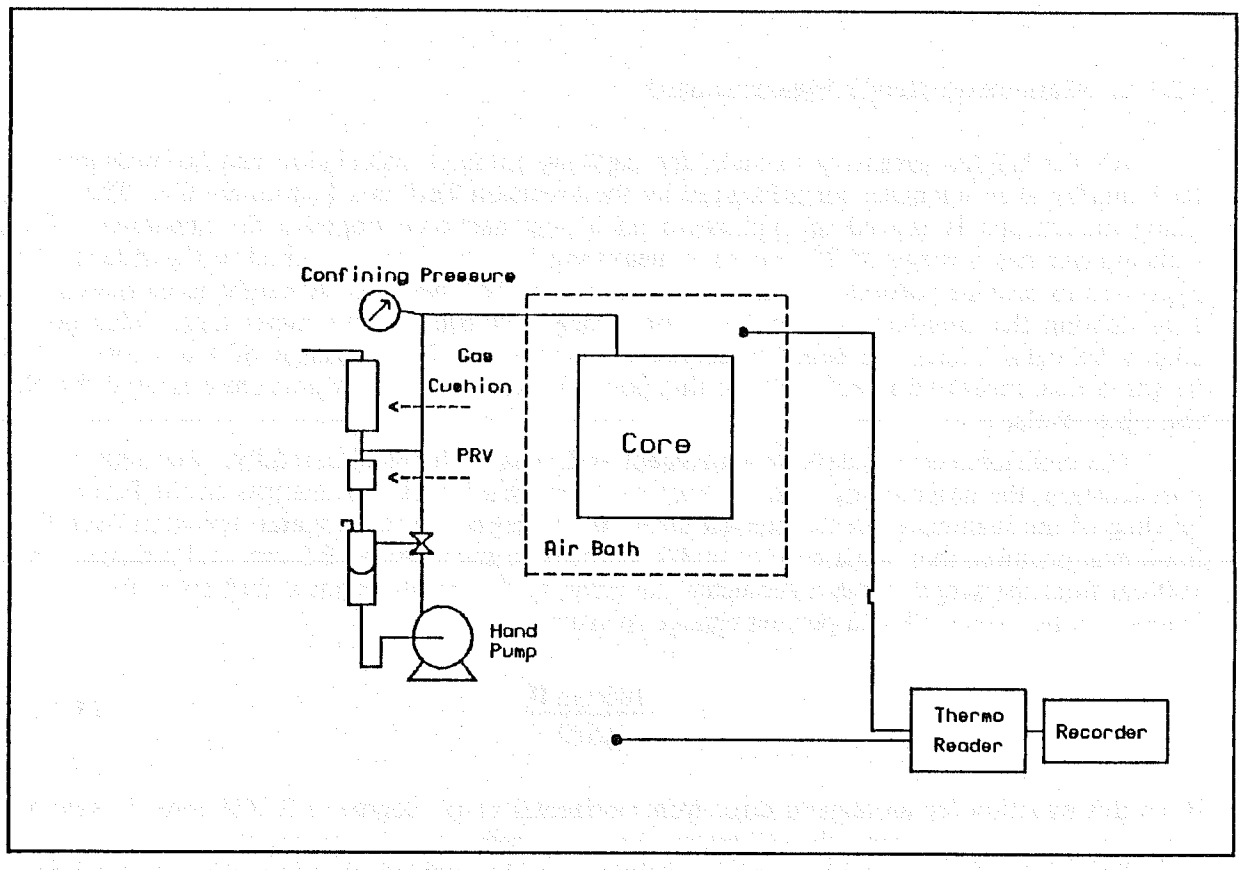

Figure 5.6 Temperature and Confining Pressure System

1.2.5.4. Temperature

The temperature system consists of a constant temperature air bath, a Thermoreader, and a chart recorder. The oven is a Blue M, model ESP-400 BC-4 and is capable of providing constant temperatures, ±1.0° F, from 100 to 500° F. If used below 100° F, the temperature of the oven will vary ±2.0° F if there is a large variation in the room temperature. The thermoreader is an Omega 199 with an accuracy of ±1.0° F and is connected to two thermocouples to monitor room and oven temperatures. Output from the monitor is digital and a Soltec 125 chart recorder is used to record the temperatures continuously for each run.

1.2.5.5. Confining Pressure

The confining pressure is provided by an Enerpac PH-39 hand pump rated to 10,000 psi. A gas cushion dampens any pressure variation that might occur due to thermal expansion of the confining fluid under small changes in oven temperature. A pressure relief valve (PRV), adjusted to 1000 psig, prevents any accidental overpressuring of the system. When the confining pressure system is drained, the fluid is retained in the catch reservoir and reused in the next run.

1.2.5.6. Manometer Height Measurements

All the heights necessary to make the capillary pressure calculation can be measured to 0.01 mm by a cathetometer manufactured by the Precision Tool and Instrument Co. The travelling microscope is moved up and down on a post anchored opposite the apparatus. The cathetometer has a range of 25 cm, so a measuring tape has been attached to the side of the apparatus to provide reference points for measuring all the heights. A height is measured by first sighting the crosshairs of the scope on a major division of the meter tape. This point should be below the point being measured but within the 25 cm range of the scope. The height is then measured in reference to this point and recorded. This procedure is used for all the other levels.

The cathetometer is a delicate instrument and must be handled carefully. Because of the post location, the accuracy of each reading can be affected by small changes in the horizontal leveling of the instrument. If the contact angle, θ , is defined as the angular deviation from the horizontal position, then for a core of 40.0% porosity, a thickness of 2.5 cm, and a distance of 100 cm from the scope to the manometer, the error, ε, that results from a shift away from horizontal can be expressed as a percent change in saturation.

$$\varepsilon = \frac{100 \tan \theta}{0.539} \tag{5.4.1}$$

From this equation for an angular error from horizontal of ± 1 degree, a 3.24% error in saturation is measured. By using the calibrated tape as a reference, the inherent error due to the releveling of the instrument after a position change can be avoided. It is important to avoid any jarring of the equipment that might result in the movement of the cathetometer or the reference tape.

1.2.5.7. Porosity Measurement

The porosity of the sand pack can be determined from two separate measurements. First, a precise weight of the sand in the core holder is necessary to have and second, the length of the piston shaft that protrudes from the top of the core holder must be measured. The procedure is as follows:

1. After determining the approximate weight of Ottawa sand needed, weigh the sand and follow the packing procedure as outlined in Section 5.2.2.

2. Because Ottawa sand is nearly 100% quartz, the weight of sand used, in grams, is divided by 2.65 gms/cm^3, the density of quartz. This gives the sand grain volume, V_s in cm^3.

3. The bulk volume, V_b in cm^3, is calculated by first measuring the length of the piston shaft, l_p in cm, that protrudes from the top of the coreholder. This is done with the cathetometer. The Swaglock fitting is not included in the measurement. The bulk volume in cubic centimeters is then calculated.

$$V_b = (l_p - 4.497)\ 61.292 \tag{5.5.1}$$

4. The porosity, ϕ, is then determined by Eq. (5.5.2).

$$\phi = [\ (\ V_b - V_s\ )/V_b\ ]\ 100.0 \tag{5.5.2}$$

1.2.6. CAPILLARY PRESSURE EQUATIONS

The capillary pressure equations can be derived from the fluid heights and and their densities using Fig. 6.1. Subscripts a–g refer to height locations as indicated in Fig. 6.1, and subscripts hg, o, and w refer to mercury, oil, and water respectively. Capillary pressure is defined as $P_c = p_{nw} - p_w$ where p_{nw} is the pressure in the oil phase on the core side surface of the porous plate and p_w is the pressure in the water phase at the same location. The top surface of the porous membrane is designated as d and the datum line is 0 cm on the metric tape attached to the side of the apparatus. The pressure equations on the oil-mercury side of the apparatus

$$p_a - p_b = -\rho_{hg}\ g(h_1 - h_2) \tag{6.1a}$$

$$p_b - p_c = -\rho_o\ g(h_2 - h_3) \tag{6.1b}$$

$$p_c - p_{do} = -\rho_o^T\ g(h_3 - h_d) \tag{6.1c}$$

ρ_o^T = the density of oil at experimental conditions.

Solving for p_{do} in Eq. (6.1c) by substitution with Eqs. (6.1a) and (6.1b), the pressure in the oil phase at point d is given by Eq. (6.2).

$$p_{do} = p_a + \rho_{hg}\ g(h_1 - h_2) + \rho_o\ g(h_2 - h_3) + \rho_o^T\ g(h_3 - h_d) \tag{6.2}$$

Next, consider the water side of the manometer.

$$p_g - p_e = -\rho_w\ g(h_5 - h_4) \tag{6.3a}$$

$$p_e - p_{dw} = -\rho_w^T\ g(h_4 - h_d) \tag{6.3b}$$

In Eq. (6.3b), ρ_w^T is equal to the density of water at experimental conditions. Solve for p_{dw} by making the necessary substitutions from Eq. (6.3a)

$$p_{dw} = p_g + \rho_w\ g(h_5 - h_4) + \rho_w^T\ g(h_4 - h_d) \tag{6.4}$$

Using Eqs. (6.2) and (6.4), substitute into Eq. (6.5) to obtain the expression for P_c as a function of the various heights measured.

$$P_c = p_{do} - p_{dw} \tag{6.5}$$

$$P_c = \rho_{hg}\, g(h_1 - h_2) + \rho_o\, g(h_2 - h_3) + \rho_o^T\, g(h_3 - h_d) - \rho_w\, g(h_5 - h_4) + \rho_w^T\, g(h_4 - h_d) \tag{6.6}$$

In Eq. (6.6), it was assumed that $p_g = p_a$ because the contribution due to the weight of nitrogen gas can be neglected.

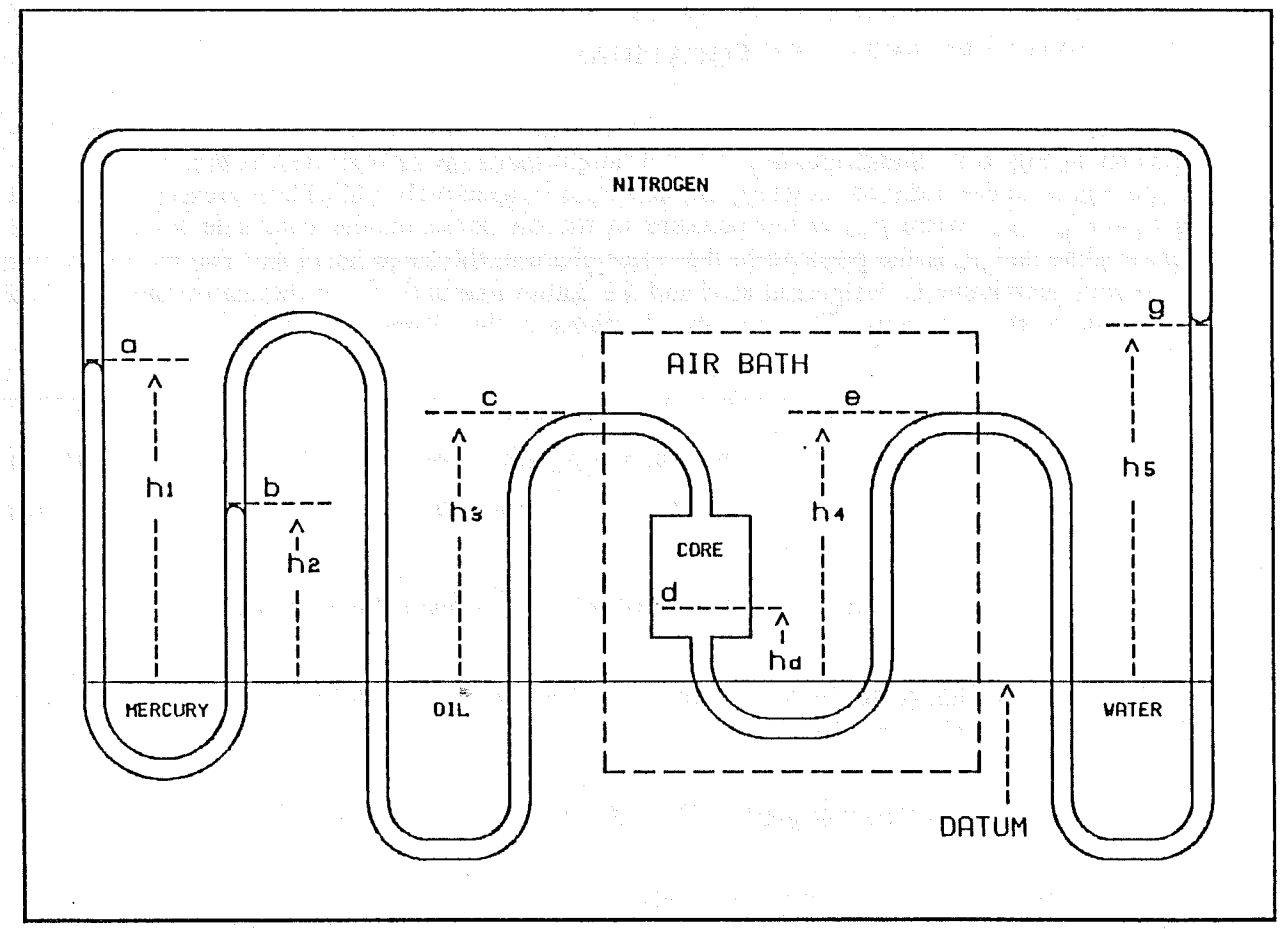

Fig. 6.1 Fluid Height Diagram

1.2.7. RESULTS

To test the apparatus, a run was made at 120° F with 200 psig confining pressure and 50 psig pore pressure.

1.2.7.1. Capillary Pressure Curve - Unconsolidated Core

The results of the test are given in Table 7.1 and Figs. 7.1 and 7.2. The Ottawa sand core had a grain size distribution given in Table 5.1 and a porosity of 0.42. The measured data point at $S_w = 0.096$ deviates from the other points and is probably a recording error.

TABLE 7.1
CAPILLARY PRESSURE RESULTS - RUN 1

Temp = 120° F
P_{cf} = 150 psig
P_p = 50 psig

S_w frac	P_c psi	S_w frac	P_c psi
1.000	0.00		
1.000	0.45	0.446	0.91
0.986	0.68	0.384	0.94
0.923	0.71	0.324	0.97
0.867	0.77	0.171	1.11
0.807	0.79	0.096	1.11
0.752	0.80	0.048	1.67
0.685	0.84	0.023	2.73
0.617	0.85	0.019	3.46
0.560	0.87	0.014	4.52
0.507	0.90	0.011	6.52

The total time for the drainage displacement was 1274 hours. The measured data is given in Appendix B. Figure 7.2 shows the displacement results on a pressure step basis and this was used to determine when each step had achieved equilibrium.

1.2.7.2. Experimental Apparatus

The apparatus functioned without any real problems for the 53 days of the experiment. A small leak developed on top of the oil-mercury manometer which resulted in the loss of about 1 cc of oil per week but this didn't effect the measurement process as there was more than enough oil in the system to complete a run. An oxide layer started to develop at the mercury-nitrogen interface after about 45 days but its thickness was not measurable with the cathetometer. This layer could be neglected in the capillary pressure calculation.

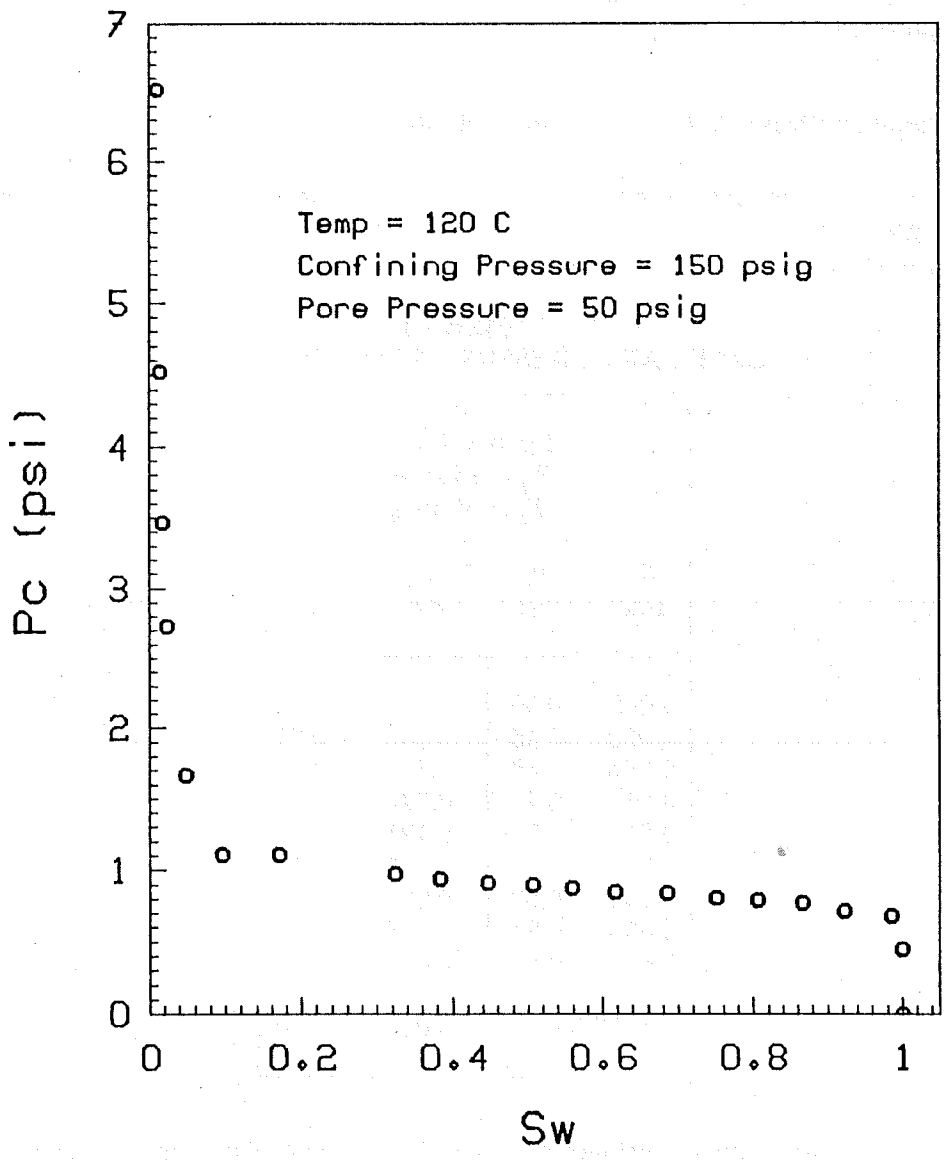

Figure 7.1 Capillary Pressure Drainage Curve - Run 1

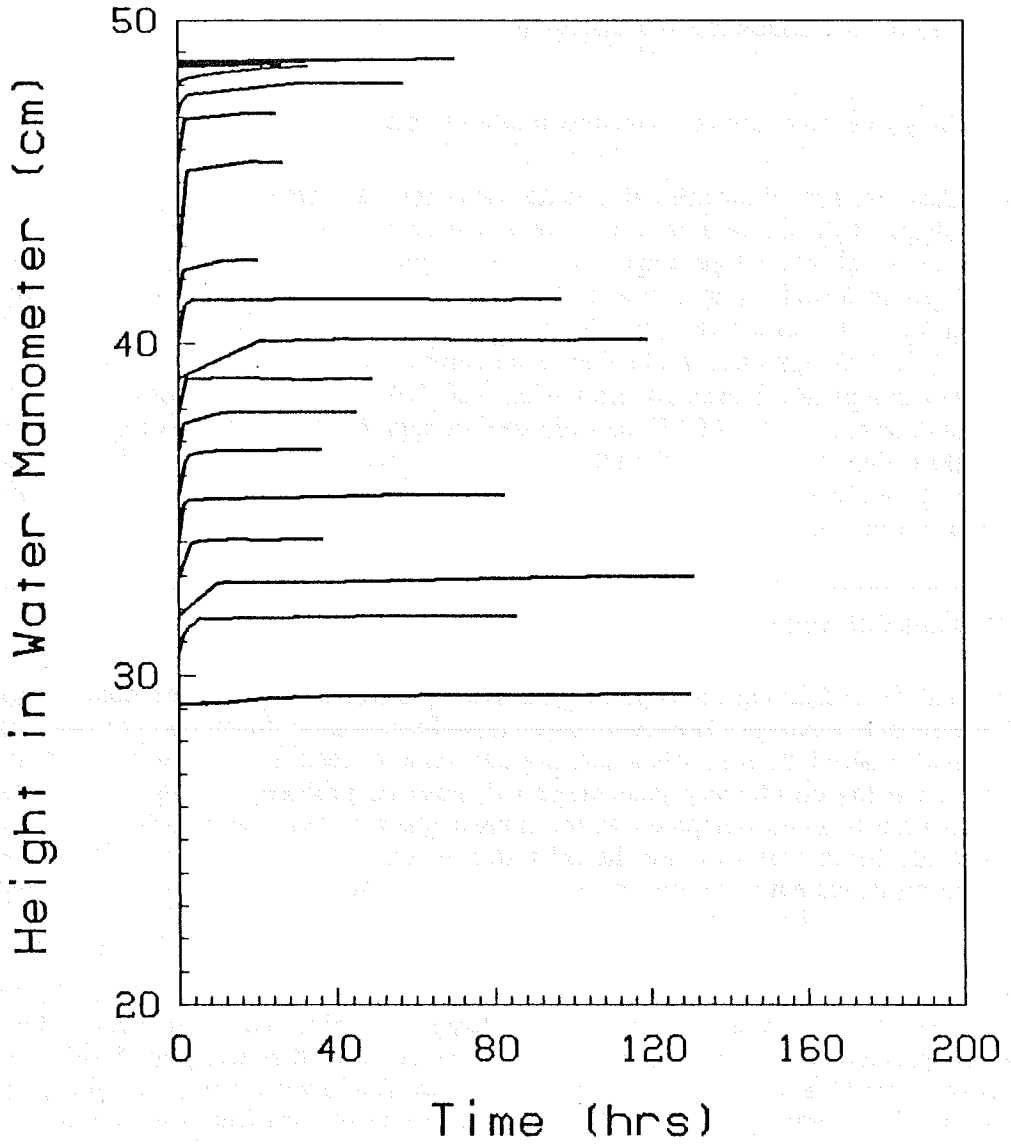

Figure 7.2 Height of Water vs Time - Run 1

1.2.8. DISCUSSION

A new apparatus for establishing capillary pressure curves using the restored state method was built and tested. The following is a discussion of the results.

1.2.8.1. Capillary Pressure Curve - Unconsolidated Core

The capillary pressure drainage curve determined for the Ottawa sand pack is shown in Fig. 7.1. The shape of the curve agrees with what is shown in the literature and is what would be expected from a highly homogeneous core. The results show a threshold pressure between 0.45 and 0.68 psi followed by a gently sloping region with a sharper upward turn around $S_{wi} = 0.1$ and a $P_c = 1.0$. The estimated time to equilibrium for each datum point is 20-25hrs as seen in Fig. 7.2. The apparent irreducible water saturation was reached at about $S_w = 0.01$. The curve is not completely consistent with what Sufi (1982) observed in dynamic displacement runs on similar cores. At 120° F, he observed an apparent S_{wi} of approximately 0.07 at a flow rate of 400 cc/hr. The reasons for the differences between this result and Sufi's result is not known. It is not possible to make any more quantitative statements about the results without more experimental data.

1.2.8.2. Experimental Apparatus

The method for measuring the fluid heights is simple and accurate. The fluid levels can be sighted easily and quickly. However, care must be taken to level the cathetometer to minimize the error that might arise when rotating the scope to read the heights from the metric tape. Oil loss from the oil-mercury manometer will pose no problem as long as the pressure decrease versus time is small compared to the time it takes to reach equilibrium in the core. This does preclude being able to close the oil-water material balance. However, the average water saturation measurement is dependent only on the amount of water in the water manometer so the data should still be valid.

The drop in water heights, shown in Table B.2, at Steps 13-14 and Steps 17-18, results from draining the water manometer in order to facilitate measuring the water level. This provides an added pressure drop across the core. The oxide layer that tends to develop at the mercury-nitrogen interface will not cause any problems for several runs; but the mercury manometer should be cleaned periodically to prevent any interference from this nuisance. The oxide layer may be caused by contaminated nitrogen gas because the problem persisted even after extensive cleaning of the manometer arm. This problem needs to be investigated more thoroughly.

1.2.9. CONCLUSIONS AND RECOMMENDATIONS

The development of a new technique for establishing capillary pressure curves has been presented and discussed. The results from the test run are encouraging, but a few uncertainties need to be clarified.

1.2.9.1. Conclusions

1. The capillary pressure apparatus designed and constructed in this study will provide accurate drainage capillary pressure data for unconsolidated sand packs at reservoir temperature and pore pressure and low confining pressures using the restored state method. More information is necessary to establish its usefulness at high confining pressures.

2. The time to equilibrium for unconsolidated Ottawa sand packs is approximately 20-25 hrs for each data point. It may be necessary to use thinner sand packs to speed up equilibrium times in capillary pressure drainage determination.

1.2.9.2. Recommendations

1. More experimentation is necessary to determine the confining pressure limit for the coreholder. If another highly water-wet semipermeable material, which is of higher shear strength and is inert to reservoir fluids and temperatures becomes available, it should be tested for use in the apparatus.

2. A rigid connection between the lines in the oven and outside the oven is needed to facilitate the height determination of the lines going into the oven.

3. An arm to secure the mercury manometer pigtail should be installed directly below the mercury manometer at the base of the apparatus. Presently, the pigtail is attached to one side and pulls the mercury manometer to the side as it is raised.

4. The problem of the oxide layer in the mercury manometer needs to be investigated.

5. The cathetometer should be moved closer to the apparatus to minimize errors in measurement resulting from angle deviation.

6. An easier method for tightening down the bottom flange needs to be developed to reduce the risk of plate breakage while assembling the coreholder.

1.2.10. NOMENCLATURE

A_T = adhesion tension, dynes/cm
$J(S_w)$ = J-Function, dimensionless
k = absolute permeability, cm^2
k_{ro} = relative permeability to oil, dimensionless
P_c = capillary pressure, dynes/cm^2 or psi
p_{cf} = confining pressure, psig
p_p = pore pressure, psig
r_t = capillary tube radius, cm
r_1 = wetting phase principal radius, cm
r_2 = non-wetting phase pendular radius, cm
r_m = mean pendular radius, cm
S_{or} = residual oil saturation, fraction of total pore volume
S_{wi} = irreducible water saturation, fraction of total pore volume
ϕ = fractional porosity
σ = interfacial tension, dynes/cm
σ_{sw} = solid-water interfacial tension, dynes/cm
σ_{so} = solid-oil interfacial tension, dynes/cm
σ_{wo} = water-oil interfacial tension, dynes/cm
θ = contact angle, degrees

1.2.11. REFERENCES

1. Bethel, F. T., and Calhoun, J. C., Jr.: "Capillary Desaturation in Unconsolidated Beads," *Trans. AIME 198,* 197 (1953).

2. Dobrynin, V. M.: "Effect of Overburden Pressure on some Properties of Sandstones," *Trans. AIME 360,* (1962).

3. El-Hadidi, S. M.: "Measurement of Imbibition Rate at Elevated Temperatures," Ph.D. Dissertation, Stanford University (1974).

4. Everett, D. H., and Haynes, J. M.: Model Studies of Capillary Condensation, I. Cylindrical pore Model with Zero Contact ," *J. Coll. Interfacial Sci. 38,* 125 (1972).

5. Habowski, E.: "The Effect of Large Temperature changes on Relative Permeability Ratios," M.Sc. Thesis, Penn. State U. (1966).

6. Hocott, C. R.: "Interfacial Tension between Water and Oil under Reservoir Conditions," *Trans. AIME 131,* 184 (1938).

7. Kyte, J. R., Naumann, V. O., and Mattax, C. C.: "Effect of Reservoir Environment on Water-Oil Displacement," *Trans. AIME 597,* (1961).

8. Leverett, M. C.: "Flow of Oil-Water Mixtures through Unconsolidated Sands," *Trans. AIME 132,* 381 (1939).

9. Lo, H. Y., and Mungan, N.: "Effect of Temperature on Water-Oil Relative Permeabilities in Oil-Wet and Water-Wet Systems," Paper SPE 4505, presented at the 48th SPE Annual Fall Meeting, Las Vegas, Nev., Sept. 30-Oct. 3, 1973.

10. Mungan, N.: "Certain Wettability Effects in Laboratory Waterfloods," *Trans. AIME 273,* 247 (1966).

11. Okandan, E.: "The Effect of Temperature and Fluid Composition on Oil-Water Capillary Pressure Curves of Limestones and Sandstones and Measurement of Contact Angles at Elevated Temperature," Ph.D. Dissertation, Stanford University (1973).

12. Poston, S. W., Ysrael, S., Hossain, A. K. M. S., Montgomery, E. F., and Ramey, H. J., Jr.: "The Effect of Temperature on Relative Permeability of Unconsolidated Sands," *Soc. Pet. Eng. J. 10,* 171 (1970).

13. Rose, W. D., and Bruce, W. A.: "Evaluation of Capillary Characters in Petroleum Reservoir Rock," *Trans. AIME 186,* 127 (1949).

14. Sanyal, S.K.: "The Effect of Temperature on Electrical Resistivity and Capillary Pressure Behavior of Porous Media," Ph.D. Dissertation, Stanford University (1971).

15. Sinnokrot, A. A.: "The Effect of Temperature on Capillary Pressure Curves of Limestones and Sandstones," Ph.D. Dissertation, Stanford University (1969).

16. Sufi, A.: "Temperature Effects on Oil-Water Relative Permeabilities for Unconsolidated Sands," Ph.D. Dissertation, Stanford University (1982).

17. Wagner, O. R., and Leach, R. O.: "Improving Oil Displacement Efficiency by Wettability Adjustment," *Trans. AIME 216,* 65 (1959).

18. Wagner, O. R., and Leach, R. O.: "Effect of Interfacial Tension on Displacement Efficiency," *Trans. AIME 273,* 335 (1966).

19. Willman, B. T., Valleroy, V. V., Runberg, G. W., Cornelius, A. J., and Powers, L. W.: "Laboratory Studies of Oil Recovery by Steam Injection," *Trans. AIME 681,* (1961).

APPENDIX A

Porous Medium Properties

Ottawa sand	170-200 mesh
Length of core	2.5 in.
Diameter of core	4.0 in.

Porous Diaphragm Properties

Material	ceramic
Porosity	to be measured
Dimensions	4 in. diameter; 0.25 in. thickness
Threshold Pressures	gas-water.....greater than 60 psig
	oil-water.....greater than 32 psig

APPENDIX B

Table B.1 Cumulative Data for Run 1.

V_p =	76.86	(cm^3)			
h_3 =	19.665	(cm)			
h_4 =	17.128	(cm)			
h_d =	8.247	(cm)			
T_{rm} (°F)	T_{oven} (°F)	h_5 (cm)	h_2 (cm)	h_1 (cm)	h_T (cm)
72	120	29.158	8.274	10.882	29.158
72	120	29.446	8.623	12.411	29.446
72	120	30.683	9.914	13.868	30.683
72	120	31.804	11.019	15.287	31.804
75	120	33.000	12.176	16.570	33.000
75	120	34.093	13.453	17.900	34.093
76	120	35.413	14.665	19.343	35.413
77	120	36.762	16.034	20.760	36.762
77	120	37.900	17.260	22.110	37.900
72	121	38.942	18.413	23.400	38.942
72	121	40.159	19.694	24.730	40.159
71	120	41.400	21.000	26.208	41.400
73	120	42.586	22.142	27.540	42.586
76	120	45.623	25.200	31.355	45.623
74	121	32.455	26.727	31.790	47.121
70	122	33.393	27.800	35.744	48.059
73	121	33.888	28.234	41.732	48.554
73	120	33.976	28.419	45.700	48.642
74	120	23.072	28.443	50.419	48.738
75	120	23.128	28.575	60.918	48.794

V_p = pore volume, (cm^3)
h_3 = height of oil line into oven, (cm)
h_4 = height of water line into oven, (cm)
h_d = datum line, (cm)
T_{rm} = room temp, (^oF)
T_{oven} = oven temp, (^oF)
h_5 = height in water manometer, (cm)
h_2 = height in oil/Hg manometer, (cm)
h_1 = height in Hg manometer, (cm)
h_T = cumulative displacement of water, (cm)

See Fig. 6.1 for further details.

Table B.2

STEP 1

Time (*hrs*)	Height of Water (*cms*)
0.00	29.158
11.33	29.192
23.50	29.332
34.25	29.360
38.00	29.406
130.00	29.446

STEP 2

Time (*hrs*)	Height of Water (*cms*)
0.00	29.446
47.00	30.602
72.00	30.668
165.00	30.683

STEP 3

Time (*hrs*)	Height of Water (*cms*)
0.0	30.683
1.00	31.180
2.60	31.458
3.88	31.566
4.78	31.661
5.75	31.698
52.67	31.797
72.00	31.785
85.33	31.804

STEP 4

Time (*hrs*)	Height of Water (*cms*)
0.00	31.804
10.00	32.771
12.67	32.818
36.67	32.819
82.00	32.921
110.83	32.988
131.00	33.000

STEP 5

Time (*hrs*)	Height of Water (*cms*)
0.00	33.000
2.83	33.915
4.00	34.013
5.67	34.040
9.17	34.080
11.67	34.087
13.00	34.091
23.42	34.087
28.25	34.093
36.42	34.093

STEP 6

Time (*hrs*)	Height of Water (*cms*)
0.00	34.093
1.25	35.147
2.75	35.283
10.00	35.312
38.00	35.375
56.17	35.413
82.42	35.413

STEP 7

Time (*hrs*)	Height of Water (*cms*)
0.0	35.413
1.67	36.433
2.67	36.593
3.92	36.665
7.17	36.700
11.67	36.731
22.17	36.731
27.83	36.765
36.25	36.762

STEP 8

Time (*hrs*)	Height of Water (*cms*)
0.00	36.762
1.25	37.554
9.67	37.842
13.17	37.899
34.67	37.899
38.08	37.899
44.83	37.900

STEP 9

Time (*hrs*)	Height of Water (*cms*)
0.00	37.900
2.00	38.920
15.00	38.967
27.00	38.933
30.75	38.897
43.00	38.923
49.00	38.942

STEP 10

Time (*hrs*)	Height of Water (*cms*)
0.00	38.942
20.67	40.101
25.17	40.101
33.67	40.119
45.67	40.164
48.42	40.164
60.83	40.164
65.00	40.164
72.83	40.129
84.17	40.148
119.17	40.159

STEP 11

Time (*hrs*)	Height of Water (*cms*)
0.00	40.159
1.33	41.150
3.33	41.364
45.50	41.387
81.67	41.360
88.00	41.407
93.67	41.407
97.00	41.400

STEP 12

Time (*hrs*)	Height of Water (*cms*)
0.00	41.400
1.25	42.254
11.33	42.569
12.75	42.569
16.75	42.602
20.00	42.586

STEP 13

Time (*hrs*)	Height of Water (*cms*)
0.00	42.586
2.25	45.338
15.75	45.594
19.00	45.648
21.67	45.633
26.33	45.623

STEP 14

Time (*hrs*)	Height of Water (*cms*)
0.00	30.986
1.67	32.287
17.17	32.455
24.67	32.455

STEP 15

Time (*hrs*)	Height of Water (*cms*)
0.00	32.45[illegible]
0.50	32.701
1.00	32.808
1.58	32.902
2.00	32.956
3.00	33.033
30.75	33.387
56.75	33.393

STEP 16

Time (*hrs*)	Height of Water (*cms*)
0.00	33.393
1.00	33.452
2.00	33.493
3.00	33.533
4.00	33.568
7.00	33.638
10.00	33.697
12.33	33.727
20.00	33.801
22.00	33.831
25.17	33.852
33.00	33.888

STEP 17

Time (*hrs*)	Height of Water (*cms*)
0.00	33.888
1.83	33.893
3.00	33.893
19.75	33.965
23.83	33.976
26.25	33.976

STEP 18

Time (*hrs*)	Height of Water (*cms*)
0.00	22.976
14.75	23.029
18.75	23.040
24.00	23.044
41.00	23.072

STEP 19

Time (*hrs*)	Height of Water (*cms*)
0.00	23.072
14.50	23.072
21.50	23.098
39.33	23.114
45.67	23.118
53.50	23.118
67.50	23.128
70.00	23.128

APPENDIX C

Temperature and pressure can have a large influence on the density of reservoir fluids. However, a hydrocarbon with a density of 0.85 gm/cm^3 at 60°F and 14.7 psia shows a density change of less than 0.59% when measured at 60°F and 500 psia.[1] Due to the low operating pressures of the system, the oil density changes due to pressure can be neglected. This reasoning can be extended to include water and mercury which have smaller compressibilities than oil.[2]

C.1. WATER DENSITY

Temperature versus specific volume data are shown in Table C.1.[3]

TABLE C.1
SPECIFIC VOLUMES OF WATER.[1]

Temp (^oF)	Specific Volume[1] (cc/gm)	Calculated Sp. Vol. (cc/gm)	Temp (^oF)	Specific Volume[1] (cc/gm)	Calculated Sp. Vol. (cc/gm)
10	1.000	0.999	85	1.033	1.032
15	1.001	1.000	90	1.036	1.036
20	1.002	1.002	95	1.040	1.040
25	1.003	1.003	100	1.044	1.043
30	1.004	1.005	105	1.048	1.047
35	1.006	1.006	110	1.052	1.052
40	1.008	1.008	115	1.056	1.056
45	1.010	1.010	120	1.060	1.060
50	1.012	1.013	125	1.065	1.065
55	1.015	1.015	130	1.070	1.070
60	1.017	1.017	135	1.075	1.075
65	1.020	1.020	140	1.080	1.080
70	1.023	1.023	145	1.085	1.086
75	1.026	1.026	150	1.091	1.091
80	1.029	1.029			

After the appropriate unit conversions, the data were then curve-fitted using the following polynomial form and the coefficients were determined:

$$\ln(\rho_w) = a + bT + cT^2 \qquad \text{(C.1)}$$

1 Adapted from The Engineering Data Book, 1972.
2 Handbook of Chemistry and Physics, 1979.
3 Adapted from Keenan, Keyes, Hill, and Moore, Steam Tables, 1969.

where:

a = 4.3909388×10^{-3}

b = $-2.7032325 \times 10^{-5}$

c = $-9.1533970 \times 10^{-7}$

ρ_w = gm/cc

T = ^oF

The asteriks in Fig. C.1 show the converted data from the steam tables while the solid line shows the result of the curve-fit which gives a maximum error of 0.076% for the temperature range given.

C.2 OIL DENSITY

The measured temperature-density data of Kadol are given in Table C.2.

TABLE C.2
KADOL OIL DENSITIES

Temp (^oF)	Measured Density (gm/cc)	Calculated Density (gm/cc)	Temp (^oF)	Measured Density (gm/cc)	Calculated Density (gm/cc)
71.	0.8739	0.8740	125.06	0.8553	0.8557
92.84	0.8672	0.8666	141.8	0.8504	0.8501
104.	0.8628	0.8628	159.8	0.8443	0.8442
114.44	0.8590	0.8593	174.92	0.8392	0.8392
119.84	0.8572	0.8575			

The densities were determined by immersing a pycnometer, filled with Kadol, in a water bath at successively higher temperatures and recording the weight of oil that occupied the pycnometer volume at each temperature. Since the volume of the pycnometer changes with temperature, it was necessary to calibrate the vessel. Because distilled water is easy to handle, and the nature of its temperature-density relationship is well established, it was used for the calibration. The temperature-specific volume data for water are given in Table C.1 and the temperature-density data for Kadol are plotted on Fig. C.1. The data were then curve-fitted using a least-square method derived from the isobaric thermal expansion equation, Eq. C.2.

$$\beta = \frac{1}{V}\left[\frac{\partial V}{\partial T}\right]_p \qquad \text{(C.2)}$$

where

β = coefficient of thermal expansion.

1 Adapted from Keenan, Keyes, Hill, and Moore, Steam Tables, 1969.

By multiplying both the top and bottom of the right- hand side by (m/V^2), rearranging the terms, integrating and then evaluating the function at $T_o = 0$, the following exponential form was derived and the coefficients were calculated.

$$\ln(\rho_o) = a + \beta T \tag{C.3}$$

where

$a = -1.06890071 \times 10^{-1}$
$\beta = -3.91240498 \times 10^{-4}$
$\rho_o = gm/cc$, and
$T = {}^oF$

This is assuming that β is constant over the temperature range of interest. The circles in Fig. C.1 show the measured data from Table C.2 while the solid line shows the results of the curve-fit which gives a maximum error of 0.073% for the temperature range of the measured data.

C.3 MERCURY DENSITY

When the data for mercury from Table C.3 were plotted in Fig C.2, a linear relationship between temperature and density of mercury became apparent[1]. A straight line, least square curve fit was performed on the data and the coefficients were determined:

$$\rho_{hg} = a + bT \tag{C.4}$$

TABLE C.3
MERCURY DENSITIES.[1]

Temp (^oF)	Measured Density (gm/cc)	Calculated Density (gm/cc)	Temp (^oF)	Measured Density (gm/cc)	Calculated Density (gm/cc)
59	13.5585	13.5583	104	13.4973	13.4974
68	13.5462	13.5461	122	13.4729	13.4731
77	13.5340	13.5339	140	13.4486	13.4487
86	13.5217	13.5218	158	13.4244	13.4244
95	13.5095	13.5096	176	13.4003	13.4000

where

$a = 1.36380963 \times 10^{1}$
$b = -1.35259259 \times 10^{-3}$
$\rho_{hg} = gm/cc$, and
$T = {}^oF$

For the temperature range shown, the curve-fit gives a maximum error of 0.00194 %.

1 Handbook of Chemistry and Physics, 1979.

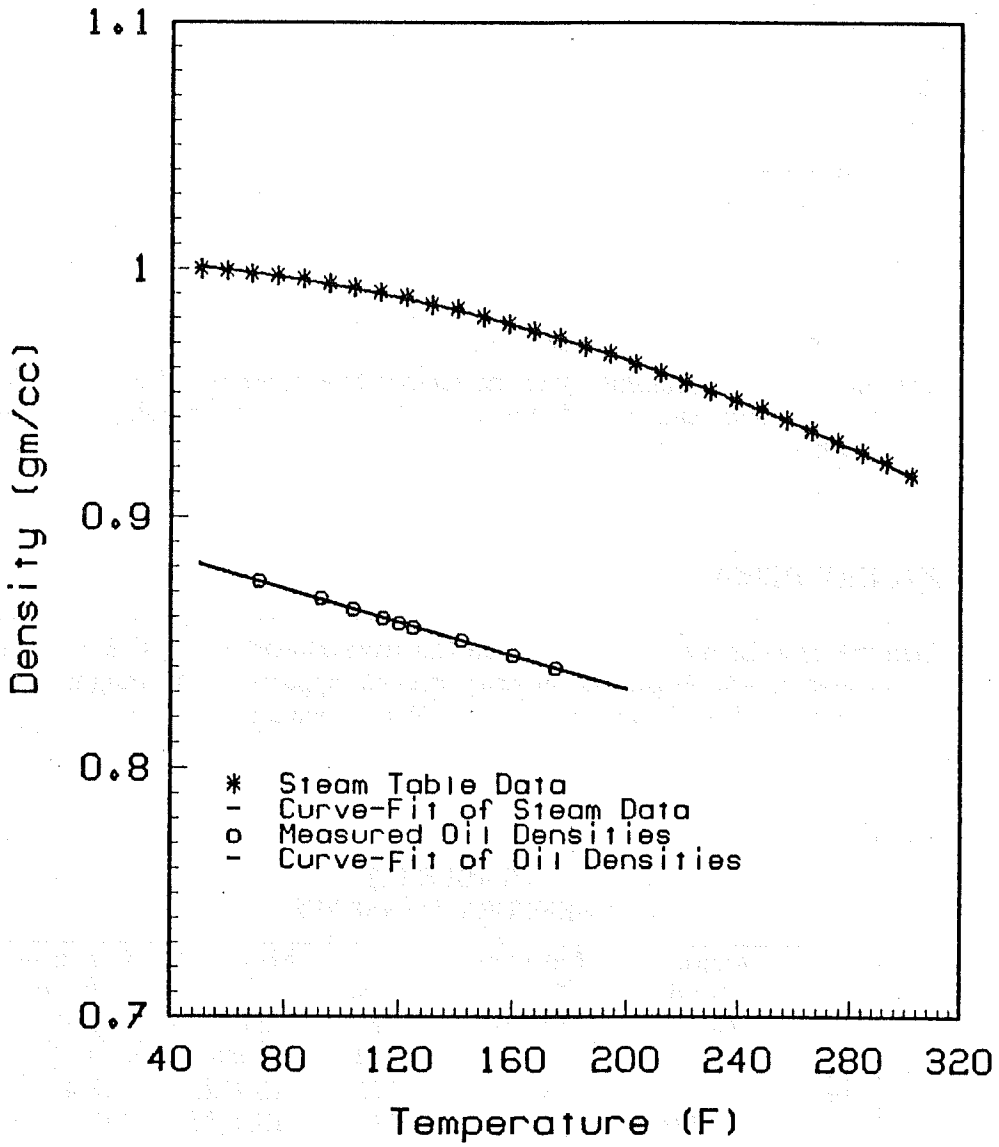

Fig. C.1 Oil and Water - Temperature vs Density

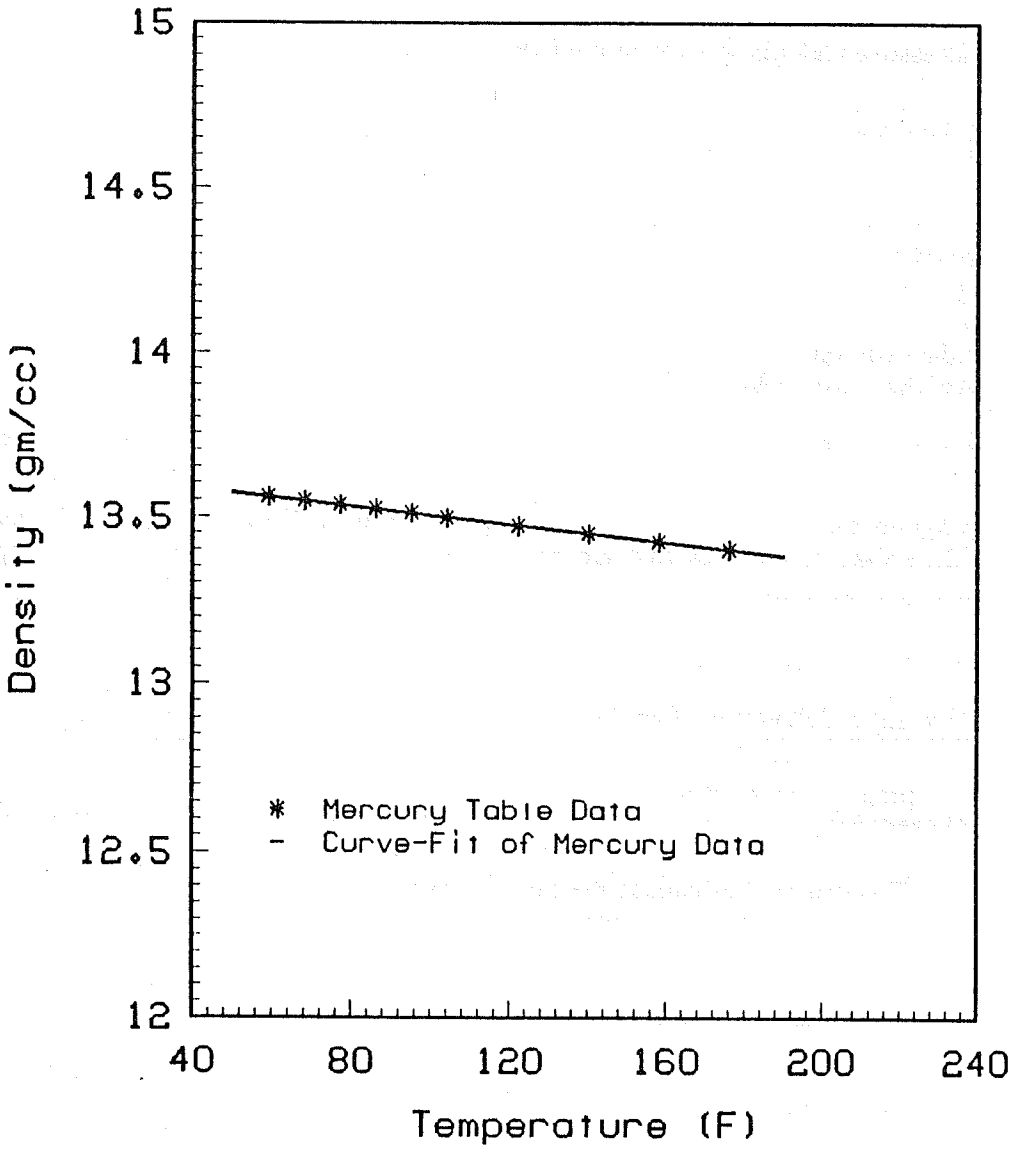

Fig. C.2 Mercury - Temperature vs Density

APPENDIX D

Capillary Pressure Calculation Command Program

```
shell program "cap"
*************************************************************************
for i
do
cp run$i run.dat
capsatprog
rm run.dat
mv capsat.dat capsat$i
mv capsatrof.dat capsatrof$i
done
*************************************************************************
```

This csh program can be used to run the capillary pressure calculation program "capsatprog" and to produce data output files that are compatible with the graphing program "graph" and "vtroff".

Capillary Pressure Calculation Program

```
      program capsatprog
c*************************************************************
c
c     This program calculates the capillary pressure at
c     each step in the experimental run.
c
c
c     Data input file = run[n].dat
c       n = run #
c
c     To run this program, use the csh file:
c
c           cap run[n]     <cr>
c
c
c     pvol = pore volume in cc
c     hlino = height of oil line into oven(cm)
c     hlinw = height of water line into oven(cm)
c     hdat = datum line (usually same as height of
c           membrane and sand pack) (cm)
c     tmr =  room temp deg F
c     tmc =  oven temp deg F
c     htw =  height in water manometer(cm)
c     htom = height in oil/Hg manometeri(cm)
c     hthg = height in Hg manometer(cm)
c     htdh = cumulative displacement of water
c           starting from initial htw(cm)
c
```

```
c      data output = satpres.dat and satprestrof.dat
c                    (fractional water saturation
c                      and psi)
c
c*****************************************************************
 open(unit=7,file='run.dat')
 open(unit=8,file='capsat.dat')
 open(unit=9,file='capsatrof.dat')
c*****************************************************************
c
c                   INPUT DATA
c
c*****************************************************************

     grav= 980.6
     read(7,*) pvol,hlino,hlinw,hdat
     read(7,*,end=300) tmr,tmc,htw,htom,hthg,htdh
     htdh1 = htdh
     go to 75
50    continue
     read(7,*,end=300) tmr,tmc,htw,htom,hthg,htdh
75   continue
c*****************************************************************
c
c                MERCURY CONTRIBUTION
c
c*****************************************************************

       a= 13.6380963
       b= -0.00135259259
       hgrho=a+(b*tmr)
       fhg= hgrho*grav*(hthg-htom)

c*****************************************************************
c
c                   OIL CONTRIBUTION
c
c*****************************************************************

      d= -0.106890071
       e= -0.000391240498
       orhoc =exp(d+(e*tmc))
       orhorm=exp(d+(e*tmr))
       foil=orhorm*grav*(htom-hlino) + orhoc*grav*(hlino-hdat)

c*****************************************************************
c
c                   WATER CONTRIBUTION
c
c*****************************************************************

       a=4.3909388e-3
       b=-2.7032325e-5
       c=-9.153397e-7
```

```
      wrhorm=exp(a+(b*tmr)+(c*(tmr**2.)))
      wrhoc =exp(a+(b*tmc)+(c*(tmc**2.)))
      fwat=wrhoc*grav*(hlinw-hdat)-wrhorm*grav*(htw-hlinw)

c*************************************************************
c
c                  CAP PRESSURE
c
c*************************************************************

      cap = fhg + foil + fwat
      cap = cap*0.0000145074
      sat = 1.-((htdh-htdh1)*3.87/pvol)
      write(8,*) sat,cap
      write(9,220) sat,cap
220    format(f5.1,'/',f6.4)
      go to 50
300    continue
   close(unit=7)
   close(unit=8)
   close(unit=9)
   stop
 end
```

Data File for Computer Program

Use this format for the data file when using the above computer program. See Table B.1 in Appendix B for a line by line description of the data file.

Table D.1 Data File for Computer Program

76.86					
19.665					
17.128					
8.247					
72	120	29.158	8.274	10.882	29.158
72	120	29.446	8.623	12.411	29.446
72	120	30.683	9.914	13.868	30.683
72	120	31.804	11.019	15.287	31.804
75	120	33.000	12.176	16.570	33.000
75	120	34.093	13.453	17.900	34.093
76	120	35.413	14.665	19.343	35.413
77	120	36.762	16.034	20.760	36.762
77	120	37.900	17.260	22.110	37.900
72	121	38.942	18.413	23.400	38.942
72	121	40.159	19.694	24.730	40.159
71	120	41.400	21.000	26.208	41.400
73	120	42.586	22.142	27.540	42.586
76	120	45.623	25.200	31.355	45.623
74	121	32.455	26.727	31.790	47.121
70	122	33.393	27.800	35.744	48.059
73	121	33.888	28.234	41.732	48.554
73	120	33.976	28.419	45.700	48.642
74	120	23.072	28.443	50.419	48.738
75	120	23.128	28.575	60.918	48.794

PROJECT 2: IN-SITU COMBUSTION

This project has two main areas of research. It focuses on experimental and theoretical determination of the kinetics of the reactions occurring in *in-situ* combustion and an understanding of the combustion process in field application.

2.1 KINETICS OF IN-SITU COMBUSTION EFFECT OF METALLIC ADDITIVES
(Carlos De Los Rios)

2.1.1. INTRODUCTION

The oil oxidation reactions of *in-situ* combustion have been adequately studied and modeled. The overall oxidation mechanism of crude oil in porous media is an overlap of several consecutive reactions which can be divided into three sequences:

1. Low-temperature oxidation reactions which are heterogeneous (gas-liquid) and produce no carbon oxides.
2. Medium-temperature fuel deposition reactions, which are homogeneous (gas phase), involving the oxidation of the products of distillation and pyrolysis.
3. High-temperature, fuel combustion reactions, which are heterogeneous (gas-solid), where oxygen reacts with the heavy oil residue deposited by medium temperature reactions.

Several investigators (Bousaid and Ramey, 1968; Johnson, *et al.*, 1968; Crawford, 1968) have noted that metallic additives have catalytic effects on these reactions. Fassihi (1981) reported that certain metallic additives will lower the activation energy of the combustion reaction. Raćz (1984) noted that fuel formation is far more intensive in the presence of metallic catalysts. The significance of these observations lies in the recognition that metallic additives, in the form of water soluble compounds, might be introduced into a reservoir through a wet combustion process in order to promote combustion where the fuel concentrations are normally too low to maintain a self-sustained combustion.

The objective of this study is to determine the effect of a wide range of metallic salts on the oxidation reaction kinetics of *in-situ* combustion.

2.1.2. EXPERIMENTAL APPARATUS

Figure 1 shows a schematic of the apparatus used to study the reaction kinetics of oil oxidation in porous media. The system is basically similar to the one built by Fassihi (1981) with some modifications. Its main components are a combustion cell placed in a furnace, three continuous gas analyzers, and equipment for the measurement and control of temperature and flow rate.

2.1.3. COMBUSTION CELL

The combustion cell, Fig. 2, is made of a 4¼-inch long, 1-inch O.D., thick wall stainless steel pipe which is closed on both ends by plugs held in place by screwed on caps. The high-temperature gas seal is achieved with two brass "0" rings located between the end plugs and the pipe.

Two thin-wall cups are housed inside the combustion cell; both with perforated bottoms. The lower cup, which is 1-1/16-inches high, is filled with dry sand, thus acting as a preheater and distributor for the gas feed. The upper cup, which is packed with the oil/sand sample, is 2 inches high and rests on the lower cup. A 2-inch long, 1/8-inch O.D. tube that runs along the

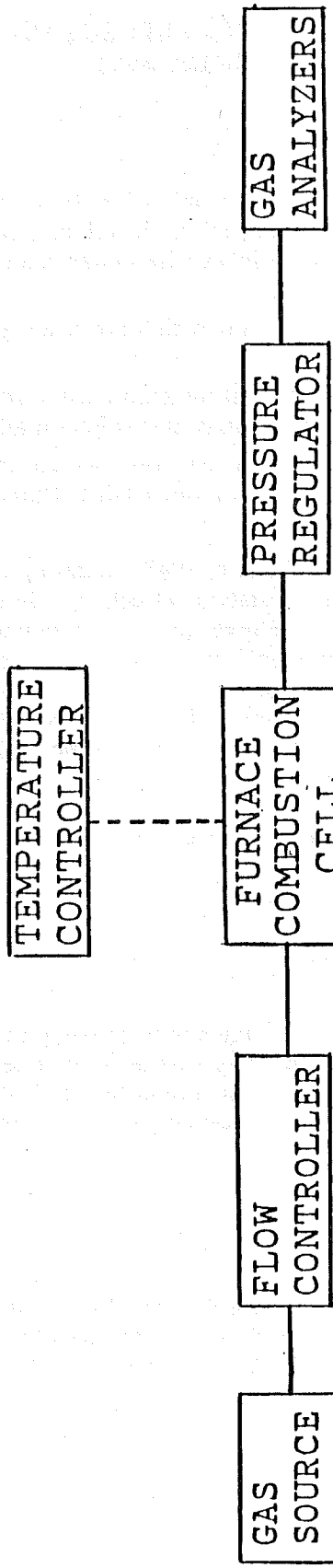

Fig. 1 Schematic Diagram of Apparatus for Kinetics Studies of *In-situ* Combustion

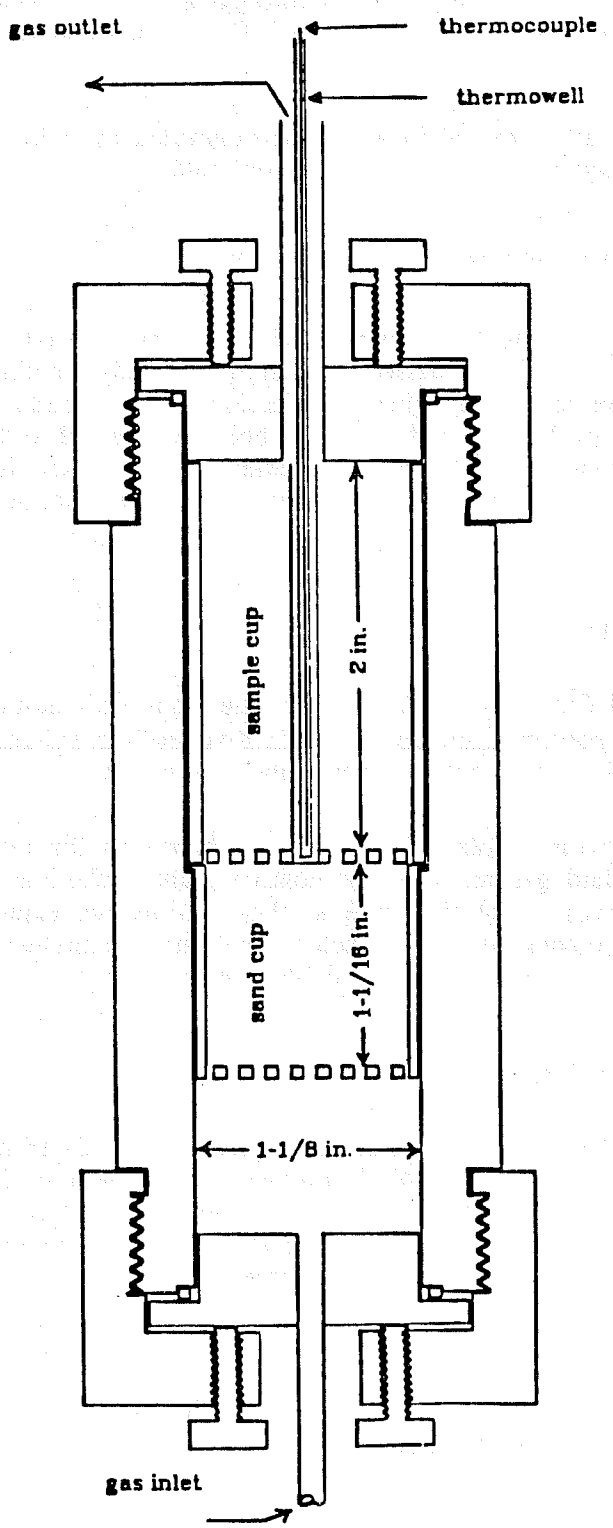

Fig. 2. Pyrolysis Cell

axis of the cell is soldered to the bottom of the sample cup, acting as a guide for the thermowell which houses a thermocouple. Screens of 200 mesh are placed at the bottom of the cups for added support. Gas enters the cell through a coil of 1/8-inch O.D. tubing, which serves as a preheater, and exits through a 1/4-inch O.D. tube. specifications of the combustion cell components.

The combustion cell is heated in a furnace controlled by a log/linear temperature controller which can be programmed for different heating rates.

2.1.4. GAS FLOW AND PRESSURE REGULATION

Feed gas is supplied by high pressure cylinders and the flow rate is regulated by an electronic mass flow controller. Gas is passed through dreirite beds for filtration and drying before entering the combustion cell. The effluent gas is cooled by a condenser made of a 1/8-inch O.D. tubing coil in on ice bath. Another dreirite bed is connected to the condenser. A 0-500 psi, adjustable back-pressure regulator, placed after the condenser, is used to maintain the desired system pressure. Effluent gas is then metered with an electronic mass flow meter and vented to the atmosphere.

2.1.5. GAS ANALYSIS

Concentrations of CO, CO_2 and O_2 in the effluent gas are measured by three on-line gas analyzers. A constant portion of the gas stream is diverted into the analyzers and then recombined with the rest of the stream before it enters the flow meter.

The gas analyzers are calibrated initially with nitrogen for the zero points and then periodically with standard gas mixtures for upscale points. Calibration is performed at the same conditions of pressure and flow rate as those during the experiment. Two four-way valves control the calibration and flow lines to minimize disturbances in the system when switching the analyzers between on-line and calibration modes.

2.1.6. DATA COLLECTION

Readings from most of the instruments are scanned by Esterline Angus PD2064 data logger and recorded by a Tektronix 4054 computer at three-minute intervals. These instruments include the combustion cell temperature indicator, the mass flow meter, and the three gas analyzers. Those readings are also recorded on strip charts for monitoring and backup purposes. Data are then processed, analyzed, and printed by a VAX 11750 computer.

2.1.7. PROCEDURE

In this section, properties of the sand and crude oil used in the experiment are discussed as well as procedure for preparation of sand packs.

2.1.7.1. Crude Oil Properties

Crude oil from the Huntington Beach field is being used in this experiment. Table 1 lists some of its basic properties as well as an elemental analysis. Figure 3 shows a distillation analysis of the oil.

2.1.7.2. Sand Pack Properties

All runs are made using clean, unconsolidated, 20-30 mesh Ottawa sand. Table 2 shows a sieve analysis of the sand.

2.1.7.3. Operation

All runs are made with mixtures of sand, oil, and water, in proportions that yield approximate values of desired porosity and saturation. A typical run is started by adding 2 ml of a solution containing varying concentrations of metallic salts in water to about 40 g. of premixed oil/sand mixture. The oil saturation (about 15 percent) was chosen as to minimize oxygen consumption and hence heat generation.

After tamping the mixture into the sample cup, the combustion cell is pressure tested with nitrogen and placed inside the furnace. The system is brought to desired operating pressure by flowing air and adjusting the back pressure regulator. The bed is then subjected to a linear temperature rise until the amount of produced carbon oxides becomes insignificant. After the system has cooled, the contents of the sample cup are examined and weighed.

2.1.8. DATA ANALYSIS

Figure 4 shows a typical response of effluent gas composition vs. time for a crude oil in a porous media subjected to a linear temperature rise. There are two apparent peaks at different temperatures in the production of carbon oxides and the consumption of oxygen. These peaks represent an overlap of three sequences of oxidation reactions.

At low temperatures, the crude oil undergoes an oxidation reaction without production of carbon oxides. At higher temperatures, the oxygen consumption increases and carbon oxides are generated. Under these conditions, distillation coupled with pyrolysis produces hydrogen gas and some light hydrocarbons in the gas phase. A major part of these hydrocarbons are produced without being oxidized. However, oxygen reacts with the remainder of these gases and hence, medium-temperature oxidation occurs. At still higher temperatures, the amount of consumed oxygen is comparable to the produced carbon oxides (i.e., $CO_2 + 1/2\ CO$). Here, oxygen reacts with the heavy residue of oil that is deposited on the solid matrix as a result of medium temperature reactions. This pattern is the basis for analysis of the data for these separate reactions are described in the following paragraphs.

2.1.8.1. Modeling of the Reactions

The experimental data were evaluated for activation energies, Arrhenius constants, and reaction orders using a model which was based on Weijdema's kinetic equation (1968) as outlined by Fassihi (1981).

TABLE 1
CRUDE OIL PROPERTIES

Field	Zone	Gravity (°Ari)	%C	%H	Atomic Wc Ratio	%N	*MW*
Huntington Beach	Lower Main Zone	18.5	84.50	11.53	1.64	0.86	386

TABLE 2
SIEVE ANALYSIS OF SAND

Sieve Size	Percent by Weight Retained
20	0.40
24	41.40
28	57.70
32	0.43
60	0.05
60	0.02
	100.00

TABLE 3
CALCULATED *E/R* (°K × 10^{-3})

Run	Low-Temperature Oxidation	Fuel Deposition	Fuel Composition
201	14.82	8.333	7.462
202	14.03	8.340	8.515
203	14.83	9.655	9.318
204	14.91	9.820	8.457
205	15.24	10.92	10.38
206	13.64	10.40	6.775
Fassihi (1981)	16.20	9.551	8.059

CRUDE PETROLEUM ANALYSIS

Bureau of Mines Bartlesville Laboratory
Sample 55141

IDENTIFICATION

Huntington Beach field
Jones sand, offshore (Upper Miocene)
6,300 feet

California
Orange County

GENERAL CHARACTERISTICS

Specific gravity, 0.945 A. P. I. gravity, 18.2° Pour point, ° F., 15
Sulfur, percent 1.46 Color, brownish black
Saybolt Universal viscosity at 100° F., 870 sec.; Nitrogen, percent, 0.830
at 130° F., 400 sec.

DISTILLATION, BUREAU OF MINES ROUTINE METHOD

STAGE 1—Distillation at atmospheric pressure, 756 mm. Hg
First drop, 71 ° C. (160 ° F.)

Fraction No.	Cut temp. ° F.	Percent	Sum, percent	Sp. gr., 60/60° F.	° A. P. I., 60° F.	C. I.	Refractive index N_D at 20° C.	Specific dispersion	S. U. visc., 100° F.	Cloud test, ° F.
1	122									
2	167									
3	212	1.7	1.7	0.749	57.4	-)				
4	257	3.0	4.7	.763	54.0	33)	1.41593	122.7		
5	302	3.3	8.0	.783	49.2	35	1.42922	126.1		
6	347	2.6	10.6	.803	44.1	39	1.44154	130.5		
7	392	3.0	13.6	.829	39.2	43	1.45399	135.6		
8	437	3.5	17.1	.849	35.2	47	1.46534	141.5		
9	482	4.4	21.5	.862	32.7	48	1.47332	151.5		
10	527	9.0	30.5	.872	30.8	48	1.48202	158.8		
STAGE 2—Distillation continued at 40 mm. Hg										
11	392	1.0	31.5	0.880	29.3	48	1.48696	142.5	43	Below 5
12	437	3.3	34.8	.897	26.3	52	1.49610	149.2	55	10
13	482	5.7	40.5	.916	23.0	58	1.50672	142.5	87	20
14	527	4.4	44.9	.927	21.1	60	1.51560	-	200	45
1/ 15	572	6.8	51.7	.950	17.5	-	-	-	Over 400	55
Residuum.		48.2	99.9	1.022	7.0					

Ramsbottom carbon residue: Residuum, 10.9 percent; crude, 5.7 percent.
Equivalent Conradson carbon residue: Residuum, 13.4 percent.

APPROXIMATE SUMMARY

	Percent	Sp. gr.	° A. P. I.	Viscosity
Light gasoline	1.7	0.749	57.4	
Total gasoline and naphtha	10.6	0.778	50.4	
Kerosine distillate	-	-	-	
Gas oil	21.8	.861	32.8	
Nonviscous lubricating distillate	5.9	.891-.917	27.3-22.8	50-100
Medium lubricating distillate	4.4	.917-.927	22.8-21.1	100-200
Viscous lubricating distillate	9.0	.927-.963	21.1-15.4	Above 200
Residuum	48.2	1.022	7.0	
Distillation loss	1			

1/ Distillation discontinued at 565° F.

Fig. 3. Distillation analysis of the Huntington Beach crude oil.

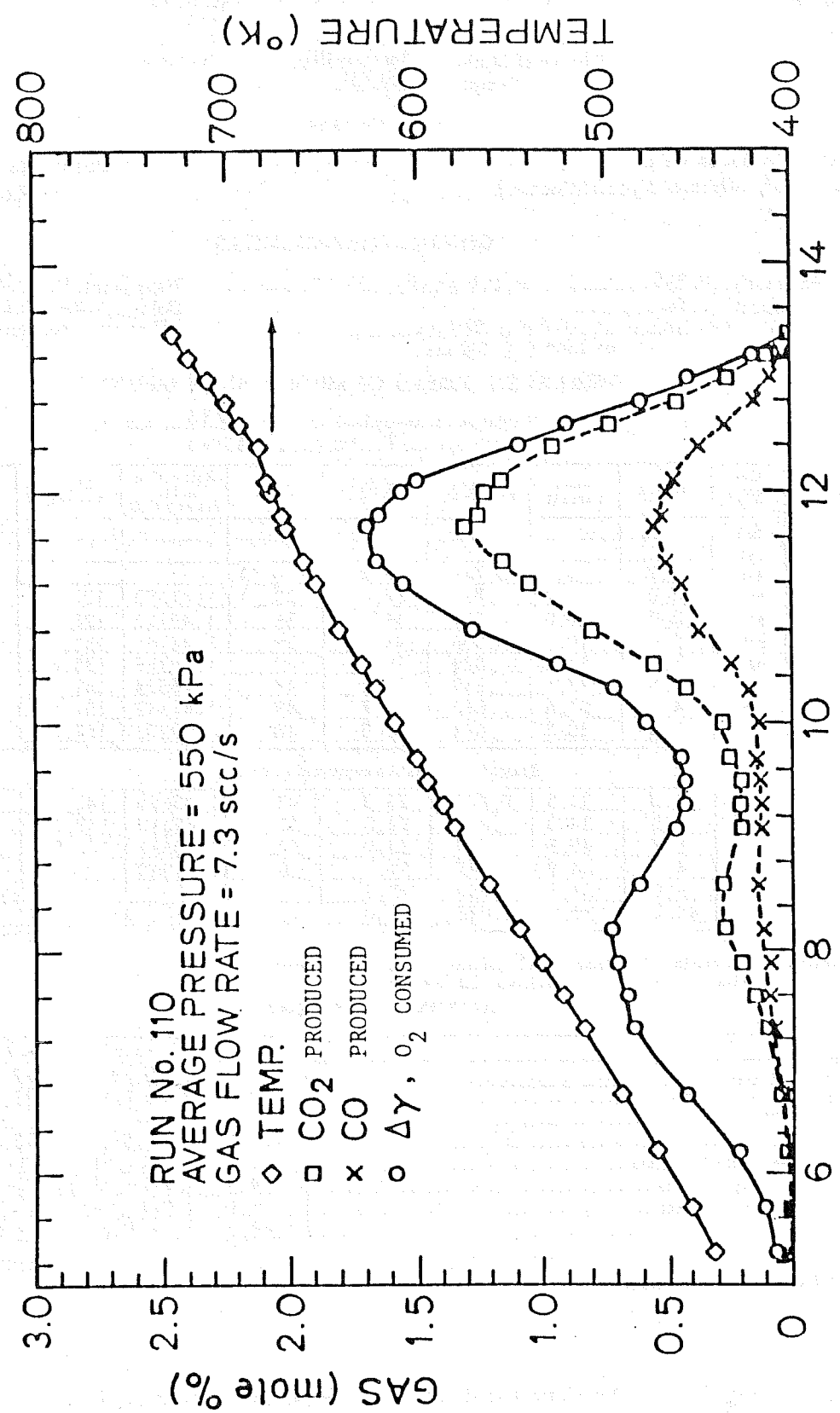

Fig. 4. Gas composition and temperature vs. time for Huntington Beach oil.

In this model, a plot of the logarithm of the relative reaction rate ($\Delta\gamma / \int_{+}^{\infty} \Delta\gamma \, dt'$, where $\Delta\gamma$ is oxygen consumed) vs. the inverse of temperature yields a straight line with a slope proportional to the activation energy, for single reactions. Figure 5 shows such a plot for Run 110 (Fassihi, 1981). At high temperatures, the data fall on a straight line as predicted by the model, but deviate at lower temperatures (higher $1/T$ values).

It is assumed that this reaction also occurs at lower temperatures according to an extrapolation of the high temperatures data. By subtracting this extrapolation (Curve I, Fig. 6) from the original $\Delta\gamma$ curve, a new curve (Curve II, Fig. 6) is obtained which describes the oxidation behavior at medium temperatures. Likewise, Curve III (Fig. 6) is obtained which describes the production of carbon oxides at medium temperatures.

From Curve II, calculation of the relative reaction rate as a function of $1/T$ leads to the curve labeled II on Fig. 7, which is not linear. However, a plot of an equivalent term for carbon oxides formed, $\partial / \int_{+}^{\infty} \delta dt'$, where $\delta = CO_2 + 1/2\ CO$ from Curve III, shows a definite straight line (Fig. 6). An activation energy for the medium temperature oxidation reaction is calculated from the slope of this line by assuming that the oxygen consumption curve follows the same slope as the carbon oxides curve. The oxygen consumption for the medium temperature can then be calculated and subtracted from Curve II of Fig. 5, giving Curve V which represents oxygen consumed in the low temperature reaction.

When Curve V is evaluated using the Weijdema integral, $\Delta\gamma \int_{+}^{\infty} \Delta\gamma \, dt'$, and the result is graphed as a function of $1/T$, an activation energy for the low-temperature oxidation reaction may be determined.

Using the computer interactively, the same analysis is applied to other experimental data.

2.1.9. RESULTS

At the time of this report, six runs had been completed; two with no metallic additive (Runs 201 and 202); two with 1.02 percent $CuSO_4$ solution added (Runs 203 and 204), and two with 0.501 percent $CuSO_4$ solution added (Runs 205 and 206). The calculated activation energies are listed in Table 3 along with the average values obtained for the same oil by Fassihi (1981).

The activation energies for Runs 201 and 202 show good agreement with those determined by Fassihi, with deviations ranging from 0.57 to 1.3 percent. This result verifies the repeatability of the experimental procedure and data analysis technique.

The activation energies determined from the runs of varying $CuS0_4$ concentration (Runs 203-206) do not show significant deviation from those without additive (Runs 201 and 202). Therefore, at these concentrations, $CuSO_4$ does not have a catalytic effect on the reactions.

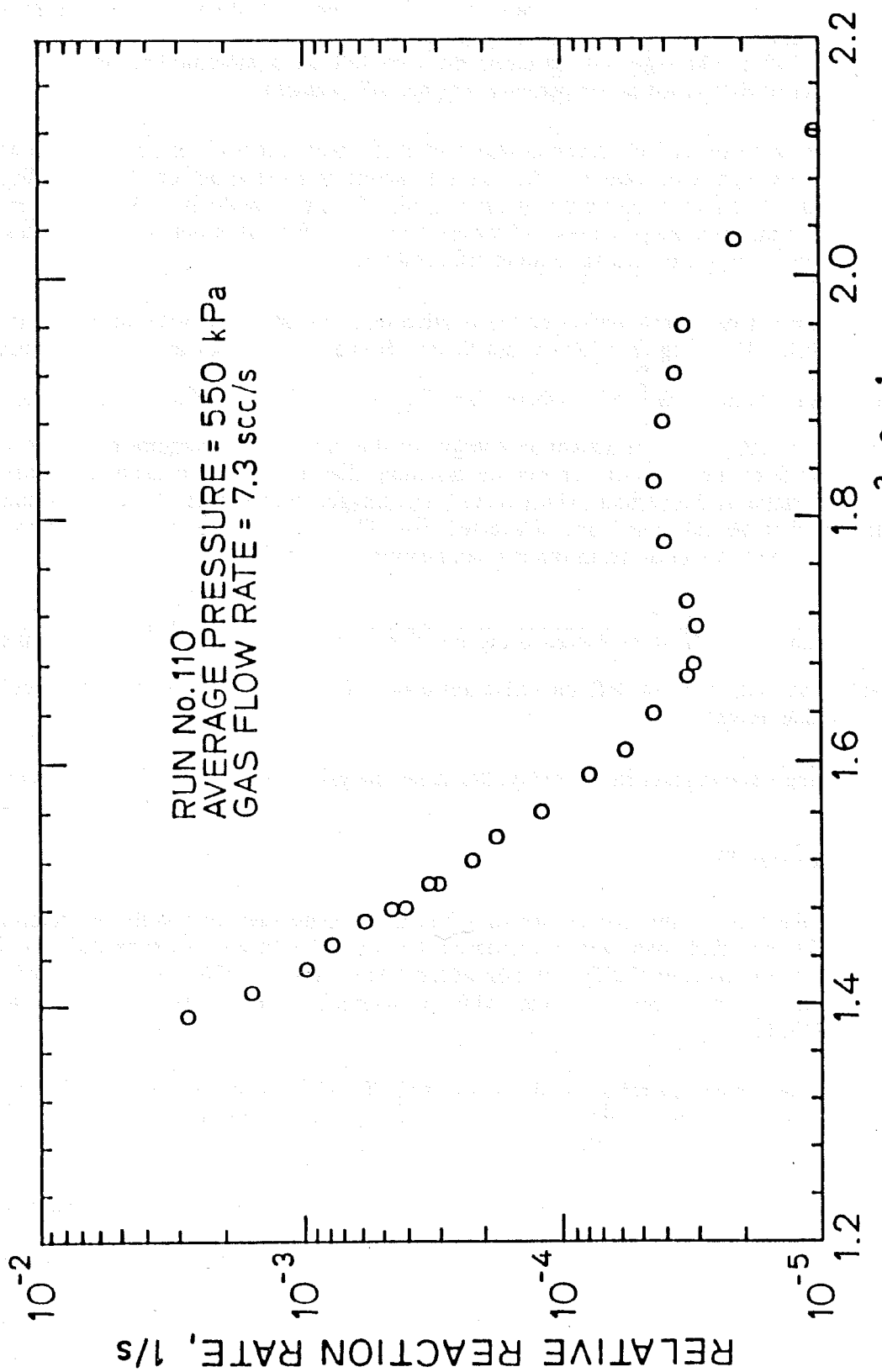

Fig. 5. Relative reaction rate vs. inverse temperature for Run No. 110.

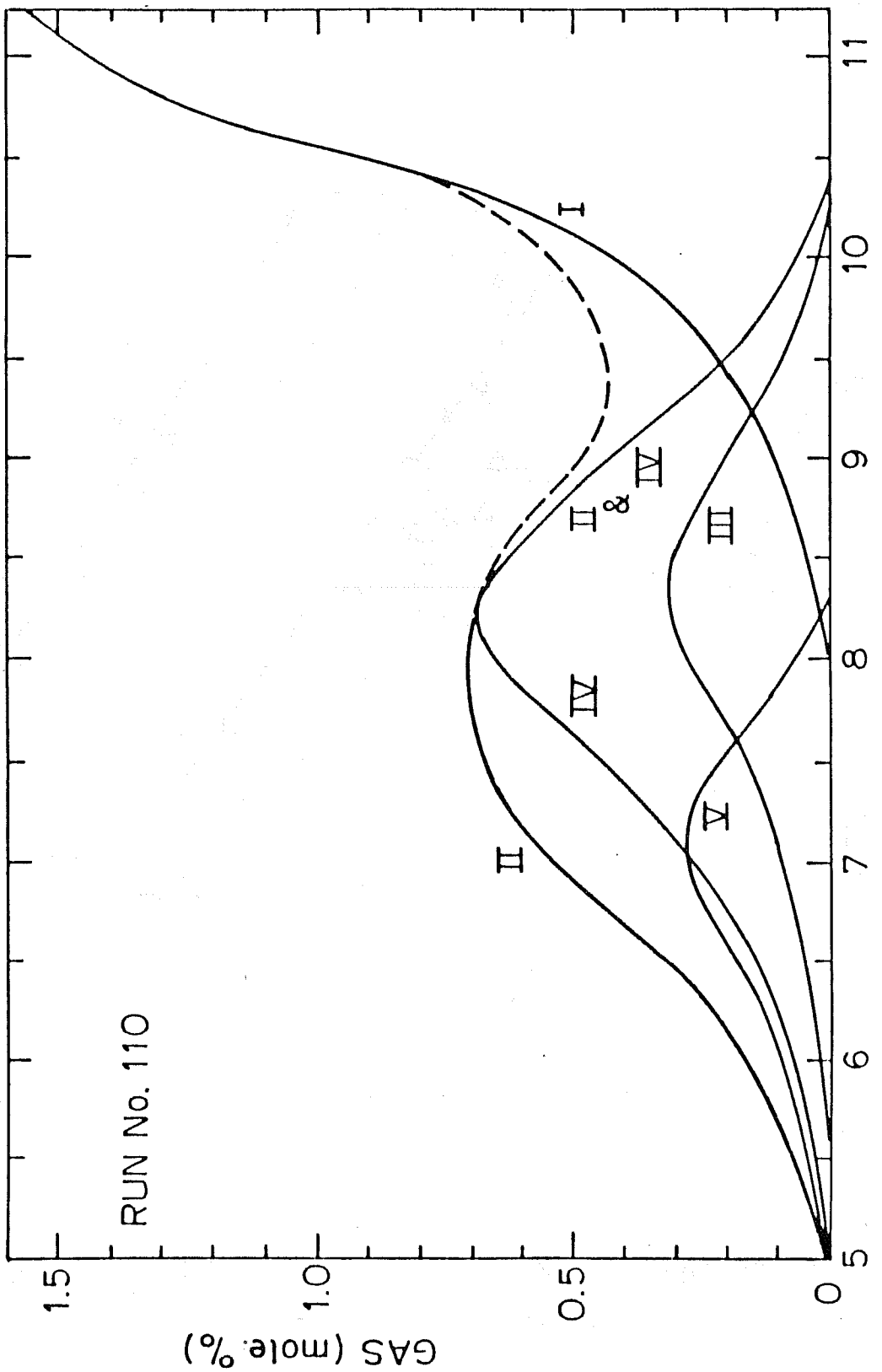

Fig. 6. Decomposition of the consumed oxygen in LTO fuel deposition and fuel combustion reaction.

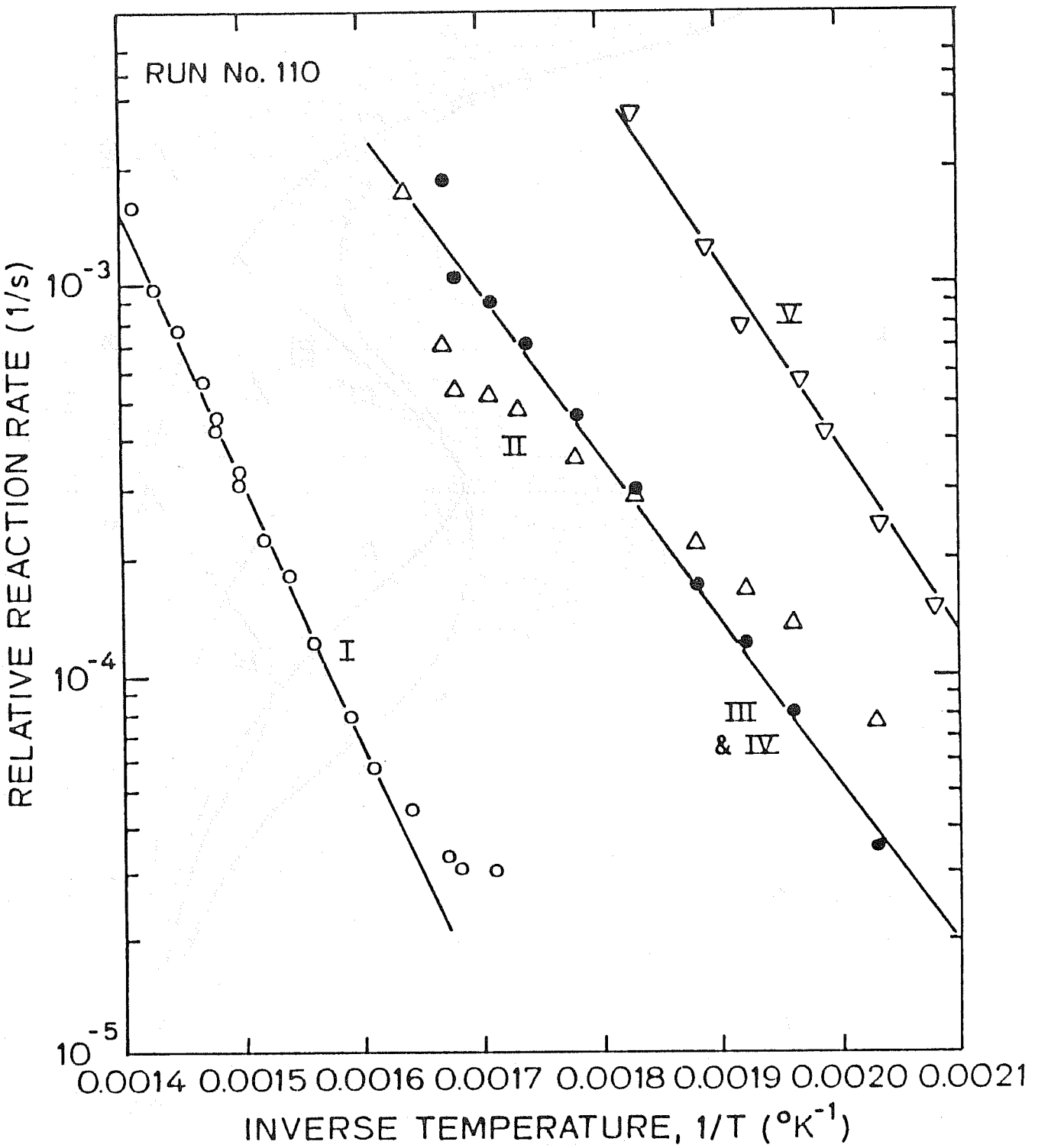

Fig. 7. Arrhenius plot for Run No. 110.

2.1.10. FUTURE WORK

Future work in this study will progress in two steps:

1. Continued testing of the catalytic effect of various metallic salts, at different concentrations, on the constants of the reaction kinetics equation (i.e., activation energy, Arrhenius constant, reaction orders).
2. A combustion tube study to observe the effect that such a catalyst might have on *in-situ* combustion process variables such as the velocity and temperature of the burning front, the thickness and temperature of the steam zone, fuel consumption, etc.

2.1.11. REFERENCES

1. Bousaid, I.S., and Ramey, H.J., Jr.: "Oxidation of Crude Oil in Porous Media," *Soc. Pet. Eng. J.* (June 1968) 137-148; Also *Trans. AIME 243.*

2. Crawford, P.B.: "Water Technology--Underground Combustion of Hydrocarbons," *Producers' Monthly* (June 1968) 15.

3. Fassihi, M.R.: "Analysis of Fuel Oxidation in *In-situ* Combustion Oil Recovery," PhD dissertation Stanford University (May 1981).

4. Johnson, H.R. and Burwell, E.L.: "Carbon Deposition for Thermal Recovery of Petroleum--A Statistical Approach to Research," *Producers' Monthly* (July 1968) 8-15.

5. Raćz, D.: "Development and Application of a Thermocatalytic *In-situ* Combustion Process in Hungary," Proceedings, Third European Symposium on Enhanced Oil Recovery, Rome, Italy (November 1984).

6. Weijdema, J.: "Determination of the Oxidation Kinetics of the *In-situ* Combustion Process," *Report from Koninklijke/Shell, Exploratic En Produktic Laboratorium, Rijswijk,* The Netherlands (1968).

2.2 CO_2 - HEAVY OIL PVT PROPERTIES AT HIGH TEMPERATURE
(Jeffrey Wingard)

2.2.1. CO_2 – H_2O HEAVY OIL RESEARCH

2.2.1.1. Literature Survey

Literature survey was done at the Stanford Librarys. The results of the search were generally negative. Without exception, the previous studies of the CO_2 and H_2O - heavy oil systems have been carried out at much lower temperatures and pressures.

A number of correlations for viscosity and density of CO_2 heavy oil mixtures have also been examined. Again, the data and correlations are for temperatures significantly below the conditions that will be examined in this study.

2.2.1.2. PVT Equipment Design

The preliminary design of the PVT apparatus has been finished. Capital equipment is being priced and ordered. An HP 5880A Gas Chromatagraph has been delivered and supplies for its operation (gases and wiring changes) ordered. It is expected to be operational by the end of the November. A schematic of the proposed PVT cell is shown on the following page.

The PVT cell will be a 32 cc blind stainless steel microreactor. Additional capital equipment will consist of capillary tubes for the measurement of viscosity. A double-barrel, 500 cc RUSKA pump and an oven were available from other SUPRI experiments.

The following problems are anticipated with the design of the PVT equipment.

1. The need for a backpressure regulator to operate at the high temperatures planned for the experiment (450 - 600 °F). This problem may be solved by using a push-pull system with two positive displacement pumps.
2. Mixing of the CO_2 and oil in the PVT cell needs to be accelerated by some method. Since these oils are viscous the diffusion of CO_2 into the oils will be slow and time consuming. Presently, we are planning to have a rocking motor installed into the oven and an agitator ball in the PVT cell.
3. General problem of working with CO_2 at high temperatures with the gas dissolving the seals in many of the fittings normally used. Metal or exotic seal material may be necessary for the high temperature fittings.
4. The pressure transducers for the viscosity measurements should ideally be inside the oven at the high temperature. This may not be possible and in an alternative arrangement the transducer would be mounted outside the oven with the taps extending into the heated area.

2.2.1.3. Core Flood Equipment Design

The preliminary design of the core flooding apparatus has been completed. The design parameters were chosen to match the conditions that should exist down stream of an *in-situ* oxygen combustion fireflood. The stoichiometric calculations were carried out using the data from the combustion tube runs by Sidqi Abu-Khamsin at SUPRI. A rough schematic of the design is provided on the next page.

Concurrent with the initial calculations, a core sleeve was ordered and has arrived. The tube is a 6 ft, 3 in. i.d. of 316 stainless steel with a 1/2-in. wall thickness. Machining of the tube and the stand for the pipe has been delayed until the PVT measurement apparatus is operational

2.2.1.4. Laboratory Preparation

A laboratory space was made available in the Mitchell Earth Sciences building. The lab's floor had a number of cracks and other holes which were patched with cement and sealed to prevent mercury from becoming lost in the floor. The floor was sealed with an epoxy paint to provide a tight surface.

Other lab preparation will be completed by the beginning of November and the construction of apparatus will begin.

2.2.2. COMPUTER MAINTENANCE

A significant portion of time was spent maintaining the VAX computer system used by SUPRI. Installation and development of software for data analysis, word processing and graphic output have been among the projects completed this year.

PROJECT 3: STEAM INJECTION WITH ADDITIVES

The goal of this project is to determine the mechanisms involved in the effects of *foaming* additives on a steam injection process.

3.1 MEASUREMENT OF APPARENT VISCOSITY OF FOAM
(Richard Treinen)

A technical report by Richard J. Treinen, W.E. Brigham, and L.M. Castanier was submitted to DOE on this topic; the following is an abstract of these results.

3.1.1. ABSTRACT

The apparent viscosity of surfactant foam in a sand pack model was measured at reservoir flow velocities. The effects of foam quality, surfactant concentration, and flow rate were investigated.

Ottawa sand, 120 to 140 mesh, was packed into a 1 by 24 inch tube. Porosity was 38%, and permeability ranged from 5 to 8 darcies. Foam of a known quality and flow rate was continuously injected into the sand pack until a steady state condition was reached. Pressure drop was measured across three different segments of the sand pack. A system back pressure of 50 psig was applied to minimize changing foam quality caused by gas expansion. The surfactant used in this study was Suntech IV. All measurements were made at room temperature.

Results show that the apparent viscosity of surfactant foam ranges from 50 to 70 centipoise at reservoir flow velocities. Increasing the foam quality resulted in a small increase in the apparent viscosity of foam. Changes in surfactant concentration from 0.005 to 0.05 wt% caused a rapid increase in apparent viscosity. Changes in concentration above 0.05 wt% had little effect on apparent viscosity. Increasing the flow rate resulted in a reduction of the apparent viscosity of foam. This pseudoplastic flow behavior has been widely reported in the literature. The apparent viscosity of foam in porous media was significantly affected by flow rate history.

3.2 AN APPROXIMATE MODEL FOR TWO-DIMENSIONAL DISPLACEMENT OF OIL BY FOAM
(S.M. Mahmood)

3.2.1. INTRODUCTION

Steam has a much higher mobility and lower density than the heavy oils in those reservoirs where steam flooding is the recovery mechanism. Thus it has a tendency to channel through high permeability zones or zones with low oil saturation, and it has a tendency to rise to the top in relatively thick oil zones. After steam breakthrough the produced steam/oil ratio climbs, with the result that much of the injected heat merely cycles through the reservoir only gradually heating the untouched portions of the oil zone by conduction.

Often the dominant recovery mechanism in such systems is a heat augmented gravity drainage process. Due to the high mobility of the steam, the Darcy pressure drop is small compared to the gravity forces. Typically in steam floods, approximately one-third of the oil (or its equivalent in gas or coal) is burned to produce the remaining oil. Thus, while a successful steam project may recover as much as 55% of the oil in place the net effective oil recovery is only about 35% of the oil in place.

In recent years considerable interest has been focused on developing some means of reducing the mobility of steam to reduce its rate of channeling. The injection of foaming surfactants along with steam is one of the methods studied, for it is well known that foams may have apparent viscosities as high as 100 cp. Laboratory studies have shown that it is possible to find foaming agents which are chemically stable at high temperatures (Al-Khafaji *et al.*, 1982) and field tests using foaming agents have significantly improved the oil producing rates and the steam/oil ratios (Brigham *et al.*, 1984; Dilgren *et al.*, 1982; and Ploeg and Duerksen, 1984).

Although these laboratory and field results are encouraging, it is clear that these tests have not been optimized. Nor could they be expected to be, for the basic flow mechanism of steam foam flow systems is not known. The work reported here is a first step in an attempt to describe foam flow in a porous medium in the presence of oil and water. The system studied is a low pressure, low temperature displacement using nitrogen and surfactant solution, thus it does not include the effects of heat nor the vapor collapse which occurs with steam, but it does include the relative effects of the gravity and Darcy forces and the resulting oil recovery.

3.2.2. EXPERIMENTAL EQUIPMENT

The apparatus used was a two-dimensional vertical slice (x, z) model, 4-feet long, 1-foot high and 0.25 in. thick. It is an aluminum frame, with a stainless steel lining as a back plate and a 1-in. thick glass plate for the front (Fig. 1). This glass plate allowed visual observation of the flow behavior during the experiments. Appropriate Viton rubber gasketing was used at all the joining surfaces.

Considerable care was required to ensure a good seal along the upper surface. This surface had to have the capability to be opened for packing the 180-220 mesh Ottawa sand into the model and to still seal the system against gas leaks to a pressure of 20 psig. The system was packed at 50 psig to assure a positive force on the sand pack and assure that no sand settling occurred after the runs were begun. Details in this procedure can be found in Mahmood (1985).

The inlet and outlet headers in the model were divided into five separate sections so that various injection and production modes could be tested. After each run, the model was thoroughly cleaned using CO_2, water, mineral spirits and tertiary butanol. Then the model was saturated with distilled water and displaced to residual water saturation with the oil to be used in the test (approximately 5 PV oil was needed).

3.2.3. EXPERIMENTAL PROCEDURE

There are three common methods for injecting surfactant solutions and gas in a porous medium:

1. Alternate slug injection,
2. Preformed foam injection, and
3. Simultaneous surfactant solution and gas injection.

In all these, the production was from the bottom section of the outlet header. Of these three, for this model, simultaneous injection into the top section of the injection header was shown to be the superior injection mode. This method was seen experimentally to recover almost twice as much oil as the other methods.

When alternate slugs were injected it was found that gravity segregation was more pronounced. Small slugs improved the behavior, but only partially. The glass front plate was invaluable to help discern why recovery was reduced for this mode of operation compared to simultaneous injection. Due to the underride, most of the surfactant was not entering the top-zone where gas would flow when injection resumes, hence was not contributing to foam generation.

When preformed foam injection was used the volume of surfactant solution sustained by the foam body was limited due to gravity segregation at the inlet header. Thus the mass of surfactant that was carried into the gas zone was limited. The result was that a large volume of injected foam was necessary before foam could be seen to begin propagating through the porous medium.

In all forms of injection, there was a delay before foam began to be generated in the porous medium; once foam was generated it could easily be seen, and at the same time the pressure drop began to rise and the oil recovery rate began to increase. This delay, however, was far more pronounced when preformed foam was used.

We should emphasize that these results are specifically related to this model and may not be quite the same near the wellbore in a reservoir where the early flow is radial and the wellbore volume is much smaller than the equivalent "wellbore" volume used in this model.

After some preliminary runs, all subsequent runs were made using simultaneous injection of surfactant solution and gas, due to its superiority, and these are the runs reported herein.

For these runs, several refined oils were used whose viscosities ranged from 0.6 cp to 150 cp at room temperature. For the aqueous phase distilled water was always used. The surfactant used was Suntech IV at concentrations ranging from 0.01% to 1% and various ratios of surfactant solution to nitrogen were injected ranging from an apparent quality of 70% to 98%.

Normally, when considering experiments of this sort, one immediately considers using dimensionless variables to correlate the recovery behavior versus the volume injected. For this system, the Capillary Number (ratio of capillary to viscous forces), the Bond Number (ratio of

gravity to capillary forces) or the ratio of these two, the Gravity Number (ratio of gravity to viscous forces) would be used as correlating parameters. In addition the mobility ratio would be expected to be important.

When these criteria were used for correlation purposes, they did not work. The reason was that in all the runs there was low recovery at the beginning and then later the recovery rate started to increase (Fig. 2). In every case, this increase in recovery rate corresponded to the time at which foam began to be generated inside the model (as seen visually), and with a concomittant increase in pressure drop. The time for this delay was found to be dependent in a complex way in the relative rate of gas and surfactant injection, the concentration of the surfactant and the overall injection rate. But it was not dependent on the viscosity of the oil present.

In general this delay in foam flow always occurred, and we would expect it would occur in any system. The reasons are not clear--gravity segregation of the surfactant solution, in part, probably absorption in the oil, in part, and possibly adsorption on the sand surfaces; or any combination of the three. We would expect that the effects would not be the same in differing porous media, especially if they contain clays. We would also expect differences if the water contained salts, especially divalent ions. Reservoir oils rather than refined oils, and other types of surfactants would be expected to behave differently. Also the flow geometry of the porous medium could have an important effect. However, for the system studied here we were able to devise an empirical equation which predicted the delay in onset of *in-situ* foaming. The equation is

$$(G_i)_{fg} = \left[\frac{q_g}{q_g + q_s}\right]\left[3 \log \frac{1}{C} + \frac{1}{3} \log q_s + 0.25\right] \qquad (1)$$

where

$(G_i)_{fg}$ = Gas throughout at which foam generation starts, pore volumes
q_g = Gas injection rate, std cm^3/min
q_s = Surfactant solution injection rate, cm^3/min
C = Surfactant concentration, wt %

Equation (1) was an important key to our understanding of the flow behavior of the system. It was used to predict the on-set of foam generation at which gas mobility was changed to foam mobility, for comparison of predicted and observed recoveries.

3.2.4. MODELING FOAM FLOW

From our visual observations it was clear that, at the beginning, the gas formed a thin gravity tongue along the top of the model and the surfactant solution formed a slower moving gravity tongue along the bottom until the delay time was reached after which *in-situ* foam began to flow. After that, a foam bank was seen to propagate along the same finger as that which had contained gas (Fig. 3). The bank did not displace oil directly since it flowed in the area where gas had already displaced oil to near its residual saturation. This foam bank flowed more slowly than either the gas or the surfactant.

To model this process it appeared that both gas and surfactant flows could be assumed to be taking place in separate gravity tongues. The gas tongue could be handled in a fashion suggested by Dake (1977), assuming Buckley-Leverett displacement mechanism. The surfactant solution tongue could be treated as a Dietz (1953) tongue. However, these tongues have to be

combined to conserve Darcy's law. The approach would be to assume that each gravity tongue acted independently of the other. The method as described here is to develop the equations modeling this system for the time after breakthrough of both gravity tongues, and then later to simplify the resulting equations as needed to describe the behavior. A pictorial model of the system is shown in Fig. 3.

A pressure balance across a minute portion of the surfactant solution oil interface (Fig. 3) results in

$$\frac{dy}{dx}\Big|_x = \frac{\frac{\partial p_s}{\partial x} - \frac{\partial p_0}{\partial x}}{(\rho_s - \rho_0)g} \tag{2}$$

where

y = Vertical thickness of the surfactant solution tongue

x = Horizontal distance

The subscript, s, stands for surfactant solution, and 0, stands for oil. Later, g, will be used for gas. The other symbols are standard SPE nomenclature. Substituting Darcy's law into this equation for the pressure drop terms results in,

$$\frac{\partial y}{\partial x} = \frac{\mu_0}{k_0 g(\rho_s - \rho_0)} \left[- \left[\frac{q_s}{y} \right] \frac{\mu_s/k_s}{\mu_0/k_0} + \frac{q_t - q_s - q_g}{h - y - \overline{y}} \right] \tag{3}$$

where

q_t = Total injection and production rate

$\overline{y}$ = Vertical thickness of the gas tongue

q_s and q_g = Surfactant solution and gas injection rates

Defining mobility ratios of surfactant solution to oil (m) and gas to oil ($\overline{m}$),

$$m = \left[\frac{k_s/\mu_s}{k_0/\mu_0} \right] \tag{4}$$

$$\overline{m} = \left[\frac{k_g/\mu_g}{k_0/\mu_0} \right] \tag{5}$$

and substituting, Eq. (3) simplifies to,

$$\frac{\partial y}{\partial x} = \frac{\mu_0}{k_0 g \Delta\rho} \left[- \left[\frac{q_s}{y} \right] \frac{1}{m} + \frac{q_t - q_s - q_g}{h - y - \overline{y}} \right] \tag{6}$$

The ratio of gas and surfactant solution flow is defined here as $R = q_g/q_s$. Using this definition for R we can relate $\overline{y}$ to y.

$$\overline{y} = R\frac{m}{\overline{m}}\, y \tag{7}$$

For simplification, the expression $[1 + R(m/\overline{m})]$, which appears rather frequently in the following developments, is defined as β:

$$\beta = 1 + R\frac{m}{\overline{m}} \tag{8}$$

Substituting Eq. (8) into Eq. (6) results in,

$$\frac{k_0 g\Delta\rho}{\mu_0}\,\frac{\partial y}{\partial x} = \left[\frac{q}{h-\beta y} - \left[\frac{1}{my} + \frac{1}{h-\beta y}\right] q_s - \frac{q_g}{h-\beta y}\right] \tag{9}$$

Differentiating this equation with respect to x results in:

$$\frac{k_0 g\Delta\rho}{\mu_0}\,\frac{\partial^2 y}{\partial x^2} = \frac{q\beta}{(h-\beta y)^2}\,\frac{\partial y}{\partial x} + \frac{q_s}{my^2}\,\frac{\partial y}{\partial x} - \frac{1}{my}\,\frac{\partial q_s}{\partial x} - \frac{1}{h-\beta y}\,\frac{\partial q_s}{\partial x}$$

$$- \frac{\beta q_s}{(h-\beta y)^2}\,\frac{\partial y}{\partial x} - \frac{1}{h-\beta y}\,\frac{\partial q_g}{\partial x} - \frac{q_g\beta}{(h-\beta y)^2}\,\frac{\partial y}{\partial x} \tag{10}$$

For fully segregated flow in which the flow is through gravity tongues, the curvatures of the tongues may be assumed negligible near the producing end, i.e., $\partial^2 y/\partial x^2 \simeq 0$. This assumption is not valid near the injection well due to the sharp curvatures encountered there. The error will be small, however, since this development will be used only after surfactant breakthrough. The resulting equation after rearrangement is,

$$\frac{q\beta}{(h-\beta y)^2}\,\frac{\partial y}{\partial x} + \left[\frac{1}{my^2} - \frac{\beta}{(h-\beta y)^2}\right] q_s\,\frac{\partial y}{\partial x} - \frac{\beta q_g}{(h-\beta y)^2}\,\frac{\partial y}{\partial x}$$

$$- \left[\frac{1}{my} + \frac{1}{h-\beta y}\right]\frac{\partial q_s}{\partial x} - \frac{1}{h-\beta y}\,\frac{\partial q_g}{\partial x} = 0 \tag{11}$$

The surfactant and the gas rate gradients can be replaced by known and measurable parameters using the continuity equation for an incompressible fluid

$$\frac{\partial q_s}{\partial x} = -\,\phi\Delta S_s\,\frac{\partial y}{\partial t} \tag{12}$$

and

$$\frac{\partial q_g}{\partial x} = -\,\phi\Delta S_g\,\frac{\partial \overline{y}}{\partial t} \tag{13}$$

where,

ϕ = the porosity of the porous medium,

ΔS = the change in saturation of the injected fluid.

Although the gas is not incompressible, the pressure changes slowly enough that this assumption appeared not to be serious. A further assumption used was that $\Delta S_s = \Delta S_q = \Delta S$. This is not necessary for the development of the equations, but the relative permeability characteristics of the system indicated this assumption to be nearly true. Substituting Eqs. (12) and (13) into Eq. (11) results in

$$\left\{\frac{q_t\beta}{(h-\beta y)^2} + \left[\frac{1}{my^2} - \frac{\beta}{(h-\beta y)^2}\right] q_s - \frac{\beta q_g}{(h-\beta y)^2}\right\} \frac{\partial y}{\partial x}$$

$$+ \left[\frac{1}{my} + \frac{1}{h-\beta y} + \frac{\beta - 1}{h-\beta y}\right] \phi \Delta S \frac{\partial y}{\partial t} = 0 \tag{14}$$

The total flow rate can be related to the surfactant solution flow rate by Darcy's law

$$\frac{q_s}{q_t} = \frac{-y \dfrac{k_s}{\mu_s}}{-\bar{y} \dfrac{k_g}{\mu_g} - y \dfrac{k_s}{\mu_s} - (h - y - \bar{y}) \dfrac{k_0}{\mu_0}} \tag{15}$$

which, upon substitution of definitions of mobility ratio, becomes

$$q_s = \frac{my}{(h-\beta y) + my + \bar{m}\beta y - \bar{m}y} q_t \tag{16}$$

The gas flow rate can be similarly defined.

$$q_g = \frac{\bar{m}(\beta - 1)y}{(h-\beta y) + my + \bar{m}\beta y - \bar{m}y} q_t \tag{17}$$

When Eqs. (16) and (17) are substituted into Eq. (14) and the resulting equation is rearranged, it becomes

$$-\left[\frac{1}{my}+\frac{1}{h-\beta y}+\frac{\beta-1}{h-\beta y}\right]\phi\Delta S\,\frac{\partial y/dt}{\partial y/dx}$$

$$=\left\{\frac{\beta}{(h-\beta y)^2}+\left[\frac{1}{my^2}-\frac{\beta}{(h-\beta y)^2}\right]\frac{my}{(h-\beta y)+my+\overline{m}\beta y-\overline{m}y}\right. \tag{18}$$

$$\left.-\frac{\beta\overline{m}(\beta-1)y}{(h-\beta y)^2\,[(h-\beta y)+my+\overline{m}\beta y-\overline{m}y]}\right\}\;q_t$$

But, by the chain rule of partial derivatives, we can write:

$$\frac{\partial x}{\partial t}=-\frac{\partial y/\partial t}{\partial y/\partial x} \tag{19}$$

and Eq. (18) can be solved analytically. Its solution is

$$y=\frac{h\sqrt{(\alpha-\overline{\alpha}+\alpha\beta+\overline{\alpha}\beta)^2-4\alpha\beta(\alpha-\overline{\alpha}+\overline{\alpha}\beta)\left[1-\frac{mQ}{Lh\phi\Delta S}\right]}-h(\alpha-\overline{\alpha}+\alpha\beta+\overline{\alpha}\beta)}{2\alpha\beta(\alpha-\overline{\alpha}+\overline{\alpha}\beta)} \tag{20}$$

where α, $\overline{\alpha}$, and Q have been defined as follows:

Q = cumulative total throughput in pore volumes,
$\alpha = m-1$
$\overline{\alpha} = \overline{m}-1$

Due to the material balance, the ratio of swept zone thickness to the total thickness must be the same as the ratio of oil recovery to the maximum possible recovery. This can be expressed as:

$$\frac{y+\overline{y}}{h}=N_{pD} \tag{21}$$

In Eq. (21) $\overline{y}$ can be related to y as discussed earlier [Eq. (7)]. Thus Eq. (21) can be substituted into Eq. (20) to predict recovery as a function of volume injected.

$$N_{pD}=\frac{\sqrt{(\alpha-\overline{\alpha}+\alpha\beta+\overline{\alpha}\beta)^2-4\alpha\beta(\alpha-\overline{\alpha}+\overline{\alpha}\beta)\left[1-\frac{mQ}{Lh\phi\Delta S}\right]}-(\alpha-\overline{\alpha}+\alpha\beta+\overline{\alpha}\beta)}{2\alpha(\alpha-\overline{\alpha}+\overline{\alpha}\beta)} \tag{22}$$

By definition, the throughput in movable pore volumes is given by:

$$Q_D = \frac{Q}{Lh\phi\Delta S} = \text{movable pore volume} \tag{23a}$$

Also, the following group of terms can be redefined for simplification:

$$\text{Let} \quad C = \alpha - \bar{\alpha} + \bar{\alpha}\beta = (m-1) + R\frac{m}{\bar{m}}(\bar{m}-1) \tag{23b}$$

Substituting for C and Q_D from Eqs. (23a) and (23b) in Eq. (22) gives:

$$N_{pD} = \frac{\sqrt{(C+\alpha\beta)^2 - 4\alpha\beta C(1-mQ_D)} - (C+\alpha\beta)}{2\alpha C} \tag{24}$$

The recovery due to surfactant drive up to the surfactant breakthrough is expressed by a material balance on the surfactant.

$$(N_{pD})_s = W_{iD} = \frac{G_{iD}}{R} \tag{25}$$

but

$$(G_{iD})_{bt} = \frac{R}{m}$$

so,

$$(N_{pD})_{bt} = \frac{1}{m} + \frac{1}{(\bar{m}-1)}\left[2\sqrt{\frac{\bar{m}}{m}R} - 1 - \frac{R}{m}\right] \tag{26}$$

Hence surfactant breakthrough occurs when oil production has reached the volume as given by Eq. (26).

Prior to surfactant breakthrough, the recovery in the gas tongue is defined by an equation which only includes that one tongue, plus a material balance term for the surfactant injection. Prior to gas breakthrough, the recovery is simply calculated by material balance. Thus the resulting equations for early time are all like Eqs. (24) and (26) but simpler. They can be summarized as follows:

3.2.5. SUMMARY OF RECOVERY EQUATIONS

Oil recovery prior to gas breakthrough:

$$N_{pD} = G_{iD} + \frac{G_{iD}}{R} \tag{27}$$

Volume injected at gas breakthrough time

$$(G_{iD})_{gbt} = (N_{pD})_{gbt} = \frac{1}{\overline{m}} + \frac{1}{\overline{m}R} \tag{28}$$

Oil recovery prior to surfactant breakthrough:

$$N_{pD} = \frac{G_{iD}}{R} + \frac{1}{(\overline{m}-1)}\left(2\sqrt{\overline{m}G_{iD}} - 1 - G_{iD}\right) \tag{29}$$

Recovery at surfactant breakthrough time:

$$(N_{pD})_{bt} = \frac{1}{m} + \frac{1}{(\overline{m}-1)}\left[2\sqrt{\frac{\overline{m}}{m}R} - 1 - \frac{R}{m}\right] \tag{26}$$

Oil recovery after breakthrough to the end of flood:

$$N_{pD} = \frac{\sqrt{(C+\alpha\beta)^2 - 4\alpha\beta C(1-mQ_D)} - (C+\alpha\beta)}{2\alpha C} \tag{24}$$

To use these equations, it still remained to determine the gas mobility. As soon as foam began to be generated within the porous medium, the gas mobility began to drop and it continued to drop as the foam moved through the model. It would be best to use a varying gas mobility as the foam front moved through the system, however, it was found that using an average value of the gas mobility was accurate enough for the model. For example, when the oil viscosity was 1 cp the gas foam mobility ratio used was 200/1 and the average foam mobility used was 80/1. These numbers were based on the pressure drops seen and they were invariant from run to run.

Using principles similar to those used in deriving Eqs. (2)-(29), the pressure drop equations could also be derived. We will not detail the development here, but they can be seen in Mahmood (1986).

$$p_0 - p_x = -\frac{q_s\mu_s}{k_s\, w\, \overline{h}}\,\frac{mLQ_D}{(\alpha\beta - C)}\left[\alpha^2\beta^2 \ln\frac{(y+\alpha\beta y)}{(\overline{h}+\alpha\beta y)} - C^2 \ln\frac{(y+Cy)}{(\overline{h}+Cy)}\right.$$

$$\left. + \frac{\alpha^3\beta^3(\overline{h}-y)}{(\overline{h}+\alpha\beta y)(1+\alpha\beta)} - \frac{C^3(\overline{h}-y)}{(\overline{h}+Cy)(1+C)}\right] \tag{30}$$

All the terms in this equation have been previously defined.

3.2.6. EXPERIMENTAL AND MODELING RESULTS

In brief, nearly all the experiments run using simultaneous injection of surfactant solution and nitrogen were adequately modeled using the equations outlined above. The match of calculated versus actual recoveries were particularly impressive while the match of pressure drops

3.2.6. EXPERIMENTAL AND MODELING RESULTS

In brief, nearly all the experiments run using simultaneous injection of surfactant solution and nitrogen were adequately modeled using the equations outlined above. The match of calculated versus actual recoveries were particularly impressive while the match of pressure drops was less accurate. Many runs were made, but for illustrative purposes only a few will be shown here.

An example run is shown in Fig. 4a and 4b. Figure 4a shows the experimental recovery data compared to the model prediction. The fit was excellent. Figure 4b shows the pressure data compared to the prediction from the model equation. The fit is less satisfactory. The rises and drops in the model pressure predictions occur due to abruptly changing the gas mobility rather than gradually changing mobility as the experiments indicated. In this run, decane (1 cp) was displaced by nitrogen at 1 std cm^3/min and 1% surfactant solution at 0.167 cm^3/min.

Figure 5 shows a comparison of predicted versus actual recovery for a flood of hexane (0.6 cp) with nitrogen at 200 std cm^3/min and 1% surfactant solution at 5 cm^3/min. Note more recovery with fewer volumes injected. This is due to the lower oil viscosity and the higher injection rate which caused foam to be generated more rapidly *in-situ*.

Figure 6 is for a flood with Blandol (15 cp), again with nitrogen at 200 std cm^3/min and with 1% surfactant solution at 5 cm^3/min. Notice the recovery in this run is less and it requires a considerably greater injection volume. This is due to the higher viscosity of Blandol. Notice also, in Figs. 5 and 6, that the gravity tongue recovery model quite successfully modeled the actual recovery behavior.

Finally in Fig. 7, we show the recovery data from a run that operated in a completely different injection mode. In this run cyclohexane (1 cp) was originally displaced by nitrogen at 200 std cm^3/min and by 1% surfactant solution at 5 cm^3/min until the injection pressure rose to 20 psig after *in-situ* foam generation began at about 2 PV injected. After that the injection pressure was held constant, and the gas injection rate dropped due to the lowered gas mobility. This resulted in a sharp recovery increase with volume injected (however, still relatively slowly with time). To model this it was necessary to take into account that the gas/surfactant solution ratio varied. The recovery model, however, quite accurately matched the production history.

3.2.7. CONCLUSIONS

1. In this two-dimensional model, simultaneous injection of nitrogen and surfactant solution was found to be the most efficient for recovery.
2. There was always a delay before foam flow occurred *in-situ* in the gas tongue of the model. This delay was found to be predictable by an empirical equation which was a function of the ratio of gas and surfactant solution injected, the injection rate and the surfactant concentration.
3. A simple mathematical model was derived based on the concept of gravity-tongues including the changing mobility in the gas tongue. It was found to match the recovery behavior of the experiments quite accurately. It also matched the pressure behavior, but with somewhat less accuracy.

3.2.8. REFERENCES

1. Al-Khafaji, A.H., Wang, P.F., Castanier, L.M., and Brigham, W.E.: "Steam Surfactant Systems at Reservoir Conditions," Paper SPE 10777 presented at the California Regional Meeting of the SPE of AIME, San Francisco, California (July 1982).

2. Brigham, W.E., Marcou, J.A., Sanyal, S.K., Malito, O.P., and Castanier, L.M.: "A Field Experiment of Improved Steam Drive with In-situ Foaming," Paper SPE 12784 presented at the California Regional Meeting, Bakersfield, California (March 27-29, 1985).

3. Dake, L.P.: "Fundamentals of Reservoir Engineering," Elsevier Scientific Publishing Company, New York, (1978).

4. Dietz, D.N.: "A Theoretical Approach to the Problem of Encroaching and By-Passing Edge Water." Akad. van Wetenschappen, Amsterdam, Proc. V.56-B: 83 (1962).

5. Dilgren, R.E., Deemer, A.R., and Owens, K.B.: "The Laboratory Development and Field Testing of Steam/Non-Condensible Gas Foams for Mobility Control in Heavy Oil Recovery," Paper SPE 10774 presented at the California Regional Meeting of SPE, San Francisco, California (March 24-26, 1982).

6. Mahmood, Syed M.: "The Two-Dimensional Displacement of Oil by Gas/Surfatant Solutions Under Foaming Conditions," Ph.D. dissertation, Stanford University, Stanford, California (1986).

7. Ploeg, J.F. and Duerksen, J.H.: "Two Successful Steam/Foam Field Tests, Sections 15A and 26C, Midway-Sunset Field," Paper SPE 13609 presented at the California Regional Meeting, Bakersfield, California (March 27-29, 1985).

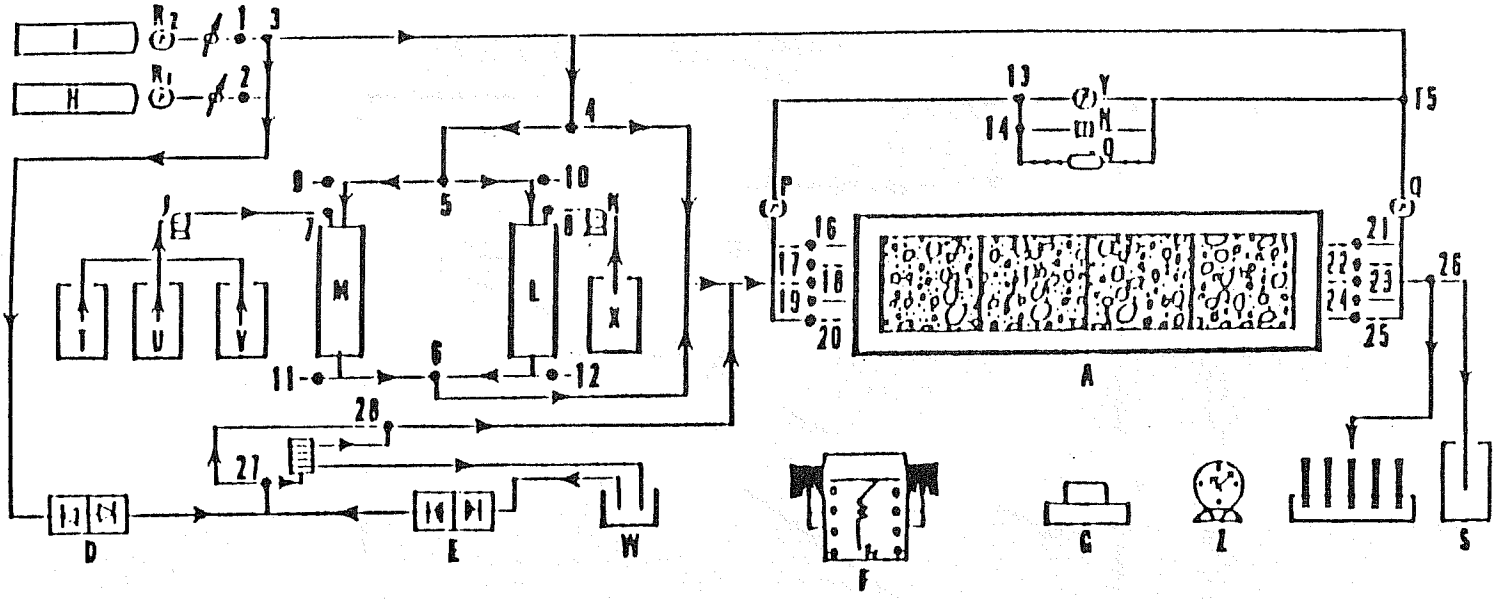

A. The Glass Model
B. Fraction Collector
C. Foam Generator
D. Gas Metering Pump
E. Liquid Metering Pump
F. Chart Recorder
G. Automatic Camera
H. N_2 Source Cylinder
I. CO_2 Source Cylinder
J. Pump for non-aqueous phase
K. Pump for aqueous phase
L. Slug Vessel for aqueous phase
M. Slug Vessel for non-aqueous Phase
N. Differential Pressure Transducer
O. Differential Press. digital readout
P. Press. Gauge for upstream pressure
Q. Press. Gauge for downstream pressure
R1. Pressure Regulator & Gauges for N_2
R2. Pressure Regulator & Gauges for CO_2
S. Drain Storage Container
T. 3-Butanol Reservoir
U. Mineral Spirit Reservoir
V. Oil Reservoir
W. Surfactant Reservoir
X. Distilled Water Reservoir
Y. Pressure Gauge for Differential Press.
Z. Time Counter

Fig. 1. Schematic diagram of the test apparatus.

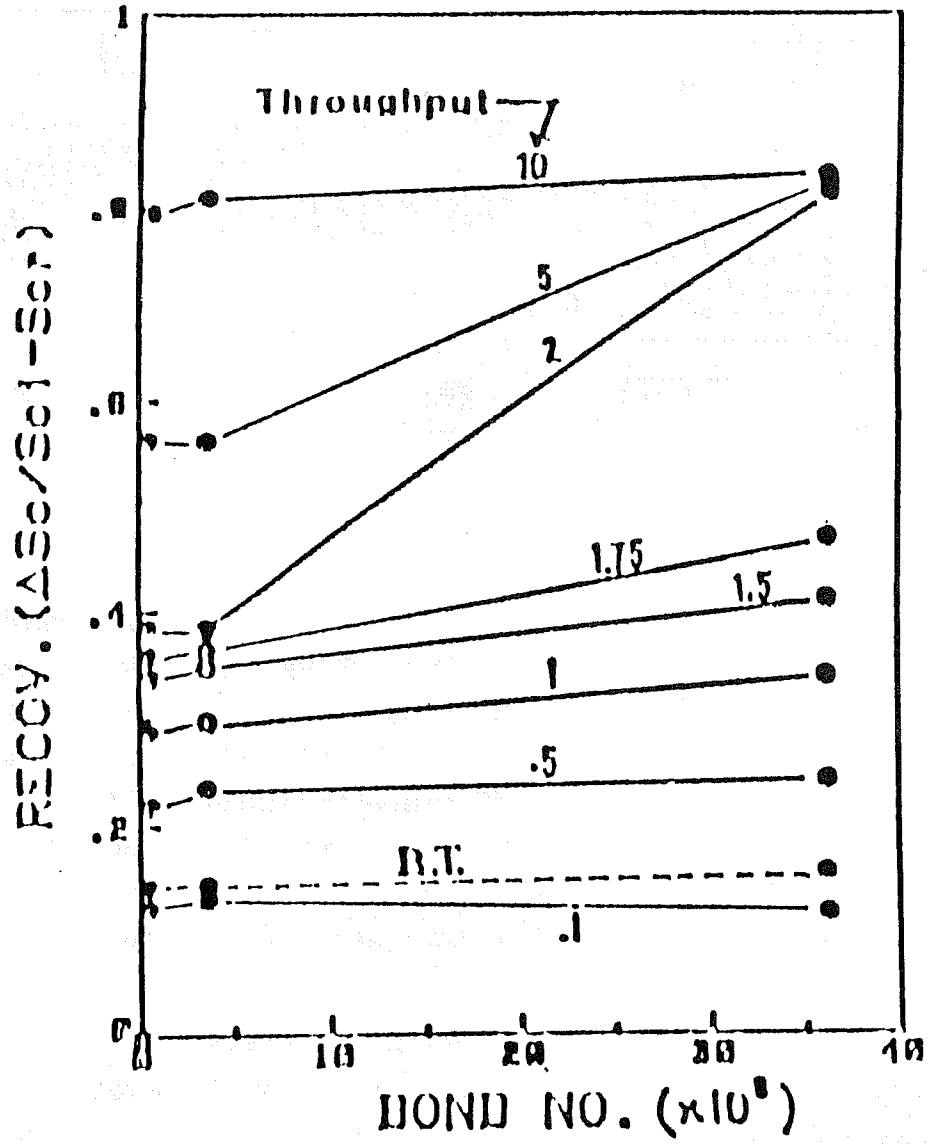

Fig. 2. Effect of bond number (gravity to capillary forces) on recovery history.

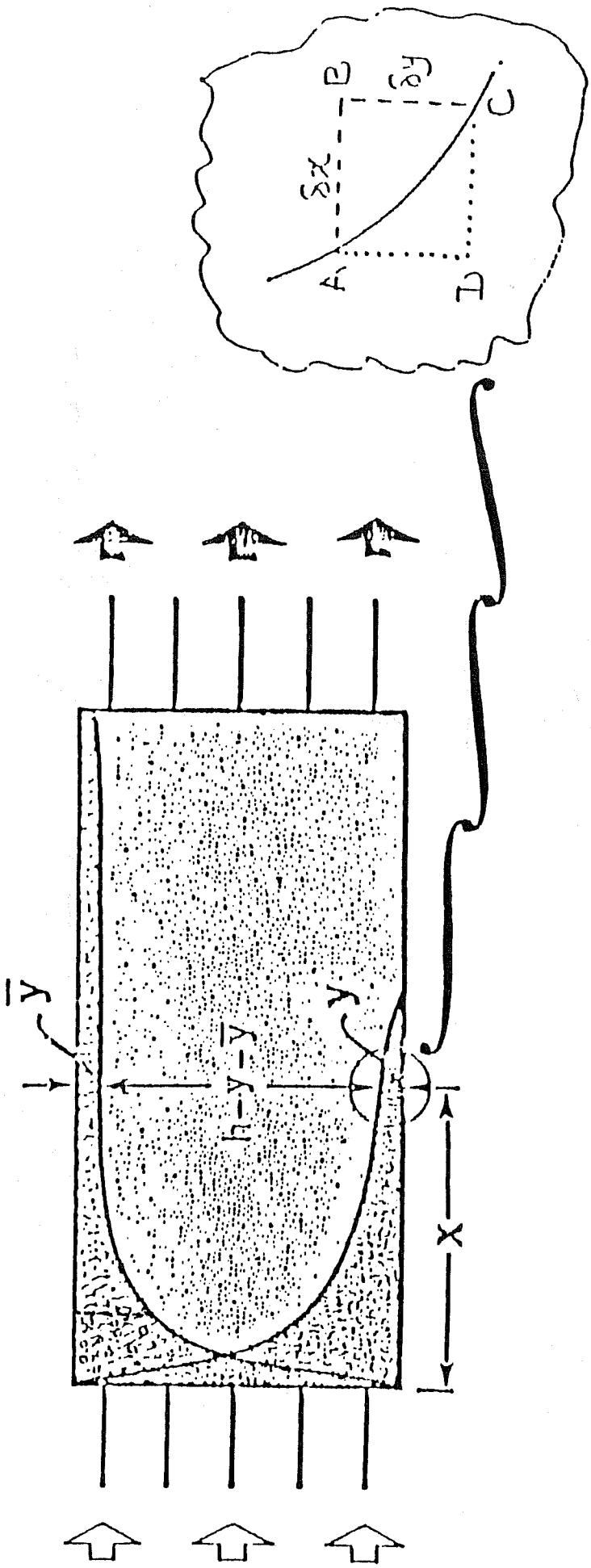

Fig. 3. Idealized model of surfactant foam displacement with detail of surfactant oil displacement front.

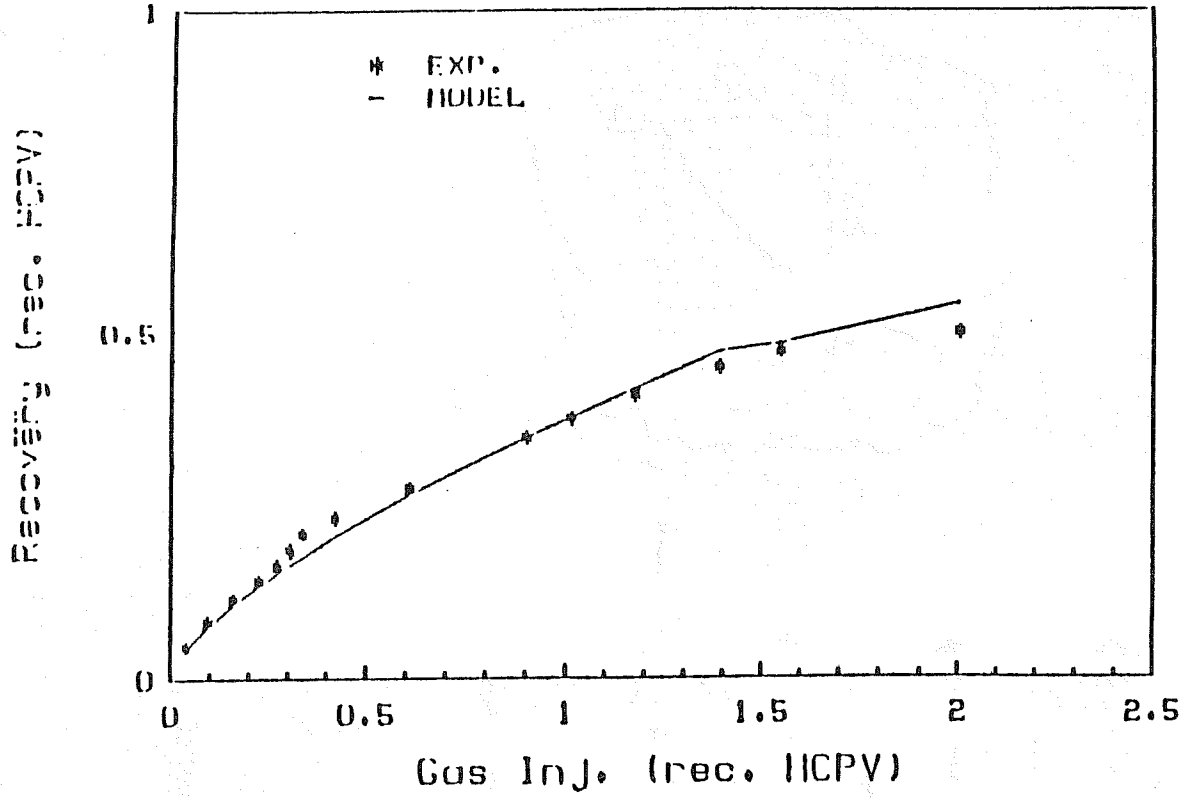

Fig. 4a. Comparison of predicted and experimental recovery. Displacement of decane by nitrogen (1 std. cm^3/min) and 1% surfactant solution 0.167 cm^3/min.

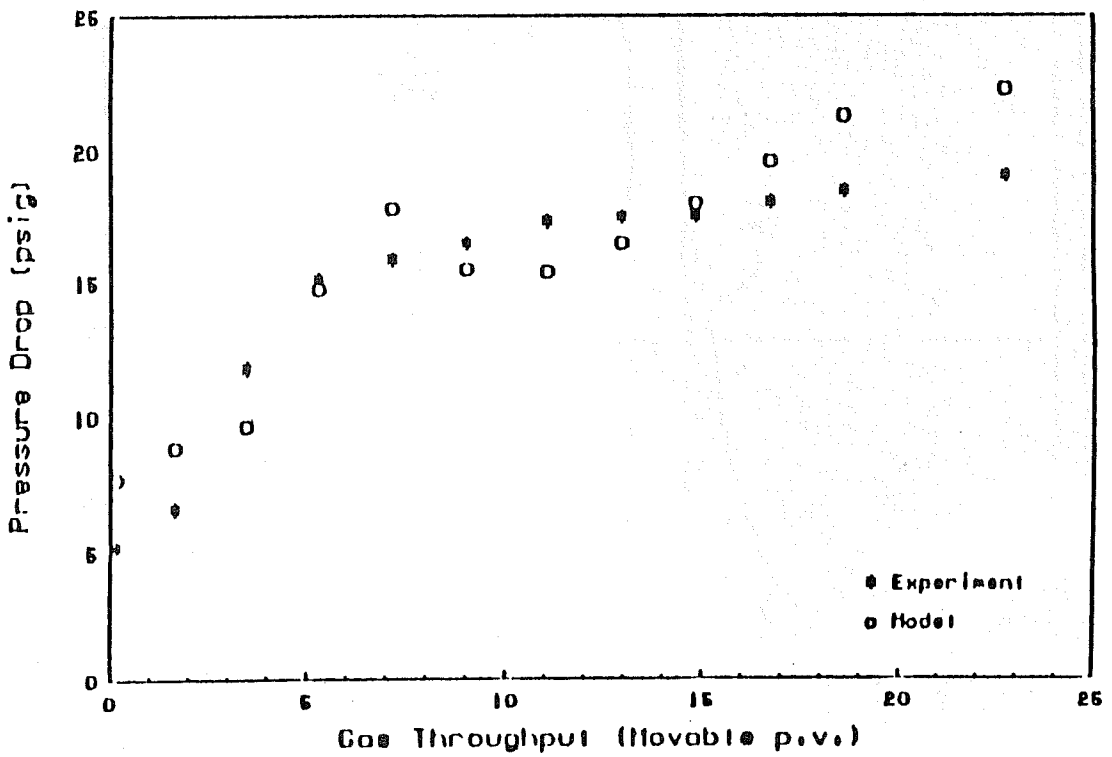

Fig. 4b. Comparison of predicted and experimental pressure drop. Displacement of decane by nitrogen (1 std. cm^3/min) and 1% surfactant solution 0.167 cm^3/min.

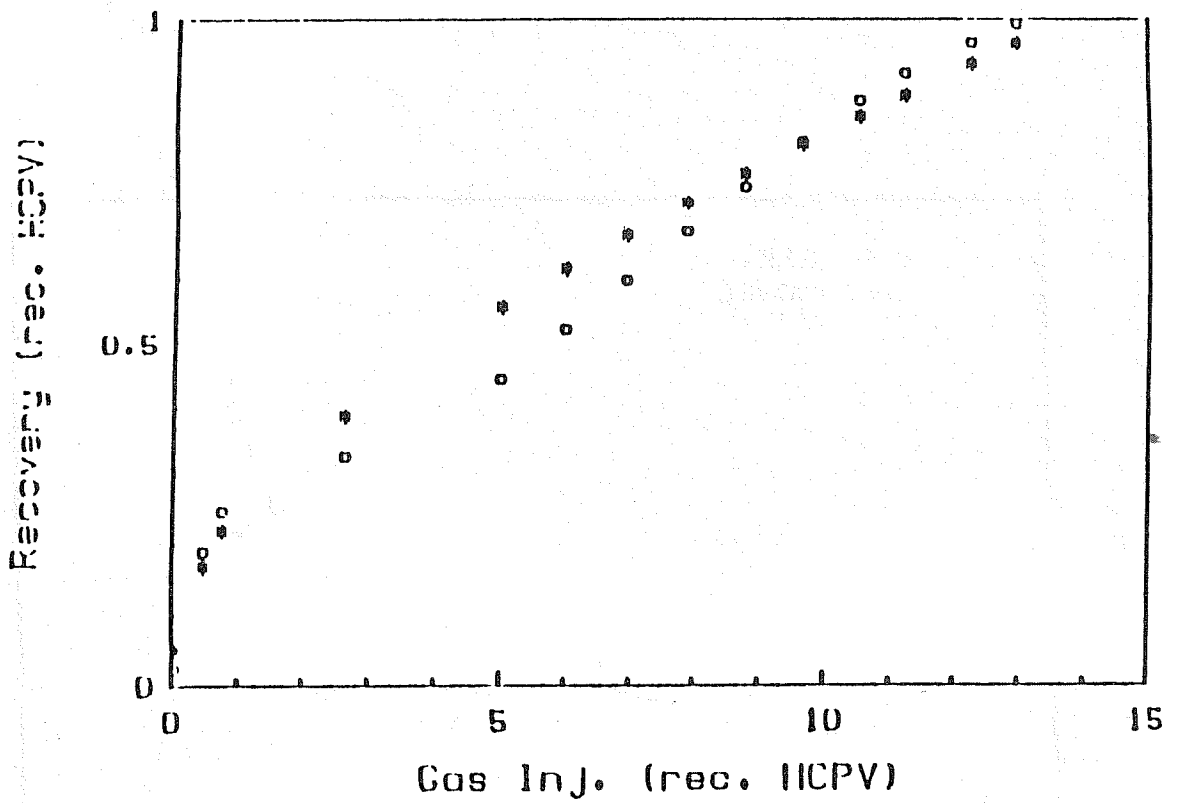

Fig. 5. Recovery comparison for displacement of hexane by nitrogen 200 std. cm^3) and 1% surfactant solution (5 cm^3/min).

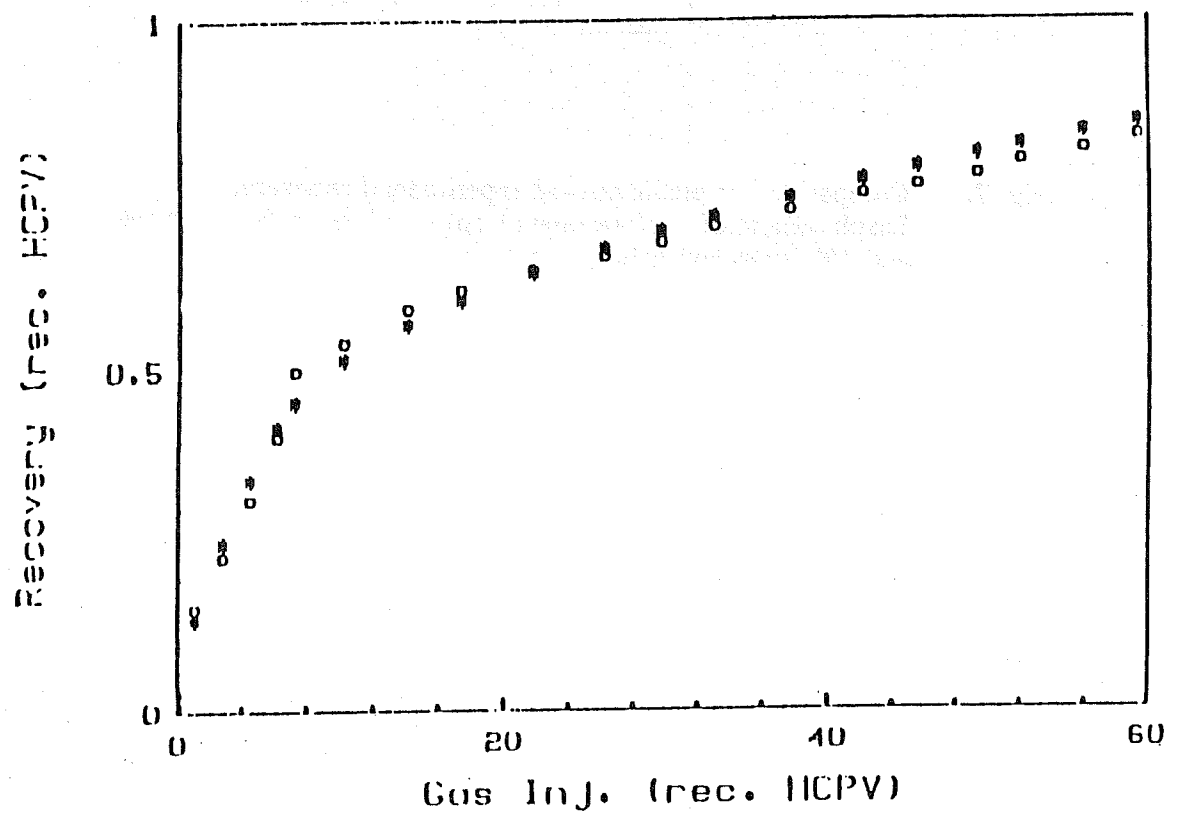

Fig. 6. Comparison of predicted and experimental recovery. Blandol (15 cp) displacement by nitrogen (200 std. cm^3) and 1% surfactant solution (5 cm^3/min).

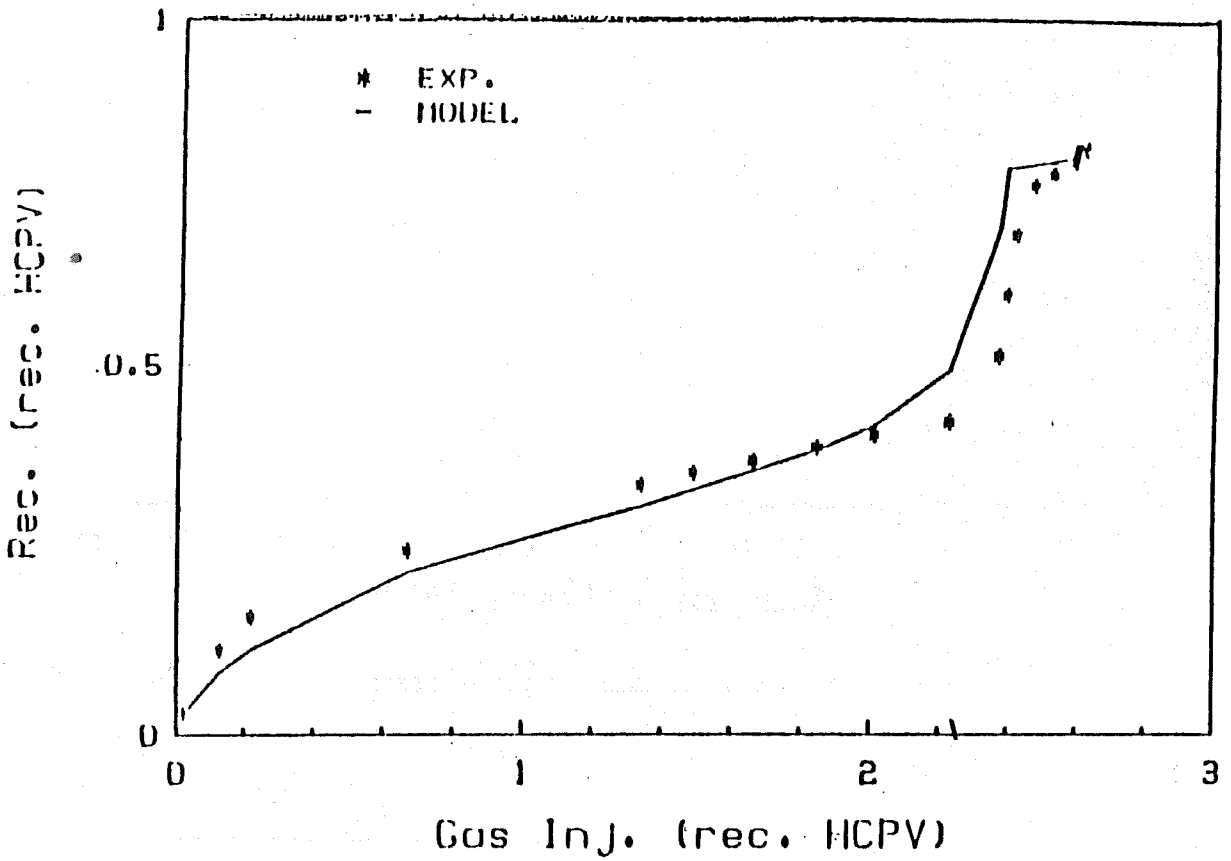

Fig. 7. Comparison of predicted and experimental recovery. Displacement of cyclohexane (1 cp) by nitrogen (variable rate) and 1% surfactant solution (5 cm^3/min).

3.3 A STUDY OF HEAT TRANSFER OF STEAM DISPLACEMENT
(Fred Wang)

This study is part of the project of steam injection with additives and begins with a brief description of mathematical modeling of steam injection in a cylindrical core, followed by a sensitivity study of various factors on the heat-frontal movement. Then, comparisons between the experimental data and the semi-analytical solution are discussed. Lastly, the theory of developing of the steam swept volume is reexamined and a method for approximating the steam swept volume is presented.

3.3.1. MATHEMATICAL MODEL

The main component of the laboratory model shown in Fig. 1 is a cylindrical core surrounded by layers of insulation. Steam is injected into the core and heat is lost radially through the insulation. The combined steam and hot water zone is considered as a heated zone with a step function temperature profile between the heated and unheated zones. The temperature remains constant throughout the heated zone and the thermal conductivity of the insulation is independent of temperature. The heat conduction in the insulation along the steam flow direction is neglected. Accordingly, the movement of the heat front can be described by an equation similar to that of Marx and Langenheim:

$$\dot{H}(t) = \int_0^t \left\{ -k \left[\frac{\partial T(t-\tau)}{\partial r} \right]_{r=r_1} 2\pi r_1 \left[\frac{dX}{d\tau} \right] \right\} d\tau + (\rho C)_R \Delta T \, \pi r_1^2 \frac{dX}{dt} \qquad (1)$$

where

$\dot{H}(t)$ = Rate of heat injected
T = Temperature in the insulation
ΔT = Difference between steam and initial reservoir temperature,
k = Thermal conductivity of Layer 1,
$\frac{dX}{dt}$ = Heat frontal velocity,
r_1 = Radius of the sandpack,
$(\rho C)_R$ = Volumetric heat capacity of reservoir.

The rate of heat loss per unit area at the sandpack boundary $[(\partial T/\partial r)_{r=r_1}]$ is given by the heat conduction in a composite, finite radial system. The mathematic description of this system was given by Wang (1984). The solution of Eq. (1) in Laplace space can be inverted into the real time solution (X_D) numerically by the Stehfest algorithm (1970). The dimensionless parameters used in deriving X_D are given in the nomenclature. The heat efficiency is:

$$E_h = \frac{H_R}{H_{inj}} = \frac{X_D}{t_D} \qquad (2)$$

for constant heat injection rate.

3.3.2. SENSITIVITY STUDY

In this model, it is assumed that the temperatures of the sand and the fluid are the same, and the pressure drop across the steam zone is negligible. For steam injection, the heat transfer coefficient (h_f) between the fluid and the sand is large. If the size of the sand grains is small, one can assume that the temperature of the fluid and of its adjacent grains are the same (Jenkins and Aronofsky, 1954). Factors which may affect the steam zone development are inner and outer boundary conditions and the volumetric heat capacity ratio. Lastly, a comparison between a single-layer model, a two-layer model and a lumped single-layer model is shown. The values of various parameters for the base case are listed in Table 1, which are for a bench model used in this study.

3.3.2.1. Heat Transfer Coefficients at Inner and Outer Boundaries

Estimation of Heat Transfer Coefficient

Numerous studies on both the theory and the measurement of the heat transfer coefficient at the tube wall for packed and fluidized beds can be found in the literature. Colburn (1931), Leva (1947) and Leva *et al.* (1948) showed that the heat transfer coefficient at tube wall decreases with the decrease of particle sizes when D_p/D_t is smaller than 0.15. Leva *et al.* studied the heat transfer coefficient for cooling of gases through packed tubes and proposed the following equation for estimating the heat transfer coefficient:

$$h_f = 3.5\frac{k_l}{D_t}e^{-4.6\frac{D_P}{D_t}}\left[\frac{D_p\dot{m}}{\mu}\right]^{0.7} \tag{3}$$

where

h_f = heat transfer coefficient, Btu/$h \cdot °F \cdot ft^2$,
$\dot{m}$ = mass injection rate, $lb_m/h \cdot ft^2$,
k_l = thermal conductivity of the flowing liquid, Btu/$h \cdot °F \cdot ft$,
μ = viscosity of the flowing liquid, $lb_m/h \cdot ft$,
D_p = particle diameter, ft
D_t = tube diameter, ft.

Figure 2 shows their data of effects on rate and particle size on the heat transfer coefficient.

The study of reservoir heating by hot fluid injection into cylindrical cores is analogous to the Leva *et al.* study. However, the ratio of D_p/D_t for sandpacks is normally in the order of 10^{-3} or less. The value of $\exp(-4.6D_p/D_t)$ is very close to one and Eq. (3) can be reduced to

$$h_f = 3.5\frac{k_l}{D_t}\left[\frac{D_p\,\dot{m}}{\mu}\right]^{0.7} \tag{4}$$

Notice that for a constant tube diameter, h_f is a function of the modified Reynolds number. For sandpacks h_f estimated by Eq. (4) is fairly close to h_f for empty tubes.

Ersoy (1969) studied the effect of mass injection rate on the heat transfer of hot-water displacement in unconsolidated sandpacks. He observed that the heat efficiency of hot-water displacement decreased with the mass injection rate. Crichlow (1972) observed the same rate effect on hot-water displacement as that observed by Ersoy. He considered this effect as a result of the increase of the heat transfer coefficient at the tube wall with the mass injection rate. Arihara (1975) investigated the rate effect on hot-water displacement in synthetic and Berea sandstones. His data showed that the overall heat transfer coefficient (U) of the insulation increased with the mass injection rate. Atkinson (1977) then analyzed Arihara's data and calculated the heat transfer coefficients. He concluded that the heat transfer coefficients calculated by using Arihara's results were consistent with those reported by Crichlow and that there was no significant effect of particle size on the heat transfer coefficient when synthetic and Berea cores were used. There are not sufficient data available to find a proper correlation for the heat transfer coefficient for cores normally used in thermal recovery experiments.

The heat transfer coefficient for convection with phase change is significantly higher than that without phase change. Data on condensing heat transfer coefficient of steam at the inner surface of packed beds are scarce. Crichlow and Arihara reported overall heat transfer coefficients of their model during steam injection. The condensing heat transfer coefficients of steam at the tube wall can be evaluated from the overall heat transfer coefficient. Because of the limited data and errors in this type of experiment, the h_f was not evaluated. Nevertheless, h_f of condensing steam inside empty tubes may provide the information about the magnitude of h_f when steam is flowing in cores. Akers, Deans and Crosser (1959) gave the following correlation for evaluating h_f of condensing steam inside empty horizontal tubes as

$$N_u = 5.03 R_e P_r \qquad R_e < 5 \times 10^4 \tag{5}$$

where

$$N_u = h_f D_t / k_l$$
$$R_e = D_t \dot{m}_E / k_l$$
$$P_r = C_p \mu_l / k_l$$
$$\dot{m}_E = \dot{m}_l + \dot{m}_g (\rho_l / \rho_g)^{0.5}$$

All fluid properties are evaluated at the average film temperature. One may notice that the Nusselt number is proportional to the Reynolds number and is independent of the temperature difference. For a case of the saturated steam of 355° F (179°C) flowing through a 2 in. (0.051 m) I.D. horizontal tube at 26 $lb_m/hr \cdot ft^2$ (0.0353 $kg/s \cdot m^2$) with an average film temperature of 350°F (176.7°C) and an average steam quality of 0.5, the estimated heat transfer coefficient is 52 Btu/ft · hr · °F (295 $W/m^2 \cdot °K$). If the tube is made of an insulation material with thermal conductivity of 0.036 Btu/ft · hr · °F (0.0623 $W/m^2 \cdot °K$), the Biot modulus is 241. This value may be considered as the lower limiting Biot modulus for steam flowing through cores. The presence of noncondensable gases in steam can reduce this heat transfer coefficient.

Modified Biot Number

Biot modulus is a number that measures the relative importance of the convection and the conduction at inner or outer boundary. A modified Biot modulus is defined as

$$B_j = \frac{h_{fj} r_j}{k_S} \tag{6}$$

where

h_{fj} = Heat transfer coefficient at the inner or outer boundary,
r_j = Radius of the inner or outer boundary,
k_S = Thermal diffusivity of the reference layer.

This modified Biot modulus is proportional to heat transfer coefficient, radius of boundary, and is inversely proportional to thermal conductivity of the reference layer. Equation (6) is a generalized and convenient definition of Biot modulus, especially for composite systems. For systems with a common reference layer, this Biot modulus does not vary with the thermal conductivity of the inner or outer layer. Using this definition, the steady-state solution can be written as

$$2\sigma X_D = \ln r_{3D} - \ln r_{2D} + \frac{\ln r_{2D}}{\lambda_D} + \frac{1}{B_1} + \frac{1}{B_2} \tag{7}$$

It is noted that the variable $2\sigma X_D$ is independent of σ as expected. Therefore, $2\sigma X_D$ instead of X_D is used in the following discussion.

Figure 3 shows the effect of Biot modulus at the inner boundary (B_1) on the heat frontal movement. The heat front moves faster when Biot number is small because the rate of heat loss is small. The effect of Biot modulus is negligible when Biot number is greater than 100. In other words, the inner boundary condition can be treated as a constant-temperature one and the effect of mass injection rate on the heat frontal movement is negligible if B_1 is greater than 100. As previously discussed, for steam injection the Biot modulus is much greater than 100 and the effect of mass rate is not expected. For single-phase nonisothermal fluid flow through porous media, the process becomes rate-dependent when the Biot modulus is less than 50.

The effect of Biot modulus at outer boundary (B_2) on heat frontal movement is shown in Fig. 4. When t_D is smaller than 5, the solution is not affected by Biot modulus. When t_D is greater than 5, the effect of this coefficient becomes apparent. The heat front develops faster at smaller B_2. When this number is less than 10, this effect is significant. In the laboratory, the heat transfer coefficient varies from 1.0 to 5 depending on the operating conditions. The corresponding Biot modulus may vary from 2 to 20 and its effect on heat frontal movement is significant.

3.3.2.2. Volumetric Heat Capacity Ratio (σ)

Volumetric heat capacity ratio (σ) is defined as the volumetric heat capacity of the insulation over the volumetric heat capacity of the reservoir. This ratio changes the transient heat front solution but not the steady-state solution. Fig. 5 shows the effect of σ on the heat-frontal movement. σ varies from 0.045 to 0.075. The smaller the σ, the more slowly the heat front moves.

In the 1970's, when the multidimensional thermal simulators for steam injection first became available, researchers (Coats *et al.* 1974, Shutler 1970 and Weinstein *et al.* 1977) tried to validate their simulators by matching them with the laboratory results of steam injection from Willman *et al.* (1961). The laboratory model used could be considered as a linear core with two layers of insulation: a steel plus lead layer and an insulation layer. The calculations

of heat loss in insulations were handled differently by some researchers. Coats *et al.* lumped the steel plus lead layer into the core and Weinstein *et al.* considered this layer separately.

In Figure 6, three curves represent solutions of heat front for the model used in this study handled in three different ways. The top curve is the solution for the one-layer model; the middle curve is the solution for a two-layer model; and the bottom curve is the solution for a lumped one-layer model. The heat front for the one-layer model moves faster than that of the two-layer model because the stainless-steel layer increases both the transient and the steady-state rates of heat loss. This layer is thin and has a large thermal conductivity. The temperature of this layer quickly becomes close to the saturation temperature of steam. This layer may therefore be treated as part of the sandpack and this system becomes the so-called lumped one-layer model. The heat front for the lumped one-layer model moves slightly more slowly than the front for the two-layer model during the transient flow period because the volumetric heat capacity of the sandpack for the lumped model is larger than the two-layer one.

3.3.3. RESULTS AND DISCUSSIONS OF STEAM-DISPLACEMENT EXPERIMENTS

In the following, the results of steam-displacement experiments at various pressure levels are presented and so are comparisons between the experimental and the calculated heat frontal positions. The study on the pressure effect on heat-zone development includes:

1. Experiments at different pressure levels with a constant pressure during each experiment.
2. Experiments with variable pressure during each experiment.

The main objectives of this section are to study the temperature effect on the thermal conductivity of the insulation and the effects of pressure and heat injection rate on the heat-frontal movement.

3.3.3.1. Constant Pressure Cases

The Marx and Langenheim model for calculating the heat front is appropriate for cases with a constant temperature in the steam zone, constant volumetric heat capacity ratio, and constant thermal diffusivity of the insulation. However, in experiments, a small temperature gradient in the steam zone is always present to overcome the flow resistance and the thermal conductivity of the insulation is temperature-dependent. A nonlinear physical problem may be modeled by using the analytical or semi-analytical solutions for linear or nonlinear equations when apparent average values are used for the nonlinear coefficients. Comparisons between the calculated and the experimental results give direct support to the utility of these solutions.

The average temperature of the heat zone increases with the operating pressure. An increase in the steam zone temperature increases the rate of heat loss from the heated zone and consequently slows down the movement of the heat front. For most insulations, both the thermal conductivity and the thermal diffusivity are functions of temperature. Six runs were conducted at 0.11, 0.448, 0.586, 0.793, 1.145 and 1.42 MPa (17, 65, 85, 115, 166 and 206 psia) to find these functions. The mass rates of steam injection were $1.593 \times 10^{-2}\ kg/s \cdot m^2$ ($9.0\ \mathrm{lb}_m/h \cdot \mathrm{ft}^2$) for the run at 0.11 MPa and $3.054 \times 10^{-2} kg/s \cdot m^2$ ($22.6\ \mathrm{lb}_m/h \cdot \mathrm{ft}^2$) for the remaining runs. Other operating conditions are listed in Table 2. From material balances made during the runs the average steam saturations of Run #19, #21 and #23 were calculated; and the average steam saturation decreased slightly with time.

As these runs were performed at residual oil saturations, the pressure gradient in the steam zone was not negligible. The pressure gradients in the steam zone varied from 0.04 to

0.083 MPa/m (1.8 to 3.7 psi/ft). However, the average temperatures of the steam zone remained fairly constant. Comparisons of heat frontal positions calculated by the solution of X_D and those obtained from the six experiments are shown in Fig. 7. Except for small-time data, good matches are obtained by using apparent values for the thermal conductivity of the insulation. The discrepancy between the experimental and calculated heat fronts during early injection period was due to the excessive heating of the end flange by the injected steam or by the band heater around the flange for Run #38. The apparent thermal conductivities of the insulation obtained from these matches are plotted in Fig. 8 against the saturation temperature of steam. The curve is given by a fitted quadratic equation as follows:

$$k_S = 0.0225 + 1.47 \times 10^{-5} T + 7.16 \times 10^{-8} T^2 \qquad (8)$$

where T was in °F. Values of the apparent thermal conductivity are higher than those reported in the literature (Turner and Malloy, 1981). This was caused partly by the heat conduction through fittings, tubing and thermocouples.

3.3.3.2. Variable Pressure Cases

When steam-displacement experiments are conducted in a sandpack with movable oil, both the pressure and the temperature of the steam zone vary with time during an experiment. The movement of the heat front is complicated by the pressure change. An examination of the solution for X_D reveals that the change of the steam-zone temperature changes three things:

1. the dimensionless heat injection rate,
2. the heat content in the heated zone and
3. the rate of heat loss to the insulation.

Superposition can only handle the change of the dimensionless heat injection rate. Both the change of heat content and rate of heat loss can be treated as heat sources or sinks. However, the additional amount of increased (or decreased) heat loss is normally not available.

Prats (1969 and 1982) proposed a method for handling cases of variable injection temperature. He stated that the heat efficiency for the Marx and Langenheim (1959) model applies even if the injection temperature or mass rate varies, as long as the net rate of heat input is constant. A change in the injection temperature may result from a change in injection pressure. If the transient heat flow resulting from pressure change is not fast enough to reach equilibrium, this approach tends to give a larger steam swept volume when the steam temperature decreases with time and to give a lower steam swept volume when the steam temperature increases with time.

Prats' method is simple and efficient. The heat front at a certain time can be approximated by the Marx and Langenheim equation using the instantaneous values for the steam-zone temperature and properties of the reservoir and the insulation. When all the properties of the reservoir and the insulation are independent of temperature, the heat-frontal position is inversely proportional to the steam-zone temperature. Superposition can be applied with Prats' method to handle cases of variable heat injection rate.

For a cylindrical model, the heat efficiency is given by Eq. (2) for constant heat injection rate. In cases of variable heat injection rate, X_D is more convenient to use with superposition than E_h as

$$X(t) = \frac{1}{[\pi\alpha_S(\rho C)_R\Delta T]_n} \sum_1^n U(t - t_i)(\dot{H}_i - \dot{H}_{i-1})X_D(t_D - t_{Di-1}) \qquad (9)$$

Only the constants of the nth time step are used in Eq. (9).

Four experiments were performed at different oil and steam saturations in the steam zone to investigate the effect of pressure change on the heat-frontal movement and to verify Prats' method for handling the pressure change. The operating conditions and parameters of these experiments are listed in Table 3. The steam saturation and the oil saturation of Run #11 and #12 were distinctly different from those of other runs due to the presence of surfactant in the core. A two-inch thick insulation was used in Run #16 and #17, and a three-inch thick insulation was used in Run #10, #11 and #12. The mass injection rates were constant for Run #10, #11 and #12. Figure 9 shows the temperature profiles of Run #12. The changes of the steam plateau temperatures were caused by the changes of the pressure with time in the steam zone. As the pressure of the steam zone increased, both the steam-zone temperature and the heat loss rate increased and the movement of the heated front slowed down, and the effect is just the opposite when the pressure decreased. Figure 10 presents data of heat frontal movements of Run #10, #11, #12 and #17. Symbols indicate experimental data and the solid lines represent the heat fronts calculated by using Eq. (9). Because the apparent thermal conductivity of the insulation was dependent on temperature, the dimensionless time was determined by using the instantaneous, apparent thermal conductivity rather than an average value. The agreement between the experimental heat fronts and the calculated heat fronts by the semianalytical solution are good for all four runs.

3.3.4. EXTENSIONS OF MARX AND LANGENHEIM MODEL FOR STEAM SWEPT VOLUME

The theory of the development of the steam swept volume is discussed; the definition of the critical time is reexamined and a method for approximating the steam swept volume based on laboratory observation and physical constraints is presented.

3.3.4.1. Critical Time

The development of the steam swept volume during steam displacement is mainly dominated by the transfer of injected latent heat. The injected latent heat is consumed by the lateral heat loss and the growth of the steam swept zone. The sensible heat accelerates the development of the steam swept zone. Therefore, both the injected latent heat and sensible heat affect the development of the steam swept zone. The critical time defined by Mandl and Volek (1969) has been used by previous investigators to indicate the time when the hot liquid zone becomes significant. From the point of view of heat loss, this critical time is the time the heat loss rate from the heated zone equals the rate of the latent heat injection. When the time is greater than the critical time, the rate of heat loss from the steam swept zone must, therefore, equal the rate of latent heat injection. This is the Hearn theory (1969). Apparently, this theory has neglected the latent heat used to heat additional reservoir to steam temperature. Although models by Myhill and Stegemeier (1978), and Yortsos and Gavalas (1982) give a steam swept

volume smaller than the Hearn model when time is greater than the critical time, an unrealistic decrease of the heat loss rate from the steam swept zone occurs during most of the time of interest. It is, therefore, necessary to reexamine the concept of the critical time.

Mandl and Volek (1969) defined the critical time as the time when the velocity of the heat front equals the sharp temperature front velocity of an adiabatic hot-water displacement at the same mass injection rate and injection temperature as the steam displacement. However, from the point of view of fluid mechanics the critical time may be defined as the time when the heat frontal velocity equals the injected fluid velocity of an adiabatic hot water displacement that has the same mass injection rate and injection temperature as the steam displacement. When the heat injection rate is constant, the steam quality decreases with the increase of mass injection rate. A low-quality steam injection represents an equivalent adiabatic hot-water displacement with a high fluid velocity. The heat frontal velocity reaches this equivalent fluid velocity early and the low quality steam injection has a small critical time. This definition of the critical time will give critical times smaller than those defined by Mandl and Volek by a factor which varies from 2 to 5 depending on the ratio of fluid velocity to the temperature velocity. The following equation can be used to estimate this factor:

$$f_{tc} = \frac{(\rho C)_R}{\phi(\rho C)_w} \tag{10}$$

where $(\rho C)_w$ is the volumetric heat capacity of the hot water at injection condition. This redefined critical time is

$$t_{cD} = \frac{t_{cDMV}}{f_{tc}} \tag{11}$$

where t_{cDMV} is the Mandl and Volek critical time obtained by solving the following equation:

$$e^{t_{cDMV}} erfc(\sqrt{t_{cDMV}}) = 1 - f_{hv} \tag{12}$$

The f_{hv} is the ratio of latent heat to total heat injection.

3.3.4.2. Method For Predicting Steam Swept Volume

The development of the steam swept volume is complicated by the injected sensible heat. The heat balance equation based on either the total heat injection rate or the latent heat injection rate cannot satisfactorily describe the development of the steam swept volume. Methods applying some physical constraints may lead to a better approximation of the steam swept volume. Two physical constraints are recognized for the development of the steam swept volume. They are:

1. The rate of heat loss from the steam swept volume cannot exceed the rate of latent heat injection.
2. The rate of heat flow into the hot liquid zone increases with time, from zero to the rate of sensible heat injection.

A method for approximating the steam swept volume, which applies these two constraints, is discussed in the following.

The method proposed by Wang (1984) for calculating the steam swept volume by shifting the time scale is written as

$$V_{sD}(t_D) = \dot{H}_{fgD} G\left[\frac{t_D}{f_{hv}n}\right] = \dot{H}_D[f_{hv}G(t_D')] \tag{13}$$

where

V_{sD} = Dimensionless heated volume, V_s/h^3
$\dot{H}_D$ = Dimensionless latent heat injection rate, $\dot{H}/4\sigma k_S h\Delta T$
$\dot{H}_{fgD}$ = Dimensionless latent heat injection rate, $\dot{H}_{fg}/4\sigma k_S h\Delta T$
t_D = Dimensionless time, $4\sigma^2\alpha_S t/h^2$
σ = $(\rho C)_S/(\rho C)_R$
$f_{hv}n$ = Weighting factor.

The function $G(t_D)$, the Marx and Langenheim Equation (1959), is given by

$$G(t_D) = 2\sqrt{\frac{t_D}{\pi}} - 1 + e^{t_D} erfc(\sqrt{t_D}). \tag{14}$$

The power index (n) is a function of time, critical time, f_{hv} and geometry of the steam swept zone. The values for n as a function of f_{hv} and time may be estimated by the critical time and the two physical constraints.

3.3.4.3. Determination of n

Because it is assumed that the steam swept volume starts to deviate from the heated volume at a critical time, the n for each f_{hv} may be determined by two methods:

1. The calculated steam swept volume by Eq. (13) equals the heated volume given by the Marx and Langenheim equation, or
2. The rate of the development of the steam swept volume equals the rate of the development of the heated volume.

Whether to use method 1 or 2 is not critical because the path of the development of the steam swept volume is not really known. This n determined by the first method is represented as n_1, which is a function of t_{cD} and f_{tc}.

Further study reveals that n is not constant with respect to time. If n_1 is used for large times, the calculated rate of heat loss from the steam zone will exceed the latent heat injection rate. Therefore, an n_2 for each f_{hv} is determined so that the calculated rate of heat loss from the steam swept zone is slightly smaller than the latent heat injection rate and the estimated rate of heat flowing into the hot liquid zone is slightly smaller than the rate of sensible heat injection at large times. The determined n_2 for f_{hv} varying from 0.1 to 0.9 can be fitted into a quadratic equation:

$$n_2 = 0.28643 + 1.22115\, f_{hv} + 0.23052\, f_{hv}2\ . \tag{15}$$

The n, which varies from n_1 at the critical time to n_2 at large times, may be expressed in an exponential form:

$$n(t_D, f_{hv}) = n_2 + (n_1 - n_2)e^{-\beta(t_D - t_{cD})} \tag{16}$$

where β is also a function of time. All the equations for β are listed in Table 4.

3.3.4.4. Steam Swept Volume

Equation (13) can be used to approximate the steam swept volume under constant total and latent heat injection rates. By defining a G_1 function as

$$G_{1(t_D)} = \frac{V_{sD}}{H_D} = f_{hv}G(t'_D) \tag{17}$$

Values of G_1 for f_{hv} ranging from 1 to 0.1 are shown in Fig. 11 for the case of f_{tc} of 2.5. The curve of $f_{hv} = 1$ is for the calculation of the total heated volume. Steam swept volumes calculated by Eq. (17) are smaller than those given by previous investigators (Hearn, Myhill and Stegemeier, and Yortsos and Gavalas) as shown in Fig. 12. When the time is less than 10, the steam swept volume given by Hearn, Myhill and Stegemeier, and Yortsos and Galavas are all very close. In Fig. 13, the rate of the heat loss from the steam swept volume calculated by using three methods are presented. The straight line represents the rate of the heat loss given by the Hearn method. The diamonds represent the heat loss rate given by Yortsos and Gavalas method and the curve represents the rate given by the present study. The discrepancies of this rate using Hearn, and Yortsos and Gavalas methods are clearly shown. Only this study gives an increasing rate of heat loss from the steam swept zone with respect to time although this heat loss rate is a little less than the heat loss rate at the critical time (0.47) when t_D is less than 1. The exact heat loss rate, however, remains unknown to us. Nevertheless, the heat loss rate from the steam swept zone given by this study is more rational in a physical sense than that from previous studies.

3.3.4.5. Laboratory Result of Steam Frontal Position

The dimensionless critical time defined by Mandl and Volek (1969) is the time when the rate of heat loss from the heated zone equals the rate of latent heat injected. For a linear/tubular model, the rate of heat loss from the heated zone ($1 - dV_D/dt_D$), can be obtained from a semianalytical solution for the heat-frontal position. The Mandl and Volek dimensionless critical time can, therefore, be determined. For a case of $\sigma = 0.675$ and $f_{hv} = 0.8$, this dimensionless time is 13.7 (indicated by the solid square in Fig. 14). The dimensionless critical time corrected by the ratio of liquid velocity to the temperature velocity (f_{tc}) is 6. The experimental data of run #38 (as shown in Fig. 14) indicates that the dimensionless critical time is around 7.

The method for calculating the steam swept volume is applicable to the finitely thick insulation system. The equation stating the relationship between the power index (n) and f_{hv} is different from Eqs. (15) and (16). No attempt has been made to find the equations for this system because the equation depends on too many factors. Nevertheless, it is interesting to use Eqs. (13) and (15) to calculate the steam frontal positions of a finitely thick insulation system and to compare them to experimental data. Fig. 14 shows the comparison of the calculated

and the experimental steam fronts. Circles stand for the heat fronts, crosses for the steam fronts and curves for steam fronts with f_{hv} varying from 1.0 to 0.5. The f_{hv} of this run is 0.81. A good agreement between the calculated and the experimental heat and steam is observed.

3.3.5. CONCLUSIONS

In this study, the following conclusions have been reached:

(1) Heat frontal positions from laboratory steam injection can be satisfactorily matched by the semianalytical solutions.

(2) Prats' method can be used to approximate heat frontal positions for variable pressure cases.

(3) The definition of dimensionless time is modified to be logically correct.

(4) A new proposed method improve the approximation of steam swept volume.

3.3.6. NOMENCLATURE

B_1 = Modified Biot number at the inner boundary
B_2 = Modified Biot number at the outer boundary
C, C_p = Specific heat at constant pressure, J/kg · °K
D_p = Particle diameter, m
D_t = Tube diameter, m
E_h = Thermal efficiency, fraction
f_{hv} = Fraction of latent heat to total heat injected
f_{tc} = Correction factor for t_{cMV}
G = Function for the Marx and Langenheim Equation
$G1$ = Function for the steam swept volume
h = Thickness of formation, m
h_f = Heat transfer coefficient, $W/m^2 \cdot °K$
H_{inj} = Heat injected, J
H_R = Heat stored in the reservoir, J
$\dot{H}$ = Total heat injection rate, J/s
$\dot{H}_D$ = Dimensionless total heat injection rate, $\dot{H}/\dot{H}_{0D}$
$\dot{H}_{fg}$ = Latent heat injection rate, J/s
$\dot{H}_{fgD}$ = Dimensionless latent heat injection rate
$\dot{H}_0$ = Initial heat injection rate, J/s
$\dot{H}_{0D}$ = Dimensionless initial heat injection rate, $\dot{H}_0 / \pi L k_2 \sigma \Delta T$
k_l = Thermal conductivity of flowing liquid, $W/m \cdot °K$
k_S = Thermal conductivity of adjacent formation, $W/m \cdot °K$
k_2 = Thermal conductivity of the second layer, $W/m \cdot °K$
L = Length of the core, m
$\dot{m}$ = Mass injection rate, $kg/s \cdot m^2$

$\dot{m}_E$ = Equivalent mass injection rate, $kg/s \cdot m^2$
$\dot{m}_l$ = Mass injection rate of liquid, $kg/s \cdot m^2$
$\dot{m}_g$ = Mass injection rate of gas, $kg/s \cdot m^2$
n = Power index of f_{hv}
n_1 = Power index of f_{hv} at t_{cD}
n_2 = Power index of f_{hv} at t_{cD} = Power index of f_{hv} at large times
N_u = Nusselt number
P_r = Prantl number
r = Radial distance, m
r_D = Dimensionless radius, r/r_1
r_1 = Radial distance at the inner boundary of insulation, m
r_2 = Radial distance at the interface between insulations, m
r_3 = Radial distance at the outer boundary of insulation, m
r_{2D} = Dimensionless radial distance, r_2 / r_1
r_{3D} = Dimensionless radial distance, r_3 / r_1
R_e = Reynolds number
t = Elapsed time, s
t_{cD} = Dimensionless critical time
t_{cDMV}= Dimensionless critical time defined by Mandl and Volk
t_D = Dimensionless time, $\alpha_2 t / r_1^2$
T = Temperature,°K
T_∞ = Ambient temperature,°K
U = Overall heat transfer coefficient, $W/m^2 \cdot °K$
V_s = Steam swept volume, m^3
V_{sD} = Dimensionless steam swept volume, V/h^3
X = Longitudinal distance, M
X_D = Dimensionless distance
α_S = Thermal diffusivity of surrounding, m^2 /s
α_2 = Thermal diffusivity of the second layer, m^2 /s
β = Coefficient in n function
λ_D = Conductivity ratio
ρ = Density, kg/m^3
ρ_g = Density of gas, kg/m^3
ρ_l = density of liquid, kg/m^3
σ = Volumetric heat capacity ratio, $(\rho C)_S / (\rho C)_R$
τ = Elapsed time, s
μ = Viscosity, $Pa \cdot s$
μ_l = Viscosity of liquid, $Pa \cdot s$

Subscript

c = Critical
D = Dimensionless
fg = Latent
i = Time step
j = Layer number
R = Reservoir
s = Steam, steam front
ss = Stainless steel
sw = Saturated water
S = Surrounding (or insulation)
t = Total
w = Water
1 = Layer 1
2 = Layer 2
∞ = Ambient

3.3.7. REFERENCES

1. Akers, W.W., Deans, H.A. and Crosser, O.K.: "Condensing Heat Transfer within Horizontal Tubes," *Chem. Eng. Prog. Series 55*, No. 29 (1959), 171-176.

2. Arihara, N.: "A Study of Non-Isothermal Single and Two-Phase Flow through Porous Media," PhD Dissertation, Stanford University, Stanford, CA (1975).

3. Atkinson, P.G.: "Mathematical Modelling of Single-Phase Fluid Flow through Porous Media," PhD Dissertation, Stanford University, Stanford (1976).

4. Coats, K.H., George, W.D., Chu, C. and Marcum, B.E.: "Three Dimensional Simulation of Steamflooding," *Soc. Pet. Eng. J.* (Dec. 1974), 573-592.

5. Colburn, A.P.: "Heat Transfer and Pressure Drop in Empty, Baffled, and Packed Tubes," *Ind. Eng. Chem. 23*, No. 8 (Aug. 1931) 910-913.

6. Crichlow, H.B.: "Heat Transfer in Hot Fluid Injection in Porous Media," Ph.D. Dissertation, Stanford University, Stanford, CA (1972).

7. Ersoy, D.: "Temperature Distribution and Heat Efficiency of Oil Recovery by Hot-Water Injection," PhD Dissertation, Stanford, CA (1969).

8. Hearn, C.L.: "Effect of Latent Heat Content of Injected Steam in Steam Drive," *J. Pet. Tech.* (April 1969) 374-375.

9. Jenkins, R. and Aronofsky, J.S.: "Analysis of Heat Transfer Processes in Porous Media-New Concepts in Reservoir Heating Engineering," *Prod. Monthly* (May 1954) 37.

10. Leva, M.: "Heat Transfer to Gases through Packed Tubes," *Ind. Eng. Chem. 39,* No. 3 (July 1947) 857-862.

11. Leva, M., Weintraub, M., Grummer, M. and Clark, E.L.: "Cooling of Gases through Packed Tubes," *Ind. Eng. Chem. 40,* No. 4 (April 1948) 747-752.

12. Mandl, G. and Volek, C.W.: "Heat and Mass Transport in Steam Drive processes," *Soc. Pet. Eng. J.* (March 1969) 59-79.

13. Marx, J.W. and Langenheim, R.H.: "Reservoir Heating by Hot Fluid Injection," *Trans. AIME 216,* (1959) 312-315.

14. Myhill, N.A. and Stegemeier, G.L.: "Steam Drive Correlation and Prediction," *Soc. Pet. Eng. J.* (Feb. 1978) 173-182.

15. Prats, M.: "The Efficiency of Thermal Recovery Processes," *J. Pet. Tech.* (March 1969) 323-332.

16. Prats, M.: *Thermal Recovery,* Monograph 7, SPE of AIME, Dallas, 1982.

17. Stehfest, H.: "Algorithm 368, Numerical Inversion of Laplace Transforms," D-5, *Communication of ACM 13,* No. 1 (Jan. 1970) 49.

18. Shutler, N.D.: "Numerical Three-Phase Model of the Two-Dimensional Steamflooding Process," *Soc. Pet. Eng. J.* (Dec. 1970) 405-417.

19. Turner, W.C. and Malloy, J.F.: *Properties of Thermal Insulation,* McGraw Hill Book Co., New York, 1981.

20. Wang, F.: "A Study of Heat Transfer of Steam Injection and Effect of Surfactants on Steam Mobility Reduction," SUPRI TR 47 (Oct. 1 1983-Sept. 30 1984) [DOE-SF-11564-11], 92-109.

21. Weinstein, H.G., Wheeler, J.A. and Woods, E. G.: "Numerical Model for Thermal Processes," *Soc. Pet. Eng. J.* (Feb. 1977) 65-78.

22. Willman, B.T., Valleroy, V.V., Runberg, G.W., Cornelius, A.J., and Powers, L.W.: "Laboratory Studies of Oil Recovery by Steam Injection," *J. Pet. Tech.* (July 1961) 681-690.

23. Yortsos, Y.C. and Gavalas, G.R.:"Analytical Modeling of Oil Recovery by Steam Injection: Part II - Asymptotic and Approximate Solutions," *Soc. Pet. Eng. J.* (April 1982) 179-190.

TABLE 1
PHYSICAL PROPERTIES OF SANDPACK AND INSULATION

sandpack	
diameter (in.)	2.15
length (ft)	6.0
porosity	0.35
permeability (Darcy)	5.0
stainless steel #321	
thickness (in.)	0.049
Fiberfrax (insulation)	
thickness (in.)	2.0
dimensionless parameters	
radius ratio:	
inner layer (r_{2D})	1.05
outer layer (r_{3D})	2.78
Biot modulus:	
inner boundary (B_1)	1000
outer bounddary (B_2)	15
diffusivity ratio (α_D)	7.36
conductivity ratio (λ_D)	290.0
volumetric heat capacity ratio (σ)	0.06

TABLE 2
DATA FOR STEAM DISPLACEMENTS AT CONSTANT PRESSURE

run no.	19	21	23	25	27	38
mass injection rate (lbm/hour)	0.57	0.57	0.57	0.57	0.57	0.227
back pressure (psia)	206	166	115	65	85	17
injection pressure (psia)	219	177	127	77	103	30
injection temperature (°F)	400	387	390	386	387	290
saturated steam temperature (°F)	390	371	344	310	326	240
ambient temperature (°F)	75	70	74	71	70	73
fraction of latent heat (f_{hv})	0.71	0.74	0.764	0.795	0.78	0.814
α_S(ft ^{2}/hour)	0.022	0.023	0.021	0.020	0.020	0.018
$(\rho C)_R$ (Btu/ ft^3)	26.64	26.52	25.64	25.58	26.44	25.92
steam saturation (S_s)	0.70	0.70	0.74	0.74	0.72	0.75
residual oil saturation (S_{or})	0.16	0.16	0.16	0.16	0.16	0.16

TABLE 3
DATA FOR STEAM DISPLACEMENTS AT VARIABLE PRESSURE

run no.	10	11	12	17
mass injection rate (lb_m/hour)	0.42	0.42	0.42	0.55
back pressure (psia)	15	15	15	15
injection temperature (^oF)	402	402	397	347
ambient temperature (^oF)	72	75	70	80
steam saturation (S_s)	0.60	0.33	0.36	0.59
residual oil saturation (S_{or})	0.15	0.45	0.39	0.18
insulation thickness (in.)	3.0	3.0	3.0	2.0

TABLE 4
β AS A FUNCTION OF f_{hv}

f_{hv}	β	t_D
0.1	$1.59-0.98872\ln t_D+0.4186(\ln t_D)^2$	<4
	1.0	≥4
0.2	$1.546-0.608\ln t_D+0.1006(\ln t_D)^2$	<2.5
	1.0	≥2.5
0.3	$0.824-0.277\ln t_D+0.0787(\ln t_D)^2$	<10
	0.6	≥10
0.4	0.6	
0.5	0.1	
>= 0.6	0.05	

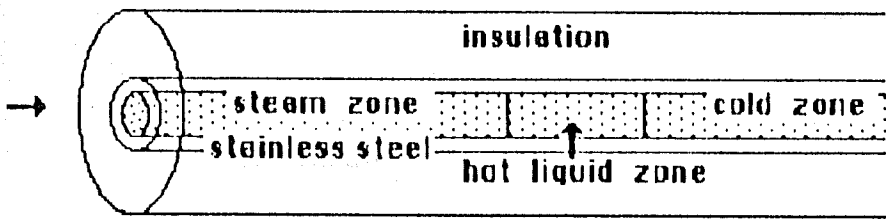

Fig. 1 Schematic diagram of a laboratory model

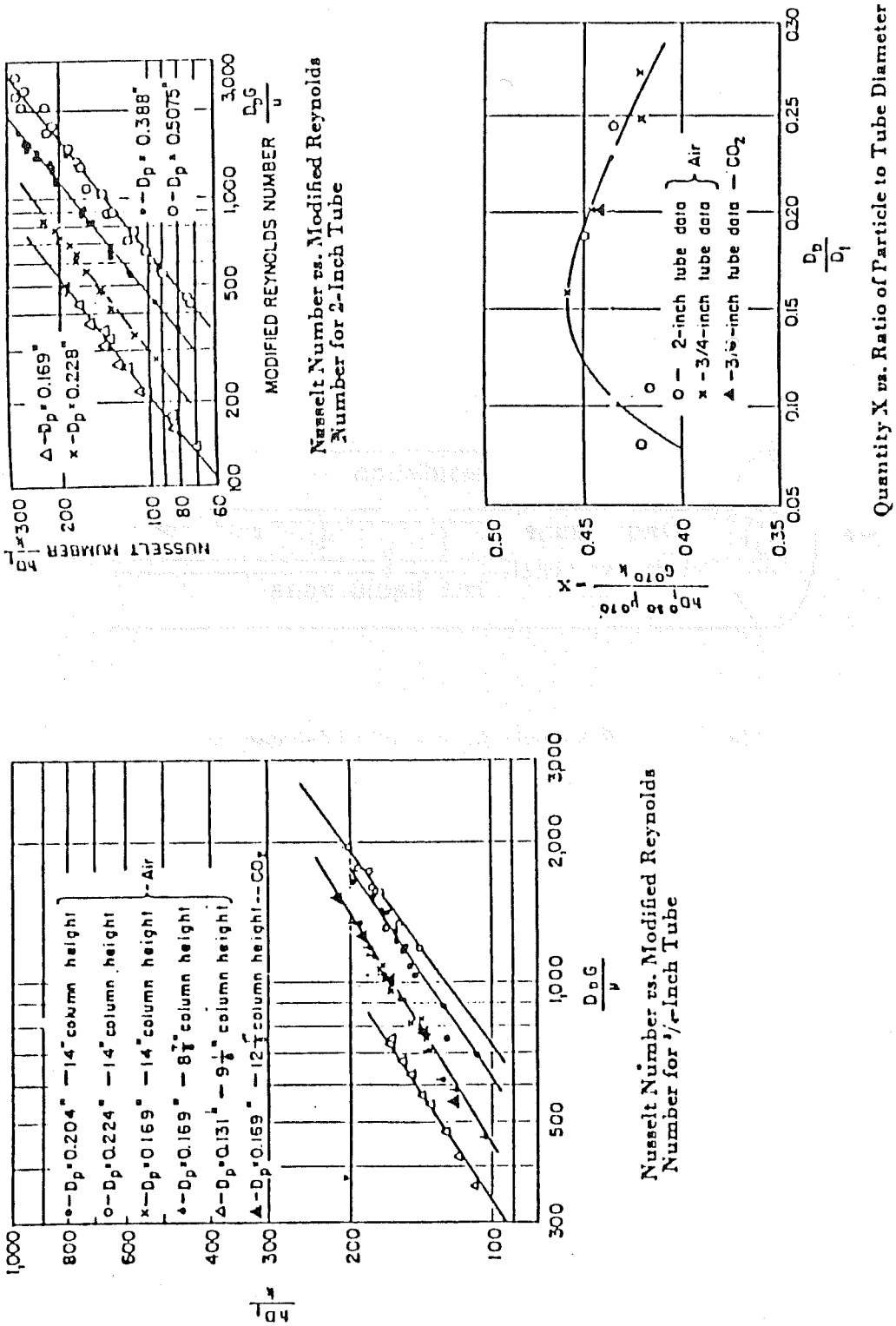

Fig. 2 Effect of particle size on wall/bed heat transfer coefficient

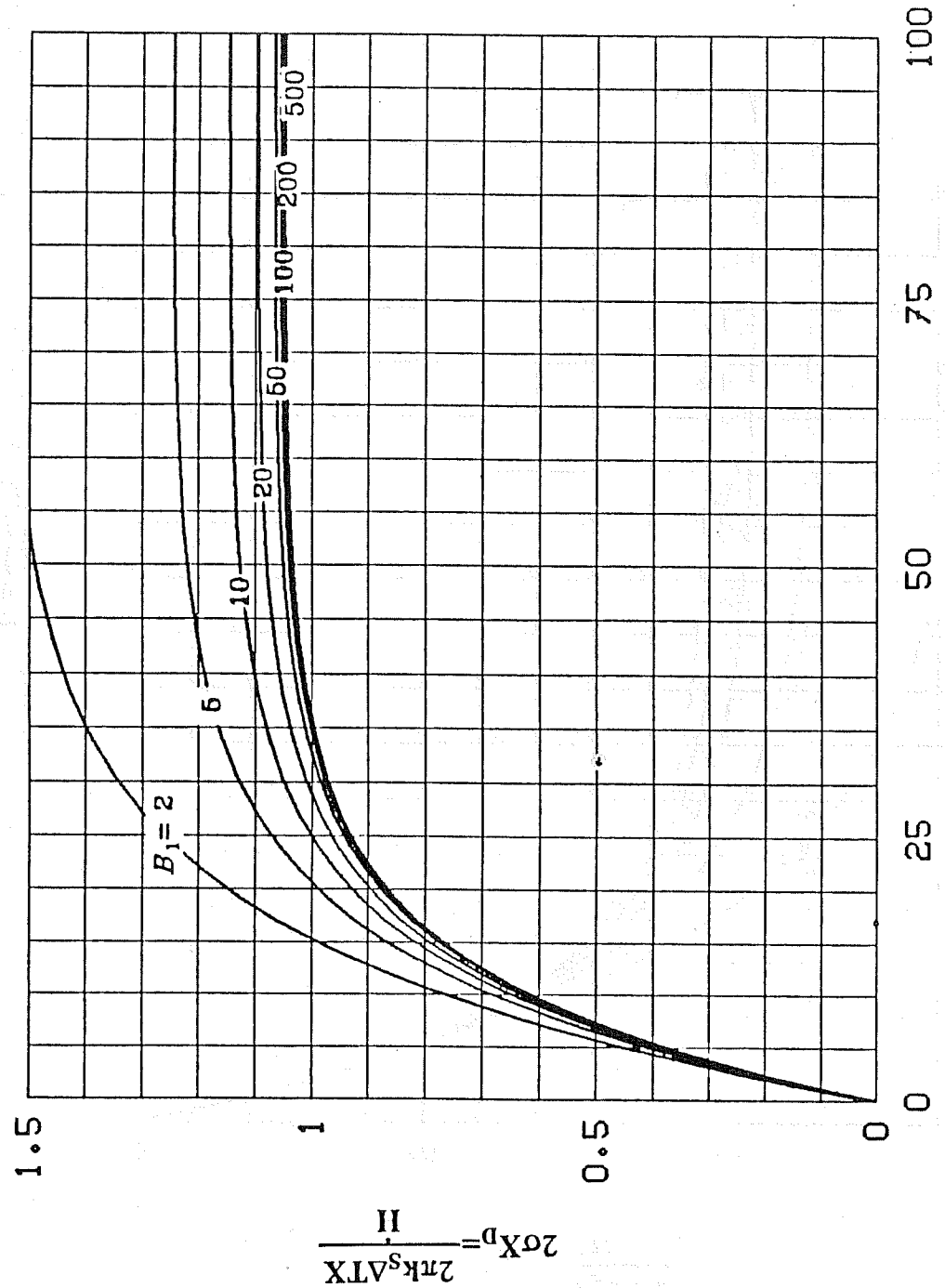

Fig. 3 Effect of Biot modulus at inner boundary on heat-front movement

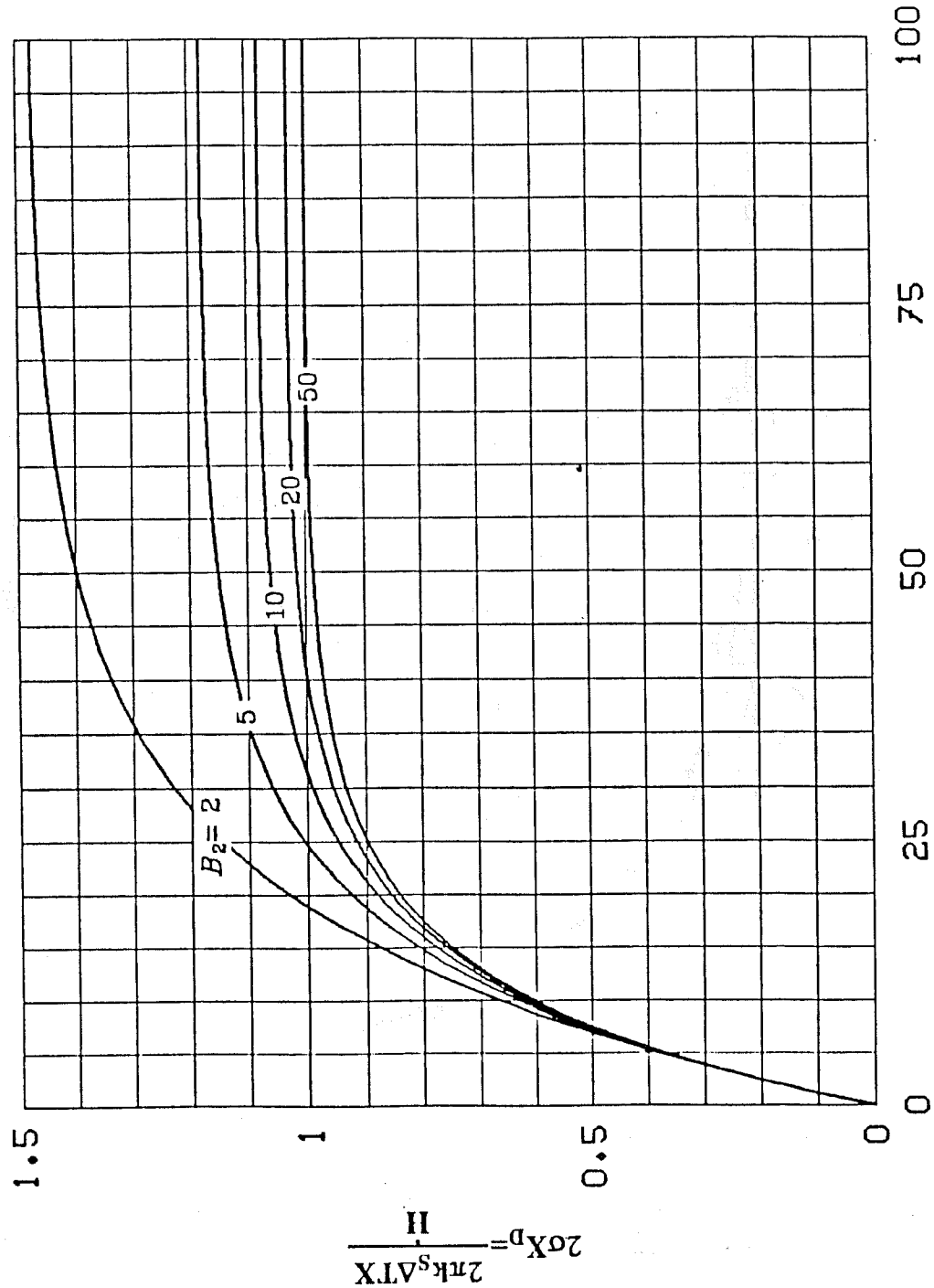

Fig. 4 Effect of Biot modulus at outer boundary on heat-front movement

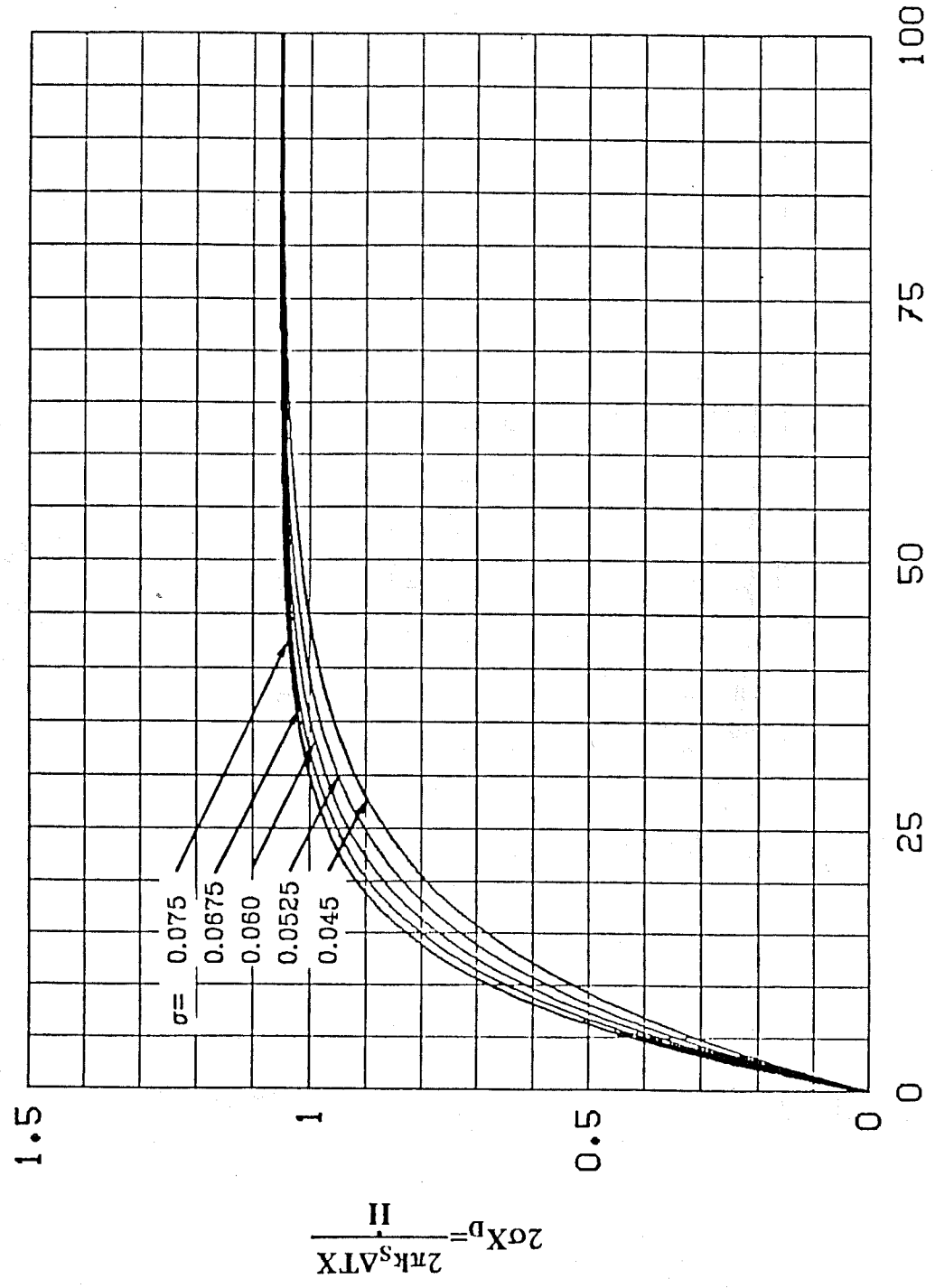

Fig. 5 Effect of volumetric heat capacity ratio on heat-front movement

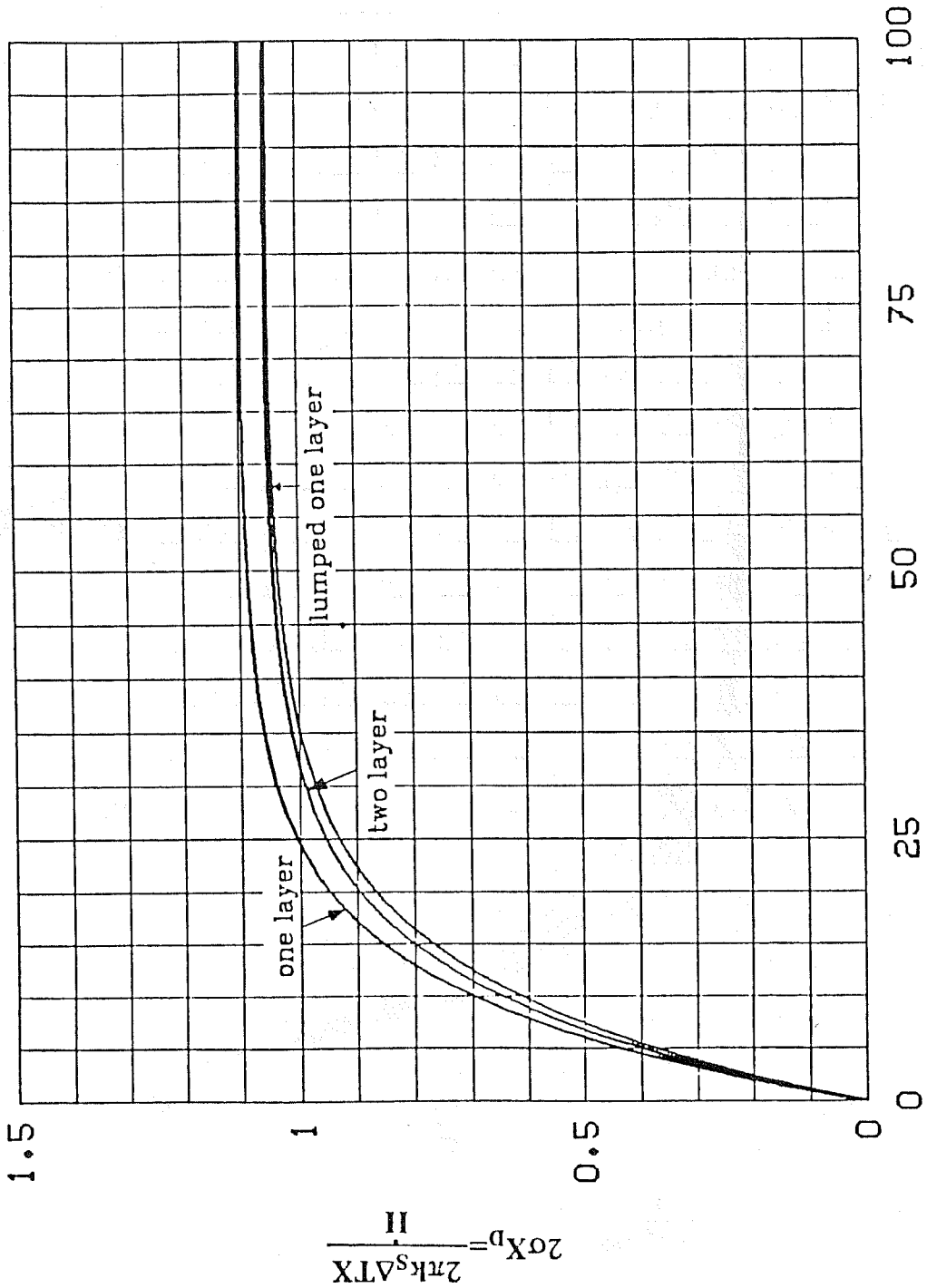

Fig. 6 Comparison among single and two layer models

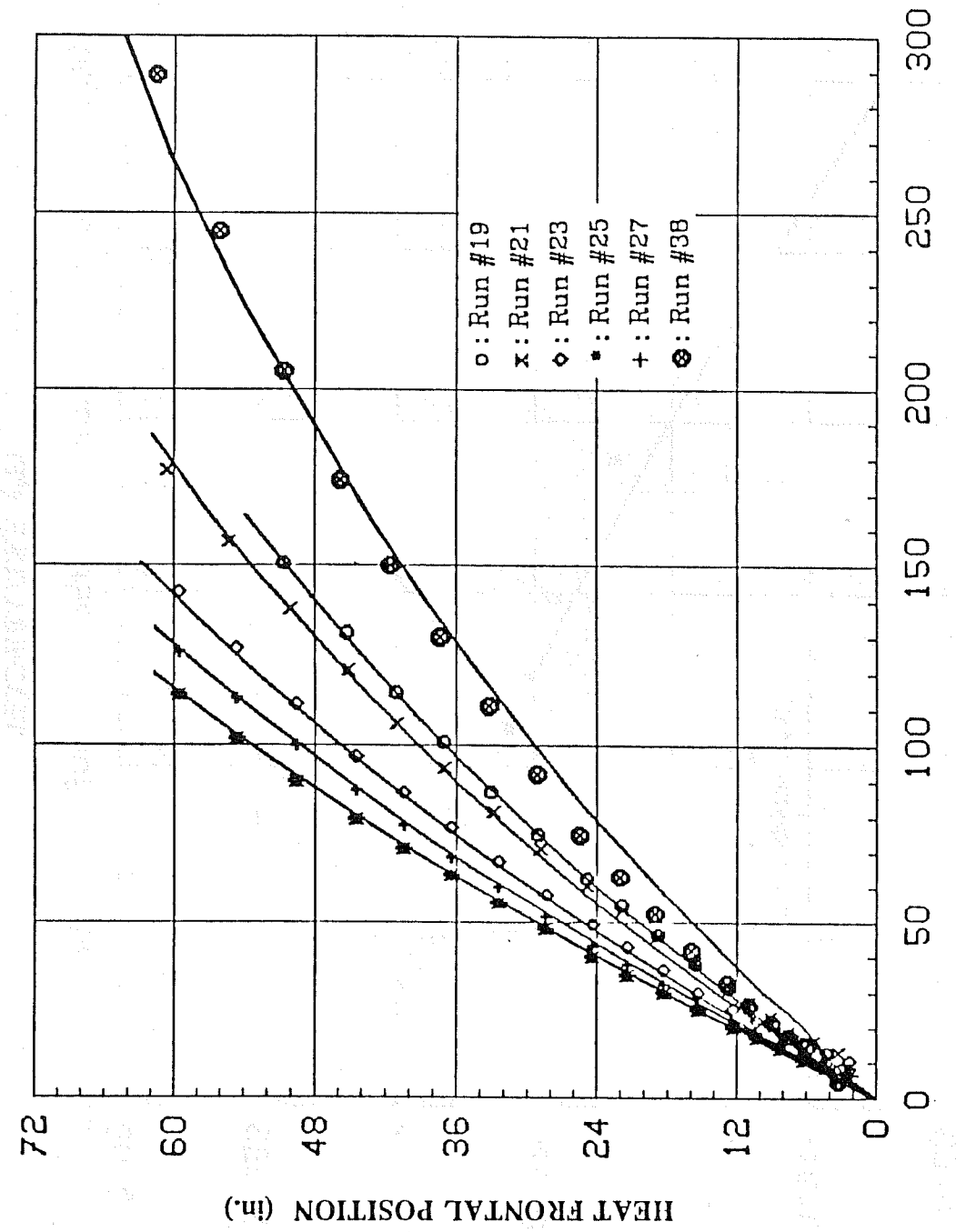

Fig. 7 Comparisons between experimental and calculated heat fronts

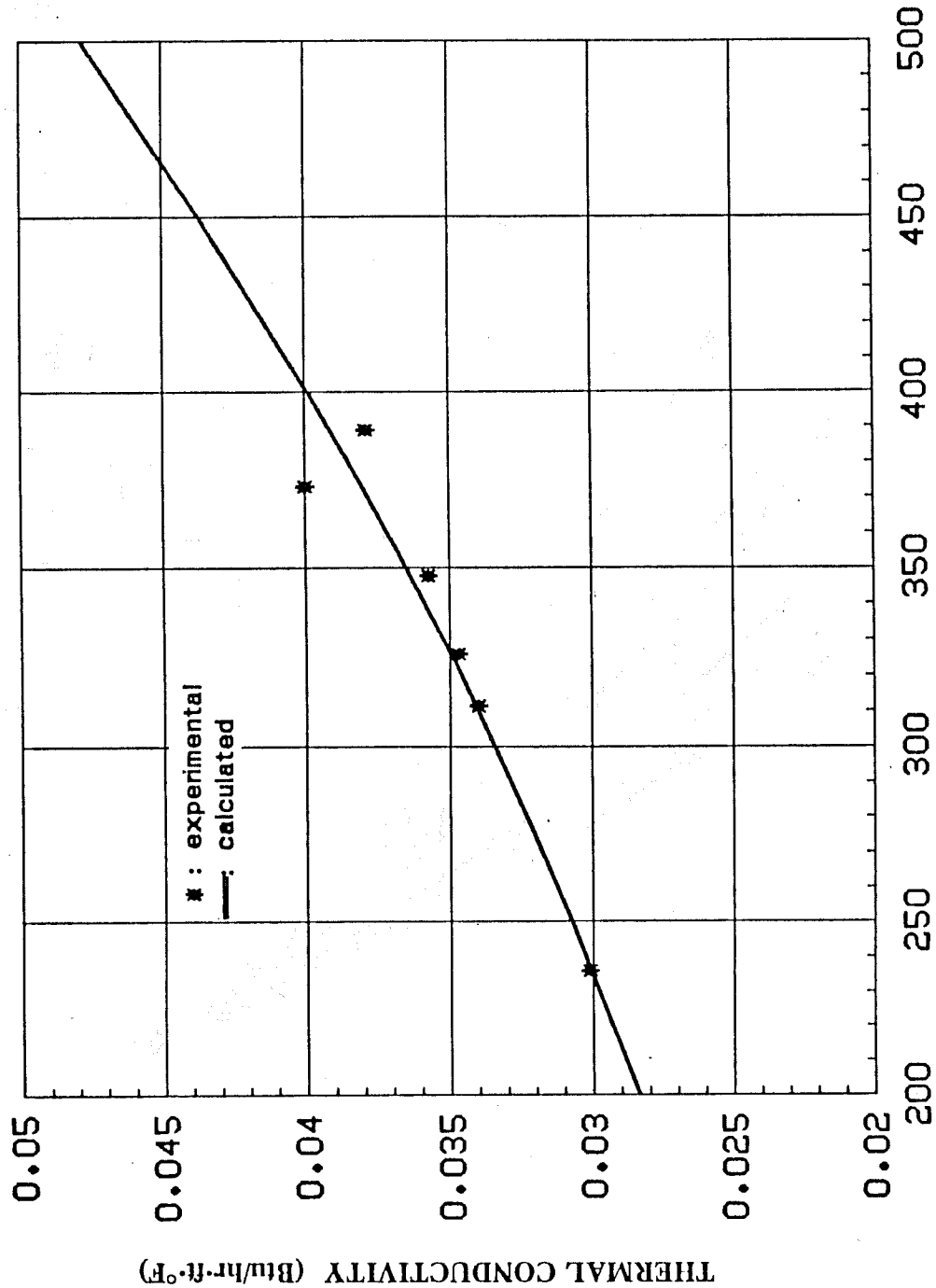

Fig. 8 Thermal conductivity of Fiberfrax vs temperature

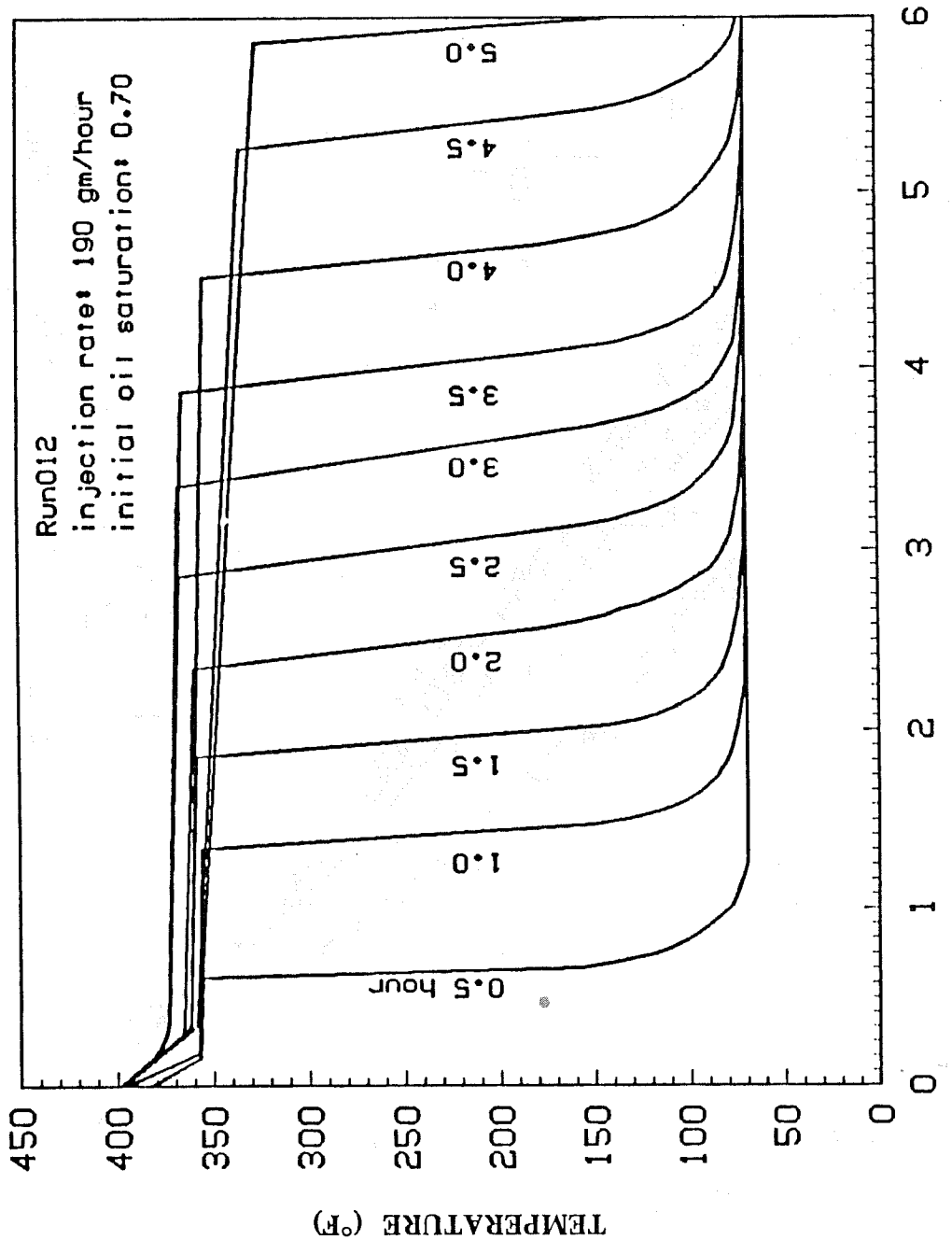

Fig. 9 Temperature profiles of Run #12

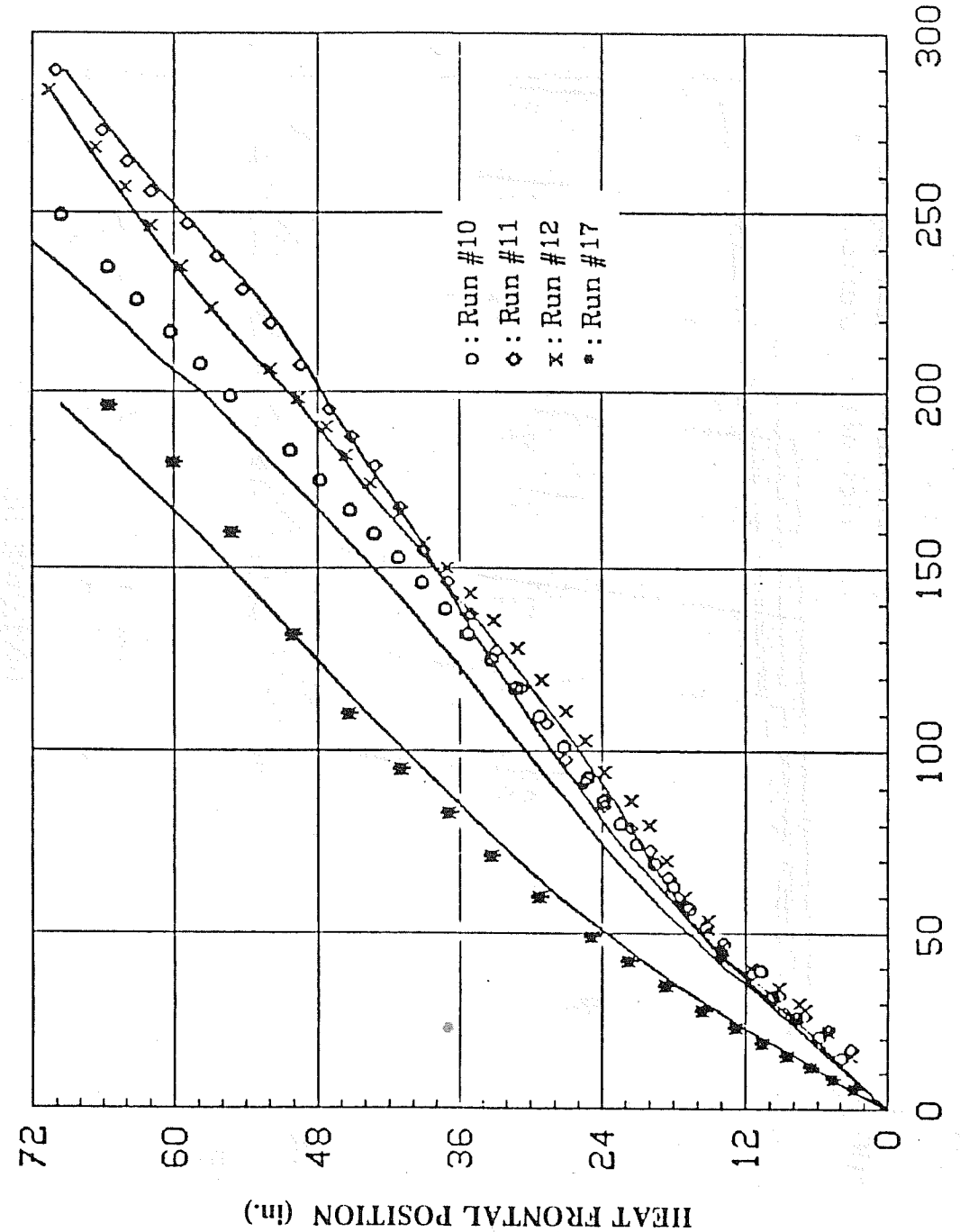

Fig. 10 Comparisons between experimental and calculated heat fronts

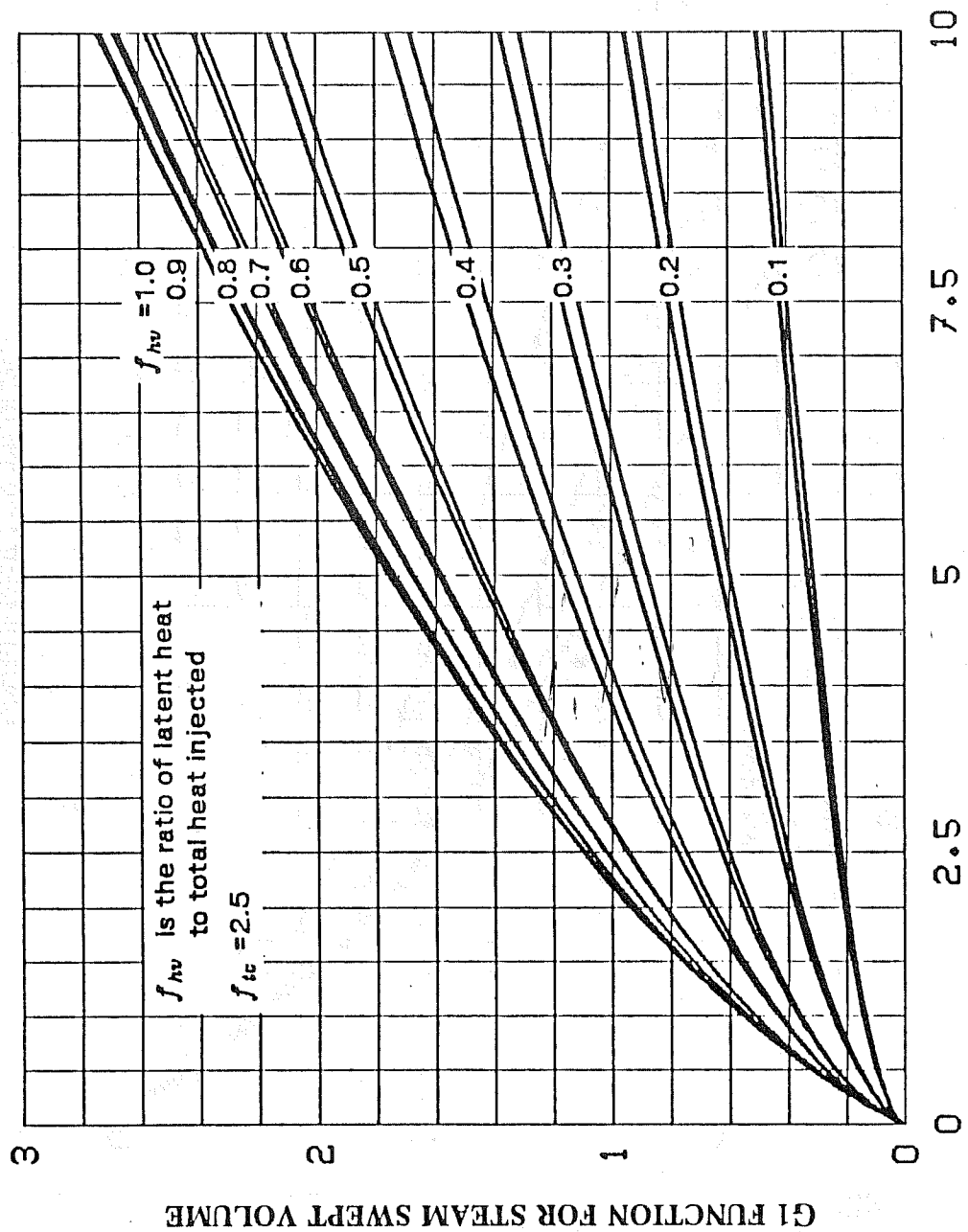

Fig. 11 G1 function for steam swept volume vs dimensionless time

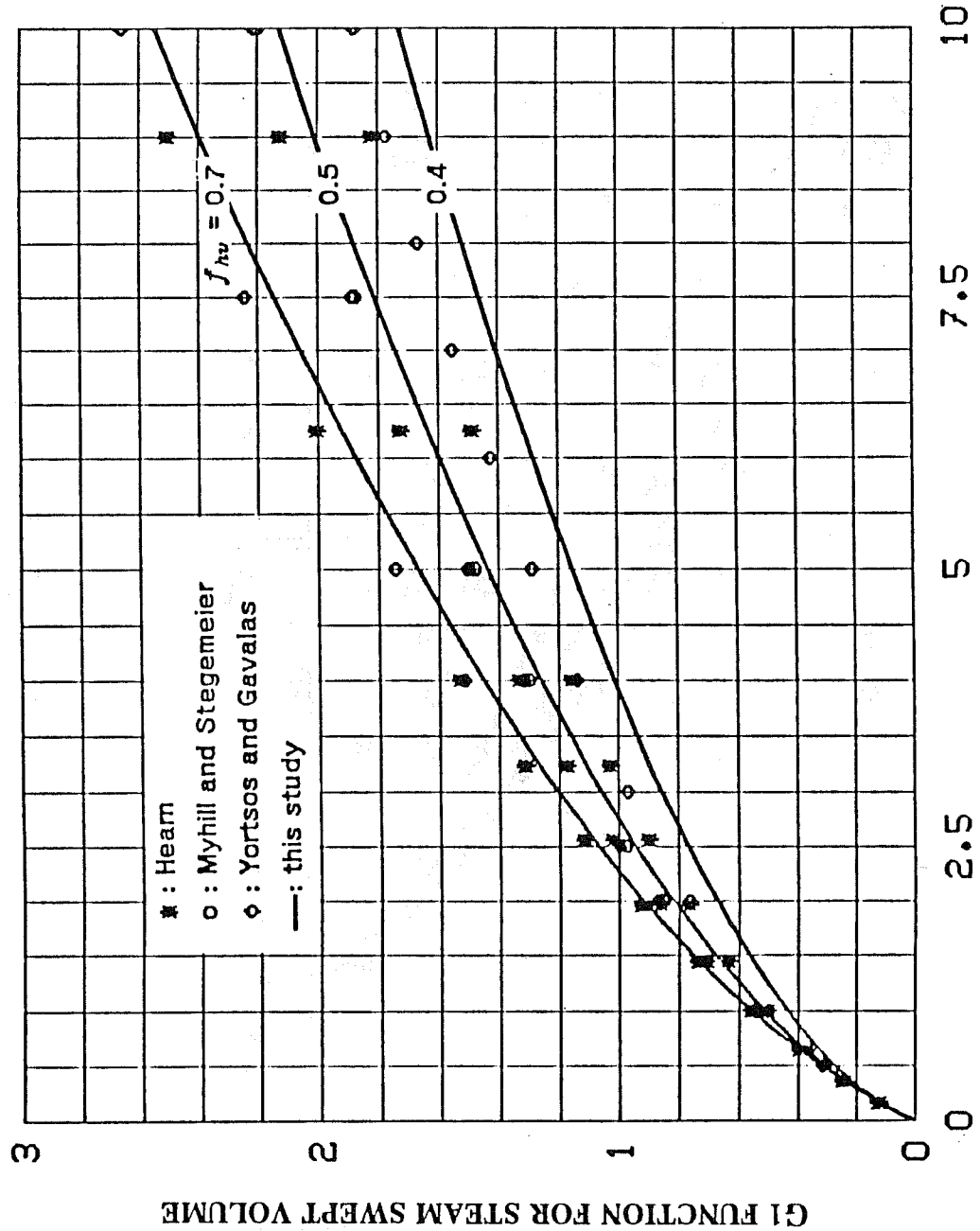

Fig. 12 G1 function for steam swept volume calculated by four methods

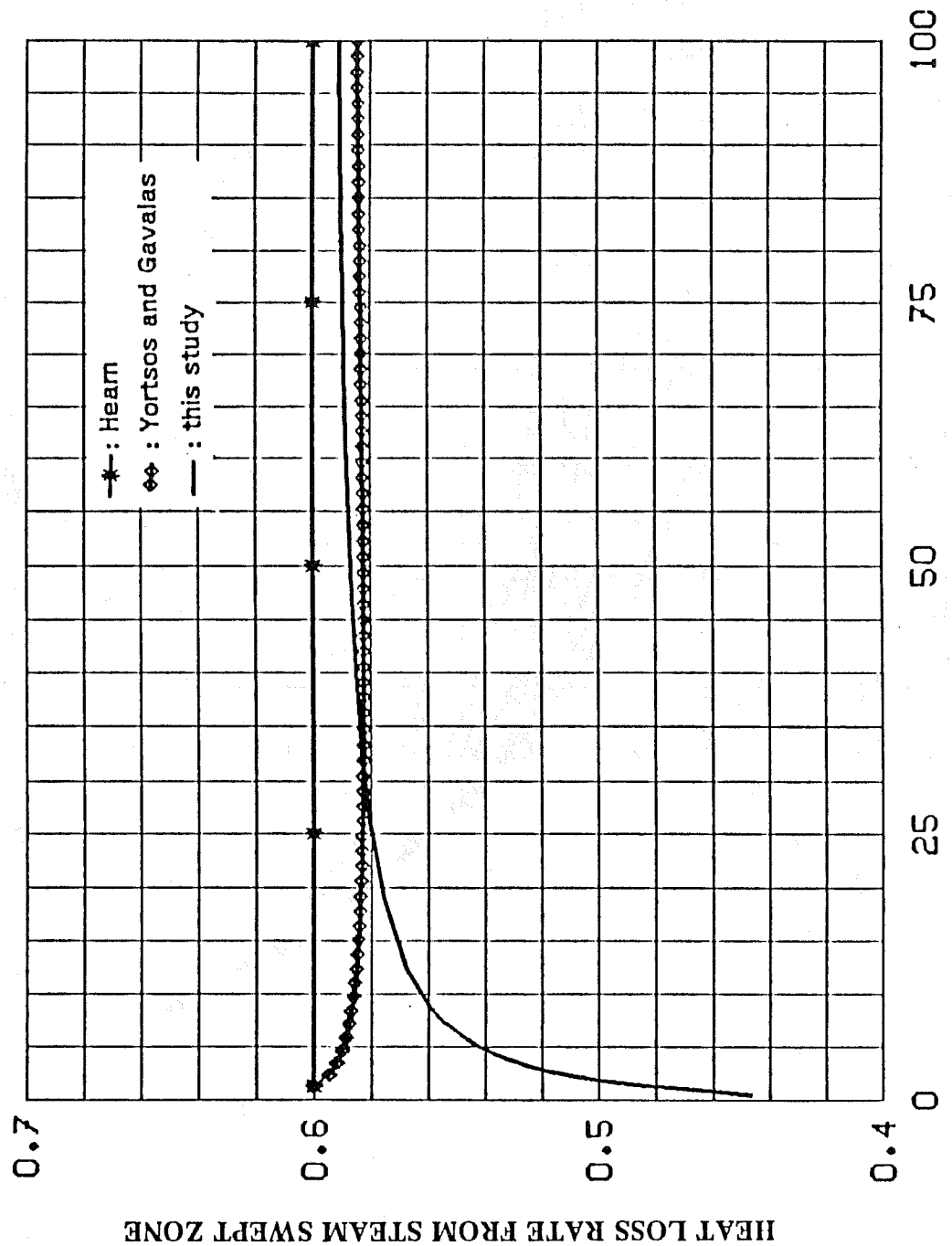

Fig. 13 Comparisons of heat loss rate calculated by Hearn, Yortsos and Galavas methods, and this study

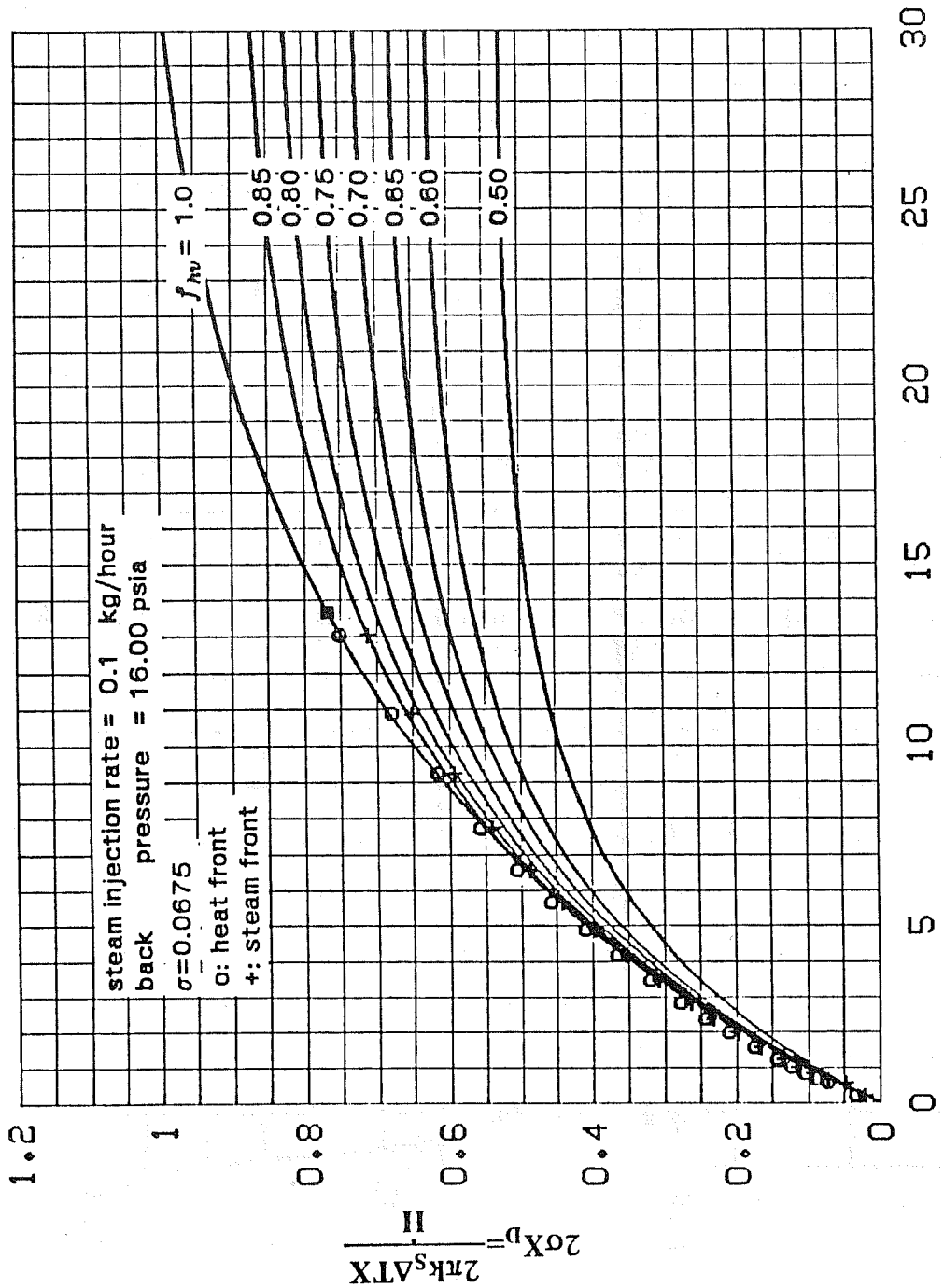

Fig. 14 Comparison between experimental and calculated steam frontal position

3.4 SURFACE VISCOMETER
(Hermann E. Gaub)

3.4.1. THEORY OF OPERATION

The surface viscosity is measured by determining the viscous drag on a rotating disc floating on the surface. This disc is a small (5mm) coverglass. To prevent it from penetrating the water, its surface is coated with covalently bound C18 hydrocarbon chains. On top is a small magnet is glued ($\approx$0.1 mm $\times$ 0.3 mm $\times$ 1 mm height). This glass vial is positioned in the magnetic field of 4 coils by a mount. The vertical position of the disc is adjusted by changing the amount of surfactant solution applied to the vial. Since clean glass is water wetting, the surface shows a slightly concave profile that keeps the hydrophobic disc positioned in the center.

The rotation of the disc is driven by an external magnetic field generated by two pairs of coils. By a driver electronic the direction of the field is rotated in the plane in a similar way, as this is done with stepper motors. The small magnet on the disc feels a torque that is given by

$$T_M = H \times M = H * M * \sin \beta \tag{1}$$

where H is the external magnetic field, M the strength of the magnet, and β the angle between both. For a field rotating with the constant frequency f, the disc will resist with the viscous drag.

$$T_F = a * f * n(f) \tag{2}$$

where a is determined by the geometry of the system and $n(f)$ denominates the possibly frequency dependent viscosity of the whole system. The equilibrium of the torques can be written as

$$n(f) = H * M * \frac{a}{f} * \sin \beta \tag{3}$$

With the given conditions, this equation would in principle allow for the determination of the viscosity by measuring the angle β. Here an alternative method is given that does not require any additional equipment and gives higher accuracy.

For a magnetic torque much higher than the friction torque, β is small. Decreasing the magnetic field with all other parameters constant wil increase β according to

$$\sin \beta \approx \frac{1}{H} \tag{4}$$

At the minimum $H_{\min}$ for which this relation is true, β reaches $\pi/2$. For values of H smaller than $H_{\min}$,β is undefined. Experimentally this means that the disc stops rotating when the magnetic torque becomes too weak to overcome the friction. Ths viscosity is thus given by

$$n = M * \frac{a}{f} * H_{\min} \tag{5}$$

The error with which n is measured is given by

$$\partial n \approx \cos \beta * \partial \beta \tag{6}$$

As $\beta \rightarrow \pi/2$ this error goes to 0. In this case, the accuracy of relative measurements is determined only by the frequency constant and the accuracy of the measurement of H_{min}. A frequency constant of 10^{-8} is easily obtained with a simple quartz oscillator. The magnetic field is measured to at least 4 digits accuracy by either measuring the current through the coils or the voltage applied to the driver electronics.

Up to now we have treated the surface and the bulk-fluid in the trough as a single system and denoted a overall viscosity n to it. For an absolute determination of the surface shear viscosity, it would be necessary to calculate the relative contributions of the bulk and of the surface. It is also necessary to compute the flow profile under the given boundary conditions to determine to detemine the geometry factor a. Both tasks seem to be tough work.

However, by calibrating the measured viscosities with the value of the clean water surface, relative viscosities of different surfactant concentrations or different surfactants can be obtained as long as the bulk viscosities stay constant.

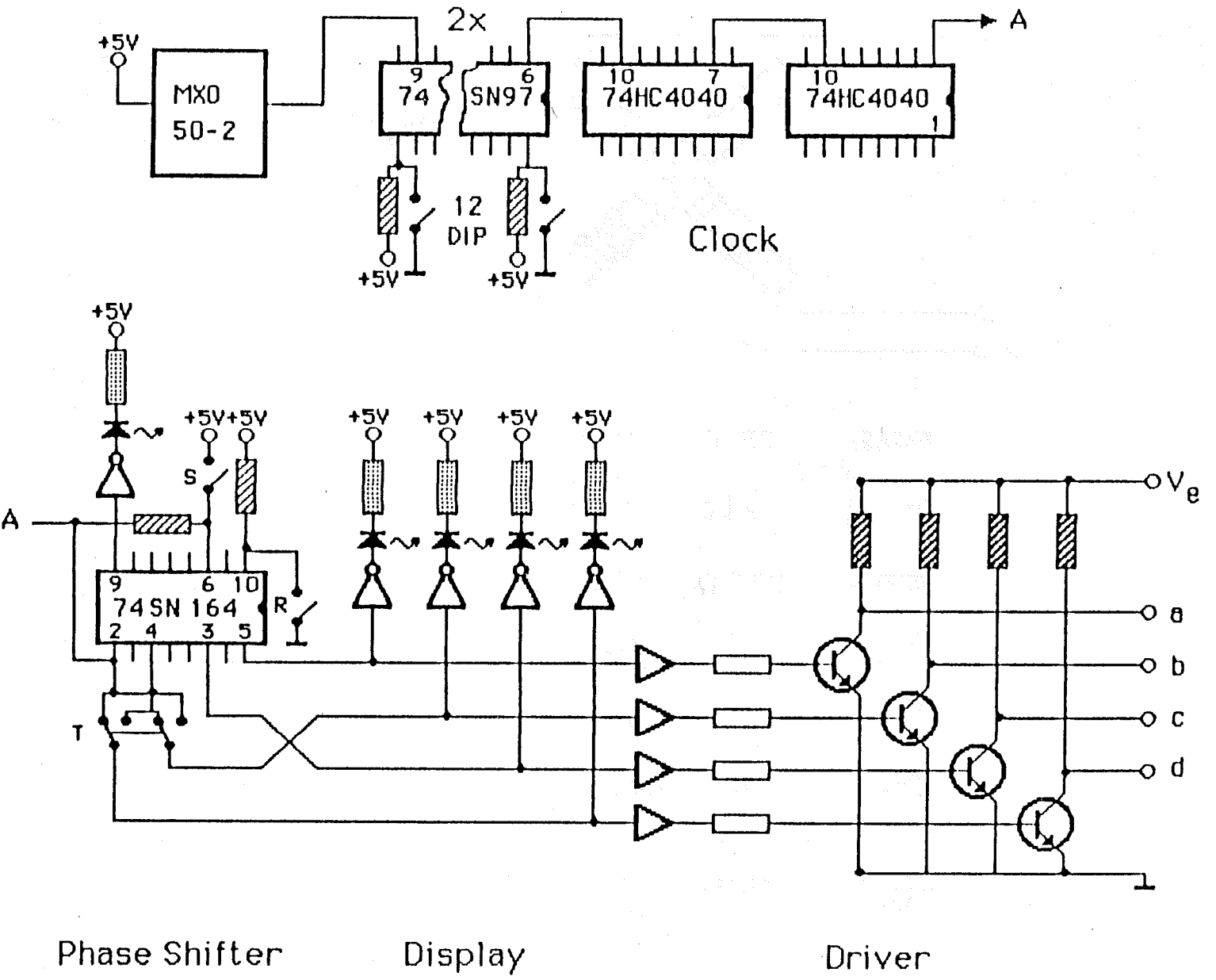

Fig. 1a Driver Electronics for Monolayer Viscosimeter

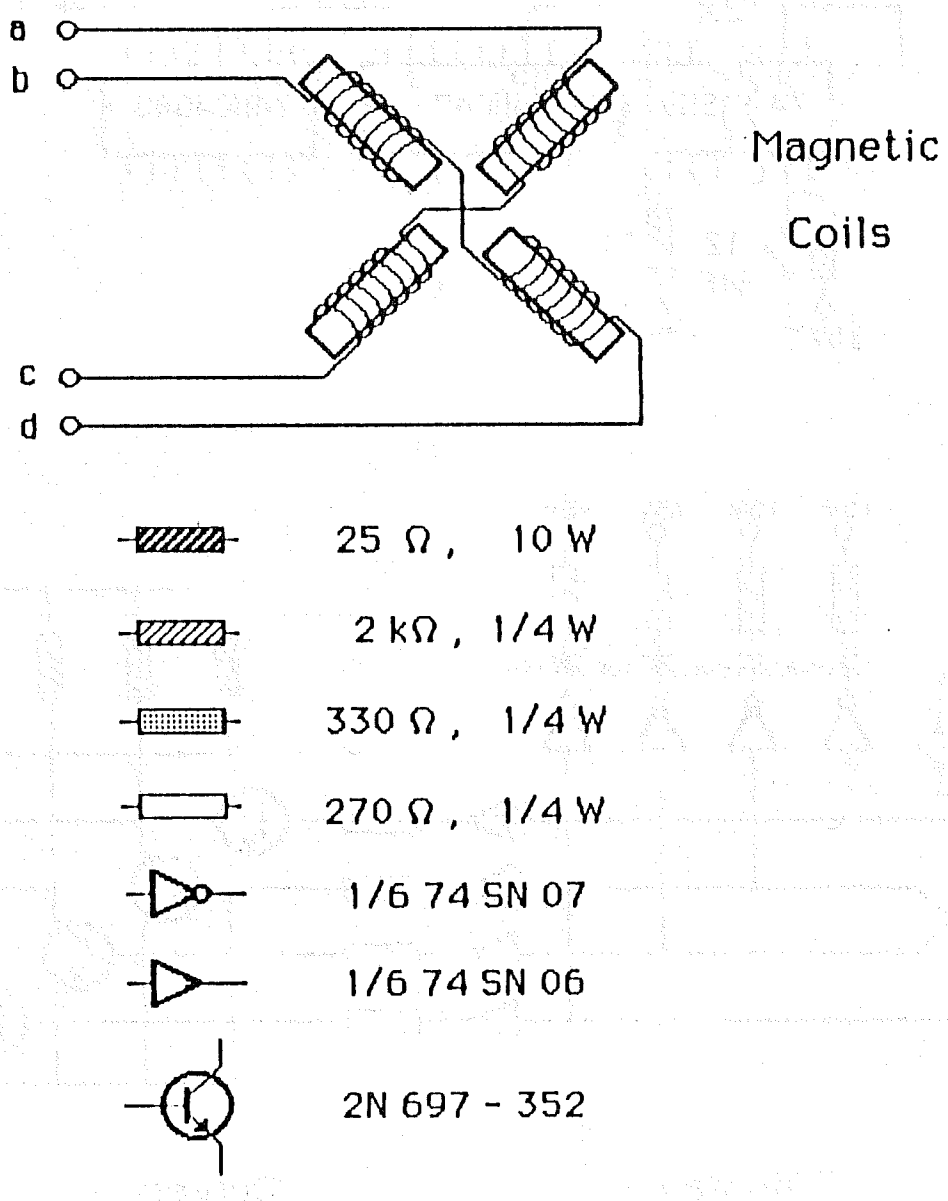

Fig. 1b Driver Electronics for Monolayer Viscosimeter

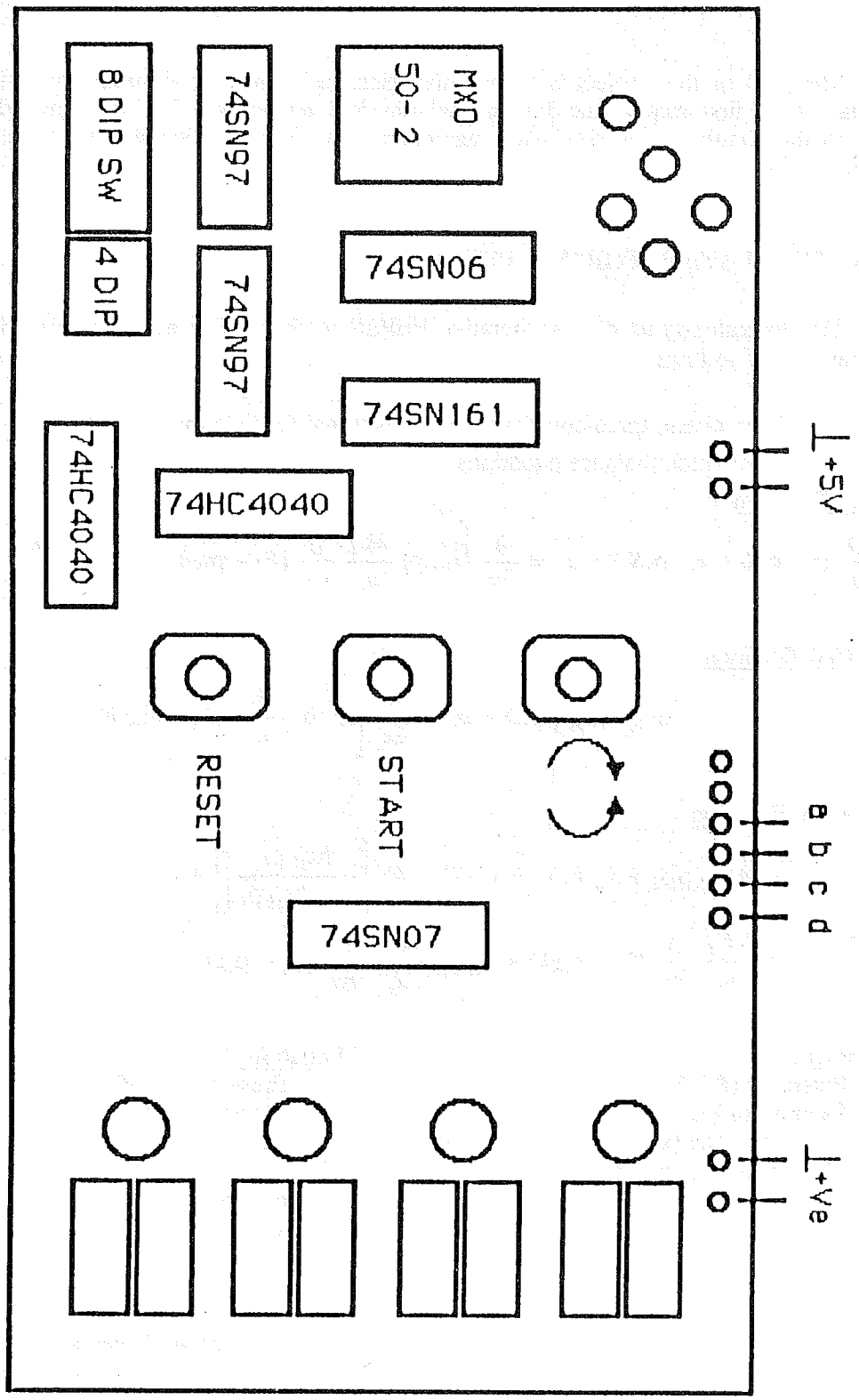

Fig. 1c Driver Electronics for Monolayer Viscosimeter

3.5 SIMULATION OF FOAM FLOW IN POROUS MEDIA
(Bret Beckner)

The goal of this project is to use numerical techniques to simulate form flow in porous media. As a first step a one-dimensional physical model (see Treinen) gave data that were used in the simulator. A reasonable agreement was obtained between numerical and experimental results.

3.5.1. SIMULATION FORMULATION

The formulation used is an iterative IMPES method. The equations describing the flow of foam are as follows:

- Two phase, three-component compositional formulation
- Three mole balance equations:

Water Equation

$$\phi \frac{\partial}{\partial t}\left(x_{wl}\,\rho_l S_l + x_{wv}\,\rho_v S_v\right) + q_w = \frac{\partial}{\partial x}\left[x_{wl}\,\rho_l \frac{kk_{rl}}{u_l}\frac{\partial}{\partial x}\left(P_l - \rho_l g h\right) + x_{wv}\,\rho_v \frac{kk_{rv}}{u_v}\left(P_v - \rho_v g h\right)\right]$$

Gas (N_2) Equation

$$\phi \frac{\partial}{\partial t}\left(x_{gv}\,\rho_v S_v\right) + q_g = \frac{\partial}{\partial x}\left[x_{gv}\,\rho_v \frac{kk_{rv}}{u_v}\left(P_v - \rho_v g h\right)\right]$$

Surfactant Equation

$$\frac{\partial}{\partial t}\left[\phi\left(x_{sl}\,\rho_l S_l + x_{sv}\,\rho_v S_v\right) + C_T\left(1-\phi\right)\left[\frac{b x_{sl}\,\rho_l}{1 + b x_{sl}\,\rho_l}\right]\right] + q_s$$

$$= \frac{\partial}{\partial x}\left[x_{sl}\,\rho_l \frac{kk_{rl}}{u_l}\frac{\partial}{\partial x}\left(P_l - \rho_l g h\right) + x_{sv}\,\rho_v \frac{kk_{rv}}{u_v}\frac{\partial}{\partial x}\left(P_v - \rho_v g h\right)\right]$$

Unknowns

2	Pressures (P_e, P_v)
2	Saturations (S_e, S_v)
5	Mole fractions (x_{wl} , x_{sl} , x_{gv} , x_{wv} , x_{sv})
2	Mole densities (ρ_v , ρ_l)
11	

Equations

1	Pressure Eq. (P_e)
1	Saturation, Eq. (sl)
1	$\Sigma S_j = 1$
2	$\Sigma x_{ij} = 1$
1	cap. pressure
1	x_{sl} equation
2	phase density equation
9	
1	x_{gv} constant if present
1	x_{sv} constant or Gibbs equation
11	

3.5.1.1. Pressure Equation

Multiply water equation by	A
Multiply gas equation by	B
Multiply surfactant equation by	C

Add three equations and find A, B, and C such that saturation at the new time level disappears.

$$x_{wl}\,\rho_l S_l \cdot A + x_{sl}\,\rho_l S_l \cdot C = 0$$

and

$$x_{wv}\,\rho_v S_v \cdot A + x_{gv}\,\rho_v S_v \cdot B + x_{sv}\,\rho_v S_v \cdot C = 0$$

or

$$A(x_{wl}\,\rho_l S_l + x_{wv}\,\rho_v S_v) + B(x_{gv}\,\rho_v S_v) + (x_{sl}\rho_l S_l + x_{sv}\,\rho_v S_v) = 0$$

$$\vdots$$

$$A(x_{wv}\,\rho_v - x_{wl}\,\rho_l) + B(x_{gv}\,\rho_v) + C(x_{Dv}\,\rho_v - x_{ol}\,\rho_l) = 0$$

Use:

$$A = 1$$

$$C = 1$$

$$B = \left[\frac{\rho_l - \rho_v(x_{sv} + x_{wv})}{\rho_v x_{gv}} \right]^{n+1} \quad ;if \quad S_v = 0 \quad B = 0$$

After substitution of A, B, and C, add three component equations to give:

$$F_{\text{press}} = f(P_e^{n+1},\ S_j^n,\ P_e^n,\ \rho_j,\ x_{ij}^n,\ q_i^{n+1})$$

$$i = \text{component},\ j = \text{phase}$$

This equation is solved using Newton's method:

$$[J] \cdot \Delta P^{n+1} = -F_{\text{press}}$$

where $[J]$ is the Jacobian matrix defined as

$$J_{ij} = \frac{\partial F_i}{\partial P_{ej}}$$

(Here i,j are gridblocks.) $\partial F_i/\partial P_j$ has terms like $(\partial \rho_v^{n+1})/(\partial P_e^n + 1)$

Notes

*The simulator uses Peng Robinson equation of state for nitrogen.

*The solution of the Jacobian system gives an approximation of $P_e^{n+1} \rightarrow$ iteration is required.

3.5.1.2. Saturation Equation

We solve the water component equation S_e^{n+1}:

$$S_e^{n+1} = [\Delta T_{we}(\Delta P_e^{v} - \gamma_w \Delta z) + \Delta T_{wv}(\Delta P_v^{v} - \gamma_v \Delta z)] + \frac{Vp}{\Delta t}(S_e x_{wl}\, \rho_l + S_v\, \rho_v x_{wv})^n$$
$$- \frac{V_p}{\Delta t} \frac{[(x_{wv}\, \rho_v)^{v} - q_w^{v})}{\left[(x_{wl}\, \rho_l - x_{wv}\, \rho_v)\right]}$$

3.5.1.3. Surfactant Equation

We solve the surfactant component equation by Newtons method, for x_{se}^{n+1}:

$$F_{ourf} = \Delta T_{se}(\Delta P_e^{v} - \gamma_e \Delta z) + \Delta T_{sv}(\Delta P_v^{v} - \gamma_v \Delta z)$$
$$- \frac{V_p}{\Delta t}\left[(x_{ol}\, \rho_l S_e)^{v} - (x_{sl}\, \rho_l S_l)^n + (x_{ov}\, \rho_v S_v)^{v} - (x_{ov}\, \rho_v S_v)^n\right]$$
$$- \frac{(V_B - V_p)}{\Delta t} \cdot C_t \cdot \left[\left[\frac{bx_{ol}\, \rho_l}{1 + bx_{ol}\rho_l}\right]^{v} - \left[\frac{bx_{ol}\, \rho_l}{1 + bx_{sl}\, \rho_l}\right]^n\right] - q_s^{v} = 0$$

$$(J_{surf}) \cdot \Delta x_{se}^{n+1} = -F_{surf}$$

where

$$(J_{surf}) = \frac{\partial F_{surf}}{\partial x_{sl}}$$

The flow chart of the simulator is presented in Fig. 1.

3.6 LITERATURE REVIEW ON FOAMS IN POROUS MEDIA
(S.S. Marsden)

3.6.1. ABSTRACT

In 1978 a literature search on selective blocking of fluid flow in porous media was done by Professor S.S. Marsden and two of his graduate students, Tom Elson and Kern Guppy. This was presented as SUPRI Report No. TR-3 entitled "Literature Review of the Selective Blockage of Fluids in Thermal Recovery Projects."

Since then a lot of research on foam in porous media has been done on the SUPRI project and a great deal of new information has appeared in the literature. Therefore we believed that a new, up-to-date search should be done on foam alone, one which would be helpful to our students and perhaps of interest to others. This has been based on references which were known to the author and supplemented by those in the MS Research Report of Bret Beckner and the drafts of the PhD dissertations of Syed Mahmood and Fred Wang. However, the interpretation and presentation of the material is the sole responsibility of the author.

The report, presently in the last stages of completion, is a chronological survey showing the development of foam flow, blockage and use in porous media, starting with laboratory studies and eventually getting into field tests and demonstrations. It is arbitrarily divided into five-year time periods ranging from the pioneer work of the 1950's to the most recent results available.

3.7 THERMAL STABILITY OF FLUORESCENT DYES

(Yathrib Al-Riyami)

3.7.1. ABSTRACT

The dyes that we investigated are rhodamine wt and fluorescein. These dyes have been used often in tracer studies in both petroleum and geothermal settings. Rhodamine Wt is more stable than Fluorescein, although both undergo almost instantaneous breakdown at 200°C in the low concentrations (200 ppb - 50 ppm) likely to be encountered in the field. At temperatures of up to 150°C, fluorescein solutions of various low strengths break down to nearly half strength within the first two to four hours, and remain approximately constant thence for up to 20 days. Rhodamine wt shows a similar trend . It breaks down to about 80% strength in the first two to four hours and remains constant up to a month. Fluorescein solutions of very high concentration (5000 ppm) remain stable at about half strength for 24 hours at temperatures as high as 250°C. But even at this higher concentration, we observed the initial breakdown to half strength within the first two to four hours. However, since it is impossible to maintain such high concentrations in the formation, we must conclude that neither of these dyes should be used for quantitative work at temperatures above 150°C.

PROJECT 4: RESERVOIR DEFINITION

This section deals with the techniques of reservoir evaluation using tracers and well tests.

4.1 MATHEMATICAL ANALYSIS OF SINGLE-WELL TRACER TEST

(G.K. Falade and E. Antunez)

A complete report is in progress and will appear as a DOE publication under Contract DOE/SF/11564.

4.1.1. ABSTRACT

The single-well tracer test as a means of evaluating reservoir *in-situ* fluid saturation has attracted much interest in recent years. The hydrodynamics of a single-well tracer test is based on the radial flow of a tracer which can partition in the fluid saturations within the reservoir. At the same time, the tracer is mildly reactive with the mobile phase fluid saturation. The mild, irreversible chemical reaction results in the formation of another tracer species called the secondary tracer. The secondary tracer is different from the parent tracer in its partitioning and chemical reaction characteristics. Typically, the secondary tracer is not reactive with, and has a near-zero partitioning-coefficient with the immobile phase fluid saturation.

To run a test, a chemical tracer is used capable of reacting irreversibly with one of the formation fluids to form a second tracer which is substantially different from the original (primary) tracer in its partitioning characteristic. The irreversible chemical reaction ensures that the formation of the second (secondary) tracer is never reversed. Thus, the retardation which the primary tracer would suffer as it is pushed deep into the reservoir is not annulled when the tracer's flow is reversed for production at the wellbore. The time lag in the arrival times of the primary and secondary tracers provides the means of evaluating *in-situ* fluid saturations.

The hydrodynamics of the above tracer system is described by a Radial-Diffusion-Convection-Reaction (R-D-C-R) type second order differential equation. The use of this equation to analyze single-well tracer test has, in the past, largely been through the application of numerical techniques. Since these techniques may suffer from inaccuracies due to adverse numerical dispersion or the problem of uniqueness arising from fitting many unknown parameters, there is a need to develop an exact analytical solution to the R-D-C-R type differential equation for accurate single-well tracer fast analyses.

R-D-C-R equations have wide applications in many specialized fields of study such as petroleum engineering (Tomich, 1973), hydrology (Sauty, 1980), ecological studies (Saffman, 1962), oceanographic and limnological diffusion studies (Okubo, 1962) to mention a few. In general, R-D-C-R system of differential equations can be written in the form:*

$$\frac{1}{r}\frac{\partial}{\partial r}\left[rD(r)\frac{\partial c}{\partial r}\right] - V(r)\frac{\partial c}{\partial r} - S(c) = \nu\frac{\partial c}{\partial t} \qquad (1)$$

where ν is a constant, $S(c)$ is a source or sink term which can account for such phenomena as chemical reactions, adsorption processes, physical loss or addition of chemicals, etc. $V(r)$ and $D(r)$ are the radius dependent convection velocity and hydrodynamic dispersion function, respectively.

For the simple cases where $V(r)$ and $D(r)$ are constants, and $S(c)$ is either zero or directly proportional to c, a Fickian solution to Eq. (1) is easily obtained (Carslaw and Jaeger, 1959;

*Nomenclature and references at the end of this report.

Skellam, 1951). However, where $D(r)$ is radially distributed, no exact analytical solutions to Eq. (1) has been reported in the literature.

In this study, the single-well chemical tracer test is the preferred option for fluid saturation evaluation largely because of the convenience of operation and also because of the economic consideration of using only one well rather than two. The primary objectives of this work therefore is to model the single-well tracer test analytically and obtain an exact solution to such an analytical model. It is hoped that the exact analytical solution so obtained can be used in subsequent tracer test designs.

Considering a first order reaction in the source term, an average velocity by material balance, and linear partitioning coefficient $k_i = \overline{C}/C$, Eq. (91) can be written in the form

$$\frac{1}{r}\frac{\partial}{\partial r}\left[rD(r)\frac{\partial C_i}{\partial r}\right] - \frac{\alpha}{r}\frac{\partial C_i}{\partial r} + k_r\left[1 + \frac{k_r S_o}{S_w}\right]C_i = \left[1 + \frac{k_i S_o}{S_w}\right]\frac{\partial C_i}{\partial t} \qquad (2)$$

Equation (2) is the basic equation to describe the process of injecting a chemical tracer moving, reacting, adsorbing and dispersing in porous medium. Equation (2) has been reported in the past as impossible to solve analytically for these stages of the single well tracer test: (1) injection, (2) shut in, and (3) production.

In this work an analytical solution for Eq. (2) is presented. The results obtained with the analytical solutions were compared to results from Antunez and Brigham (1984) semi-analytical approach. Both solutions compared well but it was observed that the approximate solutions tend to give a faster moving trailing and leading edges particularly the leading edge. This apparent fast motion at the leading edges may be due to excessive spreading in the forward direction. Since the α term is largely associated with spreading and it derives from the diffusion constant $D(r)$, the diffusion term $D(r)$ must have been underrated in the models that lead to the approximate solution under consideration. This is not surprising in that the approximate model was in fact based on the assumption that $\alpha(\partial^2 C/\partial C^2)$ term is relatively small (Brigham and Smith, 1965).

An important fact about the approximate solution which is of interest is the fact that the point of maximum tracer concentration for both exact and approximate solutions are the same. This may suggest that the approximate solution may still give good test results for single-well tracer tests even when the predicted concentration values are not correctly predicted. This arises because analyses of single-well tracer test data are based on points of maximum concentration rather than the absolution concentration values.

4.1.2. NOMENCLATURE

C = Concentration of primary tracer in water
$\overline{C}$ = Concentration of primary tracer in oil
D = Coefficient of dispersion
K_1 = Partitioning coefficient
k_r = Constant of reaction
r = Radial distance
S_o = Oil saturation
S_w = Water saturation
t = Time
V = Velocity
v = Constant
$\alpha - rv$ = Const.

4.1.3. REFERENCES

Antunez, E.U. and Brigham W.E.: "Semi-Analytic Approach to Analyze Single Well Tracer Tests," TR-44, DOE/SF/11564-7 (1984).

Brigham, W.E. and Smith, D.H., Jr.: "Prediction of Tracer Behavior in 5-Spot Flow," SPE No. 1130, Paper presented at Production Rresearch Symposium, Tulsa (May 3-4, 1965); also 40th Annual SPE Fall Meeting, Denver (October 3-5, 1965).

Carslaw, H.S. and Jaeger, J.C. : Conduction of Heat In Solids, Second Edition, Oxford University Press, Oxford (1959) Sec. 7.

Okubo, A.: "A Review of Theoretical Models of Turbulent Diffusion in the Sea," *J. Oceanographic Society*, Japan, 20th Anniversary Volume (1962) 286-320.

Sáffmann, P.G.: "The Effect of Wind Shear on Horizontal Spread from an Instantaneous Ground Source," *Quart. J. Roy. Meteorol. Soc. 88, (1962), 382-393.*

Sauty, J.P.: "Analysis of Hydrodispersive Transfer in Aquifers," *Water Resources Research 16(1),* (1980), 145-158.

Skellam, J.G.: "Random Dispersal in Theoretical Populations," *Biometrika 38,* (1951) 196-218.

Tomich, J.F., Dalton, R.L., Jr., Deans, H.A., and Shallenberger, L.K.: "Single-Well Tracer Method to Measure Residual Oil Saturation," *J. Pet. Tech.* (Feb. 1973) 211-218.

4.2 IMPROVED ESTIMATION ALGORITHMS FOR AUTOMATED TYPE CURVE ANALYSIS OF WELL TESTS

(Jawahar Barua)

4.2.1. ABSTRACT

The analysis of well test data by automated type-curve match using computers is a subject of great current interest. Although the automated type-curve matching technique is often an improvement over conventional methods there are certain practical problems that occur in its application. Except in the case of a homogeneous reservoir, most reservoir models require the estimation of several parameters. Unless the initial guess is very good, the estimation procedure for many parameters often fails to converge. This limitation could be handled by predetermining some of the parameters and holding them fixed in order to reduce the dimensions of the search space. However, the need for predetermination of some of the parameters often forces the use of straight line methods, and therefore diminishes one of the principal advantages of the automated method which does not otherwise need to be restricted to the recognition of the correct straight lines (in fact, the automated method is not restricted to the recognition of a straight line at all). In addition, a great deal of effort in the form of trial and error and user interaction may be required to get an acceptable match. Even in cases which have only a few parameters, contours of the objective function show that some parameters are inherently ill-defined.

To date most applications have utilized the Gauss method or modifications to it such as the Levenberg-Marquardt algorithm. The Newton method should be better suited to the estimation of ill-defined parameters because it uses a search direction that is aligned in the direction of these parameters. This study investigates the application of the Newton method (and an important modification, the Newton-Greenstadt method) to automated well test analysis. It shows that the added expense of the Newton-Greenstadt method is often justified by the improvement in performance achieved. This improvement in performance is important because it reduces the need for an expert at the computer to guide the estimation process. In many cases, the Newton-Greenstadt procedure converges almost as fast as the Gauss-Marquardt method, yet is more reliable in cases where one (or more importantly, more than one) parameter is ill-defined. Comparisons of the performance of the various different methods on several practical examples show more clearly the reasons why some of the methods perform better than others in specific cases. For a practical problem with given properties, the results of this work should permit the selection of an appropriate method.

4.2.2. INTRODUCTION

Although the use of computer assisted well test interpretation is not new (Earlougher, 1977; Padmanabhan and Woo, 1976; Tsang *et al.*, 1977; Padmanabhan, 1979; McEdwards, 1981; Rosa and Horne, 1983). It has become more popular now with the increasing availability of computing power. Automated well test interpretations are ideal applications for desktop microcomputers, and their use is likely to become widespread.

The advantages of *automated* well test analysis over either type-curve analysis or straight-line analysis techniques have been clearly demonstrated by, among others Barua and Horne, 1984; Barua, *et al.*, 1984; and Guillot and Horne, 1984. The advantages include much higher resolution than type-curve analysis, reduction of the danger of choosing incorrect straight lines and ease in handling of multiple flow rate history. Last , but not least, automated

match frees the analyst from either numerical or procedural errors. This is not an insignificant advantage given the growing complexity of models available and their attendant interpretation procedures.

In the past, one of the difficulties with automated well test interpretation was the evaluation of the reservoir response functions in closed form. Rosa and Horne (1983) showed that by numerical inversion from Laplace space of both function values and gradients, it is possible to fit well test data to the most complicated of mathematical models by the method of least squares and generally do a better job in parameter estimation than is possible with manual methods. A further impetus to this method of approach has been the reliability of the Stehfest (1970) numerical inversion scheme for the inversion of the Laplace transforms.

Despite the advantages of automated match, and the ability to match complex models, there remains a need for improved estimation algorithms. Barua and Horne (1984) showed that as the number of parameters becomes large it is often difficult to get good matches. Also some parameters are inherently ill-defined and prove to be difficult to determine even if the number of parameters is not large (Padmanabhan and Woo, 1976; Rosa and Horne, 1983). A typical case of such a difficulty is where a particular parameter is a function of only a specific range of the data (e.g., wellbore storage in the early data, and reservoir limit in the late data). If the required range of data is missing in the well test measurements (perhaps the test was stopped too early or started too late), then the parameter estimation algorithm may "crash", even though all of the other unknown parameters could easily be determined. This is a major deficiency that is easily avoided by a person performing a visual type curve or semilog analysis. If automated well test procedures are ever to become reliable general purpose reservoir engineering tools, algorithms that are sensitive to these difficulties must be developed.

Many of the applications to date have used the Gauss Method modified by Marquardt's (1963) algorithm. This is also termed the Levenberg, (1967) and Marquardt (1963) algorithm, which has proved both popular and easy to use in least-squares estimation. In view of the difficulties that are sometimes experienced with it, there exists a need for better estimation algorithms. This study was undertaken to try different algorithms in an effort to answer these problems. In the first instance, second order methods based on Newton's method were examined to investigate their performance compared to the first order Gauss method and its close derivatives.

This choice was prompted by the observation that second derivative methods, being second order, should be better than the first derivative methods currently used. In theory, some of the second order methods are less prone to the difficulties of parameter insensitivity, and should be useful in well test applications. Specifically, the Greenstadt (1967) modification to Newton's method should avoid parameter insensitivity by adjusting the eigenvalues of the solution matrix in such a way that the insensitive parameters are not included in the search for the optimum values of the unknown reservoir parameters that are being estimated. At the same time, the functions in use in well-test analysis are peculiar to our discipline and it is not clear whether the desired improvements in performance of the algorithms will be offset by increases in computation required.

Because of the generally complex nature of functions involved in parameter estimation, it is generally impossible to analytically prove the performance of a method on a given problem. Rather, conclusions as to the relative merits of the different estimation algorithms are reached by trying them on the chosen function(s).

Since the performance of any method is affected by the accuracy of the line-search (determination of the size of acceptable step) used, a single program was written to allow the

choice of any of the algorithms considered with the same line-search for all. Thus the performance of the methods can be directly compared.

4.2.3. DESCRIPTION OF THE PROCEDURES

The estimation of reservoir parameters from an observed well response is an *inverse problem* that requires the matching of the observed response to a model that is a function of the unknown parameters. Since all reservoir models give rise to responses that are nonlinear functions of the unknowns, a nonlinear parameter estimation procedure is required. More specifically, many common reservoir models are functions of different parameters over different time ranges (for example, the well bore storage coefficient at early time, the permeability at intermediate time and the drainage volume at later time), and are often difficult problems to solve by nonlinear regression. This section examines the properties of several common nonlinear regression methods in order to investigate which may be most useful in automated well test interpretation. For a broader view of nonlinear parameter estimation methods, see Bard (1974) and Gill, et al. (1983).

The method which is central to all of those considered here is Newton's Method. In general, a nonlinear parameter estimation procedure will minimize the sum of the squares of the differences between the observations and the reservoir model response:

$$E = \sum_{i=1}^{n} \left[y_i - F(\underline{\alpha}, x_i) \right]^2 \tag{1}$$

where (x_i, y_i) are a set of n observations of an independent and dependent variable (typically time and pressure in a well test) and $\underline{\alpha}$ are a set of m unknown reservoir parameters. The reservoir response function F is generally a nonlinear function of the unknowns $\underline{\alpha}$, hence the need for nonlinear regression. The approach used in Newton's Method is to expand the sum of squares of E in a Taylor series about an estimated value E^o obtained at a particular solution $\underline{\alpha}^o$, and to truncate the series after the quadratic terms:

$$E^* = E\Big|_{\underline{\alpha}^o} + \sum_{k=1}^{m} (\alpha_k - \alpha_k^o) \frac{\partial E}{\partial \alpha_k}\Big|_{\underline{\alpha}^o} + \sum_{j=1}^{m}\sum_{k=1}^{m} (\alpha_j - \alpha_j^o)(\alpha_k - \alpha_k^o) \frac{\partial^2 E}{\partial \alpha_j \partial \alpha_k}\Big|_{\underline{\alpha}^o} \tag{2}$$

Here E^* is the *Newton approximation* to the value of E. In order to determine the minimum of E^* with respect to $(\underline{\alpha} - \underline{\alpha}^o)$, the deviations from the first solution, E^* is differentiated with respect to each of $(\alpha_j - \alpha_j^o)$, which shall be called β_j:

$$\frac{\partial E^*}{\partial \beta_j} = \frac{\partial E}{\partial \alpha_j}\Big|_{\underline{\alpha}^o} + \sum_{k=1}^{m} \beta_k \frac{\partial^2 E}{\partial \alpha_j \partial \alpha_k} \quad \text{for } j=1 \text{ to } m \tag{3}$$

At a stationary value, these derivatives will all be zero, hence the m normal equations for $\underline{\beta}$ are

$$\sum_{k=1}^{m} \beta_k \frac{\partial^2 E}{\partial \alpha_j \partial \alpha_k}\Big|_{\underline{\alpha}^o} = -\frac{\partial E}{\partial \alpha_j}\Big|_{\underline{\alpha}^o} \quad \text{for } j=1 \text{ to } m \tag{4}$$

where

$$\left.\frac{\partial E}{\partial \alpha_j}\right|_{\underline{\alpha}^o} = -2\sum_{i=1}^{n}\left[y_i - F(\underline{\alpha}^o, x_i)\right]\left.\frac{\partial F}{\partial \alpha_j}\right|_{\underline{\alpha}^o} \tag{5}$$

and

$$\left.\frac{\partial^2 E}{\partial \alpha_k \partial \alpha_j}\right|_{\underline{\alpha}^o} = -2\sum_{i=1}^{n}\left\{-\frac{\partial F}{\partial \alpha_k}\frac{\partial F}{\partial \alpha_j} + \left[y_i - F(\underline{\alpha}^o, x_i)\right]\frac{\partial^2 F}{\partial \alpha_k \partial \alpha_j}\right\}_{\underline{\alpha}^o} \tag{6}$$

Equation (4) is a set of linear equations in terms of $\underline{\beta}$, which can be written

$$\left[H^o\right]\underline{\beta} = \underline{u} \tag{7}$$

where the symbol H is used in recognition of the fact that the solution matrix is the Hessian matrix of E with elements defined by Eq. (6) and $\underline{u}$ is the gradient of E defined by Eq. (5). Once $\underline{\beta}$ has been found by the solution of Eq. (7), a new set of values of the unknown reservoir parameters can be determined from

$$\alpha_j^1 = \alpha_j^o + \rho\beta_j \qquad \text{for } j=1 \text{ to } m \tag{8}$$

after which the procedure is repeated starting at the new values of $\underline{\alpha}$, until convergence is achieved. Notice that as convergence is approached the value of $\underline{\beta}$ will become small, and the approximation represented by Eq. (2) will become exact. Thus the stationary value of E^* will approach that of E. In Eq. (8), the relaxation parameter ρ is equal to one for the standard Newton's method, but may be greater than or less than one for extrapolation or interpolation of the step. The use of a line search procedure to extend or reduce the step taken in the calculated step direction (given by $\underline{\beta}$) can significantly speed up convergence of many methods, and can also prevent divergence in some cases. The line search procedure requires the selection of an appropriate value of ρ such that the next calculated value of E be as small as possible. The line search procedure used in all of the algorithms described in this paper is described in detail on p.112 of Bard (1974).

The difficulty with Newton's Method, is that the stationary value to which the solution converges may not be a minimum. This is likely to occur if the surface of the function E has saddle points or maxima (which unfortunately is very common in well test analysis applications). In order for the final value of E to be a minimum, the Hessian matrix H must be positive-definite. It is always positive-definite in the close vicinity of the minimum, but may not be at other more distant points. Hence Newton's Method will always converge if the initial guess is close to the solution which gives rise to the minimum sum of squares of the error, but will often diverge if the guess is further away. All of the methods used here and elsewhere to improve on Newton's Method are aimed at guaranteeing that the solution is always moving "downhill", which is usually achieved by modifying H^o in Eq. (7) such that it becomes positive-definite. Four methods will be discussed; Method of Steepest Descent, Gauss Method, Marquardt Method and Greenstadt Method.

The Method of Steepest Descent replaces (H^o) in Eq. (7) by the identity matrix (I) multiplied by a scalar λ. In this way the amount by which α_j is changed in each iteration is directly proportional the gradient of E with respect to that parameter. Thus the solution moves

downhill most steeply in the direction of the parameter which most reduces E - hence the name *steepest descent*. The method of steepest descent is very simple, however it is slow to converge and often requires hundreds of iterations to reach the minimum.

The Gauss Method treats the second derivatives $(\partial^2 F)/(\partial\alpha_k\partial\alpha_j)$ in Eq. (6) as if they were zero, which makes H^o positive-definite. In addition, it is no longer necessary to calculate the second derivatives, which reduces the calculation required and is of considerable advantage when performing the algebra during the development of an application. The Gauss method often converges almost as fast as the Newton method, which can be shown to be the most efficient in convergence as the optimum is approached (Greenstadt, 1967). Note that as the reservoir model F approaches the observations y, the term in Eq. (6) that is ignored in the Gauss method approaches zero even in the Newton method. Hence the Gauss and Newton method become approximately the same provided the model really is an appropriate match to the data. In theory, the Gauss method should always converge to a minimum if one exists, however in practice it may be sensitive to computational instability if the system is ill-conditioned, which corresponds to a near-singular solution matrix H. Unfortunately, well test analysis applications are often prone to this kind of difficulty (Rosa and Horne, 1983).

The Marquardt Method is a modification that can be made to either the Gauss or Newton methods. In the Marquardt (1963) method a constant λ is added to each of the diagonal elements of the solution matrix H. This increases the size of all of the eigenvalues of the modified matrix. In the case of the Newton method, the size of λ can be chosen such that any negative eigenvalues of the original matrix H will become positive, thus ensuring positive-definiteness. In the case of the Gauss method the eigenvalues are already always nonnegative, however the addition of the Marquardt parameter ensures that no zero or almost zero values occur, thus preventing computational singularity of the matrix. As the iteration proceeds the Marquardt parameter λ is reduced by a factor of 10 in each iteration in which the sum of squares E is reduced. Thus after several iterations λ becomes very small, and the method will approach the original method (either Gauss or Newton). Note that the addition of λ on the diagonal of the solution matrix makes the method act in a fashion similar to the method of steepest descent in the early iterations. Thus when far from the optimum the Marquardt method benefits from the rapid reduction of E characteristic of steepest descent, yet converges like Newton's method as the optimum is approached. Thus, in this and earlier studies, the Gauss-Marquardt method was often found to converge faster than Newton's method (which has a quadratic rate of convergence).

The Newton-Greenstadt Method is another way of guaranteeing positive-definiteness of the Hessian matrix H (Greenstadt, 1967). Performing a spectral decomposition of H reveals the presence of zero or negative eigenvalues, the Greenstadt procedure simply takes the absolute value of the eigenvalues before proceeding with the calculation of the inverse. If one of the eigenvalues is zero or close to zero, this means that the model is insensitive to one of the parameters or to one particular combination of the parameters. This can occur easily in well test analysis applications, for example if the model includes a boundary effect while the data do not include sufficiently late time data. Greenstadt has proposed that any zero or almost zero eigenvalue be replaced by an infinity - this is achieved by replacing the reciprocal of the eigenvalue by zero when calculating the inverse. Thus any parameter which does not affect the value of E will remain unchanged. This is exactly what is desired in an automated well test analysis and is the opposite of what will occur with Newton's method in which the least sensitive parameters are changed most.

Thus in theory the Newton-Greenstadt method should provide the best performance for automated well test analysis applications, which require an algorithm that is robust, rapidly convergent, and which is not influenced by parameters that might not affect the reservoir model

response for a particular set of data. This study set out to determine whether the Newton-Greenstadt method has the desired properties in practical application, and whether the additional effort required to calculate the second derivatives and the eigenvalues outweighs any performance advantage.

4.2.4. EVALUATION OF THE DIFFERENT METHODS

Several types of well test were analyzed using the different estimation algorithms, and two representative examples are illustrated here. The first was the field test analyzed by Rosa and Horne (1983). This test data is from a drawdown test in a homogeneous reservoir with storage and skin at the producing well. Several runs were made on this data and these are referred to as Case 1 through Case 5. The second test was a simulated test on a 2-porosity reservoir. Data for the two test cases are listed in Tables 1 and 2.

Figure 1 shows the first test data with a typical match drawn as a solid line. The response without storage is also drawn as a solid line to indicate how much semi-log straight line data would have been available for a manual match.

The parameters normally sought in this type of test are permeability, storage and skin. In addition, as shown by Barua and Horne (1984), the porosity-compressibility product can also be determined with ideal data so an estimate of this parameter was also sought in some of the runs. The experience of Gringarten *et al.* (1979) and Rosa and Horne (1983) has shown that the porosity-compressibility product is an ill-defined parameter that cannot be uniquely determined in a graphical type-curve match or by using the Gauss-Marquardt automated matching procedure. The inclusion of this parameter is therefore a stringent test of the automated methods.

The initial guesses used in the analysis of the first test are listed in Table 3. Those for the second test are listed in Table 4.

4.2.4.1. Storage and Skin, Case 1

Figure 2 shows the convergence obtained with four different estimation techniques. The Newton-Greenstadt method can be applied in two ways, in one variation negative eigenvalues are replaced by their absolute values, in the other variation all eigenvalues less than a given number are replaced by a large number. For simplicity in nomenclature we will refer to these as method (a) and method (b) respectively. Method (b) was implemented by replacing all eigenvalues smaller than 0.00001 by 5 (all negative eigenvalues would fall into this category).

The three standard parameters (k, s, C) were to be determined. Figure 2 shows that the Newton method converges fastest of all and much faster than Gauss-Marquardt. It would seem that the second order information available in the Newton method can lead to a dramatic increase in performance but, as will be shown later, this is not always true. We also see that the (b) variation of Newton-Greenstadt is nearly as good as Newton's method itself.

Figure 3 shows the variation of the eigenvalues during the iterative process of Newton's method. We see that in the early stages one of the eigenvalues is a small negative number. This illustrates one of the problems with Newton's method mentioned earlier: it works by determining where the slope of the objective function is zero and this may be either at a maximum or a minimum. So Newton's method may not necessarily proceed towards the minimum

as is desired for parameter estimation. The presence of negative eigenvalues indicates that the search vector is pointed towards the maximum in the direction of the corresponding eigenvectors.

In this case the two positive eigenvalues indicate progress toward the minimum in two directions while the negative eigenvalue shows that at the same time progress is being made towards the maximum in the third direction. So in effect we are minimizing in two directions while maximizing in the third. The (a) variation of the Newton-Greenstadt method corrects this kind of problem by changing the sign of the negative eigenvalues and in effect *turns around* the search so that it is facing downhill in all directions.

Figure 3 shows that in spite of this negative eigenvalue Newton's method still can go on, in this particular case, and find the true minimum of the objective function. This can be explained by noting that the magnitude of an eigenvalue indicates how much the objective function is changed by a move along the corresponding eigenvector. Thus a large eigenvalue means that the function changes by a large amount in the direction of its eigenvector. To use this reasoning we note that even though the smallest eigenvalue is negative, its magnitude is very small. So even though the algorithm is trying to maximize in this direction, the harm done is not much because the function value does not increase by much in this direction. Since it is at the same time minimizing in the other two directions Newton's method progresses towards the global minimum and eventually the small eigenvalue changes sign and becomes positive from the third iteration onward and then minimization occurs in all three directions.

By this reasoning we expect that when the eigenvalue is both negative and large in magnitude Newton's method will run into trouble, and we will show later that this turns out to be true.

Figure 4 shows the eigenvalues for the (a) variation of Newton-Greenstadt, prior to applying Greenstadt's modification. We see that although it has simply turned around one of the eigenvalues, this has affected the entire search process and we end up converging only after 12 iterations compared to 6 iterations for Newton's method. In the (b) variation we are in affect stopping or nearly stopping any movement in the direction of the negative eigenvalue and this converges in just 7 iterations as shown in Fig 2.

The eigenvalues for the Gauss method are always positive although they may often have very small magnitude. Fig. 5 shows the eigenvalues for the Gauss method prior to applying Marquardt's modification.

4.2.4.2. Storage and Skin, Case 2

Using the same initial guesses for k, s and C as in case 1, ϕc_t was also sought as an unknown this time. Figure 6 shows that the Gauss-Marquardt method is seriously affected by the addition of this new, ill-conditioned parameter. While the performance of all the second order methods has remained nearly the same, the Gauss-Marquardt method is converging only very slowly.

This is the kind of behavior that prompted this study; it is not uncommon in particularly complicated models for the Gauss-Marquardt method to spend scores of iterations seemingly aimlessly searching for the minimum. This was handled in previous studies (Barua and Horne, 1984; Barua *et al.*, 1984) by first doing a manual semi-log analysis to find k and s. By then holding these two fixed, the dimensions of the problem were reduced by two and convergence

could be obtained. However, the manual choice of a straight line lost one of the most important benefits of automated type curve match, i.e., the freedom from the danger of choosing the wrong straight line(s).

Figure 7 shows the eigenvalues for the Gauss method prior to Marquardt's modification. This shows that while we had just one small eigenvalue in Case 1, we now have two. The ratio of the maximum and minimum eigenvalues at the solution is commonly used as a measure of how ill-defined a problem is. The ratio in Fig. 7 of 37449 is not very much larger than the ratio of 16137 in Fig. 5. Yet the performance is so much poorer in this case that it leads us to believe that the presence of more than one very small eigenvalue has a greater debilitating effect than the magnitude of the eigenvalue ratio. This observation is confirmed later in the two-porosity reservoir example.

4.2.4.3. Storage and Skin, Case 3

While the previous two cases have shown that second-order methods converge much faster than the Gauss-Marquardt method, this is not always true. In fact we found that if the Gauss-Marquardt method converges it quite often does so faster than any second-order method.

Figure 8 shows the results of estimating k, s and C with a different set of initial guesses that were quite far from the solution (see Table 3). Thus the objective function starts at a much higher value than previously. We see in this figure that Gauss-Marquardt has converged much faster than any other method. Also Newton's method fails after 6 iterations.

Figure 9 shows the eigenvalues for Newton's method and we see that the same problem observed earlier, maximization in one direction, occurs here too, except that this time the negative eigenvalue is large in magnitude. Thus the function value is increasing by a large amount in that particular direction. In spite of that, the method was able to achieve an overall reduction in the objective function over the first 6 iterations, but after that point it could not find any step-length along the calculated step vector which would reduce the objective function further.

Figure 9 also shows why Marquardt's modification is not very beneficial for Newton's method. To make all eigenvalues positive by the Marquardt method we would need to add a very large constant, a constant that in this case would be several orders of magnitude larger than is normal in the Gauss-Marquardt method. Since a large Marquardt parameter restricts the size of the step, very poor progress would result from this. We have tried and confirmed this observation.

Figure 10 shows the eigenvalues for the Newton-Greenstadt (a) prior to modification. In this run, from the second iteration onward all the eigenvalues were positive so the method reduced to Newton's method thereafter. So it is intriguing that in spite of the fact that we are using second order information without any compromises at all the convergence is still not as good as that for the Gauss-Marquardt method.

Figure 11 explains why the convergence is so poor. Newton's method assumes that the objective function can be described by a locally quadratic model function. If this is so then a Newton step of unity (the calculated step vector multiplied by unity) takes us to the best local minimum. Therefore Newton's method is at its most efficient and converges quadratically only when the step length is unity. On the other hand we see in this Fig. 11 that except for one occurrence nowhere else has the step length of unity been chosen. Thus even though we have used second-order information, it was inadequate to describe the function exactly, and hence

the expected rate of convergence did not materialize. It is generally true that a quadratic model will not be able to exactly define the local behavior of the objective function in well test analysis. Therefore in general we cannot expect quadratic convergence from Newton's method.

4.2.4.4. Storage and Skin, Case 4.

This time we used the same initial guesses as in Case 3, only ϕc_t was also sought as an unknown. However its initial guess was left exactly at the true value. Figure 12 shows the convergence for the different methods and we see again the effects noted in Case 2. The Gauss-Marquardt method is badly affected by the introduction of the fourth parameter. Second order methods are less affected and we see the Newton-Greenstadt method (b) performs almost the same as the case where there were only three parameters. This reinforces the observations made earlier: while second order methods do not necessarily converge faster, they are more useful as the problem becomes more ill-defined.

Apart from the inconvenience of having to program second partial derivatives one factor often cited against the use of second order methods is the higher cost of their evaluation. However this difference is not very great, for this example the Newton-Greenstadt method (b) took 3.5 CPU seconds on a VAX 11/750 while Gauss-Marquardt method took 3.3 seconds. Taking into account the different number of iterations involved and time spent in disk input/output, it could be approximately stated that the second-order methods take less than twice the amount of computation per iteration required for first order methods. Since both times are quite small, and given the widespread availability of computing power, the relative costs of the methods may be insignificant compared to the desirability of getting the best results. So even though second-order methods may be slower in general, in situations where they are more likely to succeed they ought to be used.

Since the Newton-Greenstadt (b) modification has successfully turned an otherwise fragile method into a more robust one we wondered if it cannot do the same thing for the Gauss-Marquardt method. Figure 13 shows the result of such an attempt. In this case, any eigenvalue less than 0.001 was set to 5 before the Marquardt modification was made to the remaining eigenvalues. We see that this modification has not had a great effect. It is also not easy to determine the appropriate minimum eigenvalue to use in this case. Too small a cutoff leaves the problem unchanged, while too large a cutoff may affect more than one value, and more important may continue to have an effect even near the solution. By contrast the choice of 0.00001 as a cutoff for the second-order method was made relatively easily since it is only desired to affect negative eigenvalues and eigenvalues so small that they have virtually no effect on the function.

4.2.4.5. Two-Porosity Case

Two-porosity well tests are of considerable interest given their complexity in manual interpretation. Figure 14 shows the simulated well test. Note that there are only a few data points and also a small amount of *noise* was introduced by truncating all pressure values to integers. Table 2 lists the test data, and Table 4 lists the initial guesses used in the estimation process.

Figure 15 shows the convergence for 5 parameters (k, s, C, ω and λ). We see that even though there are more parameters than before, still the Gauss-Marquardt method has converged fastest. Newton's method has failed after 1 iteration while the Newton-Greenstadt (b) is second best.

Figure 16 shows the eigenvalues for the Gauss-Marquardt method. We see here that only one eigenvalue is small. This reinforces our earlier observation and allows us to enhance it further. We can see that a larger number of parameters does not necessarily mean difficulties for the Gauss-Marquardt method. A high eigenvalue ratio has less of an effect than the number of small eigenvalues. In general, one small eigenvalue can be adequately handled by the Gauss-Marquardt method.

Figure 17 shows the convergence with a sixth unknown (ϕc_t). Here again the Newton-Greenstadt (b) is unaffected by the introduction of an additional ill-defined parameter, while Gauss-Marquardt is, as expected, greatly affected. The eigenvalues shown in Fig. 18 confirm the presence of two very small eigenvalues now.

4.2.4.6. Storage and Skin, Case 5

One of the objectives of this study was to devise algorithms that would work even if some parameters were included that had not affected the reservoir response. This was checked by again analyzing the storage and skin test with the same initial guesses as case 1, but fitting it this time with the two-porosity model.

Figure 19 shows that both Newton and Gauss-Marquardt remain unaffected and converge in almost exactly the same manner as when fitting the data with the homogeneous reservoir model.

Figure 20 shows the eigenvalues for the Gauss-Marquardt method and we see that there is still only one small eigenvalue, hence the rapid convergence. This result leads us to conclude that the convergence will be more affected by how ill-defined are the model and the desired parameters, rather than by whether the effect related to a particular parameter has showed up in the well test.

4.2.5. CONCLUSIONS

A comparison of several different estimation algorithms was made. The objective was to find methods that would work in the cases where the popular Gauss-Marquardt method fails.

From the experimental results it can be concluded that when there is just one small eigenvalue of the approximate Hessian matrix then the Gauss-Marquardt method works best of all. Its performance is unaffected by an increase in the number of parameters provided no additional small eigenvalues are generated.

The most reliable second-order method is the Newton-Greenstadt method where small and negative eigenvalues are replaced by large positive numbers. Although its convergence is not very rapid, it has the great advantage that it is unaffected by an increase in the number of small eigenvalues which causes serious problems for the Gauss-Marquardt method. It should also be noted that the Gauss-Marquardt is more likely to have difficulty with noisy data because the second derivative terms that have been neglected contain the residuals $(y - F)$ as

multipliers. If these neglected terms are not small, the approximate Hessian will not necessarily approach the actual Hessian of E, even at the optimum. In such cases, the Newton-Greenstadt variant (b) will again be the preferred alternative.

The absence of the effect of a given parameter in the reservoir response does not cause the problem to become more ill-defined. The estimation is instead affected by how ill-defined the mathematical model is.

The use of second-order methods will not increase the computation effort per iteration by more than a factor of two or so. Even then the computation times are relatively modest. Given the vital importance of determining reservoir parameters from well tests any increase in computational effort is not likely to be a significant factor.

In summary, in cases where the Gauss-Marquardt method works then it usually has the fastest rate of convergence in well test analysis problems. In cases where more than one parameter is ill-defined, the Gauss-Marquardt method is likely to have difficulty in convergence. In such cases, the Newton-Greenstadt method described here as variant (b) is the best alternative.

By demonstrating a way to improve the robustness of the parameter estimation algorithms, this study represents a forward step in moving automated type-curve matching closer to automatic type-curve matching. Considering the widespread availability of computers in today's oil industry, any method that allows for easier and more accurate analysis will be a powerful tool.

4.2.5.1. Programming Considerations

As a tip for those who wish to implement second-order methods we would like to mention how we programmed the very complicated second partial derivatives. Any expression can be written as A/B or A*B, after which the chain-rule can be applied to obtain its derivatives. Then each of the terms A and B can again be written as $A1/B1$ or $A1*B1$ and the process repeated. This can go on until A and B are no longer expressions but functions (e.g., Bessel functions) or simple expressions which can be differentiated explicitly. Using this kind of approach, no partial derivative is written out explicitly, rather a step-by-step differentiation process is written. The required partial derivatives are obtained by differentiating simple expressions at the lowest level, and passing these results to the generic differentiation rules which evaluate the final answer. In this way the algorithm absorbs most of the tedious algebra. This has proven to be a compact and manageable way to handle this problem. For 6 parameters, 6 first partial derivatives and 21 second partial derivatives are needed. Evaluating even one of these second partial derivatives explicitly can prove to be a daunting and error-prone task, so this aspect of the implementation can prove to be major hurdle. The generic *differentiation rules* approach is useful in overcoming this hurdle.

As an aid to others wishing to try these techniques, Table 5 presents an example output for the estimation of Case 1 using Newton-Greenstadt variant (b). The Hessian matrices and eigenvalues are shown to demonstrate the operation of the iteration as proceeds.

4.2.6. NOMENCLATURE

E - Sum of squares of errors (objective function)
E^* - Approximation to E
F - Reservoir model function
H - Hessian matrix
I - Identify matrix
n - Number of data
m - Number of unknown parameters
$\underline{u}$ - Gradient vector
x - Dependent variable (observed)
y - Independent variable (observed)

$\underline{\alpha}$ - Vector of unknowns
$\underline{\beta}$ - Step vector
λ - Multiplying factor
ρ - Line search parameter

4.2.7. REFERENCES

1. Bard, Y.: "Nonlinear Parameter Estimation," Academic Press, Inc., Ltd., New York, 1974.

2. Barua, J. and Horne, R.N.: "Computerized Analysis of Thermal Recovery Well Test Data", paper SPE 12745, presented at the 1984 California Regional Meeting, Long Beach (April 11-13, 1984).

3. Barua, J., Kucuk, F. and Gomez-Angulo, J.: "Application of Computers in the Analysis of Well Tests from Fractured Reservoirs," paper SPE 13662, presented at the 59th Annual Technical Conference and Exhibition, Society of Petroleum Engineers of AIME, Houston (September 1984).

4. Earlougher, R.C., Jr.: "Advances in Well Test Analysis", *SPE Monograph 5*, Chapter 12, (1977).

5. Gill, P.E., Murray, W., and Wright, M.H.: "Practical Optimization," Academic Press, New York (1983).

6. Greenstadt, J.L.: "On the Relative Efficiencies of Gradient Methods", *Mathematics of Computation 21*, (1967) 360-367.

7. Gringarten, A.C., Bourdet, D.P., Landel, P.A. and Kniazeff, V.J.: "A Comparison Between Different Skin and Wellbore Storage Type-Curves for Early-Time Transient Analysis," paper SPE 8205, presented at the 54th Annual Technical Conference and Exhibition, Las Vegas (September 23-26, 1979), 23-26.

8. Guillot, A.Y. and Horne, R.N.: "Using Simultaneous Flow Rate and Pressure Measurements to Improve Analysis of Well Tests", paper SPE 12958 presented at the 1984 European Petroleum Conference, London, England (October 25-28, 1984).

9. Levenberg, K.: "A Method for the Solution of Certain Problems in Least Squares," *Quart. Appl. Math. 2,* (1944) 164-168.

10. McEdwards, D.G.: "Multiwell Variable-Rate Well Test Analysis, *SPEJ 21* (1981) 444-446; also *Transactions 271.*

11. Marquardt, D.W.: "An Algorithm for Least-Squares Estimation of Nonlinear Parameters", *J. Soc. Indust. App. Math. 11,* No. 2. (June 1963).

12. Padmanabhan, L.: "Welltest - A Program for Computer-Aided Analysis of Pressure Transients Data from Well Tests", paper SPE 8391, presented at the 54th Annual Fall Meeting of the Society of Petroleum Engineers of AIME, Las Vegas, (September 23-26, 1979).

13. Padmanabhan, L., and P.T. Woo: "A New Approach to Parameter Estimation in Well Testing", Proceeding of the Fourth SPE Symposium on Reservoir Simulation, paper SPE 5741, Los Angeles (February 1976).

14. Rosa, A.J. and Horne, R.N.: "Automated Type-Curve Matching in Well Test Analysis Using Laplace Space Determination of Parameter Gradients", paper SPE 12131, presented at the 58th Annual Technical Conference and Exhibition, Society of Petroleum Engineers of AIME, San Francisco (October 5-8, 1983).

15. Stehfest, H.: "Algorithm 368, Numerical Inversion of Laplace Transforms", D-5, *Communications of ACM 13* No. 1 (January 1970) 49.

16. Tsang, C.F., McEdwards, D.G., Narasimhan, T.N. and Witherspoon, P.A.: "Variable Flow Well Test Analysis by a Computer Assisted Matching Procedure, paper SPE 6547, 47th Annual California Regional Meeting of the Society of Petroleum Engineers of AIME, held in Bakersfield (April 13-15, 1977).

Table 1. Data for Storage and skin test

Formation thickness	69.0	ft
Oil viscosity	.9	cp
Wellbore radius	2.75	in
Oil production rate	333.95	Rbbl

Pressure - Time data

Deltat, hrs	Deltap, psi
.0167	26.
.033	53.
.05	78.
.1	148.
.15	210.
.2	267.
.3	369.
.4	454.
.5	519.
.6	572.
.8	654.
1.	719.
1.5	804.
2.	849.
2.5	859.
3.	864.
3.5	869.
4.	874.
4.5	877.
5.	882.
6.	887.
7.	893.
8.	897.
10.	905.
12.	911.

Table 2. Data for double-porosity test

Formation thickness	12.0	ft
Oil viscosity	.3	cp
Wellbore radius	3.48	in
Oil production rate	1245.0	Rbbl

Pressure - Time data

Deltat, hrs	Deltap, psi
0.01	46
0.02	74
0.03	91
0.04	102
0.06	113
0.08	119
0.10	121
0.3	126
0.5	127
0.7	128
1.	129
4.	136
7.	139
10.	140
15.	142
19.	144
24.	145

Table 3. Initial guesses used for Storage and skin test

	Permeability	skin	storage	Porosity*compr-essibility
	Darcy		bbl/psi	1/psi
Case 1	.01	7	.001	*
Case 2	.01	7	.001	.1613d-6
Case 3	.001	1	.000558	*
Case 4	.001	1	.000558	.2613d-6
	Inequality bounds for each parameter			
Minimum	.0	.0	.0	.1d-8
Maximum	1.	30.	2.6	.1d-4
	Best fit values for each parameter			
	.0155	14.9	.0085	.2613d-6

Table 4. Initial guesses used for Double porosity test

	Perm.	skin	storage	Porosity*compr-essibility	Omega	Lambda
	Darcy		bbl/psi	1/psi		
5-parm.	.152	-1.1	.001	*	.36	.8d-8
6-parm.	.152	-1.1	.001	.1d-6	.36	.8d-8
	Guesses used for storage and skin, case 5					
Case 5	.01	7	.001	*	.0	.1
	Inequality bounds for double-porosity test					
Minimum	.0	-30	.0	.1d-8	.001	.1d-10
Maximum	1.	30	.6	.1d-4	.5	.1d-4
	Inequality bounds for Storage & skin, case 5					
Minimum	.0	0	0	.1d-8	0	0
Maximum	1.	30	.6	.1d-4	1	1
	True values of parameters for double porosity test					
	.452	4.1	.0085	.1d-6	.16	2.8d-8

Table 5. Sample output for Newton-Greenstadt (b)
Storage & skin case 1
(note all internal calculations in Darcy units)
(maximum step length is MAX(1.98,distance to nearest bound))
(eigen values refer to inverse scaled decomposition of Bard)

```
INITIAL GUESSES
Permeability, md=    10.0000
Skin=                 7.00000
Storage, bbl/psi=    1.00000e-03
Objective func=    6431.58  Atm**2

****ITERATION #  1
-----------------------------------
UNSCALED HESSIAN
    0.15723e+10      -0.18554e+07        413.75
   -0.18554e+07        674.42          -0.34670
     413.75          -0.34670          0.62953e-03
-----------------------------------
CORRELATION MATRIX
     1.0000          -1.0245           0.41574
    -1.0245           1.0000          -0.53200
     0.41574         -0.53200           1.0000
-----------------------------------
unscaled gradient
   -0.18843e+07        1555.1          -1.6979
scaled gradient
    -47.505            59.000          -67.670
-----------------------------------
Old eigen values
    -0.32856e-01       0.67645           2.3564
New eigen values
     5.0000            0.67645           2.3564
-----------------------------------
Step vector v
     0.24179e-03      -0.68348           2179.4
-----------------------------------
ENTERING LINE-SEARCH ALGORITHM
Max. step length=    1.98000
Step length tried    0.99000   Objective func.    3122.64
Step length tried    1.3767    Objective func.    2519.33
     k (darcy)           s              C (cm**3/atm)
    1.03329e-02       6.05906            6337.4

****ITERATION #  2
-----------------------------------
UNSCALED HESSIAN
     0.82383e+09      -0.69000e+06        142.00
    -0.69000e+06        567.14          -0.13291
     142.00          -0.13291          0.13140e-03
-----------------------------------
CORRELATION MATRIX
     1.0000          -1.0186           0.43403
    -1.0186           1.0000          -0.48607
     0.43403         -0.48607           1.0000
-----------------------------------
unscaled gradient
     49437.            42.984          -0.54100
scaled gradient
     1.7224            1.0016          -47.195
-----------------------------------
Old eigen values
    -0.12365e-01       0.68270           2.3297
New eigen values

     5.0000            0.68270           2.3297
-----------------------------------
Step vector v
    -0.55233e-03       0.48014           5284.3
-----------------------------------
ENTERING LINE-SEARCH ALGORITHM
Max. step length=    1.98000
Step length tried    1.98000   Objective func.    418.648
Step length tried    1.58635   Objective func.    489.668
     k (darcy)           s              C (cm**3/atm)
    9.45668e-03       6.02873            13593.2

****ITERATION #  3
-----------------------------------
UNSCALED HESSIAN
     0.11985e+10      -0.80089e+06         69.745
    -0.80089e+06        548.89          -0.53915e-01
      69.745          -0.53915e-01       0.34748e-04
-----------------------------------
CORRELATION MATRIX
     1.0000          -1.0037           0.34181
    -1.0037           1.0000          -0.39332
     0.34181         -0.39332           1.0000
-----------------------------------
unscaled gradient
    -0.67431e+06        421.90          -0.13963
scaled gradient
    -16.589             10.141          -23.689
-----------------------------------
Old eigen values
    -0.51969e-02       0.78074           2.2245
New eigen values
     5.0000            0.78074           2.2245
-----------------------------------
Step vector v
     0.12727e-03      -0.24019           3393.6
-----------------------------------
ENTERING LINE-SEARCH ALGORITHM
Max. step length=    1.98000
Step length tried    0.99000   Objective func.    39.3582
Step length tried    1.17019   Objective func.    28.6691
     k (darcy)           s              C (cm**3/atm)
    9.68561e-03       6.63966            17564.3

****ITERATION #  4
-----------------------------------
UNSCALED HESSIAN
     0.93477e+09      -0.68576e+06         39.488
    -0.68576e+06        503.58          -0.31535e-01
     39.488          -0.31535e-01       0.17629e-04
-----------------------------------
CORRELATION MATRIX
     1.0000          -0.99958           0.38786
    -0.99958           1.0000          -0.33564
     0.38786         -0.33564           1.0000
-----------------------------------
unscaled gradient
     3562.6          -0.91778          -0.28703e-01
scaled gradient
     0.11652         -0.48898e-01       -4.9448
-----------------------------------
Old eigen values
     0.65997e-04       0.82429           2.1756
New eigen values
     0.65997e-04       0.82429           2.1756
-----------------------------------
Step vector v
     0.19293e-01        26.633           6719.8
-----------------------------------
ENTERING LINE-SEARCH ALGORITHM
Max. step length=    0.072873
Step length tried    0.072873  Objective func.    52.1867
Step length tried    0.293328  Objective func.    5.26865
     k (darcy)           s              C (cm**3/atm)
    1.52648e-02       14.3518            19242.0

****ITERATION #  5
-----------------------------------
UNSCALED HESSIAN
     0.36929e+09      -0.26822e+06         22.314
    -0.26822e+06        194.98          -0.16979e-01
     22.314          -0.16979e-01       0.15199e-04
-----------------------------------
CORRELATION MATRIX
     1.0000          -0.99979           0.29784
    -0.99979           1.0000          -0.31197
     0.29784         -0.31197           1.0000
-----------------------------------
unscaled gradient
     33495.            -23.726          -0.56125e-02
scaled gradient
     1.7430            -1.6995          -1.4396
-----------------------------------
Old eigen values
     0.18265e-03       0.83902           2.1681
New eigen values
     0.18265e-03       0.83902           2.1681
-----------------------------------
Step vector v
    -0.33253e-02       -4.4281           3844.49
-----------------------------------
ENTERING LINE-SEARCH ALGORITHM
Max. step length=    1.98000
Step length tried    0.990000  Objective func.    2.58818
Step length tried    0.694147  Objective func.    2.16415
     k (darcy)           s              C (cm**3/atm)
    1.29565e-02       11.278            19453.4

****ITERATION #  6
-----------------------------------
UNSCALED HESSIAN
     0.61828e+09      -0.37339e+06         26.118
    -0.37339e+06        269.23          -0.19959e-01
     26.118          -0.19959e-01       0.14568e-04
-----------------------------------
CORRELATION MATRIX
     1.0000          -0.99959           0.38849
    -0.99959           1.0000          -0.31878
     0.38849         -0.31878           1.0000
-----------------------------------
unscaled gradient
     7738.34           -0.71163          -0.15624e-02
scaled gradient
     0.33838e-01       -0.43378e-01       -4.4936
-----------------------------------
Old eigen values
     0.22771e-03       0.83652           2.1643
New eigen values
     0.22771e-03       0.83652           2.1643
-----------------------------------
Step vector v
     0.17281e-02        2.4238           3387.82
-----------------------------------
ENTERING LINE-SEARCH ALGORITHM
Max. step length=    1.98000
Step length tried    0.990000  Objective func.    1.69788
     k (darcy)           s              C (cm**3/atm)
    1.46673e-02       13.6776            19788.9

****ITERATION #  7
-----------------------------------
UNSCALED HESSIAN
     0.48574e+09      -0.29117e+06         22.726
    -0.29117e+06        289.88          -0.17171e-01
     22.726          -0.17171e-01       0.14245e-04
-----------------------------------
CORRELATION MATRIX
     1.0000          -0.99969           0.29893
    -0.99969           1.0000          -0.31464
     0.29893         -0.31464           1.0000
-----------------------------------
unscaled gradient
     3893.0            -2.2919          0.43655e-03
scaled gradient
     0.16355           -0.15860          0.11867
-----------------------------------
Old eigen values
     0.17373e-03       0.83810           2.1617
New eigen values
     0.17373e-03       0.83810           2.1617
-----------------------------------
Step vector v
     0.63442e-03       0.75760           3389.89
-----------------------------------
ENTERING LINE-SEARCH ALGORITHM
Max. step length=    1.98000
Step length tried    1.98000   Objective func.    1.66274
Step length tried    1.32271   Objective func.    1.66153
     k (darcy)           s              C (cm**3/atm)
    1.53742e-02       14.6798            19820.7
(the algoritm made one more trial iteration but did not accept it
 so it has been edited out for brevity)

 Permeability, md=    15.3742
 Skin=                14.6798
 Storage, bbl/psi=    0.48126e-03
```

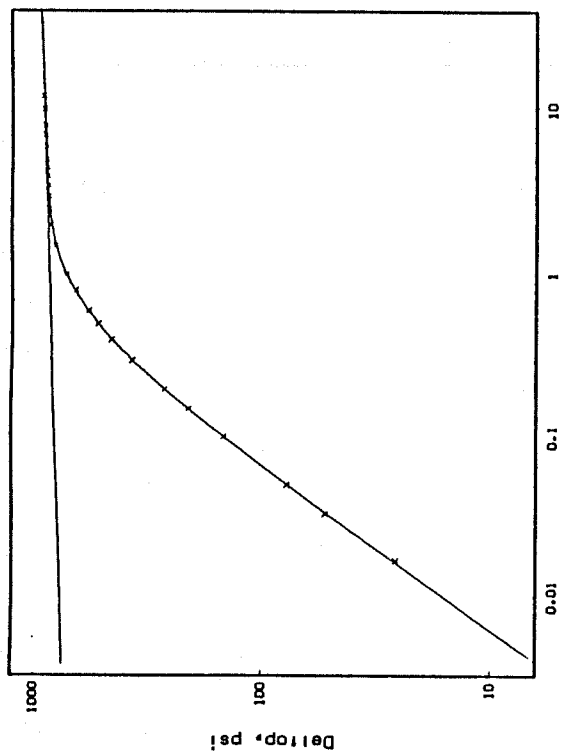

Fig. 1—First test data—homogeneous reservoir.

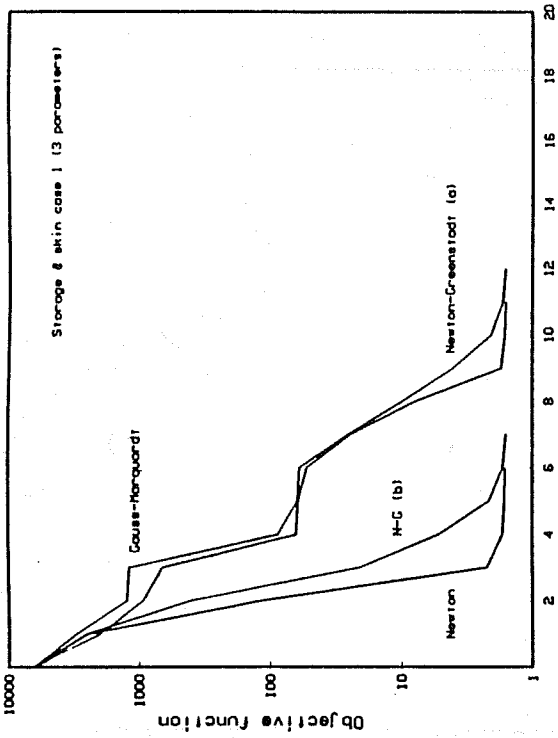

Fig. 2—Case 1—convergence.

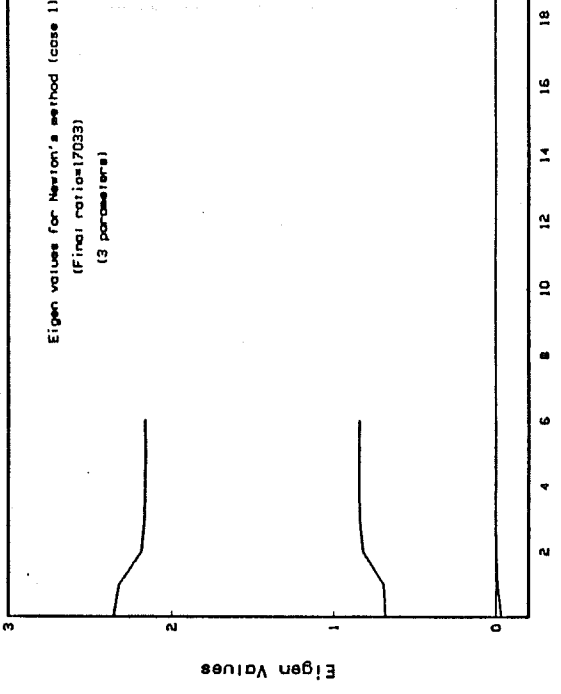

Fig. 3—Case 1—eigenvalues for Newton's method.

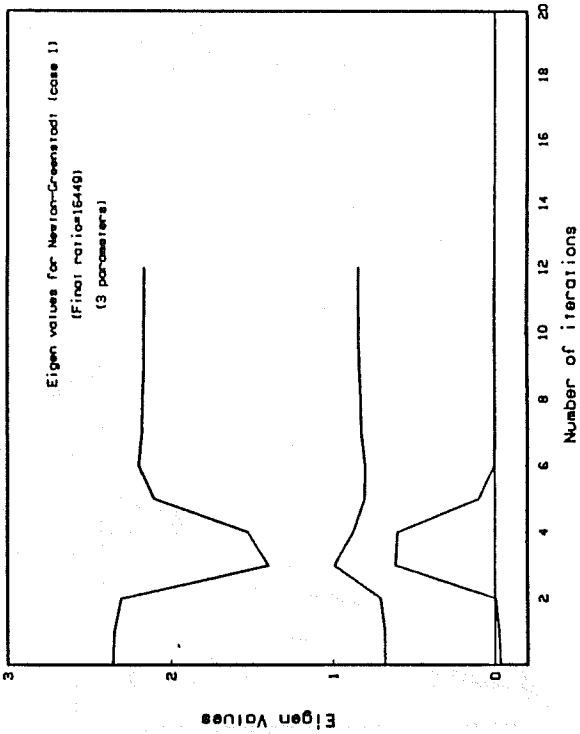

Fig. 4—Case 1—eigenvalues for Newton-Greenstadt method (a).

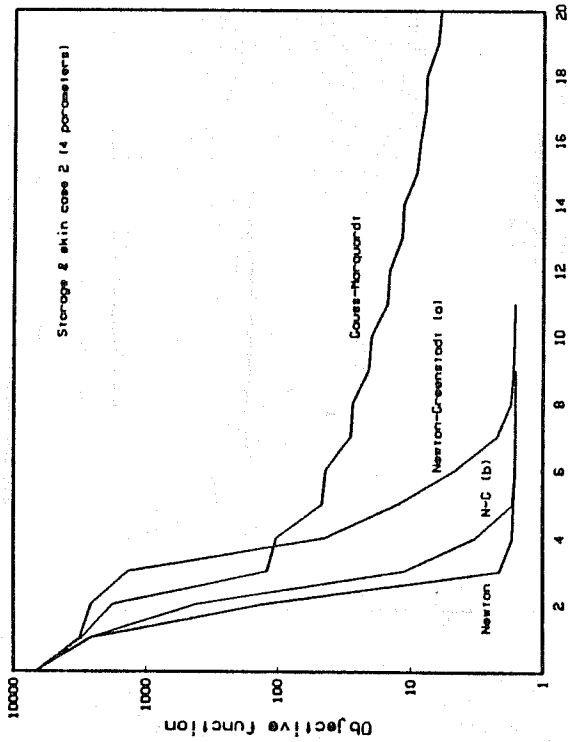

Fig. 6—Case 2—convergence.

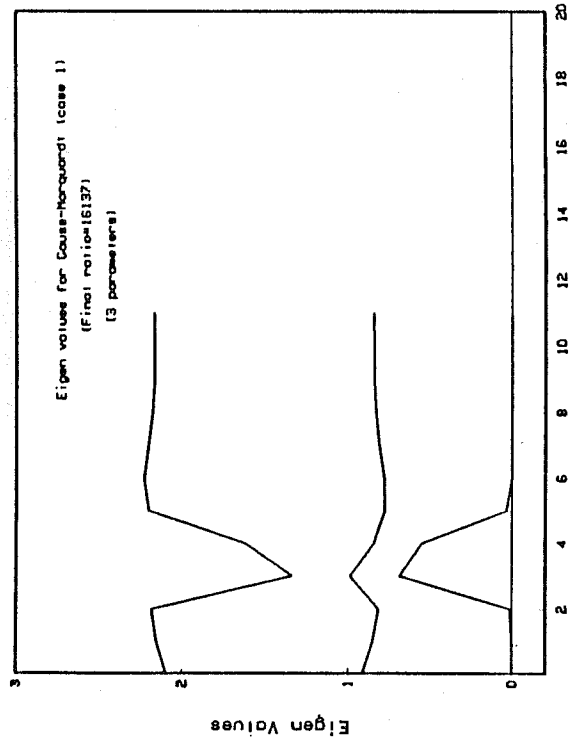

Fig. 5—Case 1—eigenvalues for Gauss-Marquardt method.

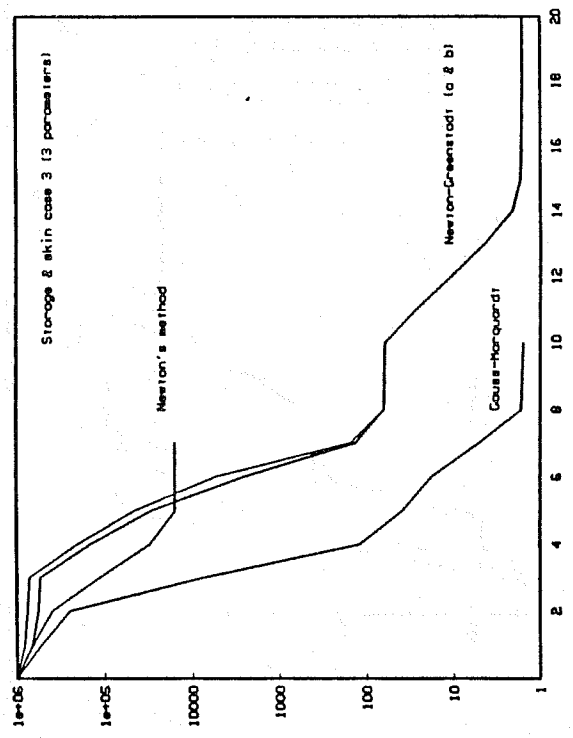

Fig. 8—Case 3—convergence.

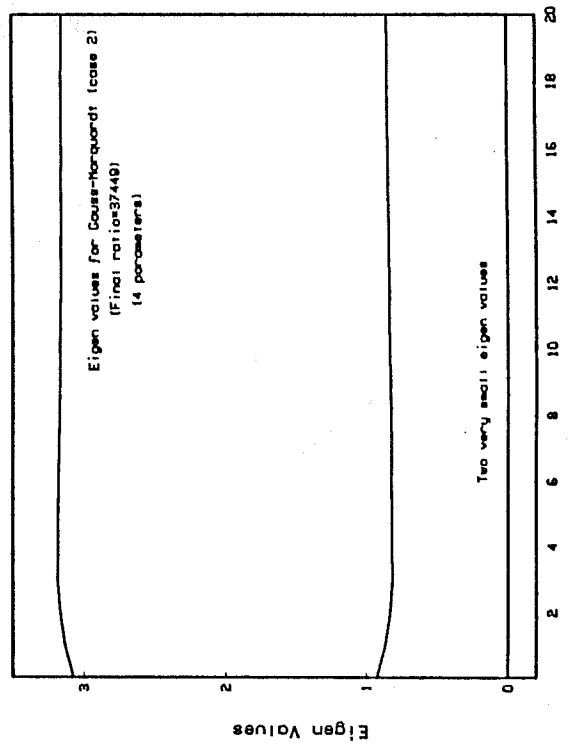

Fig. 7—Case 2—eigenvalues for Gauss-Marquardt method.

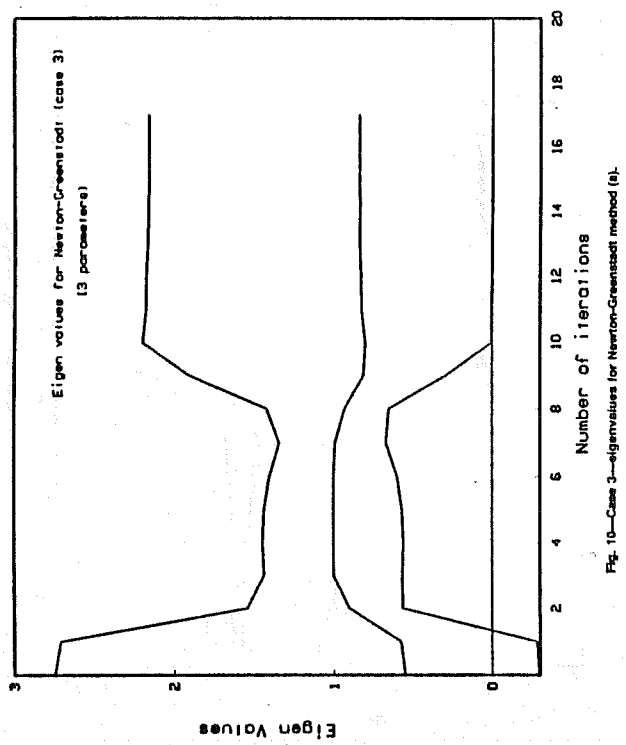

Fig. 10—Case 3—eigenvalues for Newton-Greenstadt method (a).

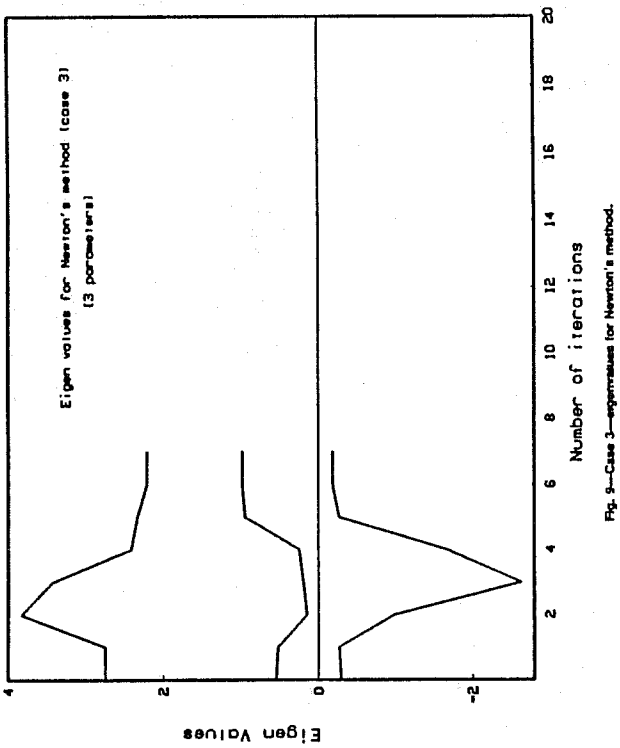

Fig. 9—Case 3—eigenvalues for Newton's method.

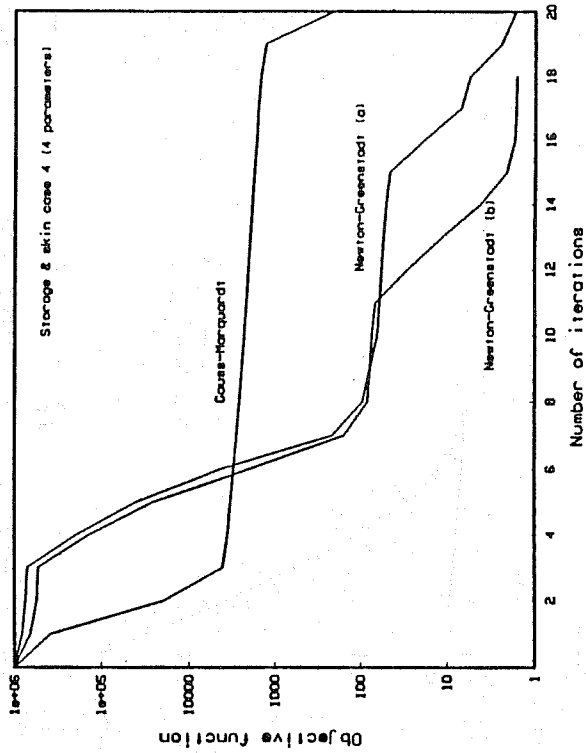

Fig. 12—Case 4—convergence.

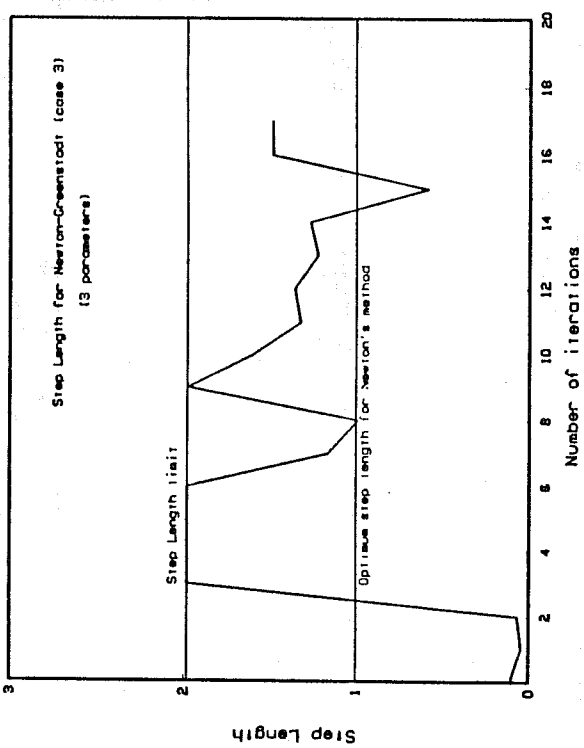

Fig. 11—Case 3—step length for Newton-Greenstadt method (a).

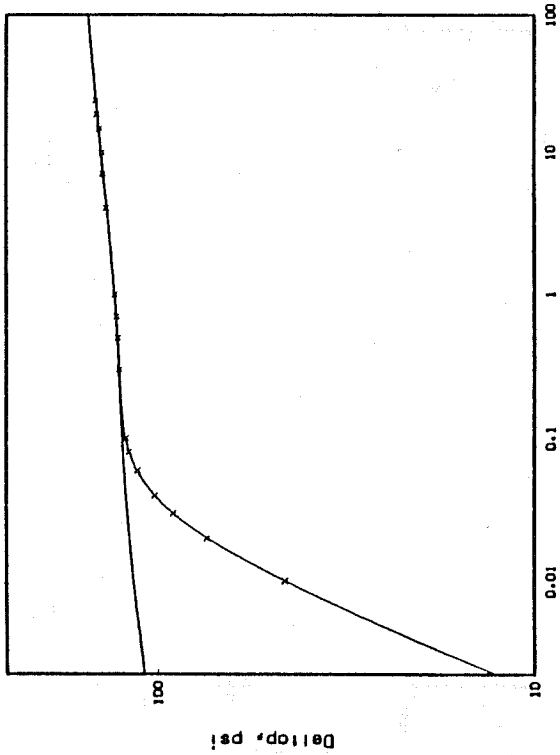

Fig. 14—Second test data—two-porosity reservoir.

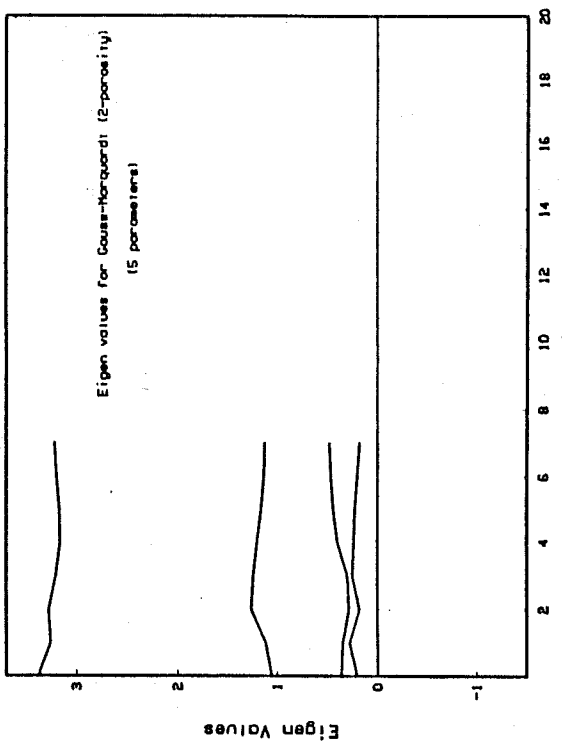

Fig. 16—Two-porosity case—eigenvalues for Gauss-Marquardt (five parameters).

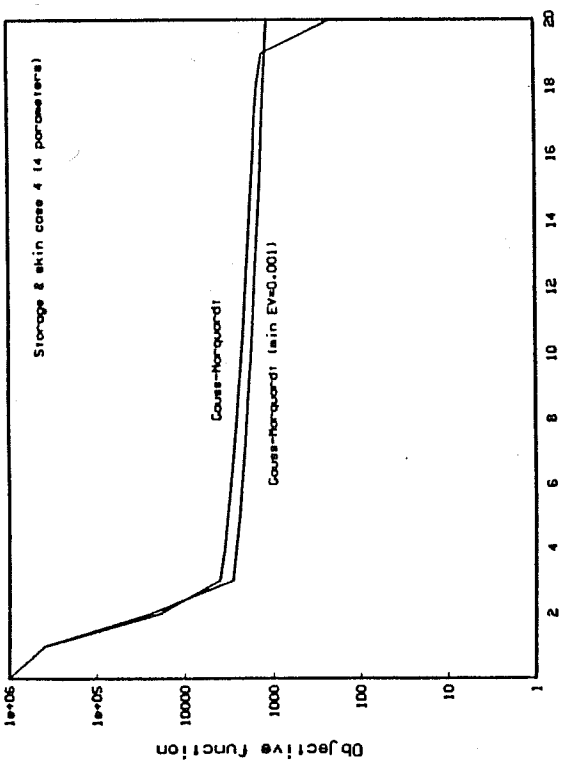

Fig. 13—Case 4—convergence of Greenstadt-modified Gauss-Marquardt method.

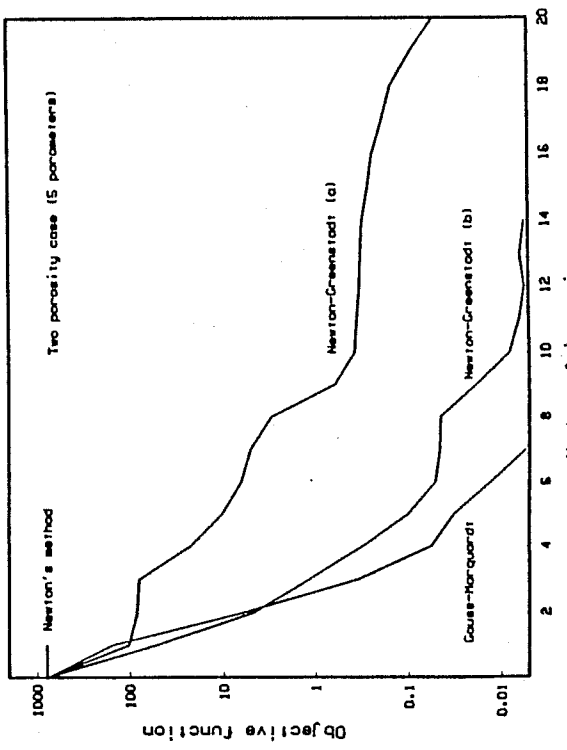

Fig. 15—Two-porosity case—convergence (five parameters).

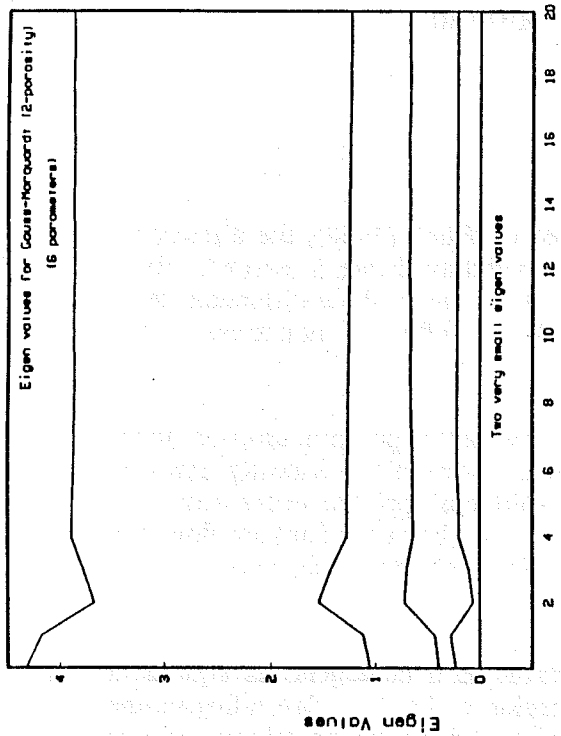

Fig. 18—Two-porosity case—eigenvalues for Gauss-Marquardt (six parameters).

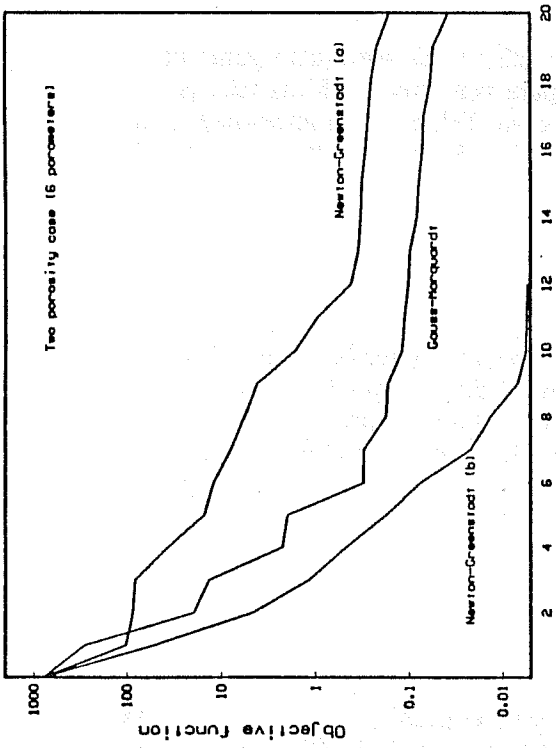

Fig. 17—Two-porosity case—convergence (six parameters).

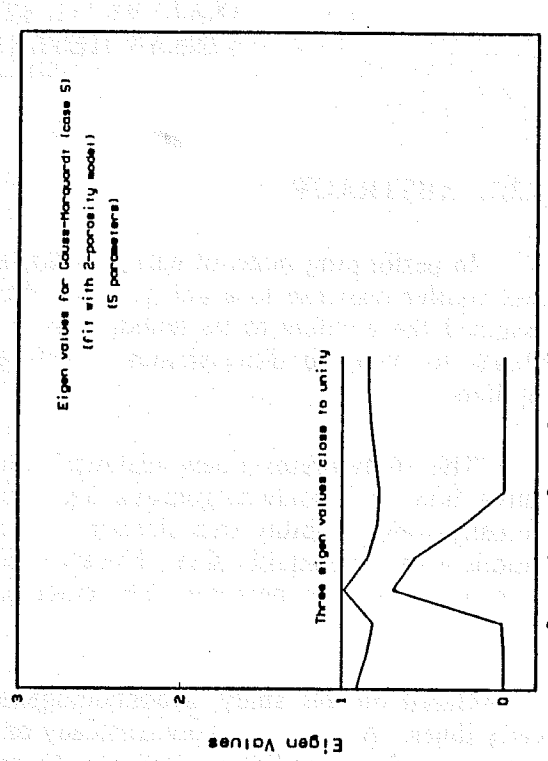

Fig. 20—Case 5—eigenvalues for Gauss-Marquardt method.

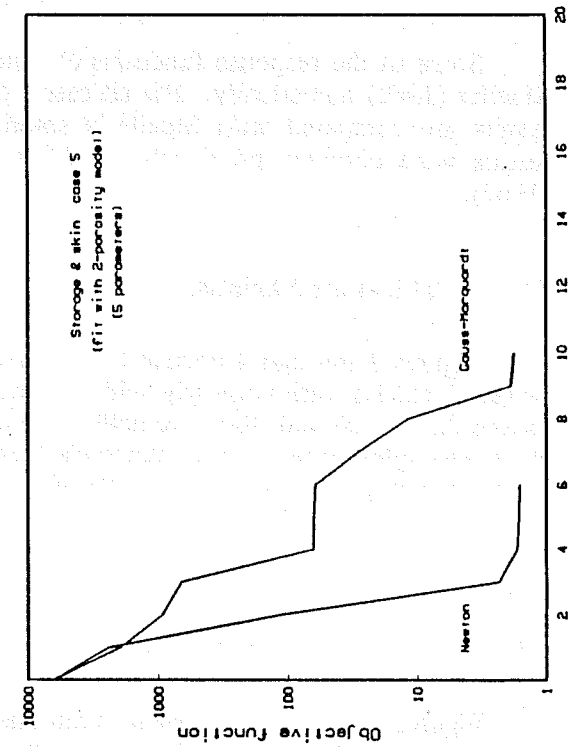

Fig. 19—Case 5—convergence of homogeneous reservoir data to two-porosity model.

4.3 AN ANALYTICAL STUDY OF TRANSIENT FLOW IN LINEAR HETEROGENEOUS AQUIFERS

(Anil K. Ambastha)

4.3.1. ABSTRACT

In performing material balance calculations as proposed by Hurst (1958), the dimensionless aquifer response to a unit pressure drop or a unit fluid-withdrawal rate is needed. Hurst assumed the aquifers to be homogeneous. Later, Mueller (1962) used finite-difference techniques to compute dimensionless pressure drop or cumulative influx of nonhomogeneous aquifers.

This study presents new analytical solutions for the dimensionless pressure drop or cumulative influx of nonhomogeneous aquifers whose thickness, permeability-viscosity ratio or porosity-compressibility vary linearly with distance. These solutions apply to linear flow conditions with finite aquifer size. The inner boundary condition could be either constant flow rate or constant flowing pressure. The outer boundary may be either closed, or at constant pressure.

Based on this study, a nonhomogeneous aquifer behaves as a homogeneous aquifer at early times. At late times, pseudosteady or steady state behavior is observed, depending on the outer boundary condition. But the dimensionless time to pseudosteady or steady state is dependent on the type and severity of property variation. Dimensionless influx rate behavior is also discussed for constant flowing pressure inner boundary condition.

4.3.2. RESULTS AND DISCUSSION

Some of the response functions obtained analytically in this work were also generated by Mueller (1962) numerically. For all cases, our results compare very well with his results. Our results are compared with Mueller's solution for one case in Table 1. Homogeneous case results were obtained previously by Miller (1962), Nabor and Barham (1964) and Mueller (1962).

4.3.2.1. Thickness Variation

Figures 1 through 4 present the solutions for various inner and outer boundary conditions where thickness varies linearly with distance. At early times, all results cluster in all cases, except for $\beta = 10$ and 100. Actually, results for $\beta = 10$ and 100 also approach the $\beta = 1$ case at dimensionless times lower than shown on the figures. At late times, flow goes to pseudosteady or steady state at dimensionless times of about 5 for all β values. When this occurs, all curves become parallel to the curve for a homogeneous aquifer case ($\beta = 1$) on a log-log graph.

4.3.2.2. Permeability Variation

Figures 5 through 8 present solutions for the cases where permeability varies linearly with distance. Again at early times, all curves (except for $\beta = 10$ and 100) are clustered together. In these cases, the aquifer approaches pseudosteady or steady state at a

dimensionless time of about 5. In the closed outer boundary cases, all curves merge with the homogeneous aquifer case solution at late times (See Figs. 5 and 7) on log-log graphs, and exhibit a unit slope. But in the constant pressure outer boundary cases, all curves become parallel to the homogeneous aquifer case, and exhibit zero slopes, on a log-log graph.

As also observed by Mueller (1962) at intermediate times, results for $\beta < 1$ are closer to the homogeneous aquifer case than are results for $\beta > 1$, for the same proportion of increase or decrease in permeability (See Figs. 5 and 7).

4.3.2.3. Porosity-Compressibility Variation

Referring to Figures 9 through 12, behavior approaches pseudosteady or steady state at a dimensionless time of about 5. For closed outer boundary cases, the response functions become parallel to the homogeneous aquifer case on a log-log graph, and for the constant pressure outer boundary cases, response functions merge with the homogeneous aquifer case. This is opposite the observation in the case of permeability variation. These observations resulted because ϕc_t appears only in the accumulation term, and permeability appears only in the diffusive term of the problem.

4.3.2.4. General

In all constant flow rate cases, dimensionless pressure drop functions for $\beta < 1$ remain above those for $\beta > 1$. That is, we incur more pressure drop for the same cumulative production when permeability, thickness or ϕc_t decreases away from the wellbore. In all constant flowing pressure cases, dimensionless cumulative influx functions for $\beta < 1$ are smaller than those for $\beta > 1$. That is, for same pressure drop, cumulative influx is greater if permeability, thickness or ϕc_t increases away from the wellbore.

Mixed inner and outer boundary conditions were not considered herein. It is fairly easy to develop solutions for such cases following the development in this study, if needed. Also we have restricted consideration to linear variation of the property. Solutions may also be obtained analytically for other types of variation of functions, e.g, power law variation (Carslaw and Jaegar, 1959).

4.3.3. CONCLUSIONS

1. Transient response problems for finite linear aquifers with linearly varying properties have been analytically solved for a variety of boundary conditions.
2. At early times, heterogeneous aquifers behave as equivalent homogeneous aquifers. After boundary effects have been felt at the reservoir-aquifer plane, there is a significant transition period before behavior goes to pseudosteady or steady state. During this transition period, response functions differ from the homogeneous aquifer solution. The severity of the variation depends upon the level of heterogeneity. Once the aquifer is in pseudosteady or steady state, response functions either merge with or stay parallel to homogeneous aquifer solutions on a log-log graph. Thus heterogeneous aquifers do not always necessarily behave as a homogeneous aquifer with equivalent properties.
3. Independent of the type and severity (up to a β of 10) of variation, aquifers go to pseudosteady or steady state approximately at a dimensionless time of about 5.
4. For constant flow rate cases, the dimensionless pressure drop functions for $\beta < 1$ stay above those for $\beta > 1$ and for constant flowing pressure cases, the dimensionless cumulative influx functions for $\beta < 1$ stay lower than those for $\beta > 1$.

4.3.4. REFERENCES

1. Carslaw, H.S., and Jaegar, J.C.: "Conduction of Heat in Solids," Second Edition, Oxford at the Clarendon Press, Oxford, England (1959).

2. Hurst, W.: "The Simplification of the Material Balance Formulas by the Laplace Transformation," *Trans. AIME* (1958) 213, 292.

3. Miller, F.G.: "Theory of Unsteady-State Influx of Water in Linear Reservoirs," *Journal Institute of Petroleum* (Nov. 1962) 48, 365.

4. Mueller, T.D.: "Transient Response of Nonhomogeneous Aquifers," *Soc. Pet. Eng. J.* (March 1962) 33-43.

5. Nabor, G.W., and Barham, R.H.: "Linear Aquifer Behavior," *J. Pet. Tech.* (May 1964) 561-563.

TABLE 1
DIMENSIONLESS PRESSURE-DROP FOR CLOSED OUTER BOUNDARY AND CONSTANT RATE INNER BOUNDARY CASE (β=4)

Dimensionless Time	Mueller's solution*	This study
.001	.035	.0343
.005	.073	.0731
.01	.1	.1
.05	.198	.1972
.1	.258	.2573
.5	.465	.4642
1	.66	.6648
5	2.3	2.2660
10	4.2	4.2653

Note* -- Read off Figure 9 of Reference 2.

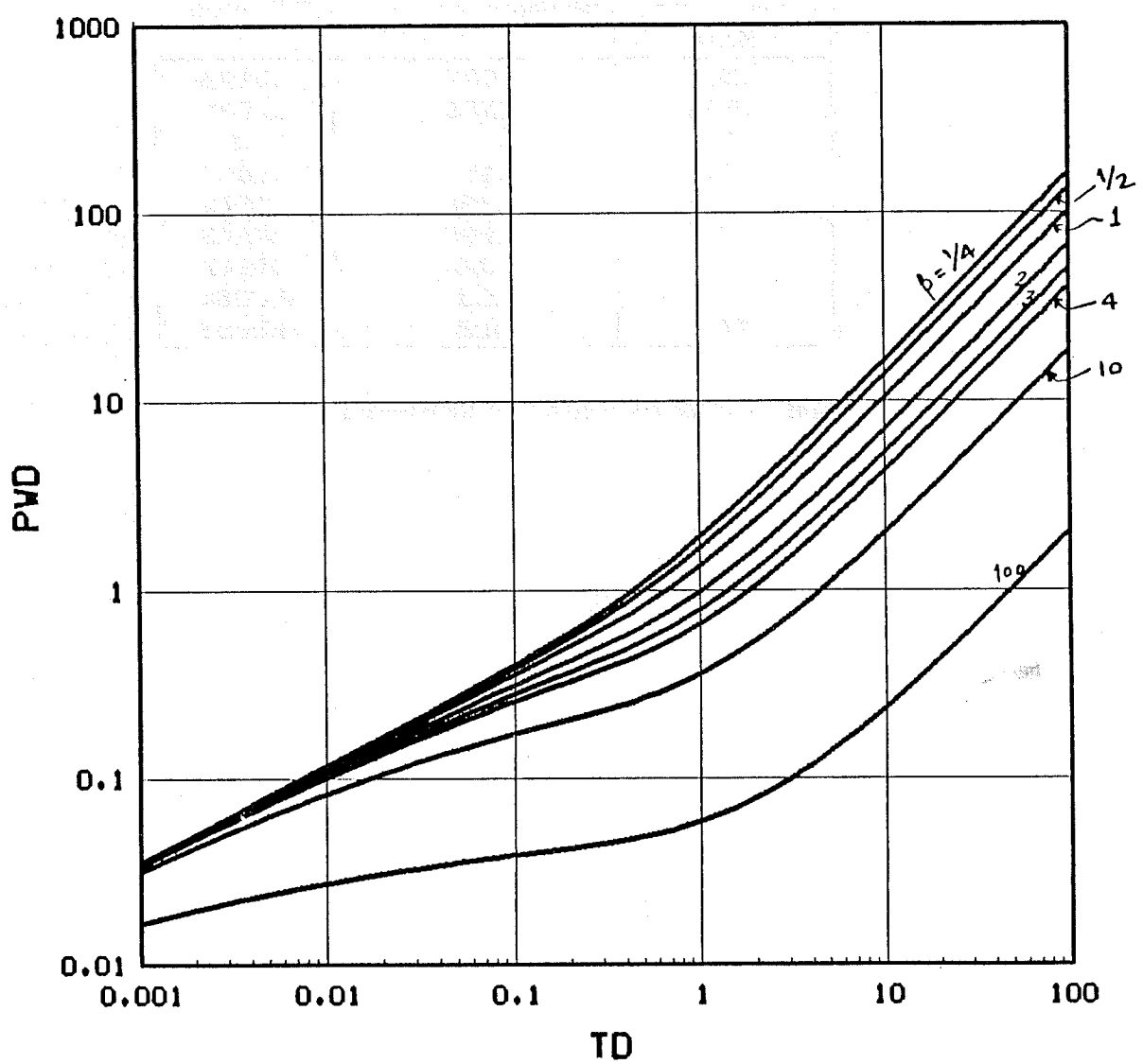

Fig. 1. Pressure-drop response function for a linear system. (Closed outer boundary, constant rate inner boundary.) Beta is the ratio of outer- to inner-boundary thickness.

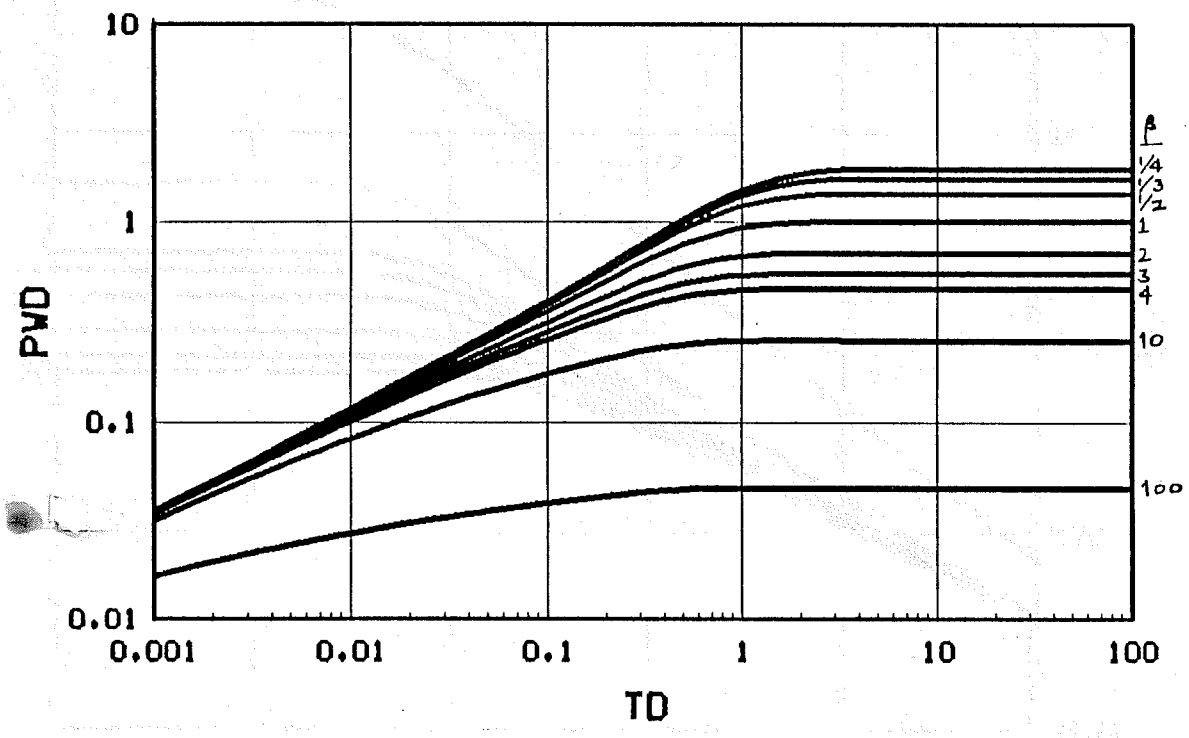

Fig. 2. Pressure-drop response function for a linear system. (Constant pressure outer boundary, constant rate inner boundary.) Beta is the ratio of outer- to inner-boundary thickness.

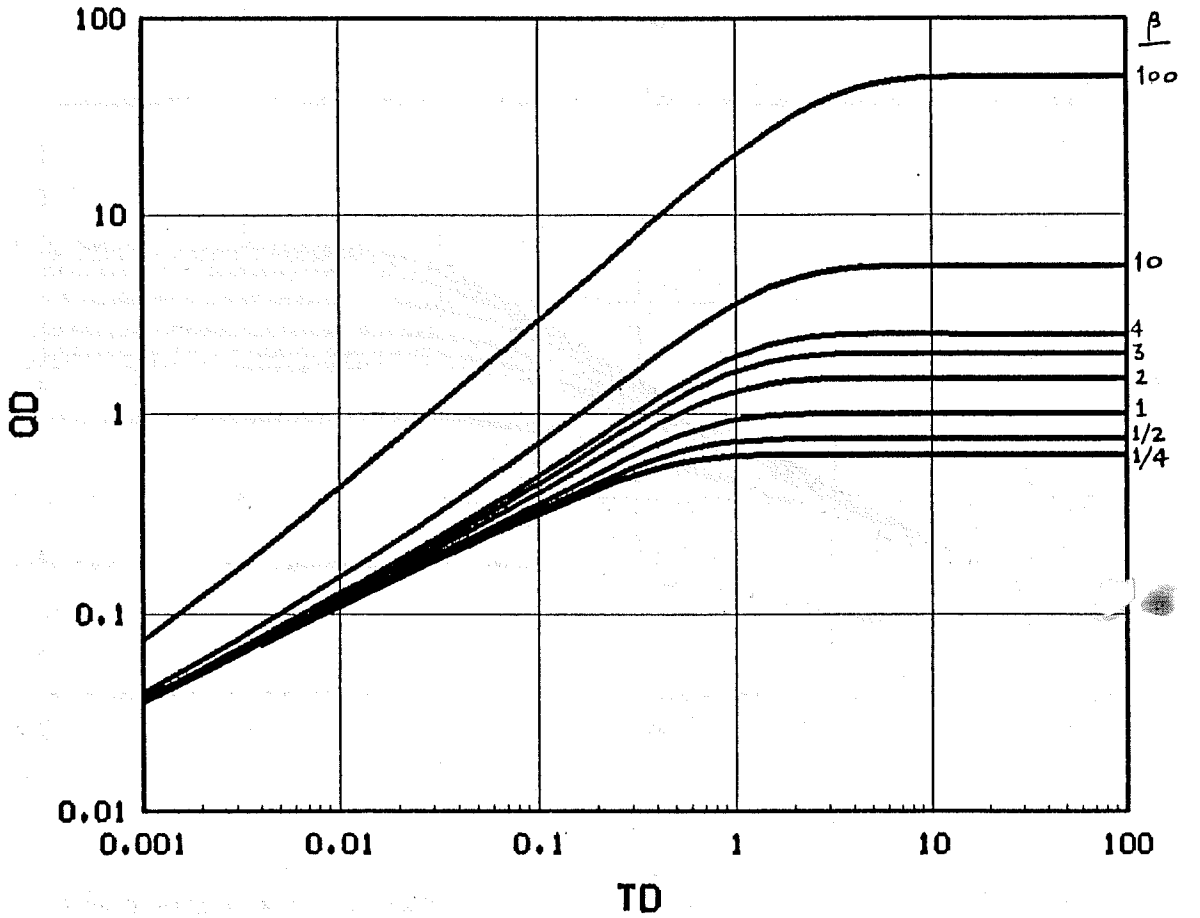

Fig. 3. Cumulative influx response function for a linear system. (Closed outer boundary, constant pressure inner boundary.) Beta is the ratio of outer- to inner-boundary thickness.

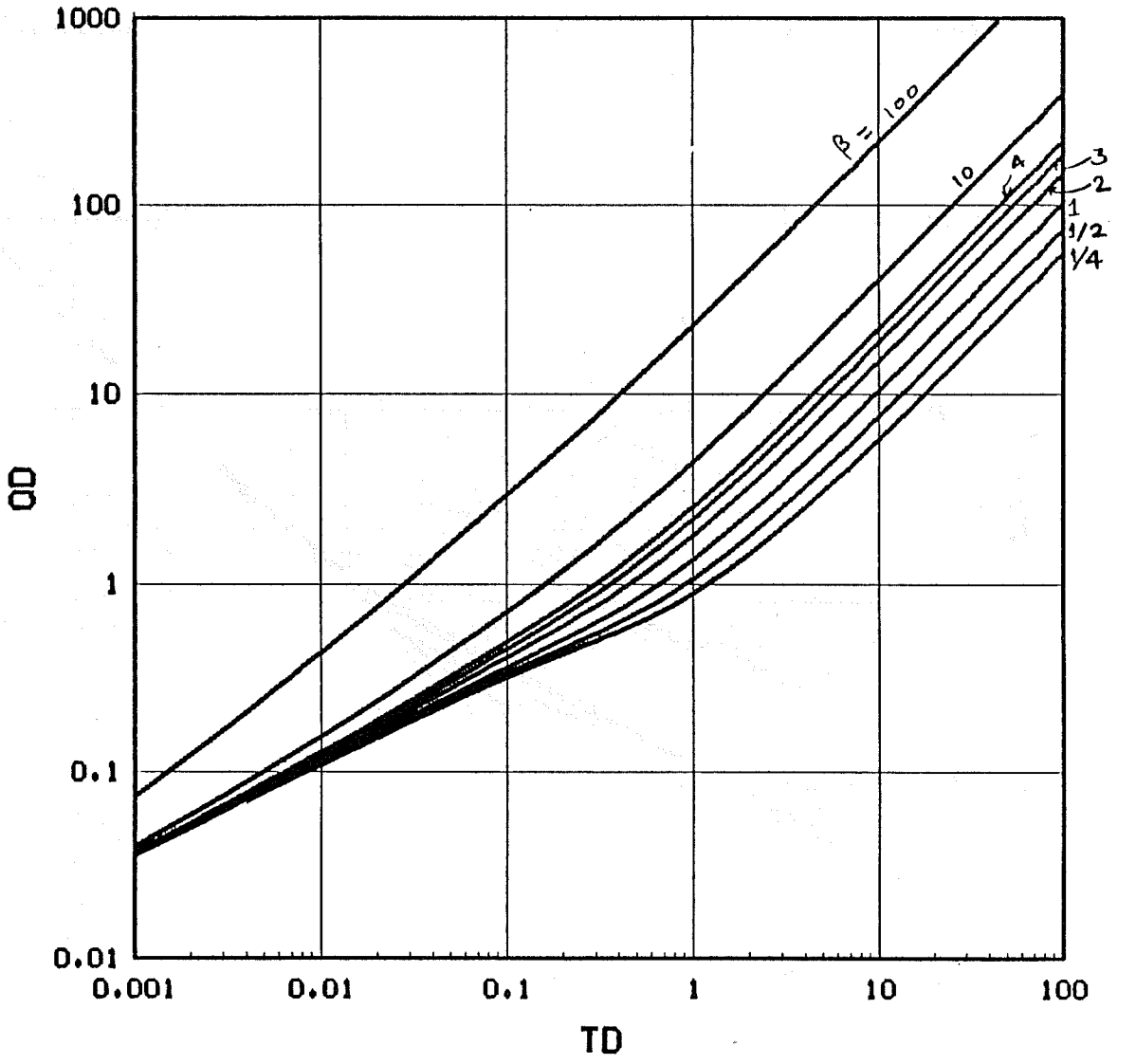

Fig. 4. Cumulative influx response function for a linear system. (Constant pressure outer boundary, constant pressure inner boundary.) Beta is the ratio of outer- to inner-boundary thickness.

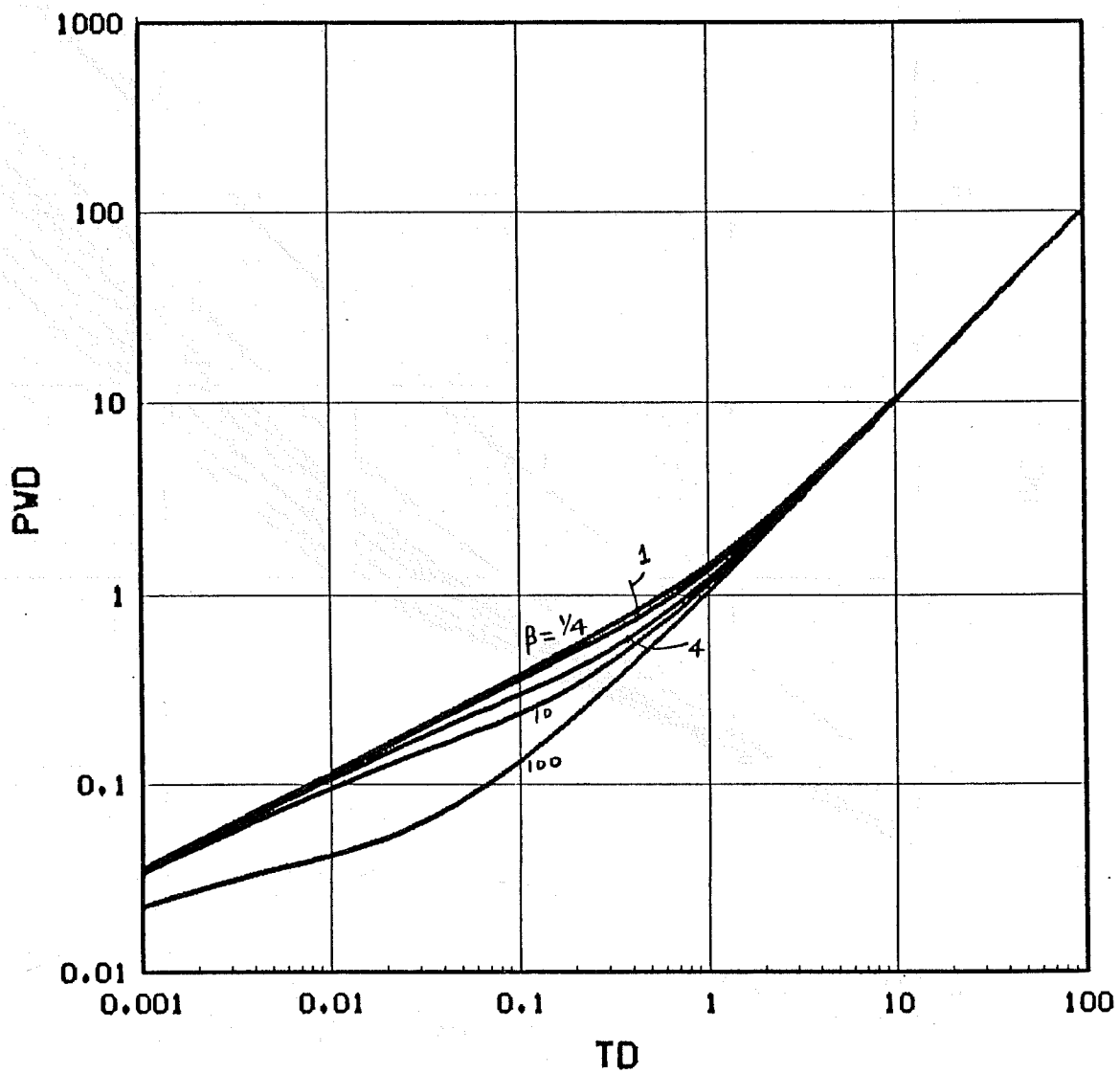

Fig. 5. Pressure-drop response function for a linear system. (Closed outer boundary, constant rate inner boundary.) Beta is the ratio of outer- to inner-boundary permeability.

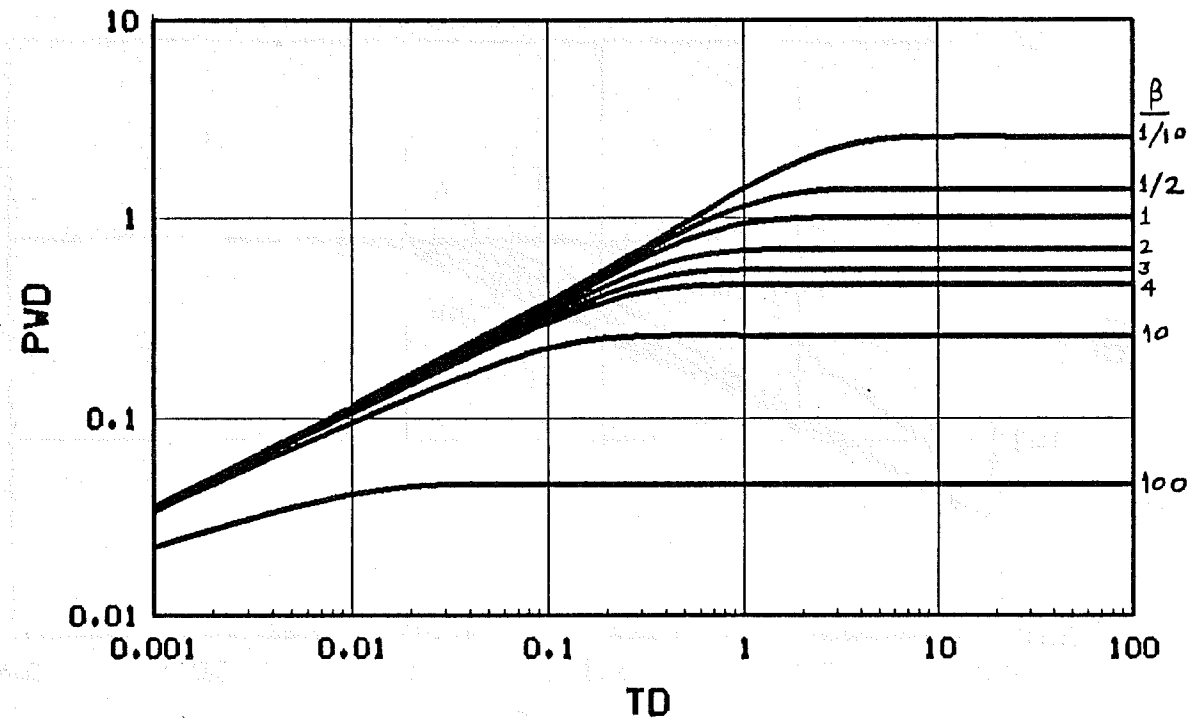

Fig. 6. Pressure-drop response function for a linear system. (Constant pressure outer boundary, constant rate inner boundary.) Beta is the ratio of outer- to inner-boundary permeability.

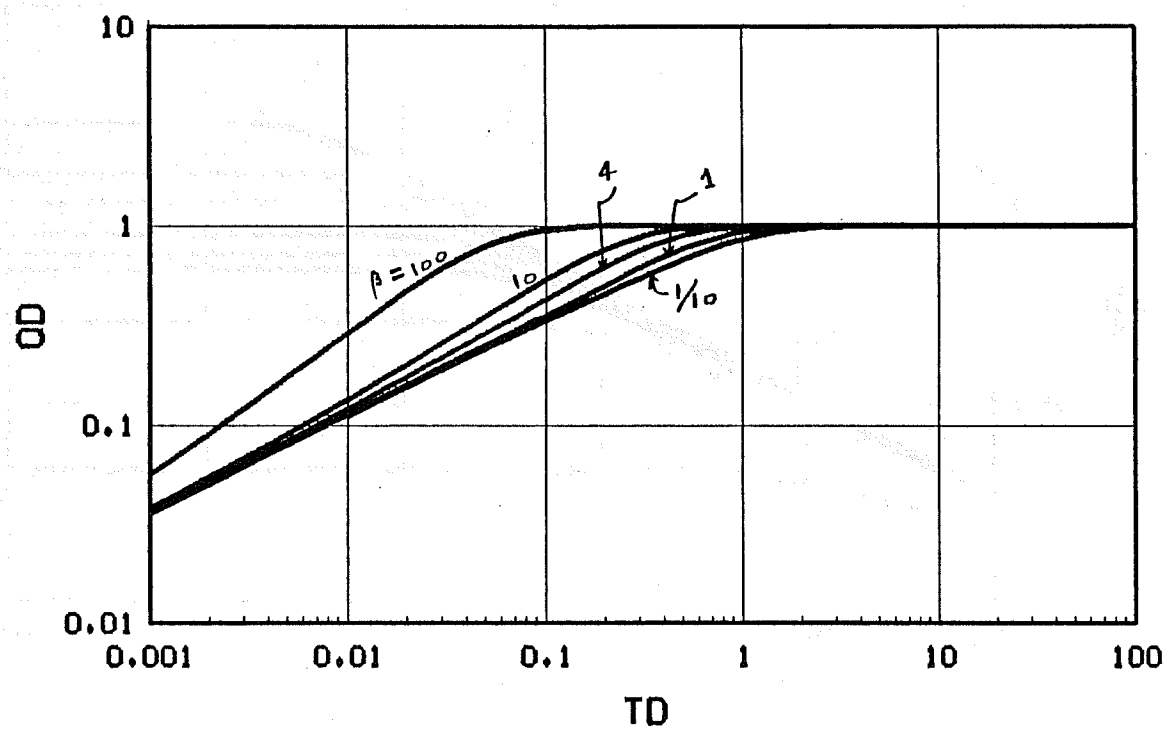

Fig. 7. Cumulative influx response function for a linear aquifer. (Closed outer boundary, constant pressure inner boundary.) Beta is the ratio of outer- to inner-boundary permeability.

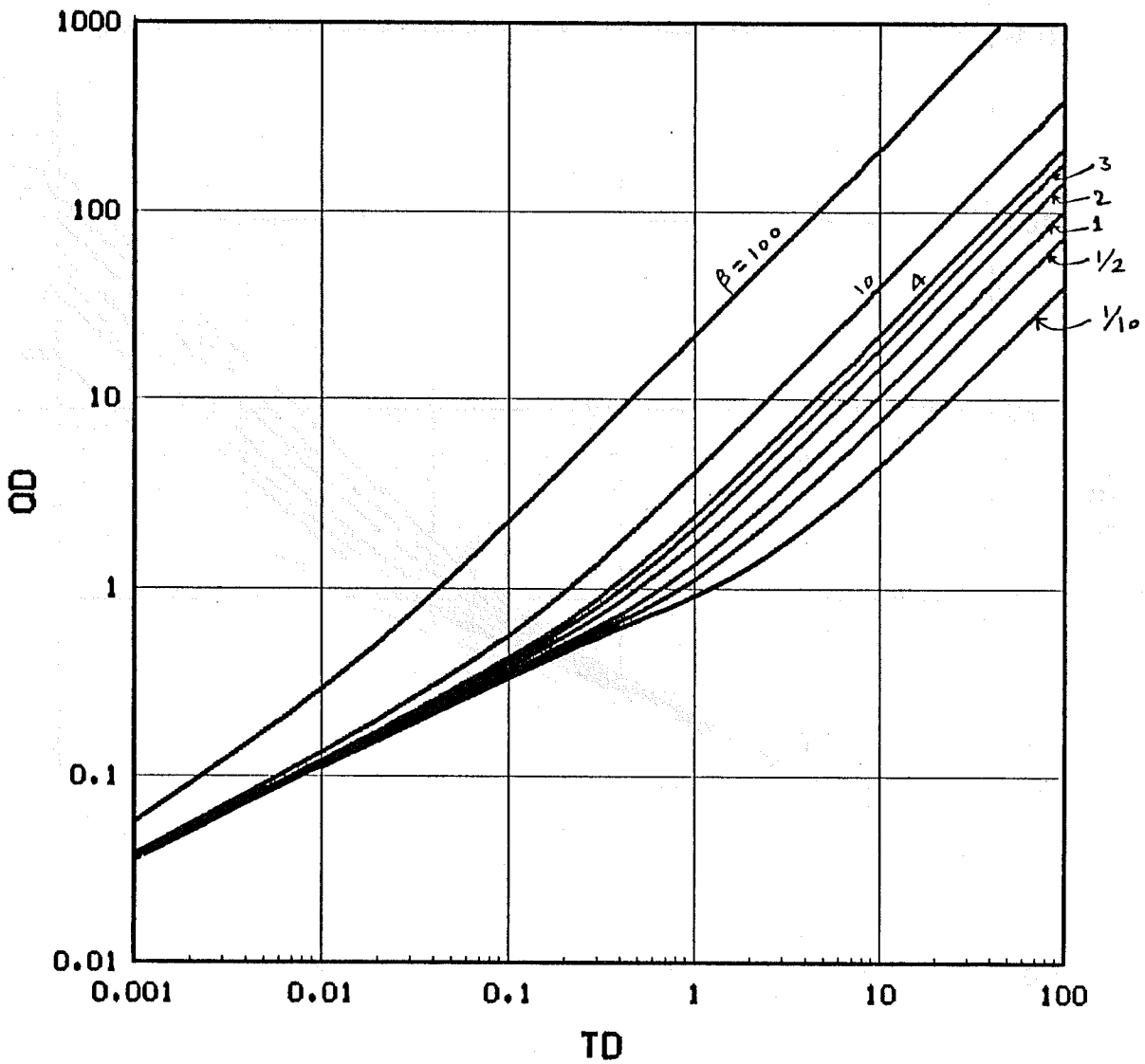

Fig. 8. Cumulative influx response function for a linear aquifer. (Constant pressure outer boundary, constant pressure inner boundary.) Beta is the ratio of outer- to inner-boundary permeability.

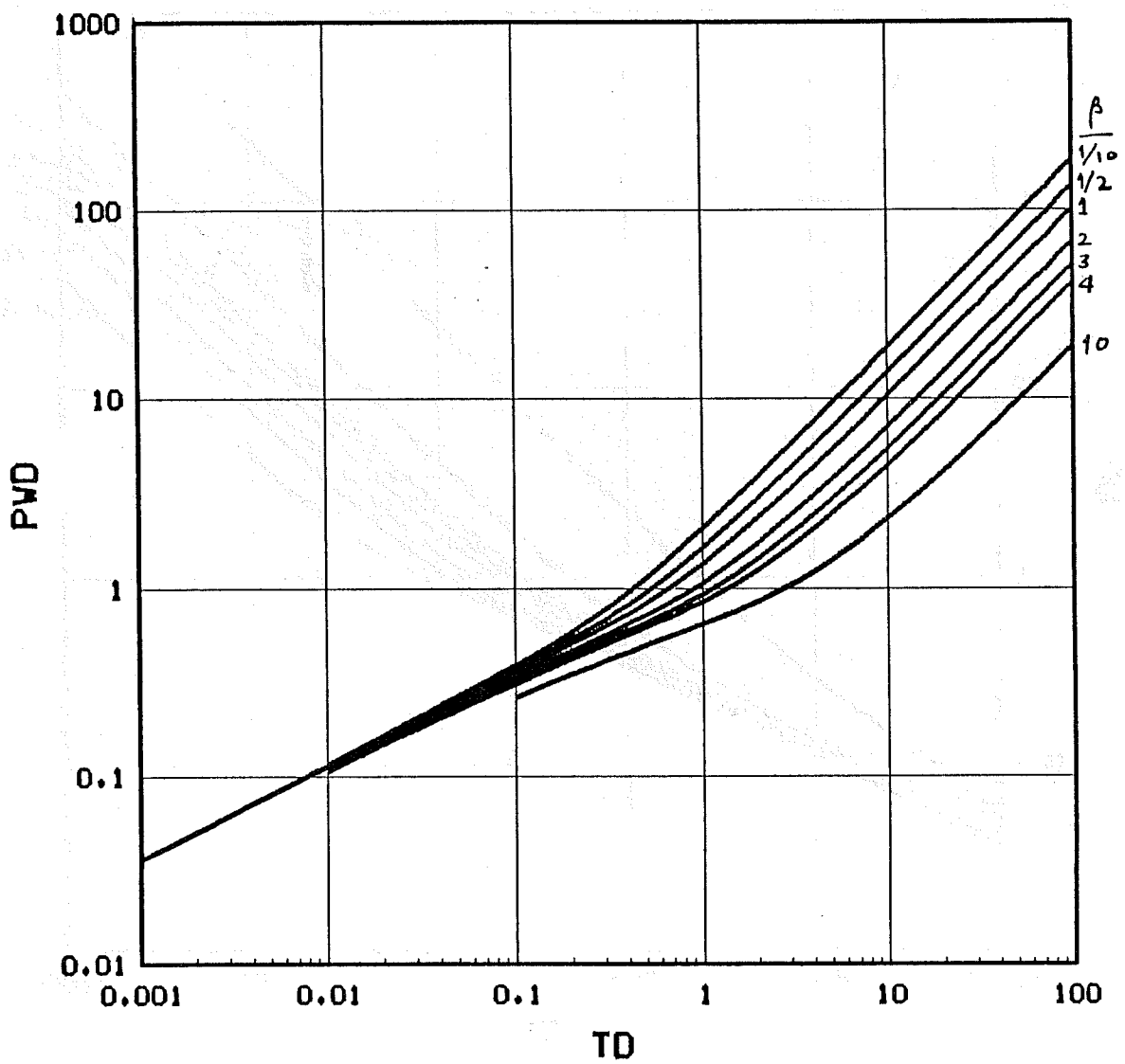

Fig. 9. Pressure-drop response function for a linear aquifer. (Closed outer boundary, constant rate inner boundary.) Beta is the ratio of outer- to inner-boundary compressibility or porosity.

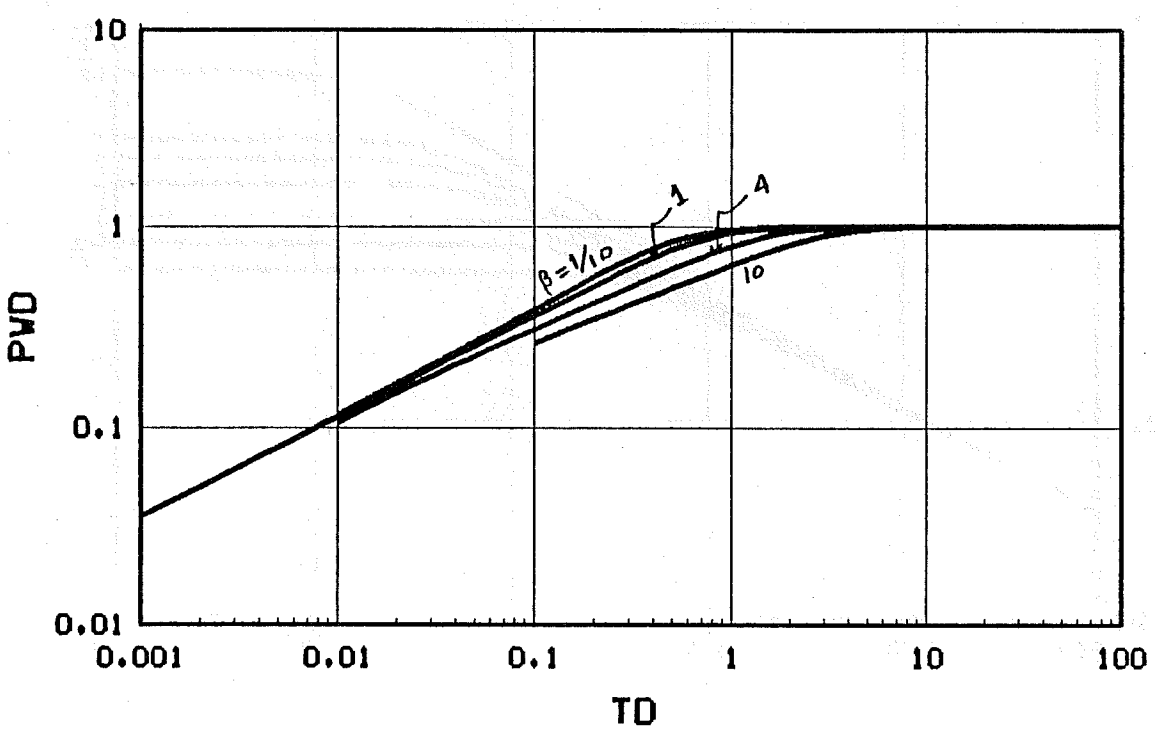

Fig. 10. Pressure-drop response function for a linear aquifer. (Constant pressure outer boundary, constant rate inner boundary.) Beta is the ratio of outer- to inner-boundary compressibility or porosity.

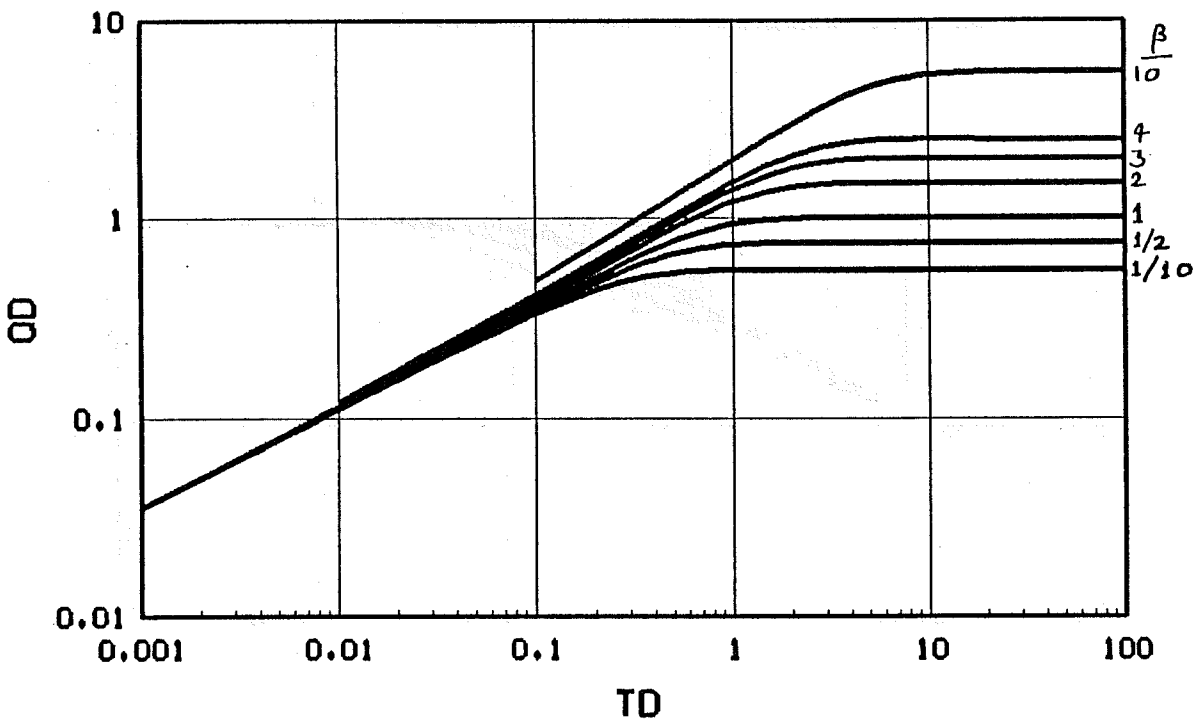

Fig. 11. Cumulative influx response function for a linear aquifer. (Closed outer boundary, constant pressure inner boundary.) Beta is the ratio of outer- to inner-boundary compressibility or porosity.

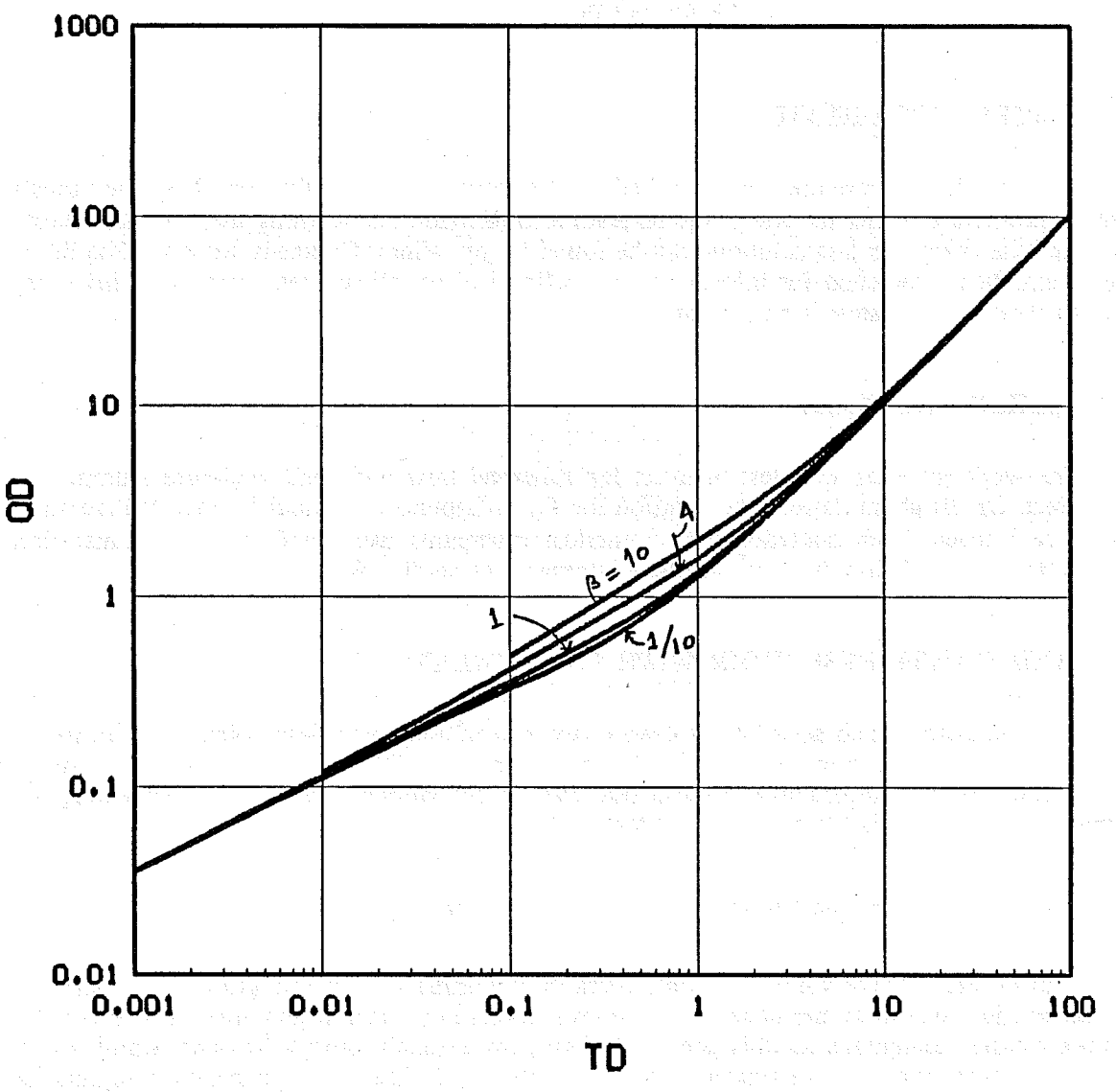

Fig. 12. Cumulative influx response function for a linear aquifer. (Constant pressure outer boundary, constant pressure inner boundary.) Beta is the ratio of outer- to inner-boundary compressibility or porosity.

4.4 WELL TESTING IN VARIOUS GEOMETRIES

(John W. Walsh Jr.)

This report summarizes the work and can be classified into four areas. For more detailed information on each area, please refer to the appropriate quarterly report.

4.4.1. INTRODUCTION

1. Literature Review
2. Spherical Flow
3. Composite Reservoir with Vertical Front
4. Composite Reservoir with Slanted Front

4.4.2. LITERATURE REVIEW

The petroleum literature was searched to determine the work that has been perviously done in pressure analysis for composite reservoirs. Information concerning the systems investigated and the corresponding solutions can be found in my Winter Quarterly Report. The literature is also being searched for information on cylindrical coordinate reservoirs (r-z) involving well test analysis or reservoir simulation.

4.4.3. SPHERICAL FLOW

The work involves well test analysis for spherical flow with both wellbore storage and skin effect. Dr. Brigham derived the solution for P_D in Laplace space and I converted the solution to real space. Both analytical and numerical inversions were performed. The analytical solution for spherical flow with just wellbore storage was studied first.

4.4.4. COMPOSITE RESERVOIR WITH VERTICAL FRONT

In 1980, Satman and associates solved a two region composite reservoir system in trying to simulate a pressure transient test for thermal reservoirs. They concluded that the swept volume could be determined from such a test. Part of the summer was spent reproducing the Satman work as it applied to thermal well test analysis.

4.4.5. COMPOSITE RESERVOIR WITH SLANTED FRONT

In most thermal reservoirs, the front separating the inner and outer regions is not vertical, but slanted due to gravity drainage. An important research project would involve solving the pressure transient equations for this geometry. Thus, my research project involves simulating a pressure transient test for a thermal injection well where the interface between two regions is slanted. During the summer, I began deriving the controlling equations and boundary conditions.

4.5 WELL TESTING FOR DRAINHOLES*

(Michael Clonts)

4.5.1. ABSTRACT

Drainholes have been drilled in several areas of the world and there is a need to understand these drainage systems for accurate well test analysis. A drainhole pressure transient solution could also aid in the evaluation of production induced drainholes. Although pressure transient analyses have considered many reservoir systems, there has been no publication to date of pressure transient analysis for horizontal drainholes.

This study presents an analytical solution for the transient pressure response of a uniform flux horizontal drainhole in an anisotropic reservoir of finite thickness. The solution also applys for a reservoir with multiple drainholes in a vertical array. The analytical solution is developed using instantaneous source functions, Green's functions and the Newman product method. The solution shows that there are two possible types of transient pressure behavior depending on the length of the drainhole relative to the height of the reservoir. If the drainhole is short, flow is characterized by three flow periods: an initial radial flow perpendicular to the drainhole axis, a transition flow period, and a pseudo-radial flow period. If the drainhole length is long relative to the reservoir height, the initial radial flow period ends instantaneously for all practical purposes. The transient pressure behavior here is identical to that of a uniform flux vertical fracture and is characterized by early time linear flow followed by a transition period and late time pseudo-radial flow.

It is demonstrated that the pressure transient response for multiple drainholes is identical to the single drainhole solution if dimensionless variables are defined relative to the number of drainholes. Consequently, the pressure response of a uniform flux vertical fracture can also be approximated by several short drainholes. The solution for infinite conductivity drainholes is also suggested by analogy to the infinite conductivity vertical fracture solution.

Log-log type curves are presented for various drainhole radii and can be used in the conventional manner to determine reservoir characteristics including directional permeability or drainhole half length. Short and long time approximations are presented along with appropriate time limits. Finally, conditions are defined for greater productivity than with vertical wells or hydraulic fractures.

---

*Clonts, M.D. and Ramey, H.J., Jr.: "Pressure Transient Analysis of Wells with Horizontal Drainholes," SUPRI TR-51, Stanford University, Stanford, Ca. (May 1986) [DE-ACO3-81SF11564].

4.6 DRILLSTEM TESTING
(Miguel A. Saldana)

4.6.1. PAPER SPE 8208, SLUG TEST DATA ANALYSIS INCLUDING THE INERTIAL EFFECT
(Kiyoshi Shinohara, Miguel A. Saldana-C., and H.J. Ramey, Jr.)

In 1976, van der Kamp described water well slug tests in which strange oscillations were observed in pressure. He presented an approximate analytic solution for the case of a slug test with inertia effects. In 1979, Shinohara and Ramey presented a study in the paper, SPE 8208, in which the complete problem described by van der Kamp was solved, using Laplace transform and approximate numerical inversion. Although the paper was accepted by publication by the Society of Petroleum Engineers, one serious question was raised. The analytic solution was subject to the assumption of a small sized slug, which corresponds to a drillstem test run with a very large liquid cushion. The importance of this assumption was not evident. This manuscript is a revised version of the original paper SPE 8208 by Shinahara and Ramey. Saldana investigated the effect of the size of slug and contributed to the preparation of this final manuscript. The results were also used to investigate the closed chamber type of drillstem test.

4.6.2. PAPER SPE 15478, WELLBORE INERTIAL AND FRICTIONAL EFFECTS ON DRILLSTEM TESTS FROM NATURALLY-FRACTURED RESERVOIRS
(Miguel A. Saldana-C., W.E Brigham, and H.J. Ramey, Jr.)

Several studies of the subject of drillstem testing and slug testing from naturally fractured reservoirs have been conducted at Stanford. The first was a study by Mateen and Ramey, and the most recent has been a study by A. Sageev. Both studies considered a fully damped flow in the wellbore and thus did not consider the possibility of either inertial or frictional effects on such tests. This paper by Saldana, Brigham, and Ramey extends the previous work of Mateen and Sageev to include both the inertia of the liquid mass in the wellbore and the frictional effects between liquid flowing in the wellbore and the drillstem. The subject solution considered the special case of a small slug (large liquid cushion). The results indicate that it may be possible to determine the interporosity flow parameter and the storativity ratio for two porosity (fissured or fractured) systems. On the other hand, there are many practical operating conditions under which it would be almost impossible to detect the difference between the double porosity and the single porosity reservoir. Perhaps the most important result of this study is that criteria were developed to estimate the potential importance of the wellbore inertial and frictional effects for practical tests.

4.6.3. PAPER SPE 15118, SLUG TEST AND DRILLSTEM TEST FLOW PHENOMENA INCLUDING WELLBORE INERTIAL AND FRACTIONAL EFFECTS
(Miguel A. Saldana-C., and H.J. Ramey, Jr.)

This paper concerns an extension of the early study of Shinohara on wellbore inertial and frictional effects during a slug test or drillstem test. A mathematical formulation of the wellbore momentum balance including a skin effect on the formation was prepared and solved using Laplace transformation with numerical inversion. Previous solutions by van der Kamp and Shinohara were reproduced and extended as special cases of a more general formulation. Practical criteria were developed to estimate the magnitude of such effects and used to analyze published drillstem test data. Results indicated that most published data are for conditions when neither inertia nor friction are significant effects, however, the developed criteria indicates that drillstem tests for deep productive systems may well be subject to significant inertial effects.

4.6.4. INERTIAL EFFECTS OF THE LIQUID-CUSHION SIZE ON DRILLSTEM TEST FLOW PHENOMENA
(Miguel A. Saldana-C. and H.J. Ramey, Jr.)

Frequently, a liquid cushion is used in drillstem testing to avoid high collapse stresses on the pipe. When a drillstem test tool is open, it is necessary to move the liquid cushion in the bore. This causes an inertial effect which can distort the flow period data. Most previous solutions have been performed under the assumption that the liquid cushion is nearly long enough to be in equilibrium with reservoir pressure or that it has negligible length. Mathematical formulation was prepared including the effects of inertia on the liquid column for different cushion lengths. This nonlinear solution was solved numerically by finite difference approximation. General solutions in terms of dimensionless groups were prepared which can be used to estimate reservoir properties from bottomhole pressure data or to design drillstem tests such that undesirable inertial effects are not present.

PROJECT 5: FIELD SUPPORT SERVICES

This section covers SUPRI participation in field-oriented studies.

5.1 THE COMPARATIVE ECONOMICS OF THERMAL RECOVERY PROJECTS
(Wayne E. Ramage)

5.1.1. OBJECTIVES

This project is an expansion and refinement of the work of R.L. Williams, *et al.*, in 1980, entitled, "A Method To Evaluate the Economics of Thermal Recovery Projects." I will undertake to accomplish the following objectives:

1. Refine the computer programs (HEATRAN and VOLBURN) of Williams, *et al.*, in order to make them more easily read and to remove minor bugs now extant. The HEATRAN program will calculate the heat losses at the surface, in the wellbore, and to the adjacent formation in order to determine the amount of oil that may be displaced and recovered in a steam-flood, based on available studies in the published literature. The VOLBURN program will determine the design parameters for *in-situ* combustion projects, based on laboratory combustion tube and field data
2. Optimize the recovery schedules of both types of thermal projects
3. Optimize the economics of each project by generating a discounted net present value, internal rate-of-return, and payout period. The various economic factors will be varied according to predictions of inflation and future price scenarios. Probabilities will be taken into account in more depth than was done previously.
4. Analyze the sensitivity of the economic outcome to inputted parameters. This will be especially helpful in determining which parameters should be estimated with the most certainty.
5. Apply this method to a number of projects beyond the So. Belridge field, although the field will be included in this report.

5.1.2. PROJECT STATUS

1. VOLBURN Computer Program: This program is a small program, requiring less input data and fewer assumptions then HEATRAN. It uses the oil recovery-volume burned method presented by Gates and Ramey in 1978 to determine air/oil ratios and total oil recovery. Input parameters require information on combustion tube data and reservoir properties. The first are based on various studies in the literature, while the latter are obtained from published field studies. From these inputs the program calculates combustion tube and reservoir variables, such as oil-in-place and displaced oil, and eventually the oil recovery rate and air/oil ratios.

   At present, the VOLBURN program has been updated and revised as stated in the objective. A sample output from this program is attached to this report.

2. HEATRAN Computer Program: This program is much larger and requires far more input parameters. In order to calculate heat losses at the surface, the surface line is considered in segments of specified lengths. The frictional pressure drop is calculated according to Earlougher, and the steam quality is determined from the heat balance equation. Heat losses in the wellbore are determined also by dividing the line into segments. The pressure drop is calculated using the Bernoulli equation, and heat losses through the tubing (assuming the steam is not injected into the casing) are estimated using Ramey's method developed in 1962. The loss of heat to

adjacent formations is based on the Marx-Langenheim method (1959), later detailed by Ramey (1964). Finally, oil recovery schedules and steam injectivities are calculated.

This program has also been revised to a large extent. The option of adding code to take the injection of foam into account is now being considered.

3. The economics computer program, a completely new program, is now in the initial stages of composition. It is expected that this will be completed by November 30.

TABLE 1
INPUT TABLE

RESERVOIR	
Area (ft. 2)	217800.0
Thickness (ft)	93.000
Initial Saturations, Oil	0.67
Initial Saturations, Gas	0.07
Initial Saturations, Water	0.26
Porosity	0.34
AFI Gravity	13.0000
Formation Volume Factor	1.030
Air Injection Rate	2.000
Total Area of Project	5.00

TUBE RUN	
Porosity	0.35
Radius, In.	1.250
Air Flux	120.0000
Velcocity of Burning Front	3.500
Gas Composition of *CO* (wt%)	3.0000
Gas Composition of CO_2, (wt%)	12.0000
Gas Composition of O_2, (wt%)	0.5000
Gas Composition of N_2, (wt%)	84.5000
Composition of Air Used O_2, (wt%)	21.0000
Composition of Air Used N_2, (wt%)	79.0000
Fuel Consumed, bbl/acre-ft	293.3668
Air Fuel Ratio	198.0068
Air Required, mmscf/acre-ft	20.3310
Original OIP, bbl/ac-ft	1715.7986
Constant AOR	14.2931
Water Fuel Ratio	1.4245
Displaced Oil, bbl/ac-ft	1422.4318
Total Oil, bbl	797846.4
Oil Recovery from Graph by Gates-Ramey	0

TABLE 2

Volume Burned %	Oil Recovered %	Reciprocal of Slope	Current AOR mscf/bbl	Excess Air Fraction	Injected AOR mscf/bbl	Time Days
5.000	1.06	5.00	71.47	-14.89	60.82	236.35
10.000	8.67	0.66	9.40	-8.05	8.65	472.70
15.000	16.67	0.63	8.93	-0.85	8.86	709.04
20.000	24.46	0.64	9.16	6.17	9.73	945.39
25.000	31.96	0.67	9.53	12.92	10.76	1181.74
30.000	39.16	0.69	9.93	19.39	11.85	1418.09
35.000	45.76	0.76	10.83	25.33	13.57	1654.44
40.000	52.06	0.79	11.34	31.00	14.86	1890.78
45.000	58.06	0.83	11.91	36.40	16.25	2127.13
50.000	63.75	0.88	12.54	41.53	17.74	2363.48
55.000	69.05	0.94	13.48	46.29	19.73	2599.83
60.000	73.84	1.04	14.89	50.61	22.42	2836.18
65.000	78.34	1.11	15.88	54.65	24.56	3072.52
70.000	82.63	1.16	16.62	58.52	26.35	3308.87
75.000	86.62	1.25	17.87	62.11	28.96	3545.22
80.000	90.32	1.35	19.32	65.44	31.95	3781.57
85.000	93.81	1.43	20.42	68.58	34.42	4017.92
90.000	96.31	2.00	28.59	70.83	48.83	4254.27
95.000	98.40	2.38	34.03	72.71	58.78	4490.61
100.000	100.00	3.13	44.67	74.15	77.79	4726.96

TABLE 3

Volume Burned %	Oil Recovered %	Oil Recovered bbl	Air Required mmscf	Cumulative AOR mscf/bbl
5.00	1.06	7031.01	472.70	67.23
10.00	8.67	57346.05	945.39	16.49
15.00	16.67	110232.73	1418.09	12.86
20.00	24.46	161815.06	1890.78	11.68
25.00	31.96	211408.50	2363.48	11.18
30.00	39.16	259017.64	2836.18	10.95
35.00	45.76	302672.03	3308.87	10.93
40.00	52.06	344346.81	3781.57	10.98
45.00	58.06	384023.41	4254.27	11.08
50.00	63.75	421678.63	4726.96	11.21
55.00	69.05	456697.47	5199.66	11.39
60.00	73.84	488409.09	5672.35	11.61
65.00	78.34	518136.50	6145.05	11.86
70.00	82.63	546541.00	6617.75	12.11
75.00	86.62	572961.13	7090.44	12.38
80.00	90.32	597392.44	7563.14	12.66
85.00	93.81	620491.50	8035.83	12.95
90.00	96.31	637004.13	8508.53	13.36
95.00	98.40	650880.25	8981.23	13.80
100.00	100.00	661430.81	9453.92	14.29

*U.S. GOVERNMENT PRINTING OFFICE: 1986-0-659-031/40034